QUANTITATIVE COSMOLOGY

- MASSIVE NEUTRINOS IN NON-LINEAR STRUCTURE FORMATION

JACOB BRANDBYGE

DEPARTMENT OF PHYSICS AND ASTRONOMY
FACULTY OF SCIENCE
AARHUS UNIVERSITY
DENMARK

PhD DISSERTATION

QUANTITATIVE COSMOLOGY

- MASSIVE NEUTRINOS IN NON-LINEAR STRUCTURE FORMATION

A DISSERTATION
PRESENTED TO THE FACULTY OF SCIENCE
OF AARHUS UNIVERSITY
IN PARTIAL FULFILMENT OF THE REQUIREMENTS FOR THE
PhD DEGREE

BY
JACOB BRANDBYGE
AUGUST 2010

Summary in English

Cosmology addresses the questions of the formation and evolution of the Universe. According to our present understanding, the Universe consists of ordinary visible matter and neutrinos, as well as a dark sector comprised of Cold Dark Matter and Dark Energy. We believe that the cosmos was created in a Big Bang, whereafter space-time expanded rapidly during a brief period of inflation. Then the perturbations created during the first second of the Universe started to evolve under the force of gravity, slowly creating the Universe surrounding us today. When the perturbations reach the non-linear regime they cannot any longer be evolved with analytical equations. Instead, these perturbations must be followed by discrete particles in N-body simulations.

This PhD dissertation presents scientific research on the effect of massive neutrinos on non-linear cosmological structure formation. It first gives a general presentation of inflation, General Relativity and the evolution of structure in the early Universe, and then reviews neutrino physics and the observations against which cosmological theories are confronted. Then three newly developed methods to include the effect of massive neutrinos in N-body simulations are described together with their strengths and weaknesses.

These methods are used to calculate the effect of neutrinos on statistical measurable quantities, such as the non-linear matter power spectrum, matter density profiles and finally the number density of halos in various halo mass intervals. This dissertation also presents calculations on the non-linear neutrino power spectrum and neutrino density profiles. Finally, the Cosmic Neutrino Background anisotropy emitted within the first second after the Big Bang is calculated for massive neutrinos.

It will be demonstrated that it is important to include massive neutrinos in models of non-linear structure formation, if these models should match the sensitivity of future high precision cosmological observations.

Finally, the scientific results presented in this dissertation are compared with the results obtained by other scientific groups. These groups base their results on different versions of perturbation theory as well as N-body simulations. Through this comparison it will be demonstrated that the methods and results presented in this PhD dissertation are robust.

Dansk resumé (Summary in Danish)

Kosmologi forsøger at finde svar på spørgsmålene om universets skabelse og udvikling. Ifølge vores nuværende forståelse, så består universet af normalt synligt stof og neutrinoer, samt af en mørk sektor som udgøres af koldt mørkt stof og mørk energi. Vi mener, at universet blev skabt ved et Big Bang, hvorefter rumtiden udviklede sig hurtigt under en kort periode med inflation. Derefter udviklede de overtætheder, der blev skabt i det første sekund efter Big Bang sig under tyngdekraftens påvirkning til det univers, vi kan observere i dag. Når overtæthederne bliver ikke-lineære kan de ikke mere beregnes med analytiske ligninger, men i stedet skal de følges med diskrete partikler i N-body simuleringer.

Denne ph.d.-afhandling præsenterer videnskabelig forskning om effekten af massive neutrinoer på ikke-lineær kosmologisk strukturdannelse. Først gives der en generel præsentation af inflation, generel relativitetsteori og udviklingen af struktur i det tidlige univers, hvorefter neutrino fysik og observationer, som de kosmologiske modeller testes imod, præsenteres. Derefter beskrives tre nyudviklede metoder, hvormed effekten af massive neutrinoer kan inkluderes i N-body simuleringer, sammen med deres styrker og svagheder.

Disse metoder bliver brugt til at beregne effekten af neutrinoer på statistiske målbare størrelser, så som det ikke-lineære power spektrum, tæthedsprofiler og endelig massetætheden af haloer i forskellige masseintervaller. Denne afhandling præsenterer også beregninger af det ikke-lineære neutrino power spektrum og af neutrino tæthedsprofiler. Endelig bliver den kosmiske neutrino baggrundsstråling, der blev udsendt inden for det første sekund efter Big Bang, beregnet for massive neutrinoer.

Det vil blive demonstreret, at det er vigtigt at inkludere neutrinoer i modeller af ikke-lineær strukturdannelse, såfremt disse skal matche den høje præcision fra kommende kosmologiske observationer.

Til sidst sammenlignes de videnskabelige resultater præsenteret i denne afhandling med resultater fra andre forskergrupper. Disse grupper baserer deres resultater på forskellige former for perturbationsteori og N-body simuleringer. Gennem denne sammenligning vil det blive demonstreret, at de metoder og resultater der er blevet præsenteret i denne ph.d.-afhandling er robuste.

Contents

Part I

Overview of Cosmological Structure Formation and Neutrino Physics

Chapter 1

Introduction

Cosmology is the branch of physics describing the formation and evolution of the Universe. It was once believed that the Universe was static and only consisted of ordinary visible matter, but this belief has been challenged within the last century by the interplay between theories and ever more sophisticated observations.

Today we believe that the Universe was created in a Big Bang and that it has been expanding ever since. We assume that it consists of ordinary visible baryonic matter together with non-luminous Cold Dark Matter (CDM), light fast-moving neutrinos and a component with exotic properties leading to the current accelerated expansion of the Universe. This component, called Dark Energy, comprises roughly 73% of the energy in the Universe, with CDM contributing approximately 22%. This leaves a meager 5% left for the matter we know, namely baryons and neutrinos with the latter making up less than 1%. But even a 1% contribution must be included in models with the aim of matching the sensitivity of future cosmological observations.

We have come a long way towards a better understanding of cosmology, but as we dig deeper new unknowns appear. We are now at a stage where we can address questions about the creation of the Universe and the ensuing inflation. We are in a position where we can create models about the fundamental physics underlying CDM and Dark Energy. For many cosmologists this dark sector merely provides a good mathematical fitting-model, our cosmological standard model, which matches current observations. Determining the numerical values of the cosmological parameters is an important first step towards the final goal of developing theories, which are capable of actually explaining the numerical values and the underlying physics in the sought after divine cosmological model.

This dissertation combines key predictions from inflation and General Relativity with assumptions about the properties and interactions between the energy components, with the objective to provide a scheme to accurately model the effect of massive neutrinos on structure formation. The emphasis is on observable statistical quantities in the non-linear regime where the density contrasts of the energy components approach and exceed unity. With N-body simulations as the tool it focuses on how the effect of the neutrino component can be reliably modelled and uses the developed schemes to calculate the non-linear distribution of CDM and neutrinos in our Universe.

This PhD dissertation includes the research from the following 5 papers, namely

The Effect of Thermal Neutrino Motion on the Cosmological Matter Power Spectrum [1],

Grid Based Linear Neutrino Perturbations in Cosmological N-body Simulations [2],

Resolving Cosmic Neutrino Structure: A Hybrid Neutrino N-body Scheme [3],

Neutrinos in Non-linear Structure Formation: The Effect on Halo Properties [4],

The Cosmic Neutrino Background Anisotropy - Linear Theory [5].

During my PhD I have also been a co-author on two additional papers, namely

Solar-like oscillations in the G2 subgiant Beta Hydri from dual-site observations [6],

Angular Signatures of Annihilating Dark Matter in the Cosmic Gamma-Ray Background [7].

These two papers have not been included in this dissertation for the dual reasons that I have only made minor contributions and that the content of these papers lies outside the main scope of this dissertation.

The scientific research papers presented in this dissertation are not completely identical to the ones published. Since the aim is to present a coherent dissertation, the introductions of some of the papers have been slightly altered with the aim of avoiding repetitions. Along the same lines, some of the theory sections in the papers have been reduced if the material has already been covered in the general presentation of cosmology. The part of the theory which is directly relevant for understanding the articles is reiterated and maintained in the papers, with the aim of avoiding multiple cross-references over many chapters in the dissertation. This has the advantage of not only repeating important theory, but also allows the papers, as they are presented in this dissertation, to be read by a practitioner in cosmology without resolving to the general cosmology part. The remaining parts of the papers, explaining the particular simulation setups and the result sections, are basically identical to the published versions. They have only been slightly modified with the aim of homogenizing the language and notation within the dissertation.

Different areas of cosmology have their own notations, and these quite often involve the use of the same letters from the Greek alphabet. This dissertation does not redefine symbols with the aim of avoiding multiple meanings of the same symbol. Instead, it uses the symbols appropriate for the particular area.

This dissertation will present a general presentation of cosmology in Part I. Due to the research emphasis on non-linear structure formation and neutrinos, the theoretical presentation will focus on theories and assumptions which directly affect the input to N-body simulations. Chapter 2 presents the cosmological Standard Model and the theory behind the evolution of perturbations in the linear regime. Then Chapter 3 gives an introduction to N-body initial conditions and how they are evolved in an N-body integrator. Chapter 4 introduces neutrino physics and in Chapter 5 cosmological observations and constraints on the neutrino mass are presented.

Part II contains the scientific research results. In Chapter 6 the particle approach to include neutrinos in N-body simulations is presented and the effect of neutrinos on the non-linear matter power spectrum is quantified. This chapter also presents calculations on the non-linear neutrino power spectrum. Chapter 7 describes the linear grid implementation of neutrinos in N-body simu-

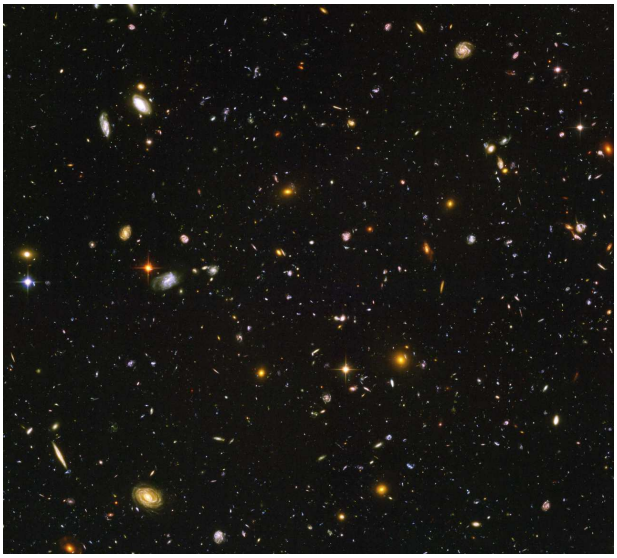

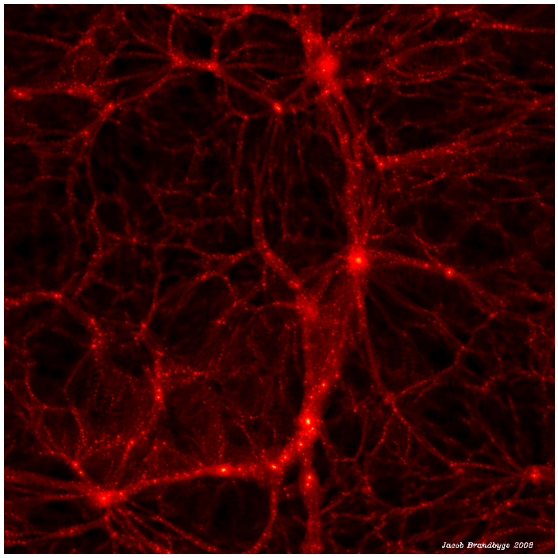

Figure 1.1: Left: Distribution of galaxies in the Universe observed with the Hubble Space Telescope [8]. Right: The CDM distribution taken from an N-body simulation. In cosmology, observations and theories are combined with the aim of increasing our understanding of the Universe.

lations and compares the method to the particle approach. Then Chapter 8 combines the best from the particle and grid approaches with the aim of allowing a more precise and efficient calculation of cosmological observables. Chapter 9 then investigates the effect of neutrinos on matter density profiles and the halo mass function as well as the density profiles of the neutrino component itself. Finally in Chapter 10 the Cosmic Neutrino Background anisotropies are calculated with linear theory.

In Part III, Chapter 11 compares the scientific results presented in Part II with those obtained by other scientific groups. Finally Chapter 12 contains our conclusions and presents reflections on how the scientific methods described in this PhD dissertation can be developed further.

Chapter 2

The Cosmological Model

This chapter will present the cosmological Standard Model which is based on the Einstein equations. These equations will be used to describe the background evolution of the Universe whereafter the theories of Big Bang and inflation will be presented. Finally the evolution of perturbations in the linear regime will be described in detail.

2.1 The general framework

This section will begin with a general introduction to metrics and how they are used in the Einstein equations. Then background evolution equations will be presented since they are needed in the presentation of inflation in the next section. The material presented in this section can be found in [9, 10, 11].

2.1.1 Coordinate systems

The Friedmann-Robertson-Walker (FRW) line element for a homogeneous and isotropic Universe is related to the invariant space-time interval ds^2 by

$$ds^2 = a^2(\tau)\left[-d\tau^2 + \frac{dr^2}{1-\kappa r^2} + r^2(d\theta^2 + sin^2\theta d\phi^2)\right], \tag{2.1}$$

where units are chosen so that the speed of light equals unity and we have used the metric signature $(-, +, +, +)$. τ is the conformal time related to the cosmic time t by $dt = ad\tau$. Since the scale factor a is a global factor r, θ and ϕ are comoving coordinates expanding with the Universe. κ determines the geometry of the Universe and is positive for a closed Universe, negative for an open Universe and equal to zero for a flat Universe. From the scale factor the redshift z is defined from $a = 1/(1+z)$.

In general a coordinate system, x^μ, and a 4×4 metric (or metric tensor), $g_{\mu\nu}$, are related by $ds^2 = dx_\mu dx^\mu = dx_0 dx^0 + dx_i dx^i = g_{\mu\nu} dx^\mu dx^\nu$. The Greek and Roman indices can take on integer values from 0 to 3 and 1 to 3, respectively, and repeated indices imply summation. x^0 represents the time coordinate whereas x^i will designate the spacial coordinates. The metric can be chosen in several ways, though of course in the end the physically measurable quantities do not depend on the chosen coordinate system. The most commonly used coordinate systems are the synchronous and conformal Newtonian (longitudinal) gauges.

The synchronous gauge earns its name from the fact that there are no perturbations to the parts of the metric tensor involving time components. It is used in the publicly available linear theory solver CAMB [12], and has the advantage that integrations should be numerically more stable as compared to the conformal Newtonian gauge.

The conformal Newtonian gauge is so-called, since it uses conformal time and reduces to the ordinary Newtonian results in the low velocity, small-scale limit. In the conformal Newtonian, contrary to the synchronous, gauge there are no spurious gauge modes for a flat cosmology except for additions of physically irrelevant constants to the metric perturbations. We choose the conformal Newtonian gauge since it provides an intuitive physical interpretation. The metric in a flat cosmology is then given by

$$ds^2 = a^2(\tau)[-(1+2\psi)d\tau^2 + (1-2\phi)\delta_{ij}dx^i dx^j], \tag{2.2}$$

where ψ and ϕ are metric perturbations encoding small deviations from flatness, and they are sourced by inhomogeneities in the energy distribution. Only two scalar and no vector or tensor metric perturbations are included in Eq. (2.2), since these are the only ones which are necessary to describe the formation of large-scale structure. Non-relativistic components such as CDM and baryons lead to $\psi = \phi$, but in the early Universe the relativistic neutrinos drive ψ and ϕ away from each other.

2.1.2 The Einstein equations

The Einstein equations, proposed by Albert Einstein in 1915 [13], postulate the relationship between the energy of the Universe and the curvature of space-time

$$R^\mu_\nu - \frac{1}{2}\delta^\mu_\nu R = 8\pi G T^\mu_\nu. \tag{2.3}$$

Here G is the Newtonian gravitational constant and the Ricci scalar, R, is given by

$$R = g^{\mu\nu}R_{\mu\nu}, \tag{2.4}$$

with the Ricci tensor, $R_{\mu\nu}$, defined as

$$R_{\mu\nu} = \partial_\rho \Gamma^\rho_{\mu\nu} - \partial_\nu \Gamma^\rho_{\mu\rho} + \Gamma^\rho_{\sigma\rho}\Gamma^\sigma_{\mu\nu} - \Gamma^\rho_{\sigma\nu}\Gamma^\sigma_{\mu\rho}, \tag{2.5}$$

and finally

$$\Gamma^\sigma_{\mu\nu} = \frac{1}{2}g^{\sigma\rho}(\partial_\mu g_{\nu\rho} + \partial_\nu g_{\mu\rho} - \partial_\rho g_{\mu\nu}), \tag{2.6}$$

are the Christoffel symbols. We will in general use the conventions $\partial_0 X = \dot{X}$ and $\delta^{ij}\partial_i\partial_j = \nabla^2$ to indicate conformal time derivatives and comoving spacial derivatives, respectively. From Eq. (2.3) - Eq. (2.6) it can be seen that the left-hand side of the Einstein equations are only related to the metric itself and its first and second derivatives. T^μ_ν is the energy-momentum tensor and it depends on the physical density, ρ, and pressure, P, of all the energy components in the Universe. The symmetric energy-momentum tensor is given by

$$\begin{aligned} T^0_0 &= -\rho = -(\bar{\rho} + \delta\rho), & (2.7)\\ T^0_i &= (\bar{\rho} + \bar{P})v_i, & (2.8)\\ T^i_j &= (\bar{P} + \delta P)\delta^i_j + \Sigma^i_j, & (2.9) \end{aligned}$$

with the trace of Σ^i_j equal to zero and $v_i = dx_i/d\tau$. In the rest frame of a cold fluid only the T^0_0 component is non-zero, and it is equal to the mass density times c^2, i.e. the energy density ρ. For a non-cold perfect isotropic fluid, the $T^1_1 = T^2_2 = T^3_3$ terms are identical and non-zero, and they encode information of, say, x-momentum in the x-direction, etc. The off-diagonal terms, which can only be present in a perturbed Universe, hold information of the flow of x^i-momentum in the x^j-direction, for $i \neq j \in (1, 2, 3)$.

The Einstein equations are the standard paradigm in cosmology today, and they have been shown to be very accurate on solar system scales. We know that they must break down on scales comparable to the extent of the wave function of particles, where a new theory of quantum gravity taking into account both gravity and quantum field theory must be employed. Throughout this dissertation the Einstein equations are assumed to be correct, also at cosmological distances, though alternative theories have been proposed [14].

2.1.3 The homogeneous background evolution

We will now derive the basic evolution equations for the Universe. Just like the metric, the evolution equations for the metric variables will be separated into background and inhomogeneous equations. We will first focus on the evolution of the scale factor a.

Two evolution equations describing the velocity and acceleration of space itself, i.e. the scale factor, can be found from the Einstein equations and the FRW metric in Eq. (2.1)

$$\mathcal{H}^2 \equiv \left(\frac{\dot{a}}{a}\right)^2 = \frac{8\pi}{3} G a^2 \bar{\rho} - \kappa, \tag{2.10}$$

and

$$\dot{\mathcal{H}} = -\frac{4\pi}{3} G a^2 (\bar{\rho} + 3\bar{P}). \tag{2.11}$$

Here $\mathcal{H} \equiv aH$, where $H = 100\,h\,\mathrm{km/s/Mpc}$ is the usual Hubble parameter parameterized by h. The '$\bar{}$'-sign denotes an average quantity. The total density is a sum of matter, Dark Energy and radiation densities. They will be denoted by m, de and r, respectively. Matter consists of CDM (c), baryons (b) and non-relativistic neutrinos (ν, m), while radiation is composed of photons (γ) and relativistic neutrinos (ν, r). With these conventions the total density is given as $\rho = \rho_m + \rho_{de} + \rho_r$, so that Eq. (2.10) can be rewritten as

$$\mathcal{H}^2 = a^2 \mathcal{H}_0^2 [\Omega_m f_m(a) + \Omega_{de} f_{de}(a) + \Omega_r f_r(a)], \tag{2.12}$$

where $\Omega_i = \bar{\rho}_{i,0}/\bar{\rho}_0$ (in a flat Universe) for energy component i, $f_i(a)$ is the corresponding energy density evolution function and the subscript '0' indicates a value today. The continuity equation can be found by combining Eqs. (2.10) and (2.11)

$$\dot{\bar{\rho}} + 3\mathcal{H}(\bar{\rho} + \bar{P}) = 0. \tag{2.13}$$

With the definition $w = \bar{P}/\bar{\rho}$ the most general solution to the continuity equation for a given energy species i is

$$\bar{\rho}_i = \bar{\rho}_{i,0} f_i(a) = \bar{\rho}_{i,0} \exp\left[-3 \int_1^a da' \frac{1 + w_i(a')}{a'}\right]. \tag{2.14}$$

Eqs. (2.12) and (2.14) determine the background evolution of a. For pressureless matter $w_m = 0$, for a cosmological constant $w_{de} = -1$ and for radiation $w_r = 1/3$ giving $f_m(a) = a^{-3}$, $f_{de}(a) = 1$

and $f_r(a) = a^{-4}$. Therefore, as is in fact the case today, Dark Energy will eventually dominate the energy budget in the Universe. The radiation component is the dominant term in the early Universe but becomes negligible at later times. While the neutrino component is relativistic its density scales as radiation $f_{\nu,r}(a) = a^{-4}$, but at later times as the neutrino velocity becomes non-relativistic it scales as matter $f_{\nu,m}(a) = a^{-3}$. The transition redshift between these regimes depends on the neutrino mass and momentum considered, but it can roughly be approximated by $z \sim 1000$ (see also Fig. 7.5 on page 74).

2.2 The early Universe

This section will describe the making of our Universe, from shortly after the formation of space-time, through inflation and the subsequent creation of elementary particles and nucleosynthesis. Special emphasis will be given to the curvature of space-time, the tilt of the perturbation spectrum and adiabatic initial conditions with Gaussian perturbations, since these predictions directly enter into N-body simulations. The presentation is based on [15, 16, 17].

2.2.1 Big Bang and its drawbacks

In 1929 Edwin Hubble discovered that the Universe is expanding [18]. He observed that galaxies at larger distances recede faster from us. The logical conclusion drawn from this observation is that the Universe began with a Big Bang from a very hot and dense phase. The Big Bang can furthermore successfully explain the existence of the Cosmic Microwave Background (CMB) and the relative abundances of light elements produced during Big Bang Nucleosynthesis (BBN). But the standard Big Bang scenario cannot explain what is known as *the horizon problem* and *the flatness problem*.

The horizon problem The CMB sky that we observe today displays a very homogeneous black-body spectrum with perturbations of the order of 10^{-5}. Assuming that the causal horizon expands with the speed of light, this homogeneity is difficult to understand since patches on opposite directions on the CMB sky cannot have been in causal contact at the time of last scattering. Assuming an initial super-luminal period of inflation, the homogeneity of the CMB can be explained by the fact that the CMB sky can have been in causal contact before inflation.

The flatness problem Using $\mathcal{H}^2 = 8\pi G a^2 \bar{\rho}/3 - \kappa$ (Eq. (2.10)), the density parameter $\Omega = \bar{\rho}/\bar{\rho}_{crit}$ and the definition of the critical density $\bar{\rho}_{crit} = 3\mathcal{H}^2/(8\pi G a^2)$ found by setting $\kappa = 0$, the following relation can be derived

$$\Omega - 1 = \frac{\kappa}{\mathcal{H}^2} \propto \begin{cases} a^2, & \text{radiation domination} \\ a, & \text{matter domination.} \end{cases} \tag{2.15}$$

In the last proportionality we have neglected κ which is justified by observation and more than accurate for our order of magnitude estimation here. Assuming a sharp transition between radiation and matter domination at matter-radiation equality (eq), the evolution of $\Omega - 1$ at some time t relative to today, t_0, is then given by

$$\frac{\Omega_t - 1}{\Omega_{t_0} - 1} = \frac{\Omega_t - 1}{\Omega_{t_{eq}} - 1} \frac{\Omega_{t_{eq}} - 1}{\Omega_{t_0} - 1} \sim \left(\frac{a_t}{a_{eq}}\right)^2 \frac{a_{eq}}{a_0} \sim \frac{a_t^2}{a_{eq} a_0} \sim 10^{-17}, \tag{2.16}$$

for $a_{eq} \sim 1/3500$ and $a_t \sim 10^{-10}$ at neutrino decoupling. Extrapolating back towards the Planck scale will further decrease $\Omega - 1$ by $\sim 10^{-44}$. In sum, for the Universe to be nearly flat today, it must have been *extremely* flat in the early Universe. Therefore, it is reasonable to conjecture that the Universe could very well be flat at a much higher level than $\sim 10^{-61}$ at the Planck scale, with the end result that the Universe is flat today with any precision that we will ever be able to measure. This is the flatness problem, and as we will see below, inflation provides a solution to this puzzle. In sum, exact flatness, $\Omega = 1$, will be assumed throughout this dissertation.

2.2.2 Inflation

Inflation is an extra feature which is added on top of the standard Big Bang scenario. It retains the confirmed predictions from the Big Bang and solves the outstanding puzzles, i.e. the flatness and the horizon problems. Inflation furthermore generates the necessary initial conditions for our Universe. The theory of inflation is today a proper science as its models can be confronted with observations, though planned future observations will not be able to rule out all but one of the different inflationary models.

The inflaton During inflation space expanded faster than light. Stated differently, the comoving Hubble length $(aH)^{-1} = \mathcal{H}^{-1}$ is decreasing as inflation progresses. Inflation can be realized by assuming a spin zero scalar field, called the inflaton χ. The action for the inflaton field is given as

$$S = \int d^4x\sqrt{-g}\mathcal{L}_\chi, \tag{2.17}$$

where the Lagrangian density, $\mathcal{L}_\chi$, is given by

$$\mathcal{L}_\chi = -\frac{1}{2}g^{\mu\nu}\partial_\mu\chi\partial_\nu\chi - V(\chi). \tag{2.18}$$

The first term is the kinetic term while the second term is the potential energy of the scalar field. The functional form of $V(\chi)$ should ideally be derived from new fundamental particle physics or alternatively from a higher dimensional theory. $V(\chi)$ includes self-couplings in the scalar field as well as couplings to other fields. Here we will focus on single field inflation with just one scalar field.

The Euler-Lagrange equation which is obtained by making variations to Eq. (2.17) with respect to χ and $\partial_\mu\chi$ is given by

$$\frac{\partial(\sqrt{-g}\mathcal{L}_\chi)}{\partial\chi} - \partial_\mu\left[\frac{\partial(\sqrt{-g}\mathcal{L}_\chi)}{\partial(\partial_\mu\chi)}\right] = 0. \tag{2.19}$$

From the Euler-Lagrange equation the evolution equation for the inflaton, the Klein-Gordon equation, can be derived

$$\ddot{\chi} + 2\mathcal{H}\dot{\chi} - \nabla^2\chi + a^2V'(\chi) = 0, \tag{2.20}$$

where $V' = dV/d\chi$.

From the definition of the energy-momentum tensor

$$T_{\mu\nu} = -\frac{2}{\sqrt{-g}}\frac{\delta(\sqrt{-g}\mathcal{L})}{\delta g^{\mu\nu}}, \tag{2.21}$$

we get

$$T^{\mu}_{\nu} = \partial_{\nu}\chi\partial^{\mu}\chi + \delta^{\mu}_{\nu}\mathcal{L}. \tag{2.22}$$

For a homogeneous scalar field the energy density and pressure are then given by

$$\bar{\rho}_{\chi} = \frac{1}{2}a^{-2}\dot{\chi}^2 + V(\chi), \tag{2.23}$$

and

$$\bar{P}_{\chi} = \frac{1}{2}a^{-2}\dot{\chi}^2 - V(\chi), \tag{2.24}$$

so that the equation of state for the scalar field is

$$w_{\chi} = \frac{\bar{P}_{\chi}}{\bar{\rho}_{\chi}} = \frac{\frac{1}{2}\dot{\chi}^2 - a^2V(\chi)}{\frac{1}{2}\dot{\chi}^2 + a^2V(\chi)}, \tag{2.25}$$

which reduces to the cosmological constant, $w = -1$, in the slow-roll limit, $\dot{\chi}^2 \ll a^2V(\chi)$. This means in turn that the potential must be very flat.

From Eq. (2.14) it can be seen that for $w \in]-1;0[$ the scalar field has the very special property that its energy density redshifts slower than ordinary matter. In effect, as the volume of space expands as a^3, scalar field energy must be created.

Assuming the slow-roll limit together with the fact that during inflation the Universe is scalar field dominated, Eq. (2.10) gives

$$H^2 \simeq \frac{8\pi G}{3}V(\chi) \tag{2.26}$$

and from the Klein-Gordon equation, Eq. (2.20), we get

$$3H\dot{\chi} + V'(\chi) = 0. \tag{2.27}$$

Notice that H and not $\mathcal{H}$ must be roughly constant during inflation, which can be seen from Eq. (2.26) for a scalar field slow-rolling in a flat potential. In Eq. (2.27) we have used $\dot{\chi} = \partial\chi/\partial t$. Throughout the dissertation we will use the convention that $\dot{\chi}$ (or the time derivative of some other perturbation variable) is taken with respect to cosmic time if H is present in the equation and with respect to conformal time whenever $\mathcal{H}$ appears.

Number of e-foldings Choosing $w = -1$, exactly, we get de Sitter exponential expansion during inflation with a fixed Hubble parameter

$$a_2 = a_1 e^{H_I(t_2 - t_1)}, \tag{2.28}$$

which can be derived using Eq. (2.26). H_I is the Hubble parameter during inflation and the subscripts '1' and '2' refer to arbitrary times during inflation. The number of e-foldings N elapsed between the beginning ($t_i = t_1$) and end ($t_f = t_2$) of inflation is defined as

$$N \equiv \ln\frac{a_f}{a_i}. \tag{2.29}$$

To solve the horizon problem the largest scale that we can observe today must be reduced to a scale which can be contained within the causal horizon before inflation. From $dx = dt/a$ it can be

seen that the current horizon distance is given by $\lambda_0 = 2/H_0$ and it must be related to its distance at the beginning of inflation by

$$\lambda_i = \frac{2}{H_0}\frac{a_f}{a_0}\frac{a_i}{a_f} = \frac{2}{H_0}\frac{a_f}{a_0}e^{-N} < \frac{2}{H_I}. \tag{2.30}$$

Rearranging and inserting $T_0 = 2.348 \cdot 10^{-4}\,\mathrm{eV}/k_B$ and $H_0 = 2.133\,h\,10^{-42}\,\mathrm{GeV}/\hbar$ with $h = 0.7$ we get

$$N > \ln\frac{T_0}{H_0} - \ln\frac{T_f}{H_I} \simeq 67.2 + \mathcal{O}(1). \tag{2.31}$$

Where $\mathcal{O}(1)$ denotes a number numerically much smaller than 67. From the definition of the number of e-foldings, Eq. (2.29), together with the slow-roll equations, Eqs. (2.26) and (2.27), we can get an equation relating the required number of e-foldings to the inflaton potential

$$N \equiv \int_{t_i}^{t_f} H_I dt = -8\pi G \int_{\chi_i}^{\chi_f} \frac{V}{V'} d\chi. \tag{2.32}$$

To sum up: Before we had a severe fine-tuning problem requiring the Universe to be flat at the 10^{-61} level at the Planck scale, because otherwise the expansion of the Universe would quickly drive $\Omega - 1$ away from zero. With inflation, the problem has been transformed to finding a flat enough potential and ensuring that inflation will last long enough. We do not need a particular value of N fine-tuned to extreme precision, N should just be larger than ~ 67.

The flatness problem is easily solved since during inflation H_I is constant and using Eq. (2.15) we get

$$\frac{\Omega_f - 1}{\Omega_i - 1} = \left(\frac{a_i}{a_f}\right)^2 = e^{-2N}. \tag{2.33}$$

Note that the flatness problem will not be solved if $\Omega_i - 1$ is extremely large.

The inflaton field stretches quantum fluctuations beyond the causal horizon. They are then frozen until the causal horizon, which expands faster than space itself after inflation, catches up with the perturbation wavelength. Once the perturbations re-enter the horizon they can grow and create structure. The evolution of the perturbations depends on the wavelength dependency of the perturbation spectrum before horizon crossing and the size of the relative density contrast in each energy component. We will now address these issues.

Perturbation spectrum Expanding the inflaton in a homogeneous and perturbed part $\chi = \bar{\chi} + \delta\chi$, and using the convention $\nabla^2 \to -k^2$ the perturbed Klein-Gordon equation is in Fourier space given as

$$\ddot{\delta\chi} + 2\mathcal{H}\dot{\delta\chi} + k^2\delta\chi + a^2 V''\delta\chi = 0. \tag{2.34}$$

Making the substitution $\delta\chi = \delta\zeta/a$ and neglecting the mass (V'') of the inflaton Eq. (2.34) gives

$$\ddot{\delta\zeta} + \left(k^2 - \frac{\ddot{a}}{a}\right)\delta\zeta = 0. \tag{2.35}$$

The solution to Eq. (2.35) is [15]

$$\delta\zeta = \left(1 - \frac{i}{k/(aH)}\right)\frac{e^{ik/(aH)}}{\sqrt{2k}}. \tag{2.36}$$

Well outside the horizon we have $k \ll aH$ and the power spectrum of the inflaton field is then given by

$$|\delta\chi|^2 = \frac{H^2}{2k^3}. \tag{2.37}$$

$\delta\chi$ will be related to the metric potentials in subsection 2.3.4.

We now expand the inflaton perturbation modes in real, $R(k)$, and imaginary, $I(k)$, parts. Inflation predicts that these parts are separately Gaussian distributed

$$P(X(k)) = \frac{1}{\sqrt{2\pi}\sigma(k)}\exp\left(-\frac{X(k)^2}{2\sigma^2(k)}\right), \tag{2.38}$$

with $X(k)$ representing either $R(k)$ or $I(k)$, and $\sigma^2(k) = \langle X^2(k)\rangle$ is the ensemble average, i.e. an average over an infinite number of realisations of the Universe. Therefore

$$\sigma^2(k) = \langle X^2(k)\rangle = \frac{1}{2}\langle|\delta\chi(k)|^2\rangle. \tag{2.39}$$

Adiabatic initial conditions We will now find the initial conditions for the density contrasts predicted by vacuum fluctuations in the inflaton field [16]. The generalized adiabatic condition is given by

$$\frac{\delta\mathcal{G}}{\dot{\mathcal{G}}} = \frac{\delta\rho}{\dot{\rho}}, \tag{2.40}$$

where $\mathcal{G}$ can be the energy density or pressure density of any energy component. Combining the generalized adiabatic condition with the homogeneous continuity equation, Eq. (2.13), which is satisfied for each species separately, the density contrasts, $\delta = \rho/\bar{\rho} - 1$, for energy components i and j are related by

$$\frac{\delta_i}{1+w_i} = \frac{\delta_j}{1+w_j}. \tag{2.41}$$

Choosing $\delta_j = \delta_\nu$ we get

$$\delta_c = \delta_b = \frac{3}{4}\delta_\gamma = \frac{3}{4}\delta_\nu. \tag{2.42}$$

As the neutrino component becomes non-relativistic δ_ν approaches δ_m on very large scales where neutrino free-streaming can be neglected. The most general energy perturbation is given as a linear combination of adiabatic and isocurvature density perturbations. Isocurvature perturbations give zero total perturbations and can only be generated by quantum fluctuations in other fields than the inflaton.

2.2.3 Particle production

Exit from inflation occurs when the slow-roll approximation is violated, i.e. when the inflaton potential becomes too steep. The inflaton field then rapidly falls towards its ground state. At the bottom of its potential it then oscillates into cold inflaton particles. These particles in turn decay into standard model particles, i.e. the fermionic leptons (e^-, μ^-, τ^-, ν_e, ν_μ, ν_τ and their anti-particles), the quarks (up, down, strange, charm, bottom, top and their anti-particles) and the gauge bosons (photons, $W^\pm$, Z^0, gluons and gravitons). Thereafter the standard Hot Big Bang continues [17].

Creation of elementary particles The heaviest particles, such as the top-quark and the only massive gauge bosons, $W^{\pm}$ and Z^0, rapidly decayed once the temperature fell below their particle mass. Thereafter the remaining quarks, anti-quarks and gluons combined into hadrons (baryons and mesons). Except for the protons and neutrons, all the other hadrons quickly decayed together with the unstable $\mu^{\pm}$ and $\tau^{\pm}$ particles. The remaining particles left over from the matter-anti-matter asymmetry were the stable electron and proton, the unstable neutron with a life time of 887 sec, the neutrinos, and finally the Universe was filled with photons coming from the annihilation of matter and anti-matter in the early Universe.

The neutrinos were in equilibrium with the rest of the primordial plasma as long as they were replenished by the reversible process

$$e^- + e^+ \leftrightarrow \nu + \bar{\nu}. \tag{2.43}$$

Thereafter, at around 0.1 sec after the Big Bang, the neutrinos decoupled. These neutrinos are now in principle detectable as the Cosmic Neutrino Background (CνB) anisotropy, which gives information on the amount of perturbation present in the Universe at the time of neutrino decoupling. We will get back to the CνB in Chapter 10.

Then an arms race ensued between on the one side the decay of the neutrons, and on the other side the capture of neutrons into light nucleons such as deuteron. After photo-disintegration of this particle ceased tritium, He-3, He-4 and Li-7 were also created in the process we generally call primordial nucleosynthesis. The calculated abundances of these nucleons are in excellent agreement with observation and lead to an estimated value of Ω_b at around 5%. This agreement between theory and observation gives credibility to the Big Bang scenario.

For the next few hundred thousand years the electrons, protons and photons were in equilibrium through the reversible reaction

$$e^- + p \leftrightarrow H + \gamma. \tag{2.44}$$

Thereafter, as the expansion of the Universe diluted the reaction rate, the photons decoupled to become the CMB anisotropy sky. To understand the evolution of the CMB and perturbations in the energy components in general, we need to take a closer look at linear perturbation theory.

2.3 The evolution of metric and energy perturbations

In this section we will find the evolution equations for the energy perturbations which enter the right-hand side of the Einstein equations. The presentation will also focus on gaining physical intuition for the derived equations. In the linear regime, where the density contrast δ is much less than unity, the equations for different Fourier modes decouple and they are also independent of their initial amplitude. Therefore the dimensionality can be significantly reduced as the equations can be solved for one mode at a time. The presentation in this section is mostly based on [9].

2.3.1 Metric perturbations

Before proceding to derive the linear equations governing structure formation, it is important to justify that the metric perturbations ψ and ϕ, which will enter these equations are much less than unity. The potential in a spherical halo of mass M is $\psi = -GM/r$ in the Newtonian approximation. Furthermore, potential and kinetic energies are roughly equal for bound galaxies and galaxy-clusters. Therefore it can be seen that $\psi \sim v^2$. The largest galaxy velocities are found in

super-clusters and are at most 1% of the speed of light, therefore ϕ and $\psi \ll 1$. This criterion is necessary to perform linear perturbation theory, where only first-order terms in the metric variables are included. The assumption of small metric variables only breaks down in the vicinity of black holes.

Note that the maximum bound on v^2 must be found from gravitational forces, so that neutrinos with a relic thermal velocity approaching unity do not affect the conclusion about the size of the metric perturbations.

The perturbed version of the Einstein equations determines how energy inhomogeneities affect the metric perturbations in an expanding Universe. The evolution equations can be found by inserting the metric from Eq. (2.2) into Eqs. (2.3), (2.4), (2.5) and (2.6). The 4 evolution equations are in Fourier space given by

$$
\begin{aligned}
k^2\phi + 3\mathcal{H}(\dot{\phi} + \mathcal{H}\psi) &= 4\pi G a^2 \delta T^0_0, && (2.45)\\
k^2(\dot{\phi} + \mathcal{H}\psi) &= 4\pi G a^2 (\bar{\rho} + \bar{P})\theta, && (2.46)\\
\ddot{\phi} + \mathcal{H}(\dot{\psi} + 2\dot{\phi}) + (2\frac{\ddot{a}}{a} - \mathcal{H}^2)\psi + \frac{k^2}{3}(\phi - \psi) &= \frac{4\pi}{3} G a^2 \delta T^i_i, && (2.47)\\
k^2(\phi - \psi) &= 12\pi G a^2 (\bar{\rho} + \bar{P})\sigma, && (2.48)
\end{aligned}
$$

where $(\bar{\rho} + \bar{P})\theta \equiv ik^j \delta T^0_j$, $(\bar{\rho} + \bar{P})\sigma \equiv -(\hat{k}_i\hat{k}_j - \frac{1}{3}\delta_{ij})\Sigma^i_j$, $\Sigma^i_j \equiv T^i_j - \frac{1}{3}\delta^i_j T^k_k$ and '$\hat{}$' indicates a unit vector. From Eq. (2.8) it can then be seen that $\theta = ik^j v_i$. Throughout this dissertation we will in general not explicitly write the k-dependence of the perturbation variables.

We only need two equations for the two metric perturbation variables. One method is to find ϕ by inserting Eq. (2.46) into Eq. (2.45), and then calculate the difference between ϕ and ψ from Eq. (2.48). When only non-relativistic matter is present we have 3 redundant equations on small scales and Eq. (2.45) reduces to Poisson's equation

$$
k^2\phi = -4\pi G a^2 \sum_s \bar{\rho}_s \delta_s, \tag{2.49}
$$

with the sum running over all particle species s. This equation is the only one of Eqs. (2.45) - (2.48) which is used in N-body simulations.

2.3.2 Non-relativistic energy components: CDM and baryons

Using D_μ as the covariant derivative, the energy-momentum conservations equations must satisfy

$$
D_\mu T^{\mu\nu} \equiv \partial_\mu T^{\mu\nu} + \Gamma^\nu_{\mu\lambda} T^{\mu\lambda} + \Gamma^\mu_{\mu\lambda} T^{\nu\lambda} = 0. \tag{2.50}
$$

The fluid evolution equations for δ and θ can be found from the perturbed part of the energy-momentum conservation equations. They are in general given by

$$
\begin{aligned}
\dot{\delta} &= -(1+w)(\theta - 3\dot{\phi}) - 3\mathcal{H}(\delta P/\delta\rho - w)\delta, && (2.51)\\
\dot{\theta} &= -\left(\mathcal{H}[1-3w] + \frac{\dot{w}}{1+w}\right)\theta + k^2\left(\frac{\delta P/\delta\rho}{1+w}\delta - \sigma + \psi\right). && (2.52)
\end{aligned}
$$

For adiabatic initial conditions $\delta P/\delta\rho - w = 0$. These equations are only used for the non-relativistic CDM and baryonic components.

CDM CDM only interacts with the other energy components through the gravitational field, and therefore the fluid equations reduce to

$$\dot{\delta}_c = -\theta_c + 3\dot{\phi}, \tag{2.53}$$
$$\dot{\theta}_c = -\mathcal{H}\theta_c + k^2\psi. \tag{2.54}$$

In Eq. (2.53) the θ_c term includes the effect of gravitational flow velocities on the growth of structure whereas the $\dot{\phi}$ term, related to structure forming in evolving potentials, only matters on large scales. In Eq. (2.54) the $\mathcal{H}\theta_c$ term encodes the effect of redshifting velocities in an expanding universe, and the $k^2\psi$ term is sourced by the energy distribution through Eq. (2.45).

Baryons Before recombination the photons and baryons interact via Thomson scattering, which is the elastic scattering of photons by electrons. Therefore the fluid equations for the baryons must be modified to take this momentum transfer into account. Relative to the CDM case it turns out that two extra terms must be added to the $\dot{\theta}$ equation

$$\dot{\delta}_b = -\theta_b + 3\dot{\phi}, \tag{2.55}$$
$$\dot{\theta}_b = -\mathcal{H}\theta_b + k^2\psi + c_s^2k^2\delta_b + \frac{4\bar{\rho}_\gamma}{3\bar{\rho}_b}an_e\sigma_T(\theta_\gamma - \theta_b). \tag{2.56}$$

Here $\sigma_T = 0.6652 \cdot 10^{-24}\text{cm}^2$ is the Thomson scattering cross section, n_e is the mean density of electrons, and we have defined the sound speed in the baryon-photon fluid as $c_s^2 = \delta P/\delta\rho = \dot{P}/\dot{\rho}$. These extra terms create acoustic oscillations in the baryon-photon fluid, with the last term proportional to $\theta_\gamma - \theta_b$ leading to momentum transfer between the two components. Therefore, on small scales the baryons cannot follow the CDM component before decoupling, in turn slowing down the growth of the CDM component.

Using μ as the mean molecular weight together with the fact that $\rho_b \propto a^{-3}$ and $P = (\rho/\mu)k_BT$, the baryon sound speed can be found to be

$$c_s^2 = \frac{\dot{P}_b}{\dot{\rho}_b} = \frac{k_BT_b}{\mu}\left(1 - \frac{1}{3}\frac{d\ln T_b}{d\ln a}\right), \tag{2.57}$$

where we have neglected the term with $\dot{\mu}$. From the first law of thermodynamics the baryon temperature is given by the equation

$$\dot{T}_b = -2\mathcal{H}T_b + \frac{8}{3}\frac{\mu}{m_e}\frac{\bar{\rho}_\gamma}{\bar{\rho}_b}an_e\sigma_T(T_\gamma - T_b), \tag{2.58}$$

where m_e is the electron mass.

2.3.3 Relativistic energy components: Neutrinos and photons

Phase space and the Boltzmann equation The energy-momentum tensor is generally given by

$$T_{\mu\nu} = \int dP_1dP_2dP_3(-g)^{-1/2}\frac{P_\mu P_\nu}{P^0}f(x^i, P_j, \tau). \tag{2.59}$$

Here $g = det(g_{\mu\nu})$, $P_0 = -(1+\psi)\epsilon$ and P_i is a conjugate momentum, related to the proper momentum p_i by $P_i = a(1-\phi)p_i$. These last two results can be found from $P_i = mU_i = mdx_i/\sqrt{-ds^2}$

and $P_\mu P^\mu = -m^2$. T^μ_ν is the tensor we are after since it enters the right-hand side of the Einstein equations, Eq. (2.3). $f(x^i, P_j, \tau)$ is the distribution function, which is needed to describe the photon and neutrino components in phase space. The number of particles dN contained in a differential phase space volume element is given by

$$dN = f(x^i, P_j, \tau) dx^1 dx^2 dx^3 dP_1 dP_2 dP_3. \tag{2.60}$$

It is convenient to define a comoving momentum q_i, related to the proper momentum by $q_i \equiv a p_i$, and further to decompose it into its magnitude q and direction n_i. The evolution of the distribution function, $f(x^i, q, n_j, \tau)$, is determined by the Boltzmann equation which can generically be written as

$$L[f] = C[f], \tag{2.61}$$

where $L[f]$ is the Liouville operator. The collision operator $C[f]$ on the right-hand side describes any possible collisional interactions. Inserting the Liouville operator we have

$$\frac{\partial f}{\partial \tau} + \frac{dx^i}{d\tau}\frac{\partial f}{\partial x^i} + \frac{dq}{d\tau}\frac{\partial f}{\partial q} + \frac{dn_i}{d\tau}\frac{\partial f}{\partial n_i} = \left(\frac{\partial f}{\partial \tau}\right)_C. \tag{2.62}$$

Due to the very small cross section for neutrinos the collisional term is only non-zero before neutrino decoupling at 0.1 sec after the Big Bang, and so these interactions should only be modelled for the hypothetical case where one is interested in scales inside the horizon at this early time. The collisional term is non-zero for photons as long as they couple non-gravitationally with the baryons, which happens until a few 10^5 years after the Big Bang.

The zeroth-order phase space distribution function is given by

$$f_0(\epsilon) = \frac{g_s}{h_P^3} \frac{1}{e^{\epsilon/(k_B T_0)} \pm 1}, \tag{2.63}$$

with the plus sign applying to fermions and the minus sign to bosons. $\epsilon = (q^2 + a^2 m^2)^{1/2}$ and T_0 is the neutrino or photon temperature today. g_s is the number of spin states which is one for neutrinos and two for photons, and h_P is Planck's constant. Based on BBN bounds we have neglected a neutrino chemical potential, which needs to be added in the case of a neutrino-anti-neutrino asymmetry. At neutrino decoupling the neutrinos are ultra-relativistic particles so that $\epsilon = q$ can be used in Eq. (2.63), not only at neutrino decoupling but also at all later times.

Neutrinos For massive neutrinos the time dependence of ϵ is non-trivial, which means that the q-dependence cannot be integrated out immediately. It is therefore necessary to follow the evolution of the neutrino component in separate momentum bins.

In a perturbed universe the phase space distribution function is expanded to first order as follows

$$f = f_0 + \frac{\partial f_0}{\partial T}\delta T = f_0(1 + \Psi), \tag{2.64}$$

with the perturbation parametrised by $\Psi = -d\ln f_0 / d\ln q \ \cdot \ \delta T/T$. Using the geodesic equation

$$P^0 \frac{dP^\mu}{d\tau} + \Gamma^\mu_{\alpha\beta} P^\alpha P^\beta = 0, \tag{2.65}$$

the Boltzmann equation for the neutrinos can be written as an evolution equation for Ψ in k-space

$$\frac{1}{f_0}L[f] = \frac{\partial\Psi}{\partial\tau} + ik\frac{q}{\epsilon}\mu\Psi + \frac{d\ln f_0}{d\ln q}\left[\dot{\phi} - ik\frac{\epsilon}{q}\mu\psi\right] = 0, \tag{2.66}$$

where $\mu \equiv n^j\hat{k}_j$. The perturbation to the distribution function can be expanded in a Legendre series as

$$\Psi = \sum_{l=0}^{\infty}(-i)^l(2l+1)\Psi_l P_l(\mu). \tag{2.67}$$

Here the P_l's are Legendre polynomials. One can then write the collisionless Boltzmann equation as a moment hierarchy for the Ψ_l's

$$\dot{\Psi}_0 = -k\frac{q}{\epsilon}\Psi_1 - \dot{\phi}\frac{d\ln f_0}{d\ln q}, \tag{2.68}$$

$$\dot{\Psi}_1 = k\frac{q}{3\epsilon}(\Psi_0 - 2\Psi_2) - k\frac{\epsilon}{3q}\psi\frac{d\ln f_0}{d\ln q}, \tag{2.69}$$

$$\dot{\Psi}_l = k\frac{q}{(2l+1)\epsilon}(l\Psi_{l-1} - (l+1)\Psi_{l+1}) \ , \ l \geq 2. \tag{2.70}$$

The second term on the right-hand side of the equation for $\dot{\Psi}_0$ encodes the effect of structure forming in evolving gravitational potentials, whereas the first term incorporates the effect of velocity on structure formation. The change in velocity is not only affected by the three terms on the right-hand side of the equation for $\dot{\Psi}_1$. When performing the time derivative on Ψ_1 in Eq. (2.73) two terms appear: The time derivative of the velocity perturbation, θ, and a term similar to the $\mathcal{H}\theta$ term in Eq. (2.54). On the right-hand side of the $\dot{\Psi}_1$ equation, the first term is related to δP_ν, whereas the second term, found from the hierarchy of $\dot{\Psi}_l$'s, incorporates the effect of momentum (and redshift) dependent neutrino free-streaming, which gives rise to less structure. The last term in the equation for $\dot{\Psi}_1$ gives the acceleration as a gradient of the gravitational potential.

In Eq. (2.70) the maximum l, at which the hierarchy must be truncated decreases significantly as the neutrinos become non-relativistic, i.e. $\epsilon_\nu \to am_\nu$. In the fluid approximation $l_{max} = 2$.

The Ψ_l's enter the energy-momentum tensor as follows

$$\delta\rho_\nu = 4\pi a^{-4}\int dq q^2 \epsilon f_0 \Psi_0, \tag{2.71}$$

$$\delta P_\nu = \frac{4\pi}{3}a^{-4}\int dq q^2 \frac{q^2}{\epsilon} f_0 \Psi_0, \tag{2.72}$$

$$(\bar{\rho}_\nu + \bar{P}_\nu)\theta_\nu = 4\pi k a^{-4}\int dq q^2 q f_0 \Psi_1, \tag{2.73}$$

$$(\bar{\rho}_\nu + \bar{P}_\nu)\sigma_\nu = \frac{8\pi}{3}a^{-4}\int dq q^2 \frac{q^2}{\epsilon} f_0 \Psi_2. \tag{2.74}$$

These equations are valid for one neutrino species (particle or anti-particle) and should be multiplied by 6 for degenerate neutrinos. In the relativistic limit, $\epsilon \to q$, Eq. (2.71) reduces to three times Eq. (2.72). In general, the fluid equations can be found by performing the momentum integral over the Ψ_l equations, i.e., the two methods are equivalent.

Photons The evolution equations for the photons are complicated by the fact that the scattering of photons off electron perturbations depends on polarization. The first two moment equations for the photons are given by

$$\dot{\delta}_\gamma = -\frac{4}{3}\theta_\gamma + 4\dot{\phi}, \tag{2.75}$$

$$\dot{\theta}_\gamma = k^2\left(\frac{1}{4}\delta_\gamma - \sigma_\gamma\right) + k^2\psi + an_e\sigma_T(\theta_b - \theta_\gamma). \tag{2.76}$$

Compared with the non-relativistic case there is an extra relativistic factor of $\frac{4}{3}$. The σ_γ term is related to a hierarchy of equations taking the effect of polarization on the scatttering cross section into account (see [9] for further details).

2.3.4 Primordial initial conditions

To solve the coupled Einstein, fluid and Boltzmann equations we need inital conditions for the perturbation variables. The numerical evolution of all modes will begin deep in the radiation dominated era, where only photons and neutrinos contribute to the total energy density, and well before the mode enters the horizon. Since $\tau = \mathcal{H}^{-1}$, a mode is said to be outside the horizon when $k\tau \ll 1$. Assuming adiabatic initial conditions we found in Eq. (2.42) that the perturbations in the density contrast are given by

$$\delta_c = \delta_b = \frac{3}{4}\delta_\gamma = \frac{3}{4}\delta_\nu. \tag{2.77}$$

Combining Eq. (2.10) with the large-scale limit of Eq. (2.45), where the $k^2\phi$ and $\dot{\phi}$ terms are neglected, the density contrasts are related to the metric perturbation ψ by

$$\delta_\nu = -2\psi. \tag{2.78}$$

The perturbations to the velocity variables can be found by inserting Eq. (2.45) into Eq. (2.46) and using $w_r = 1/3$. Then

$$\theta_c = \theta_b = \theta_\gamma = \theta_\nu = \frac{1}{2}k^2\tau\psi. \tag{2.79}$$

The initial value for σ_ν can be found by truncating Eq. (2.70) at $l = 2$, perform an integration over phase space, then use Eqs. (2.73) and (2.74) and finally make an integration over conformal time. The end result is

$$\sigma_\nu = \frac{1}{15}(k\tau)^2\psi. \tag{2.80}$$

The initial conditions for the neutrino phase space perturbations are only relevant for $\Psi_l \leq 2$, and to reproduce Eqs. (2.71), (2.73) and (2.74) they must be given by

$$\Psi_0 = -\frac{1}{4}\delta_\nu\frac{d\ln f_0}{d\ln q}, \tag{2.81}$$

$$\Psi_1 = -\frac{\epsilon}{3qk}\theta_\nu\frac{d\ln f_0}{d\ln q}, \tag{2.82}$$

$$\Psi_2 = -\frac{1}{2}\sigma_\nu\frac{d\ln f_0}{d\ln q}. \tag{2.83}$$

Inserting the large-scale limit of Eq. (2.45) into Eq. (2.48) and using the result for σ_ν from Eq. (2.80) the metric perturbations are related by

$$\phi = \left(1 + \frac{2}{5}R_\nu\right)\psi, \tag{2.84}$$

where $R_\nu \equiv \bar{\rho}_\nu/(\bar{\rho}_\gamma + \bar{\rho}_\nu)$. ψ can be written as

$$\psi = \frac{20C}{15 + 4R_\nu}\mathcal{I}(k), \tag{2.85}$$

where C is an overall normalisation of the perturbations, which should be determined from observations or ideally from a fundamental theory, and $\mathcal{I}(k)$ denotes the k-dependence of ψ to which we will turn shortly. Note that including the factor $20/(15 + 4R_\nu)$ in the definition of ψ is basically just a redefinition of the normalisation since R_ν has the same value for all the modes of interest when they enter the horizon.

ψ is related to the perturbations in the inflaton potential, $\delta\chi$, which we found in Eq. (2.37). Using the large-scale version of Eq. (2.45) and remembering that during inflation the inflaton field is potential energy dominated, $\delta\rho = \delta V = V'(\chi)\delta\chi$, we get

$$3\mathcal{H}^2\psi = -4\pi G a^2 V'(\chi)\delta\chi. \tag{2.86}$$

From this equation it can then be seen that

$$\psi(k) \propto \mathcal{I}(k) \propto \delta\chi(k) \propto k^{-3/2}. \tag{2.87}$$

Through the Poisson equation this gives a power spectrum of the matter perturbations proportional to k on large scales today. If the mass of the scalar field is included in the derivation of $|\delta\chi|^2$, Eq. (2.37), and if de Sitter expansion is not exactly satisfied during inflation, the tilt of the power spectrum will change slightly. Current estimates favour a matter power spectrum propertional to $\sim k^{0.96}$ [46].

Fig. 2.1 shows the time-evolution of the perturbations for the different energy components for the particular scale $k = 1.0\,\mathrm{Mpc}^{-1}$ and with $\Omega_\nu = 0.2$. At early times while the mode is outside the horizon, the assumption of adiabatic initial conditions can be distinguised by the fact that the radiation components are perturbed by an additional factor of $4/3$ relative to the non-relativistic matter components. As the mode catches up with the causal horizon the CDM component dominates the total matter perturbation whereas the baryons couple to the photons and perform acoustic oscillations. Both the massive and massless neutrinos free-stream almost completely out of this small-scale mode. At $\log_{10}a \sim -4$ the massive neutrinos become non-relativistic and slowly begin to track the dominant CDM component. Then a bit later at $\log_{10}a \sim -3.4$ the baryons decouple from the photons and quickly catches up with its CDM counterpart.

The perturbative analytical equations presented in this section give an accurate description of the evolution of the density contrasts as long as they remain much smaller than unity, $\delta \ll 1$. As structure evolves the smallest scales, largest wavenumbers, eventually approach the non-linear regime, $\delta \sim 1$, where perturbation theory breaks down. The validity of perturbation theory can be extended by including higher-order terms in the evolution equations.

This approach, third-order perturbation theory, has been used by S. Saito *et al.* [19, 20], Y. Y. Y. Wong [21] and M. Shoji and E. Komatsu [22]. As higher orders are included the equations

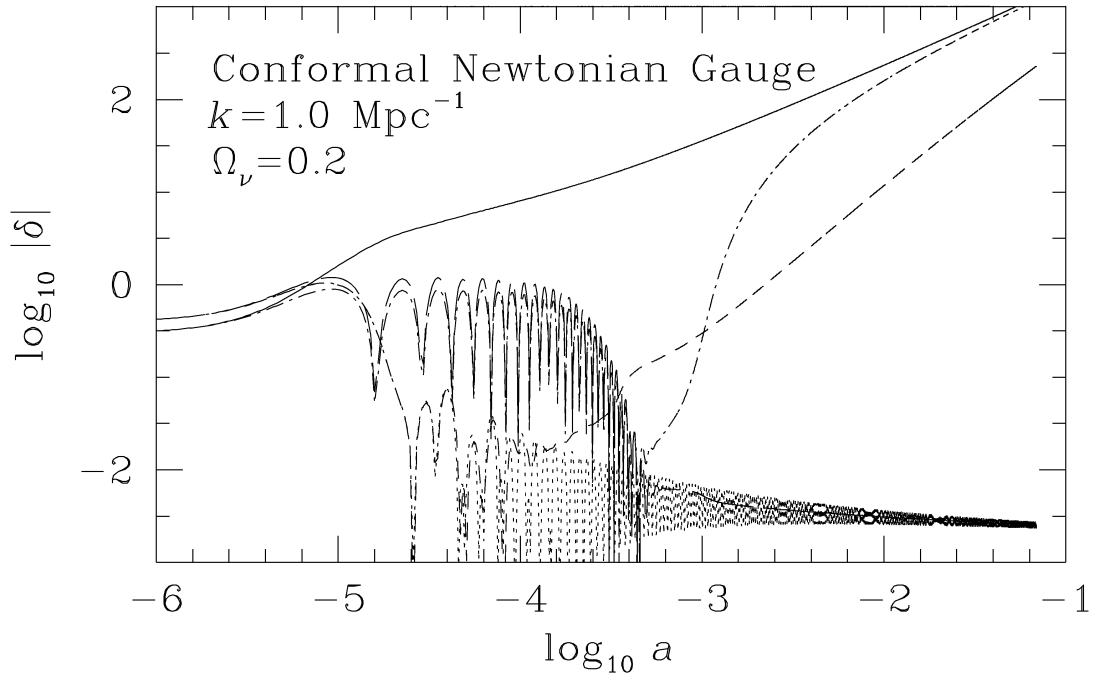

Figure 2.1: Time-evolution of the density contrasts for the CDM (solid), baryon (dot-dashed), massive neutrino (short-dashed), photon (long-dashed) and massless neutrino (dotted) components. The evolution is shown for the particular mode $k = 1.0\,\mathrm{Mpc}^{-1}$ with arbitrary normalization. The figure is taken from [9].

become more complicated and significantly time-consuming to solve numerically. This is due to the fact that in higher-order perturbation theory individual Fourier modes couple, and the evolution of one mode cannot be solved without solving for all the others. Higher-order perturbation theory has its validity and justification at higher redshifts, $z \gtrsim 3$, and mildly non-linear scales, $k \sim 0.1 - 0.5\,h\,\mathrm{Mpc}^{-1}$. Today, at all scales larger than $k \sim 0.1 - 0.2\,h\,\mathrm{Mpc}^{-1}$ the only feasible way to accurately calculate the distribution of perturbations is to make a full scale N-body simulation.

Chapter 3

N-body Simulations

This chapter will explain how N-body initial conditions can be created from the linear theory power spectrum with the Zel'dovich and 2LPT methods. Thereafter it will be described how an N-body integrator operates, with particular emphasis on force calculation, time integration and parallelization strategies.

3.1 N-body initial conditions

3.1.1 From linear theory to *N*-body particles

The redshift at which the N-body simulation should be started depends on the scales simulated, the desired accuracy, the final redshift and on whether one wants to calculate absolute or relative quantities. Starting redshifts can then vary from $z \sim 4$ for calculating changes in the matter power spectrum caused by neutrinos at non-linear scales, to $z \sim 100 - 200$ when small-scale, very non-linear objects such as galaxies are to be simulated.

Irrespective of starting redshift and scales simulated it is always necessary to create initial conditions (ICs) for the N-body simulation. The task is to transform the Fourier space information held by the wavenumber and species dependent density contrasts, $\delta_s(k)$, to a real space configuration of discrete N-body particles. These particles are initially placed on a 3D regular grid inside a periodic simulation volume, and then displaced according to a prescription taking the $\delta_s(k)$'s as input. This prescription is usually taken to be the Zel'dovich Approximation (ZA) [23] and if better precision is needed also a higher-order term calculated with second-order Lagrangian perturbation theory (2LPT) [24, 25].

More quantitatively the power spectrum of the perturbations can be factorised into a primordial power spectrum, $P_0(k) = A_s k^{n_s}$ with A_s a normalization and n_s of order unity, and a transfer function (TF), $T(k, z)$. The TF holds all information about the time-evolution of perturbations

$$P(k, z) = T^2(k, z) P_0(k). \tag{3.1}$$

The power spectrum gives the variance which enters the Gaussian distribution from which random realisations of the Fourier modes are drawn (see Eq. (2.38)). Below the equations describing the relationship between the variance and the particle grid displacements will be derived in detail (see [24, 25]).

3.1.2 ZA and 2LPT

Initially the N-body particles are placed on a regular grid, with grid points denoted by the vector quantity $\mathbf{q}$. The grid point dependent displacements will be denoted by $\Psi^i(\mathbf{q})$, where $i = x,\ y$ and z. The final comoving positions of the N-body particles are then given by

$$x^i = q^i + \Psi^i(\mathbf{q}). \tag{3.2}$$

Using cosmic time-derivatives the equation of motion for the N-body particles are found with the geodesic equation, Eq. (2.65),

$$\ddot{x}^i + 2H\dot{x}^i = -a^{-2}\delta^{ij}\partial_j\Phi. \tag{3.3}$$

By taking the divergence in comoving coordinates and inserting the Poisson equation, Eq. (2.49), and then the Friedmann equation, Eq. (2.10), with the inflationary prediction $\kappa = 0$, one arrives at the result

$$\frac{\partial}{\partial x^i}(\ddot{x}^i + 2H\dot{x}^i) = -4\pi G\bar{\rho}_m\delta = -\frac{3}{2}H^2\sum_s \Omega_s\delta_s = -\beta\delta, \tag{3.4}$$

where we have defined $\beta \equiv \frac{3}{2}H^2\Omega_m$. To move to the last equality, one species or species with the same density constrasts must be assumed. We will get back to this point later when we need to calculate ICs for a mixed N-body simulation with CDM and neutrino N-body particles. For the moment the last equality will be assumed.

Our main task now is to find equations for x^i and $\dot{x}^i$, terms which are at the moment burried inside operators on the left-hand side of Eq. (3.4). First an equation relating δ to the displacement field, $\mathbf{\Psi}(\mathbf{q})$, should be found. Consider a comoving volume d^3x and the mass contained within it dm (imagine 8 particles displaced slightly from a cubic grid). These quantities are related to the Lagrangian volume d^3q by

$$dm = \rho d^3x = \rho J d^3q, \tag{3.5}$$

where

$$J \equiv \left|\frac{dx^i}{dq^j}\right| = \left|\delta^i_j + \frac{d\Psi^i}{dq^j}\right|, \tag{3.6}$$

is the Jacobian, i.e. the determinant of the Jacobian matrix dx^i/dq^j. The mean density equals $\bar{\rho} = dm/d^3q$, so that

$$\delta = \frac{\rho}{\bar{\rho}} - 1 = \frac{1}{J} - 1. \tag{3.7}$$

Using this equation together with Eq. (3.4) we get

$$J\frac{\partial}{\partial x^i}(\ddot{x}^i + 2H\dot{x}^i) = \beta(J-1). \tag{3.8}$$

Now comes a crucial assumption: Since the N-body simulation must be started when $\delta \ll 1$, the relative displacements between adjacent grid points are small compared to the grid spacing, $\partial\Psi^i/\partial q^j \ll 1$. Stated differently, the particles are not allowed to cross each other, this then entails that the formalism we derive below cannot be used consistently on an input power spectrum which is significantly non-linear. Expanding to second order in Ψ^i and using $\Psi^i_{,j} = \partial\Psi^i/\partial q^j$ for the Lagrangian derivative the Jacobian is given as

$$J = 1 + \Psi^i_{,i} + \frac{1}{2}(\Psi^i_{,i}\Psi^j_{,j} - \Psi^i_{,j}\Psi^j_{,i}). \tag{3.9}$$

Since the ICs are to be calculated on a regular grid, the comoving derivative should be replaced by its Lagrangian counterpart. Using an arbitrary test function f, the transformation is given by

$$J\frac{\partial f^i}{\partial x^i} = f^i_{,j}C^j_i, \tag{3.10}$$

where C^j_i are the cofactors of the Jacobian, related to the minor M^i_j by $C^i_j = (-1)^{i+j}M^i_j$. A straightforward derivation gives the result

$$J\frac{\partial f^i}{\partial x^i} = f^i_{,i}(1+\Psi^j_{,j}) - f^i_{,j}\Psi^j_{,i}. \tag{3.11}$$

Since $\dot{x}^i = \dot{\Psi}^i$ and $\ddot{x}^i = \ddot{\Psi}^i$, combining Eqs. (3.8), (3.9) and (3.11) gives

$$(\ddot{\Psi}^i_{,i} + 2H\dot{\Psi}^i_{,i})(1+\Psi^j_{,j}) - (\ddot{\Psi}^i_{,j} + 2H\dot{\Psi}^i_{,j})\Psi^j_{,i} = \beta[\Psi^i_{,i} + \frac{1}{2}(\Psi^i_{,i}\Psi^j_{,j} - \Psi^i_{,j}\Psi^j_{,i})]. \tag{3.12}$$

To proceed the displacement field is expanded in first- and second-order terms

$$\Psi^i = \Psi^i_1 + \Psi^i_2. \tag{3.13}$$

First-order equations The first-order equations can then be found from Eq. (3.12)

$$\ddot{\Psi}^i_{1,i} + 2H\dot{\Psi}^i_{1,i} = \beta\Psi^i_{1,i}. \tag{3.14}$$

To the desired order we have that $\nabla_x = \nabla_q$ and by using Eqs. (3.2) and (3.4) it directly follows that

$$\Psi^i_{1,i} = -\delta(z,\mathbf{q}) = -D_1(z)\delta(z_i,\mathbf{q}). \tag{3.15}$$

In the last equality we have assumed a k-independent growth factor, D_1, which is wavenumber dependent when neutrinos are present. This is the Zel'dovich Approximation [23] and it basically states that the particle displacements can be found in Fourier space by differentiating $\delta(k) = T(z,k)\delta_0(k)$, i.e.

$$\Psi^i_1(\mathbf{k}) = -i\frac{\delta(z,\mathbf{k})}{k^2}k^i. \tag{3.16}$$

Defining $\psi^i_n(z_i,\mathbf{q})$ from

$$\Psi^i_n(z,\mathbf{q}) \equiv D_n(z)\psi^i_n(z_i,\mathbf{q}), \tag{3.17}$$

with $n \in (1,\ 2)$, Eq. (3.14) gives the time-evolution of D_1 as

$$\ddot{D}_1 + 2H\dot{D}_1 = \beta D_1. \tag{3.18}$$

Second-order equations The second-order equations can be found by collecting second-order terms in Eq. (3.12)

$$\ddot{\Psi}^i_{2,i} + 2H\dot{\Psi}^i_{2,i} + \left[\ddot{\Psi}^i_{1,i} + 2H\dot{\Psi}^i_{1,i}\right]\Psi^j_{1,j} - \left[\ddot{\Psi}^i_{1,j} + 2H\dot{\Psi}^i_{1,j}\right]\Psi^j_{1,i} = \tag{3.19}$$

$$\beta\left\{\Psi^i_{2,i} + \frac{1}{2}\left[\Psi^i_{1,i}\Psi^j_{1,j} - \Psi^i_{1,j}\Psi^j_{1,i}\right]\right\}. \tag{3.20}$$

Inserting Eq. (3.17) in all the first-order terms and using Eq. (3.18) for D_1 one arrives at

$$\ddot{\Psi}^i_{2,i} + 2H\dot{\Psi}^i_{2,i} - \beta\Psi^i_{2,i} = -\frac{1}{2}\beta D_1^2\Big[\psi^i_{1,i}\psi^j_{1,j} - \psi^i_{1,j}\psi^j_{1,i}\Big]. \tag{3.21}$$

Again using Eq. (3.17) but now in all the second-order terms we get

$$\Big[\ddot{D}_2 + 2H\dot{D}_2 - \beta D_2\Big]\psi^i_{2,i} = -\frac{1}{2}\beta D_1^2\Big[\psi^i_{1,i}\psi^j_{1,j} - \psi^i_{1,j}\psi^j_{1,i}\Big]. \tag{3.22}$$

Since the temporal and spacial parts must separately be conserved the time-evolution of D_2 is found from

$$\ddot{D}_2 + 2H\dot{D}_2 = \beta(D_2 - D_1^2), \tag{3.23}$$

and the spacial part from

$$\psi^i_{2,i} = \frac{1}{2}\Big[\psi^i_{1,i}\psi^j_{1,j} - \psi^i_{1,j}\psi^j_{1,i}\Big]. \tag{3.24}$$

Since the actual calculations are performed in Fourier space it is advantageous to introduce the following potentials

$$\phi^{,i}_{1,i} \equiv \delta(z_i, \mathbf{q}), \tag{3.25}$$

and

$$\phi^{,i}_{2,i} \equiv \frac{1}{2}\Big[\phi^{,i}_{1,i}\phi^{,j}_{1,j} - \phi^{,i}_{1,j}\phi^{,j}_{1,i}\Big]. \tag{3.26}$$

Disregarding a space-independent constant we then get $\Psi^i_1 = -D_1(z)\phi^{,i}_1$ and $\Psi^i_2 = D_2(z)\phi^{,i}_2$, giving the position and velocity displacements at each grid point up to second order as

$$x^i = q^i - D_1\phi^{,i}_1 + D_2\phi^{,i}_2, \tag{3.27}$$

and

$$v^i \equiv \frac{dx^i}{dt} = -D_1 f_1 H\phi^{,i}_1 + D_2 f_2 H\phi^{,i}_2, \tag{3.28}$$

with $i \in (x,\ y,\ z)$ and $f_n \equiv d\ln D_n/d\ln a$. $\phi^{,i}_1$ and $\phi^{,i}_2$ are found from Eqs. (3.25) and (3.26).

When neutrinos are included the growth factor becomes wavenumber and species dependent. In this case Eqs. (3.27) and (3.28) are no longer exactly accurate and especially for the neutrinos Eq. (3.28) gives a very poor description of the neutrino gravitational flow velocity. In this case two displacement fields at $z_i \pm \Delta z$ can be created, with z_i being the N-body starting redshift, and the gravitational flow velocity is then found from

$$v^i = \frac{d\Psi^i}{dt} = -a^{-1}H\frac{\Psi^i_2 - \Psi^i_1}{z_2 - z_1}. \tag{3.29}$$

Fermi-Dirac distributed thermal velocities are then added to the neutrino component.

The next step is then to evolve the particle distribution in an N-body solver. In the next section we will describe the GADGET Poisson solver.

3.2 GADGET - a Poisson solver

The overall idea of an N-body integrator is very simple: Assign position, velocity and mass to particles in a periodic 3D simulation volume and let the whole system evolve under Newtonian gravity in an expanding space-time. In reality, as will be shown below, the technical implementation of the simple physical equations is very complex.

Due to the long-range nature of gravity, falling of as r^{-2}, distant mass distributions cannot be neglected when calculating the gravitational forces. The most simple way to construct an N-body integrator is to make a direct particle-particle (PP) summation of gravitational forces between the N particles. This leads to $N(N-1)$ force computations and renders the PP method useless for more than a million particles. Therefore in N-body simulations most of the efforts are invested in finding approximations for the true gravitational force which reduce the errors to an acceptable level while improving simulation times significantly.

One of the leading N-body codes is GADGET-2 [26], developed by V. Springel and originally published in 2001 [27] (additional information can be found at the GADGET-2 homepage [28], in the user guide [29] and a test of GADGET-2 against other N-body codes can be found in [30]). The N-body simulations presented in this dissertation have been run exclusively with GADGET-2 and all the extensions made to include the effect of neutrinos are incorporated into this code. The rest of this section is mainly based on [26] in which additional information can be found.

3.2.1 The gravitational force

There are two basic equations which should be solved. First the physical gravitational potential at each particle position, i, should be found by summation over all the other particles j

$$\phi_i = -Ga^{-1} \sum_{j,j\neq i} \frac{m_j}{r_{ij}}, \tag{3.30}$$

where r_{ij} is the comoving distance between particles i and j. The acceleration on particle i is found from

$$\ddot{\mathbf{x}}_i + 2H\dot{\mathbf{x}}_i = -a^{-2}\nabla\phi_i. \tag{3.31}$$

The second term appears as a viscous drag term in comoving coordinates and arises from the expansion of the Universe. It leads to redshifting velocities in an expanding Universe, with the effect that neutrinos cluster more at low redshift.

The Tree method The gravitational force can be calculated approximately with the hierarchical multipole expansion or the so-called Tree method: The simulation volume is initially enclosed by a cubical root node, which is then subdivided into 8 identical 'daughter' nodes. This process is repeated until the final 'leaf' node containing only one particle is reached. The gravitational force is calculated by 'walking' the tree: If a node contains little mass and / or is distant, then the node does not need to be 'opened'. The monopole force of the node is then calculated by placing its mass at the node's geometrical midpoint. If on the contrary the node contains a large mass distribution and / or is close in space to the target particle, then the node should be opened, i.e. split into its 8 daughter nodes.

The process is continued until the desired level of accuracy is reached. Whether or not a given node should be opened is determined by a cell-opening criterion. Defining $r = |\mathbf{x}|$, GADGET-2 uses

the criterion

$$\frac{GM_{\text{node}}}{r^2}\left(\frac{l}{r}\right)^2 \leq \alpha|\mathbf{a}|, \tag{3.32}$$

where M_{node} is the mass of the node at distance r. l is its extension, $|\mathbf{a}|$ is the acceleration of the particle in the last time-step, and finally α is a tolerance parameter specifying the desired gravitational force accuracy. If Eq. (3.32) is satisfied the node is used, and this branch of the tree should not be walked further. The criterion makes sense, since a small mass in a small node at a large distance should not be opened if its gravitational force is less than a given fraction α of the gravitational acceleration in the last time-step. Suitable values of α should be around 0.005.

To avoid situations with Eq. (3.32) satisfied, but where a particle lies close to a node and potentially very close to another particle within the node, GADGET-2 uses the additional criterion

$$|r^i - c^i| \leq 0.6l, \tag{3.33}$$

where $i \in (x, y, z)$ and c^i is the node center coordinates. The criterion demands that the particle must always lie somewhat outside of the node.

To avoid spurious gravitational forces between particles for small particle separations the gravitational force is softened below a certain scale. In cosmological simulations this value is initially constant in comoving coordinates and then frozen in physical coordinates below a certain redshift.

When the Tree method is used alone, without the Particle-Mesh method described below, periodic boundary conditions imposed on the cubical simulation volume is enforced with Ewald summation. This method takes into account the infinite number of particle images obtained by stacking the periodic simulation volume. With the Tree method the simulation-time scale as $N\log N$, a substantial improvement over the $N(N-1)$ scaling of direct particle summation.

The PM method The gravitational force can also be calculated with the Particle-Mesh (PM) method. With this method the N-body particle mass is interpolated to a regular grid with the Clouds-In-Cells (CIC) mass assignment scheme, where the mass is interpolated trilinearly to the 8 corners of its cell. The resulting density grid is then Fourier transformed, since in k-space the gravitational potential can easily be found from the Poisson equation by dividing by k^2, i.e.

$$\phi(\mathbf{k}) = -4\pi G a^2 \frac{\delta\rho(\mathbf{k})}{k^2}. \tag{3.34}$$

Inverse Fourier transforming $\phi(\mathbf{k})$ establishes the gravitational potential in real space on the mesh, $\phi(\mathbf{x})$. GADGET-2 then calculates the forces along each coordinate direction on the mesh with the four-point differencing rule

$$\left.\frac{\partial\phi}{\partial x}\right|_{ijk} = \frac{1}{\Delta x}\left[\frac{2}{3}(\phi_{i+1,j,k} - \phi_{i-1,j,k}) - \frac{1}{12}(\phi_{i+2,j,k} - \phi_{i-2,j,k})\right], \tag{3.35}$$

where Δx is the mesh spacing. This force is then CIC interpolated to the particle positions. Altogether the force field calculated at the particle positions are convolved twice with the CIC kernel, and this effect is deconvolved by dividing twice by the term

$$\prod_{i=x,y,z} \text{sinc}^2\left(\frac{k_i R_{\text{BOX}}}{2N_{\text{mesh}}}\right), \tag{3.36}$$

where $R_{\rm BOX}$ is the box size and $N_{\rm mesh}$ is the number of mesh cells per dimension.

The PM method is the fastest one for calculating the gravitational force, but this force gets inaccurate at distances below a few mesh spacings. An advantage of the PM method is that, given the implicitly assumed periodicity in the Fourier transformation, the effect of the periodic box, i.e. the infinite number of particle images, is automatically taken into account, and the calculated large-scale force is basically exact.

The TreePM method The TreePM method combines the best from the Tree and PM methods. The long-range force is calculated fast and accurately with the PM method, and the short-range force is found with the Tree method, which does not suffer any resolution problems around and below the mesh spacing. Box periodicity is included with the PM method.

More specifically, the gravitational potential can in Fourier space be split into long- (lr) and short-range (sr) parts which must be patched together

$$\phi(\mathbf{k}) = \phi^{\rm lr}(\mathbf{k}) + \phi^{\rm sr}(\mathbf{k}) = -4\pi G a^2 \frac{\delta\rho(\mathbf{k})}{k^2}. \tag{3.37}$$

The interpolation between the two parts should be performed with a filter function, F, which minimizes the search region in the Tree part and at the same time suppresses the long-range force at scales below a few mesh spacings. Letting r_s denote the scale of this short-range / long-range force split, the following form for the filter function has been suggested [31]

$$F(kr_s) = e^{-k^2 r_s^2}. \tag{3.38}$$

With this filter function the long-range potential is in Fourier space given by

$$\phi^{\rm lr}(\mathbf{k}) = -4\pi G a^2 \frac{\delta\rho(\mathbf{k})}{k^2} e^{-k^2 r_s^2}, \tag{3.39}$$

and the short-range acceleration on particle i is in real space given by the expression (after Fourier transforming $\phi^{\rm sr}(\mathbf{k})$ and differentiating it)

$$\mathbf{a}_i^{\rm sr}(\mathbf{r}) = -\sum_{j, j\neq i} \frac{G m_j \mathbf{r_{ij}}}{r_{ij}^3} \left[\mathrm{erfc}\left(\frac{r_{ij}}{2r_s}\right) + \frac{r_{ij}}{r_s\sqrt{\pi}} \exp\left(-\frac{r_{ij}^2}{4r_s^2}\right) \right], \tag{3.40}$$

where erfc is the complementary error function. It can be seen that the usual acceleration is corrected by the term inside the squared parenthesis, which picks out the short-range Tree force only.

Sensible values for r_s should be ~ 1.5 mesh spacings and the local tree walk around each particle should only be conducted out to $r_{\rm cut} \sim 5$ mesh spacings.

3.2.2 Time integration

GADGET-2 uses the logarithm of the scale factor as the time variable. The time-evolution of the particle distribution must be sampled at a number of finite steps. The particles are moved with the 'drift', D, and 'kick', K, operators which operate during a finite time interval Δt on particle i. During a drift operation the velocity is preserved, $\mathbf{v}_i \rightarrow \mathbf{v}_i$, while the position drifts as

$$\mathbf{x}_i \rightarrow \mathbf{x}_i + \frac{\mathbf{p}_i}{m_i} \int_t^{t+\Delta t} \frac{dt}{a^2}, \tag{3.41}$$

whereas during a kick operation the position is preserved, $\mathbf{x}_i \rightarrow \mathbf{x}_i$, while

$$\mathbf{p}_i \rightarrow \mathbf{p}_i - a m_i \nabla \phi_i \int_t^{t+\Delta t} \frac{dt}{a}, \tag{3.42}$$

where $\mathbf{p}_i = a^2 m_i \dot{\mathbf{x}}_i$ is the canonical momentum (see [32] for a detailed derivation).

From these operators one can construct the kick-drift-kick leapfrog integrator with time-evolution operator $T(\Delta t)$ as

$$T(\Delta t) = K\left(\frac{\Delta t}{2}\right) D(\Delta t) K\left(\frac{\Delta t}{2}\right), \tag{3.43}$$

which is used in GADGET-2.

Due to the large dynamic range in density in cosmological N-body simulations, it is advantageous to incorporate individual adaptive time-steps with the aim of decreasing the overall simulation time. In low density void regions the accelerations on particles change much more slowly than inside very high-density galaxy clusters. In the latter case, the time-steps should therefore be much shorter. The time-line of the short-range force can be subdivided into power of 2 time-scales. The time-evolution operator then takes the following form

$$T(\Delta t) = K_{\mathrm{lr}}\left(\frac{\Delta t}{2}\right)\left[K_{\mathrm{sr}}\left(\frac{\Delta t}{2 \cdot 2^m}\right) D(\frac{\Delta t}{2^m}) K_{\mathrm{sr}}\left(\frac{\Delta t}{2 \cdot 2^m}\right)\right]^{2^m} K_{\mathrm{lr}}\left(\frac{\Delta t}{2}\right), \tag{3.44}$$

where m is a positive integer.

The gravitational time-step used for each N-body particle in the Tree part is found from

$$\Delta t_{\mathrm{grav}} = \min\left[\Delta t_{\mathrm{max}}, \left(\frac{2\eta\epsilon}{|\mathbf{a}|}\right)^{1/2}\right]. \tag{3.45}$$

Δt_{max} is the maximal allowed time-step, η is an accuracy parameter, ϵ is the gravitational softening and finally $|\mathbf{a}|$ is the particle acceleration. In the TreePM mode, the PM time-step is set by Δt_{max}, but reduced if the particles travel more than a given small fraction of the mesh size. This latter criterion is frequently invoked when fast moving neutrino particles are included in the N-body simulation.

3.2.3 Parallelization and domain decomposition

Due to the very large particle load in cosmological simulations it is paramount to use many CPUs. Each CPU receives a fraction of the total data, which is stored on the local processor only. The CPUs then perform local calculations on their own particle sets, whereafter the local information and partial results are distributed to all or a fraction of the other processors with the Message Passing Interface (MPI). The parallelization of the problem in turn leads to a much higher algorithmic complexity.

To reduce communication between the processors, the particles in the simulation volume should be distributed to the processors in such a way that the surface-to-volume ratio for the local particle distribution is minimized. The domain decomposition is constructed with the space-filling fractal Peano-Hilbert curve, which has the desired property that it makes the domain decomposition independent of the number of processors used. With this method 3D space is transformed into a 1D curve, in such a way that points which are close in 3D space also will be close along the 1D

curve. The domain decomposition is then constructed by partioning the 1D curve and distributing the resulting pieces to each processor.

Branches of the tree not reciding on the local processor is represented by pseudo-particles. If the cell-opening criterion demands these pseudo-particles to be opened, the local particle is sent to the processor holding the pseudo-particle. This local processor then does the tree walk along the given branch and sends the final result back to the first processor. Due to the reduced surface-to-volume ratio arising from the domain decomposition, particle communication involving pseudo-particles is significantly reduced.

The parallel Fast Fourier Transform (FFT) is constructed by chopping up the 3D mesh along one of the coordinate directions and assigning the resulting slabs to the processors. The more or less cubical particle distributions are CIC interpolated to a more or less cubical grid, and the resulting density field is then sent to the processors holding the slabs used for the FFT.

The desired goal of the parallization strategy is to reduce the simulation time linearly with the number of processors used. The scalability clearly depends on the simulation setup, particularly the number density of N-body particles. Over a wide range of CPUs GADGET-2 achieves this linearity, though the simulation time saturates (and could potentially increase) for smaller particle-load-to-CPU ratios. This fact is due to the very high level of processor communication required. The tree force calculation consumes roughly half of the simulation time, with work-load imbalances between the CPUs and the domain decomposition contributing around one-fourth. Finally, the PM part only contributes around 5% to the simulation time.

3.2.4 Technical implementation of neutrinos in GADGET-2

This subsection will briefly describe the changes we have made to the GADGET-2 code. The implementation will focus on three areas, namely the generation of ICs, the inclusion of neutrinos and finally on-the-fly calculation of statistical properties.

Initial conditions As in every ANSI C program the code begins by calling main.c. From this routine GADGET-2 then calls begrun.c, which in the base version reads in the parameter file and the initial conditions. In the amended version the code calculates the ICs upon started-up if specified. It reads in the TFs and a thermal velocity table for the neutrinos and then loops over the desired number of N-body particle species and adds a 2LPT correction if specified. During the calculation of the ICs, the particle data is stored in a separate structure which saves roughly 60% memory due to the omission of non-relevant parameters from the usual particle structure. Particle ICs are then written to the desired number of files, and read in in the usual way. If needed a neutrino Fourier grid is then created.

When calculating the ICs a base grid-size should be specified. This base grid is used to ensure that several particle grids with different sizes have the same large-scale structure. This corresponds to drawing the same sequence of random numbers for the common wavenumbers. The code allows the particle grid-sizes to be equal to, larger or smaller than the base grid. Identical random numbers are achieved by assigning an IC seed to each slab in the base grid. For particle grid sizes smaller than the base grid, random numbers must be 'burned', i.e. only the relevant numbers are picked out, whereas for larger particle grid sizes new IC seeds are created from the base grid ones. This method allows for a processor independent random number sequence.

Neutrinos When a neutrino component is included the code also allows it to be represented as a Fourier grid, which is updated whenever a PM time-step is performed. It is furthermore possible to convert a specified fraction of the neutrino grid to sets of neutrino N-body particles. The usual way to initiate this particle creation cascade is to specify a ratio of the CDM particle velocity to the neutrino thermal velocity. The neutrino thermal velocity is taken to be the upper velocity corresponding to $q/T = 1$. Thereafter this ratio can either scale as the next q/T bin or all the neutrino momentum bins up to a certain maximum q/T value should be dumped to particles in consecutive time-steps. As will be demonstrated in Chapter 8, the second option is generally preferred. Upon restart the code keeps track of the number of momentum bins converted to particles, and the neutrino module is in general fully compatible with the restart mode in GADGET-2.

Statistics The code supports on-the-fly calculation of statistical quantities such as the species dependent power spectrum, velocity distribution and zoomed-density grids. In the latter case extra parameters, such as smoothing lengths and densities, are added to the usual particle structure.

3.3 Extracting the power spectrum from N-body simulations

Throughout this dissertation the power spectrum will be used as a statistical tool to quantify the effect of massive neutrinos on non-linear structure formation. A few comments on the power spectrum are therefore appropriate.

For Gaussian distributed primordial initial conditions, the power spectrum gives a full statistical description of the underlying N-body particle density field as long as the particle distribution is linear. In this case the power spectrum gives the variance of the Gaussian distributed N-body particle displacements. In the non-linear regime this distribution is no longer Gaussian and the power spectrum no longer provides the full statistical description. Higher-order statistics such as the bispectrum and the trispectrum are then needed. In this dissertation we only calculate the power spectrum since this is the quantity reported by current observations.

From N-body simulations the power spectrum is calculated by interpolating the particle distribution with the CIC kernel to a regular grid. The density field is then Fourier transformed and the final power spectrum is found after deconvolving the CIC kernel as explained in Eq. (3.36).

In mathematical terms the Fourier space density contrast is found from

$$\delta(\mathbf{k}) = \frac{1}{N_{\rm PM}^3}\left(\frac{R_{\rm BOX}}{2\pi}\right)^{3/2}\sum_{\mathbf{x}}\delta(\mathbf{x})e^{i\mathbf{k}\cdot\mathbf{x}}, \tag{3.46}$$

where $R_{\rm BOX}$ is the simulation volume sidelength and $N_{\rm grid}$ is the 1D size of the regular grid. The wavenumber is found from $\mathbf{k} = 2\pi/R_{\rm BOX}\cdot\mathbf{n}$, where $\mathbf{n}$ has individual components spanning the range $-N_{\rm grid}/2$ to $N_{\rm grid}/2-1$ in integer steps. The power spectrum is then constructed from

$$P(k) \equiv |\delta(k)|^2, \tag{3.47}$$

where the assumption of isotropy has been used to eliminate the effect of the direction of the wavevector on the power spectrum.

Since only a few Gaussian distributed realisations of the linear theory power spectrum are drawn at wavenumbers close to the fundamental mode of the simulation volume, $k_{fm} = 2\pi/R_{\rm BOX}$, the

large-scale distribution comparable to or somewhat smaller than the box size suffers from cosmic variance. The true N-body power spectrum can only be recovered by making an ensemble average over an infinite, or at least a large, number of realisations of the linear theory power spectrum. Cosmic variance at a given scale can also essentially be removed by enlarging the simulation volume, but the trade-off is then reduced resolution at small scales for a fixed number of N-body particles. The definition in Eq. (3.46) ensures that $P(k)$ is independent of the size of the simulation volume.

The cosmological parameter σ_8, or in general σ_R, is constructed from the power spectrum by integrating over all k-space

$$\sigma_R^2 \equiv \int d^3k W^2(kR) P(k), \tag{3.48}$$

where $W(kR)$ is the top-hat window function

$$W(kR) = 3\left[\frac{\sin(kR)}{(kR)^3} - \frac{\cos(kR)}{(kR)^2}\right]. \tag{3.49}$$

The derived quantity, σ_R, is in real space equivalent to averaging the density contrast in spheres of radius R.

Chapter 4

Neutrino Physics

Neutrino means 'small neutral one' in italian. It is a light elementary particle which is part of the Standard Model of particle physics, and it was first proposed by Wolfgang Pauli in 1930 to safeguard the various conservation laws in the β-decay process $n \rightarrow p + e^- + \bar{\nu}_e$. It has a half integer spin, $\frac{1}{2}\hbar$, so that it must be a fermion obeying Fermi-Dirac statistics, and it couples to the other Standard Model particles through gravity and the weak force.

We believe that there are 3 neutrino species or flavours labelled the electron (ν_e), muon (ν_μ) and tau (ν_τ) neutrinos and their corresponding anti-particles. This number beautifully fits into the overall picture of 6 leptons and 6 quarks. Neutrinos have left-handed helicity states with their spin anti-parallel to their momentum, while anti-neutrinos have right-handed helicity states. There might also exist so-called sterile neutrinos which have no weak interaction and Majorana neutrinos, where the neutrino can change into its anti-particle by flipping its spin state.

According to the Standard Model of particle physics neutrinos should be massless. But by observing neutrinos from the Sun and from the decay products from cosmic rays, so-called *atmospheric neutrinos*, it is today known that neutrinos oscillate between its three flavours. This in turn leads to the conclusion that neutrinos have a small, but finite mass.

From the point of view of structure formation and N-body simulations we need 4 key characteristics about neutrinos: The number of neutrino species, their mass, the neutrino temperature and finally how much the neutrinos contribute to the density parameter Ω_ν. This chapter is based on [17, 33, 34, 35] in which additional information can be found.

4.1 The number of neutrino species and their mixing matrix

The number of neutrinos, N_ν, is constrained by the decay of the Z boson to be extremely close to 3. This does not rule out extra sterile neutrinos to which the Z boson cannot decay. In fact, cosmology (CMB) seems to prefer a value which could be consistent with 4. Hints for sterile neutrinos have also recently been reported by the MiniBooNE Collaboration [36], and subsequently a two sterile neutrino scenario with a total mass of $\sim 0.8\,\mathrm{eV}$ was found to be consistent with cosmology [37]. Even without sterile neutrinos N_ν is slightly larger than 3 (3.046 is preferred by the Standard Model), due to the convention of assigning to N_ν the extra energy injected into the neutrino component from $e^- e^+$ annihilation.

The fundamental idea underlying neutrino oscillations is the following: Neutrinos are created and destroyed as flavour eigenstates (ν_e, ν_μ, ν_τ), but they propagate as mass eigenstates. The

3 mass eigenstates are denoted by ν_1, ν_2 and ν_3, and they are related to the flavour states by a unitary transformation matrix of the form [33]

$$\begin{pmatrix} \nu_e \\ \nu_\mu \\ \nu_\tau \end{pmatrix} = \begin{pmatrix} 1 & 0 & 0 \\ 0 & c_{23} & s_{23} \\ 0 & -s_{23} & c_{23} \end{pmatrix} \begin{pmatrix} c_{13} & 0 & s_{13}e^{-i\delta} \\ 0 & 1 & 0 \\ -s_{13}e^{i\delta} & 0 & c_{13} \end{pmatrix} \begin{pmatrix} c_{12} & s_{12} & 0 \\ -s_{12} & c_{12} & 0 \\ 0 & 0 & 1 \end{pmatrix} \begin{pmatrix} \nu_1 \\ \nu_2 \\ \nu_3 \end{pmatrix}. \quad (4.1)$$

Here $c_{ij} = \cos\theta_{ij}$ and $s_{ij} = \sin\theta_{ij}$, with θ_{ij} being the mixing angle between states i and j, and δ is a charge-parity violating phase.

Due to the different masses of the neutrino mass eigenstates they will propagate through space with different velocities which leads to flavour oscillations. To investigate how flavour oscillations are related to the mass eigenstates we will look at a simplified 2-dimensional neutrino mass mixing scenario

$$\begin{pmatrix} \nu_e \\ \nu_\mu \end{pmatrix} = \begin{pmatrix} \cos\theta & \sin\theta \\ -\sin\theta & \cos\theta \end{pmatrix} \begin{pmatrix} \nu_1 \\ \nu_2 \end{pmatrix}. \quad (4.2)$$

The evolution of mass eigenstate i is given by

$$\nu_i(t) = \nu_i(0)e^{-iE_i t}, \quad (4.3)$$

and for relativistic particles $E_i \simeq p + m_i^2/(2E)$, where the small difference in energy between the mass eigenstates only arises from the different masses. Assuming that all neutrinos start out as electron neutrinos, denoted by $\nu_e(0)$, the time-dependent amplitude of the electron neutrinos are given as

$$A_e(t) = \frac{\nu_e(t)}{\nu_e(0)} = \cos^2\theta\ e^{-iE_1 t} + \sin^2\theta\ e^{-iE_2 t}. \quad (4.4)$$

The probability for an electron neutrino to stay in that state is then given as

$$P_{\nu_e \to \nu_e} = A_e(t)A_e^*(t) = 1 - \sin^2(2\theta)\ \sin^2\left(\frac{\Delta m^2}{4E}t\right), \quad (4.5)$$

where $\Delta m^2 = m_2^2 - m_1^2$. Therefore, measuring the relative fraction of a given neutrino flavour will constrain $m_i^2 - m_j^2$ and not the absolute mass values. It can also be seen that a longer propagation path (larger t) can probe smaller mass square differences. This is exactly the case with solar neutrinos, to which we will now turn.

4.2 Neutrino oscillation observations and experiments

In the core of the Sun only electron neutrinos are produced. This happens in nuclear fusion processes such as

$${}^1_1H + {}^1_1H \to {}^2_1H + e^+ + \nu_e. \quad (4.6)$$

Due to the very small neutrino cross section, these electron neutrinos move freely to Earth. Observations then found the number of neutrinos detected to be a factor of 3 short of the number predicted from stellar models. This is the so-called *Solar Neutrino Problem*, and it is solved by neutrino oscillations: The neutrinos are created as electron neutrinos in the core of the Sun, but

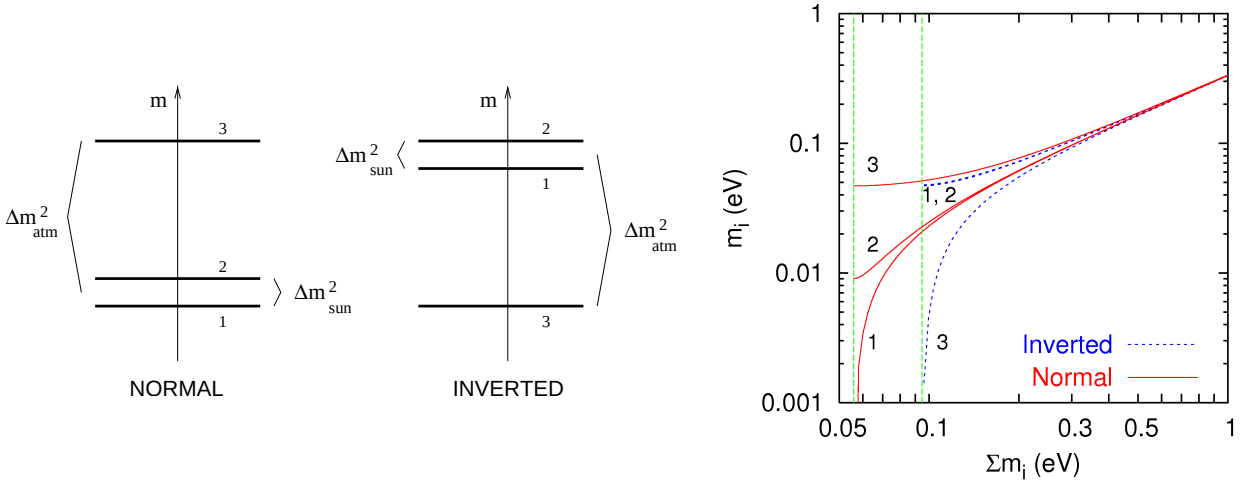

Figure 4.1: The normal and inverted hierarchies are displayed in the left panel, whereas the right panel shows how the neutrino masses evolve in the two hierarchies as a function of $\sum m_\nu$. The figures are taken from [10].

they oscillate into μ neutrinos on their way to Earth. Taking the effect of solar matter on neutrino oscillations into account, the so-called MSW mechanism, the number of electron neutrinos are diluted by the required factor of 3. Since the current bounds on θ_{13} is consistent with zero, it is reasonable to assume that the electron neutrino does not oscillate into its tau counterpart. These solar neutrinos have been observed at various underground locations, for instance at the Sudbury Neutrino Observatory.

When cosmic rays, such as protons, collide with the atmosphere and produce decaying pions, atmospheric neutrinos are subsequently created in processes such as

$$\pi^+ \rightarrow \mu^+ + \nu_\mu, \tag{4.7}$$

and thereafter

$$\mu^+ \rightarrow e^+ + \nu_e + \bar{\nu}_\mu. \tag{4.8}$$

From these reactions the expected flux ratio of muon to electron neutrinos should be two. In reality they are observed to be unity since half of the μ neutrinos have oscillated into τ neutrinos. The μ neutrinos have not had time to oscillate into electron neutrinos due to the small value of Δm^2_{21}. Atmospheric neutrinos have been measured in the Super-Kamioka Nucleon Decay Experiment.

The KATRIN tritium β-decay experiment, which will begin to collect data in 2012, will measure the mass of the electron neutrino directly with a sensitivity of 0.2 eV.

4.3 Neutrino mass hierarchies

Neutrino oscillations have also been observed from man-produced experiments. The KamLAND experiment [38] measures the neutrino flux from nearby nuclear plants. Together with the solar neutrino experiments [39] it provides constraints on the neutrino mass splitting $\Delta m^2_{\text{sol}} = \Delta m^2_{21}$ and

the mixing angle $\sin^2\theta_{\rm sol} = \sin^2\theta_{21}$. The solar neutrino mass splitting is measured to be $\Delta m^2_{\rm sol} = 7.65^{+0.23}_{-0.20} \cdot 10^{-5}\,{\rm eV}^2$ with 1σ errors indicated [40]. In $\sin^2\theta_{\rm sol}$-$\Delta m^2_{\rm sol}$ space the solar and KamLAND data give roughly perpendicular likelihood contours, signifying the importance of combining solar neutrino observations with man-produced experiments.

The atmospheric neutrino observations are complemented by accelerator experiments such as K2K and MINOS, and the atmospheric neutrino mass splitting is measured to be $|\Delta m^2_{\rm atm}| = |\Delta m^2_{31}| = 2.40^{+0.12}_{-0.11} \cdot 10^{-3}\,{\rm eV}^2$ [40]. Fits for the mixing angles are roughly given by ($\sin^2\theta_{21}$, $\sin^2\theta_{32}$, $\sin^2\theta_{31}$) = (0.304, 0.50, 0.01). It can be seen that the mixing between eigenstates 2 and 3 is close to maximal whereas the one between eigenstates 1 and 3 is consistent with zero.

While $\Delta m^2_{21} > 0$ the sign of Δm^2_{31} determines whether we have a normal ('+'-sign) or an inverted ('−'-sign) hierarchy. These hierarchies are schematically illustrated in the left panel of Fig. 4.1. If we assume a normal hierarchy then the smallest value of m_3 can be found by setting m_1 equal to zero. The lower bound is then $m_3 = 0.049\,{\rm eV}$ and $m_2 = 0.0087\,{\rm eV}$ giving $\sum m_\nu > 0.058\,{\rm eV}$. Assuming an inverted hierarchy and setting $m_3 = 0$ we get $m_1 = 0.049\,{\rm eV}$ and $m_2 = 0.050\,{\rm eV}$ giving $\sum m_\nu > 0.099\,{\rm eV}$. Of course these are just lower bounds and the total neutrino mass can be much higher. If this is the case then the neutrinos become more and more mass degenerate, i.e. get identical masses, as the neutrino masses increase. This is illustrated in the right panel of Fig. 4.1 and justifies the assumption of degenerate neutrinos for $\sum m_\nu \gtrsim 0.3\,{\rm eV}$.

In our N-body simulations we have chosen to simulate mass degenerate neutrinos. This choice does of course not strictly obey the results from neutrino oscillations unless the neutrino mass is very high. The choice is though conceptually much more simple, it facilitates comparisons as the neutrino mass is varied and it captures the essence of the underlying physics. To perform N-body simulations with neutrinos correctly, one should include 3 different neutrino species, with separate TFs, Fermi-Dirac distributions and N-body particle masses. This level of rigour is only necessary for neutrinos close to the lower mass bound, in which case the grid method described in Chapter 7 will be most appropriate.

During structure formation the neutrinos can be modelled as exact mass eigenstates [41]. Initially the neutrino is created in a flavour state with a relativistic energy. The flavour state is a superposition of three mass states and these states also receive the same relativistic energy. As the expansion of the Universe redshifts the neutrino momenta into the non-relativistic regime, the 3 mass eigenstates get different velocities and decohere. The Cosmic Neutrino Background floating in the Universe therefore consists of 3 separated mass eigenstate wave functions, with thermal velocity distributions equal to 3 different Fermi-Dirac distributions which are themselves functions of the mass of the particular mass eigenstate. For mass degenerate neutrinos the situation is less complicated since $m_1 = m_2 = m_3$ entails $m_e = m_\mu = m_\tau$ and the neutrino component can be modelled as consisting of one particle type with one Fermi-Dirac distribution.

4.4 The neutrino temperature

We can relate the neutrino temperature to the photon temperature [11, 17, 33]. They will not be identical since the neutrinos decoupled before the photons were heated by the annihilating electrons and positrons. The entropy density, s, is defined as

$$s \equiv \frac{\rho + P}{T}. \tag{4.9}$$

The density of the photon component with its two spin states, $g_s = 2$, is

$$\rho_\gamma = g_s \int \frac{d^3p}{(2\pi)^3} \frac{p}{e^{p/T} - 1} = g_s \frac{\pi^2}{30} T^4, \tag{4.10}$$

where we use units so that $\hbar = c = k_B = 1$. Since for a relativistic component $P_\gamma = \frac{1}{3}\rho_\gamma$, the entropy density for the photons is given by

$$s = g_s \frac{2\pi^2}{45} T^3. \tag{4.11}$$

For fermions the effect of the different distribution function is to decrease the entropy density by a factor of 7/8. Before e^-e^+ annihilation at temperature T_1, the photons contributed a factor of 2 to g_s, one for each spin state. The electrons and positrons have 2 spin states each, and the 3 neutrinos and their anti-particles have 1 per particle. In sum, for the bosonic and fermionic states we get $2 + \frac{7}{8}10 = 43/4$. After annihilation the electrons and positrons have disappeared from the budget and the photons and neutrinos have acquired different temperatures. Using the fact that the expansion of the Universe is adiabatic we have $s_1 a_1^3 = s_2 a_2^3$. Since the neutrino temperature just redshifts as $a_1 T_1 = a_2 T_2$, it is related to the photon temperature by

$$T_\nu \simeq \left(\frac{4}{11}\right)^{1/3} T_\gamma. \tag{4.12}$$

Since the neutrino component is slightly heated by the e^-e^+ annihilation this equation is only accurate at the 1% level. It can be seen that the neutrinos are cooler than the photons by a factor of ~ 0.71. From measurements of the CMB blackbody spectrum it is known that $T_\gamma = 2.725\,\mathrm{K}$ from which it can be found that the neutrino temperature is $T_\nu = 1.945\,\mathrm{K}$ today. This important parameter enters the neutrino distribution function.

4.5 Relation between Ω_ν and $\sum m_\nu$

It is possible to derive a very important relation between Ω_ν and m_ν. For a non-relativistic neutrino component, $\epsilon = a m_\nu$, the neutrino density is today ($q = p$) given by

$$\rho_\nu = g_s m_\nu \int \frac{d^3q}{(2\pi)^3} \frac{1}{e^{q/T_\nu} + 1}. \tag{4.13}$$

Performing the integral and dividing by $\rho_{crit} \propto h^2$ we get

$$\Omega_\nu \simeq \frac{\sum m_\nu}{94\, h^2\,\mathrm{eV}}. \tag{4.14}$$

To get this equation we have multiplied Eq. (4.13) by a factor of 2 to take anti-particles into account. The sum in Eq. (4.14) therefore runs over the ν_e, ν_μ and ν_τ neutrinos and not their anti-particles. It should be noted that the total neutrino mass is independent on whether the summation is performed over the flavour states or the eigenstates. Eq. (4.14) states the very important fact that increasing $\sum m_\nu$ increases Ω_ν. This is related to the fact that the number density of neutrinos is constant, $n_\nu = \frac{3}{11} n_\gamma = 112\,\mathrm{cm}^{-3}$, so that Ω_ν must be directly proportional to $\sum m_\nu$.

For a flat Universe consisting only of neutrinos this leads to an upper bound on the total neutrino mass of $94\, h^2\,\mathrm{eV} \sim 46\,\mathrm{eV}$ for $h = 0.7$. If we assume that the neutrinos only make up the

CDM content in the Universe, then for $\Omega_c = 0.25$ the upper bound on the total neutrino mass is reduced to 12 eV. On the other hand the final neutrino distribution function for, say the Milky Way, cannot attain a value which is larger than the maximum value of the initial neutrino distribution function, i.e. 1/2. This leads to a lower bound on the neutrino mass of 25 eV if the dark matter is to be comprised of ordinary neutrinos. For less massive galaxy systems this lower bound is increased. These two inconsistent values for the neutrino mass, i.e. $\lesssim 12\,\text{eV}$ and $\gtrsim 25\,\text{eV}$, lead to the conclusion that neutrinos are not the CDM candidate but instead a sub-dominant component.

Eq. (4.14) also states that the neutrino velocity cannot be chosen at random. For a given Ω_ν the neutrino mass is fixed for degenerate neutrinos, and this in turn fixes the neutrino velocity distribution. One cannot arbitrarily construct a small neutrino thermal velocity by increasing the neutrino mass while decreasing the number density of neutrinos. If only $\sum m_\nu$ is known one will only have the freedom to shift the total neutrino mass around between the 3 eigenstates. To make the neutrino mass cluster the most, one needs almost all of the mass to be contained in just one eigenstate. Of course, this freedom disappears once the two extra equations found from neutrino oscillation experiments are included.

Chapter 5

Comparing the Cosmological Model with Observations

This chapter will present current and future constraints on the total neutrino mass. A current robust upper limit at the 2σ level is $\sum m_\nu \sim 1.5\,\mathrm{eV}$. Before turning to these constraints we will describe various cosmological parameter spaces as well as the observational data sets themselves.

5.1 Cosmological parameters

When comparing data with a cosmological model the number of free parameters should be determined. The minimal cosmological (vanilla) model contains 6 free parameters, namely the baryonic, Ω_b, and CDM, Ω_c, density parameters, the Hubble parameter h, the optical depth to reionization τ, the amplitude of the scalar spectrum A_s (or equivalently σ_8, see Eq. (3.48)) and finally the scalar spectral index n_s. In sum, $vanilla = (\Omega_b,\ \Omega_c,\ h,\ \tau,\ A_s,\ n_s)$.

There are many extended models built on top of the vanilla model, each with their respective extra free parameters. When considering neutrinos, $\sum m_\nu$ and the effective number of relativistic species after matter-radiation equality, N_{eff}, should be included. Dark Energy can be modified by allowing w to be time-dependent and therefore $w \neq -1$. Considering inflation, extra parameters can allow for a non-flat Universe $\Omega_k \neq 0$, deviations from a power law of the inflaton perturbations, a running spectral index $dn_s/d\ln k$ and finally the assumptions of adiabatic and Gaussian initial perturbations can be relaxed.

These parameters would encode new physics on top of the vanilla model and more exotic parameters and physics surely do exist. Furthermore, it should always be remembered that when fitting parameters to data it is always done within a given theory: We assume inflation and take the Einstein equations for granted. If these assumptions are not correct, then the values of the cosmological parameters will of course change.

The result of the above considerations is that the values and standard deviations of the parameters depend on the dimension of parameter space. When more parameters are added degeneracies between parameters appear, since the change in one parameter can be offset by appropriate values for the newly added parameters. This has the implication that the total neutrino mass is less constrained in more extended models.

HALOFIT [42] is used to calculate the non-linear matter power spectrum, but it has not so far been calibrated against N-body simulations with massive neutrinos included. This dissertation

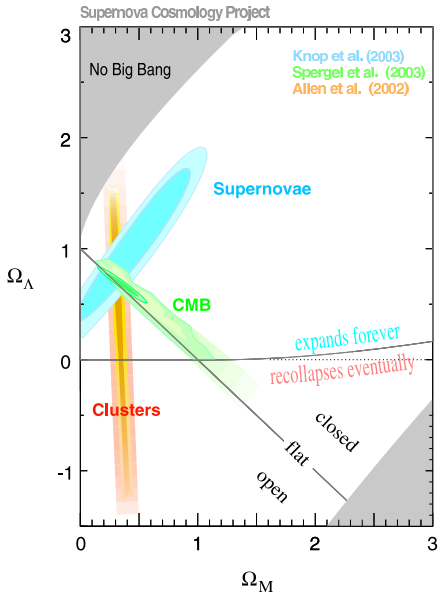

Figure 5.1: This figure illustrates how the use of several data sets can alleviate parameter degeneracies. The figure is taken from the Supernova Cosmology Project [43].

devises different methods for how neutrinos can be incorporated into N-body simulations in a fast and accurate way. These methods are important for accurate modelling in the non-linear regime, which must match the sensitivity of future cosmological precision data. It is therefore important to calibrate HALOFIT against neutrino N-body simulations.

5.2 Observations

The parameter degeneracies can be alleviated by fitting the cosmological parameters within the chosen cosmological framework to several data sets. The reason is that various cosmological data sets probe different redshifts and spatial scales, and therefore have various sensitivities to different parameters. These data sets include, among others, observations of the CMB, the large-scale structure (LSS), supernova data and data from the Hubble Space Telescope (HST) Key Project. An example of the combined use of CMB, LSS and supernova data sets, which lead to consistent results and constrain the Universe to be nearly flat, is shown in Fig. 5.1.

Another example of the combined use of cosmological data sets is shown in connection to the linear matter power spectrum in Fig. 5.2. The figure is qualitatively useful in the sense that it displays at which scales different data sets constrain cosmological parameters (see [45] for how various measurements are mapped onto k-space). From the figure it can be seen that CMB data constrain the largest scales, with galaxy and weak lensing surveys measuring linear and mildly non-linear scales. At even smaller scales Lyman-α forest data provide useful information. With upcoming CMB experiments such as Planck, CMB data will constrain even smaller scales. On the other hand, as LSS observations can be carried out at higher redshifts, larger volumes can be probed in turn constraining the power spectrum at larger scales.

The most important observations of the CMB to date come from the space borne Wilkinson

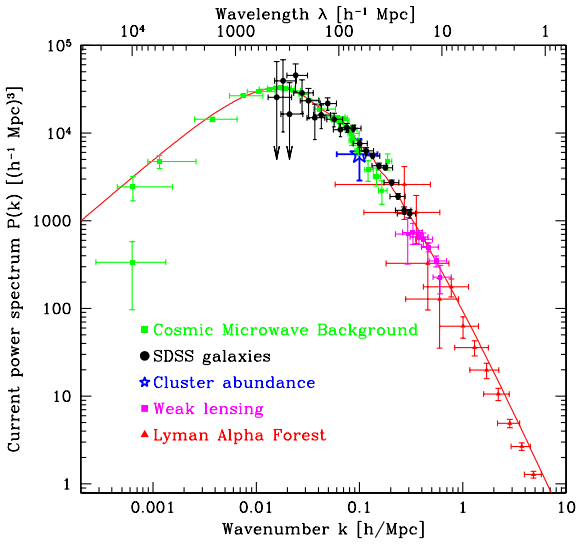

Figure 5.2: The figure, taken from [44], shows the mapping of various cosmological data sets onto k-space, as explained in [45].

Microwave Anisotropy Probe (WMAP) 7-year data which is cosmic variance limited out to the multipole moment $l \sim 550$ [46]. On smaller scales ACBAR [47] and QUaD [48] provide better constraints on the temperature power spectrum.

The best LSS data to date come from the ground based Sloan Digital Sky Survey (SDSS) Data Release 7 (DR7), which measured the angular positions and redshifts of more than 930.000 galaxies. A slice of the observed volume is shown in Fig. 5.3. The matter power spectrum can be reconstructed from the galaxy distribution. To perform this mapping one needs a theory relating the galaxy distribution to its matter counterpart. Finding this so-called bias is non-trivial, since it is not only a function of the scales considered, but also depends on galaxy type, which in turn is related to the galaxy formation history. In sum, accurately modelling the bias limits how far out in k-space the matter power spectrum can be extracted from LSS data. A further complication is related to the fact that galaxies are measured in redshift space. Due to the peculiar motions of galaxies, they will be displaced along the line-of-sight, the so-called Finger-Of-God effect, which needs to be corrected.

To alleviate the problem with relating the galaxy distribution to the matter power spectrum the latter can be reconstructed from Luminous Red Galaxies (LRGs) [50], which constitute a more homogeneous sample due to their higher age and absence of recent large merger events. The resulting power spectrum is called the Halo Power Spectrum (HPS). From LRG data the Baryon Acoustic Oscillations (BAO), with wavelengths of roughly $0.1\,h\,\mathrm{Mpc}^{-1}$, can be observed in the constructed power spectrum [51]. The LRG HPS with the BAO signal imprinted is shown in Fig. 5.4. In Chapter 6 we will calculate the matter power spectrum for various neutrino cosmologies.

Weak gravitational lensing directly measures the matter distribution. The technique is based on the fact that matter perturbations distort the shape of light arriving from distant galaxies, so that measuring the shape of many galaxies can be used to deduce the underlying perturbed matter distribution. Since the measurements are carried out in 2D, the integration along the third radial

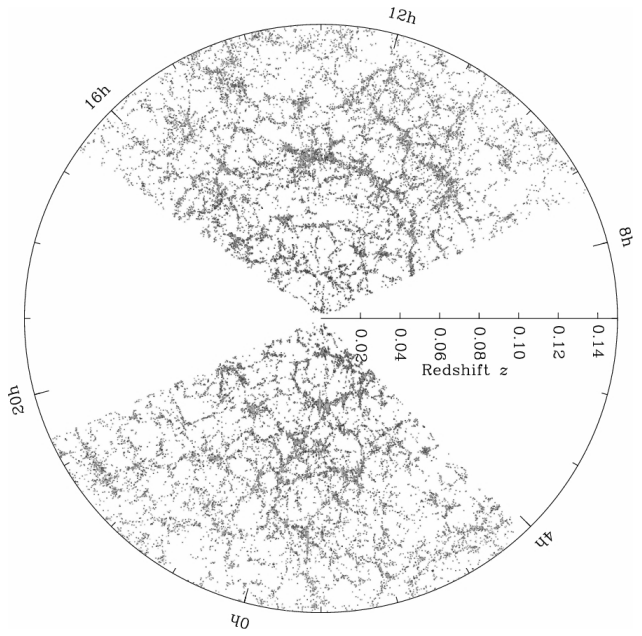

Figure 5.3: The figure shows a slice of the volume probed by SDSS. The Earth is placed at the origin with each point representing a galaxy. The void regions are not mapped due to dust in our own Milky Way. The figure, slightly modified, is taken from [49].

dimension mixes large- and small-scale modes, in effect requiring that non-linearities are correctly modelled.

Cepheids and Type Ia supernovae can be used to probe distances in the Universe. Cepheids are pulsating variable stars which have a well defined period-luminosity relation, which must be calibrated by knowing the distance to a single Cepheid. Since they are up to 30.000 times more luminous than the Sun, they can be seen at large distances. A Type Ia supernova is an exploding white dwarf which has accreted matter from a binary companion, and the resulting luminosity profiles of Type Ia supernovae are thought to be very similar. Whereas Cepheids can be seen out to tens of Mpc, Type Ia supernovae can be observed at Gpc scales. In the overlapping region, Cepheids can be used to calibrate Type Ia supernovae light curves [52, 53]. The HST Key Project used Cepheids and Type Ia supernovae to measure extragalactic distance scales with the aim of measuring the Hubble parameter with a precision of 10% [54]. The derived value for the Hubble parameter from these measurements will be denoted by H_0 in the following section.

Furthermore, bounds on $\sum m_\nu$ can be derived from Lyman-α forest data. The Lyman-α line has a wavelength of 1216Å and is emitted from quasars, which are distant, very luminous galaxies with active galactic nuclei. Due to the expansion of the Universe the line is absorbed at different wavelengths by intermediate neutral hydrogen gas clouds, giving rise to the so-called Lyman-α forest.

The halo mass function, to which we will turn in Chapter 9, is found from the number density of halos in various mass intervals. Clusters can be detected by the Sunyaev-Zel'dovich (SZ) effect, which is the scattering of CMB photons by high energy electrons. X-rays from hot cluster gas can also be used to probe the cluster mass. Finally, the cluster mass can be measured by weak lensing.

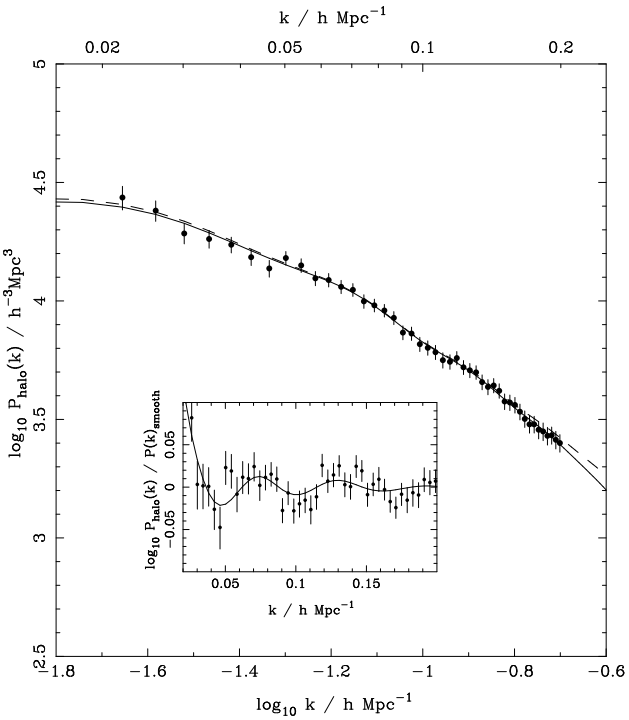

Figure 5.4: The figure, taken from [50], displays the halo power spectrum found from LRGs together with best-fitting WMAP5+LRG ΛCDM models. The inset shows the baryon acoustic oscillations.

In Chapter 9 we will also calculate the radial distribution of matter, the matter density profile, for various halo masses. In individual galaxies it can be found by measurements of the rotation curve, while weak lensing surveys are needed to map the density profiles in clusters of galaxies.

From rotation curves in spiral galaxies it is in principle possible to reconstruct the density profile. For a spherical system, the mass contained within a given radius, $M(< r)$, is related to the circular velocity at that radius, $V(r)$, by the simple relation $M(< r) = rV^2(r)/G$. Spiral galaxies are clearly not spherical systems, though at larger distances from the centers the more or less spherical distribution of the CDM component gives the dominant contribution to $V(r)$.

For a more accurate calculation of the density profile it is necessary to simulate theoretical halos which reproduce the rotation curve and then from these models calculate the density profile. But the presence of bulges, bars and spiral arms as well as late time infall of satellite galaxies distort the rotation curve. To average out these random encounters it is necessary to separately bin many observed and simulated galaxies, which should have the same optical appearance. Given the current constraints on CPU resources and the difficulty with implementing baryonic physics in hydrodynamical simulations, it will be extremely difficult to extract the small contribution from the neutrino mass from observed matter density profiles.

Finally, the cosmological neutrino distribution is very difficult, if not to say impossible, to measure due to the very small neutrino cross section. Measuring the neutrino power spectrum or neutrino density profiles directly will likely remain an impossible goal. This does of course not rule out the possibility to theoretically calculate the distributions, as is in fact done in Part II of this

dissertation.

5.3 Constraints on $\sum m_\nu$

By combining the above mentioned observations different bounds can be set on the total neutrino mass. At present the cosmological data sets are not sensitive to the masses of the individual neutrino eigenstates. The inferred bounds will of course depend on the size of the model space. For a given model the parameter space is usually sampled using the Markov-chain Monte Carlo method as implemented in the code CosmoMC [12] with priors set on the parameters. Below we will only quote 2σ bounds.

Using WMAP data only with the vanilla model extended by $\sum m_\nu$ only, i.e. fixing $N_{\rm eff} = 3.04$ as is predicted from the Standard Model, the upper bound on $\sum m_\nu$ is 1.3 eV. Combining WMAP+BAO+H_0 the upper bound reduces to $\sum m_\nu < 0.58\,\text{eV}$ and if the assumption of a Dark Energy cosmological constant is relaxed, $w \neq -1$, the bound again widens to 1.3 eV [46]. There exists an anti-correlation between $\sum m_\nu$ and w [55]. It is related to the fact that increasing the neutrino mass increases Ω_m which can be offset by $w < -1$ which is allowed by supernovae data. If LRG instead of BAO data is used, these last two bounds are lowered to 0.44 eV and 0.71 eV, respectively.

Allowing $N_{\rm eff}$ to float increases the upper bound on the total neutrino mass to 0.89 eV if data from WMAP+BAO+H_0 is used [56]. Furthermore, allowing $w \neq -1$ relaxes the bound to 1.47 eV. If HPS data is used instead of BAO data the bound is lowered to 1.16 eV and $N_{\rm eff} = 4.79^{+2.02}_{-2.02}$, hinting at the existence of extra neutrino species.

Recently Viel *et al.* [57] found an upper bound on the total neutrino mass of 0.9 eV based on modelling the Lyman-α forest. We will return to this article in subsection 11.2.2.

In sum, all observations to date are consistent with an upper bound of $\sum m_\nu \sim 1.5\,\text{eV}$ for a vanilla + $\sum m_\nu$ + $N_{\rm eff}$ + w model. This bound will of course be relaxed in more extended exotic cosmologies.

5.4 Future observational probes and constraints on $\sum m_\nu$

Within the next few decades cosmology will be enriched by a plethora of new observations of the Universe (see [41] and references herein). Planck is the successor to WMAP, and it is currently measuring the CMB anisotropy sky with such a precision that the angular power spectrum will be cosmic variance limited out to $l \sim 2000$. Moreover, Planck will use the SZ effect to create a catalogue of galaxy clusters. It has been estimated that Planck by itself will constrain the total neutrino mass with a sensitivity of $\sum m_\nu \sim 0.4 - 0.6\,\text{eV}$, and with lensing extraction this number lowers to $0.10 - 0.15\,\text{eV}$ (all quoted sensitivities in this section are at the 1σ level).

In the future several LSS data sets will become available. The Baryon Oscillation Spectroscopic Survey (BOSS) is a continuation of the SDSS project. It will measure the redshift of 1.5 million galaxies out to $z = 0.7$, and it will also provide 160.000 Lyman-α forest spectra originating from quasars. The Wide-Field Multi-Object Spectrograph (WFMOS) is also a galaxy redshift survey which will provide measurements out to $z \sim 4$, and finally the Hobby-Eberly Telescope Dark Energy Experiment (HETDEX) will observe 1 million galaxies at a distance of 10 billion light-years.

Combining cosmological data from these LSS surveys with Planck data will constrain the total neutrino mass at the 0.2 eV level. This accuracy can only be achieved if non-linearities, such as

those caused by neutrinos and baryons, are modelled correctly and the bias between the measured tracer and the matter distribution is sufficiently understood.

The planned Large Synoptic Survey Telescope (LSST) can be used to extract the weak lensing power spectrum, and combining observations from LSST with Planck data could constrain the total neutrino mass at the 0.1 eV level.

Additional surveys, such as those of the Lyman-α forest from BOSS, cluster mass surveys based on measuring X-ray luminosities as well as observations of the 21-cm line of neutral hydrogen could in conjunction with CMB data constrain the neutrino mass at the $0.0003 - 0.2\,\mathrm{eV}$ level. The smallest uncertain sensitivity comes from the 21-cm line in the more distant future. In the *much* more distant future the Cosmic Neutrino Background (CνB) anisotropy could in principle be detected. We will return to this subject in Chapter 10.

In sum, cosmology will in the foreseeable future significantly constrain the total neutrino mass at the 0.1 eV level. If the total neutrino mass is high, $\sim 0.5\,\mathrm{eV}$, cosmology will be able to provide a positive detection of non-zero neutrino masses and their semi-degeneracy. If on the contrary the total neutrino mass lies close to the lower bounds inferred from oscillation experiments, $0.05-0.1\,\mathrm{eV}$, then cosmology will not in the foreseeable future be able to determine whether the neutrino mass hierarchy is normal or inverted.

Regardless of the value of the total neutrino mass, an accurate modelling of non-linear structures will especially be important for utilising weak lensing and galaxy survey data. Part II of this dissertation, to which we will now turn, will present various methods to include the effect of neutrinos on non-linear structure formation.

Part II

Scientific Research

Chapter 6

The Effect of Thermal Neutrino Motion on the Non-linear Cosmological Matter Power Spectrum

Jacob Brandbyge, Steen Hannestad, Troels Haugbølle, Bjarne Thomsen

Abstract We have performed detailed studies of non-linear structure formation in cosmological models with light neutrinos. For the first time the effect of neutrino thermal velocities has been included in a consistent way, and the effect on the matter power spectrum is found to be significant. The effect is large enough to be measured in future, high precision surveys. Additionally, we provide a simple but accurate analytic expression for the suppression of fluctuation power due to massive neutrinos. Finally, we describe a simple and fast method for including the effect of massive neutrinos in large-scale N-body simulations which is accurate at the 1% level for $\sum m_\nu \lesssim 0.15\,\mathrm{eV}$ [1].

6.1 Introduction

Neutrinos are among the most abundant particles in our Universe and therefore play an important role in the formation of large-scale structure. In the past 10 years neutrino oscillation experiments have verified that neutrinos have small, but non-zero masses and that they therefore contribute to the dark matter density in the Universe.

Using a combination of cosmological observables such as the cosmic microwave background, large scale structure, and type Ia supernovae a bound on the sum of neutrino masses of $\sum m_\nu \lesssim 0.2 - 0.7$ eV (95% C.L.) has been derived [58, 59, 60, 61, 62, 63, 64, 65]. The actual value of the bound depends both on the specific combination of data sets used and on the cosmological model. At the moment a fairly robust upper limit can be taken to be roughly $\sum m_\nu \lesssim 0.6 - 0.7$ eV.

This bound mainly uses structure formation data in the linear regime ($k \lesssim 0.15\,h\,\mathrm{Mpc}^{-1}$), but even on such large scales some non-linear contamination is present and must be modelled. This has been done in detail for variations of the standard ΛCDM model, but so far not in a truly consistent way for models which include massive neutrinos.

For the study of neutrino mass bounds with present data the current precision of theoretical power spectrum calculations in the regime $k \sim 0.1 - 1\,h\,\mathrm{Mpc}^{-1}$ is sufficient in the sense that the final result does not depend very significantly on the method used (however, see e.g. [66] for an exception). However, future high precision lensing and galaxy redshift surveys, such as the LSST [67], will constrain the matter power spectrum to percent level precision on scales of $k \sim 0.1 - 1\,h\,\mathrm{Mpc}^{-1}$.

At this level of accuracy the inclusion of neutrinos in the calculation of the matter power spectrum will be crucial, even for neutrino masses close to the current lower bound. While the effect of neutrinos in the linear theory power spectrum is understood in detail much work remains to be done in the semi-linear and non-linear regimes. Furthermore, semi-analytic models of non-linear structure formation such as the halo model must always be checked against N-body simulations.

Neutrinos have thermal velocities which exceed typical gravitational flow velocities by an order of magnitude or more, even at low redshift. Therefore, when setting up initial conditions for N-body simulations the neutrino thermal velocities need to be added to the gravitational flow velocities found from the neutrino transfer function. Including neutrino thermal velocities in N-body simulations is not without problems because the thermal motion introduces a noise term which will affect the underlying gravitational evolution unless high resolution is used.

The problem is similar to the well known problem that particles in an N-body simulation must be put in a configuration like a grid or a glass which respects small-scale homogeneity in order not to introduce a large Poisson noise term. When thermal velocities are included momentum phase space must be sampled and the initial thermal velocities should preferably be chosen in a way where small-scale momentum conservation is enforced.

In the present paper we present the first N-body simulations in which neutrino thermal velocities have been included and convergent results achieved for $k < 1.5\,h\,\mathrm{Mpc}^{-1}$. In the early 90s [68, 69] included neutrino thermal velocities albeit for a model with much higher neutrino masses, and no convergent results were proven. We also note another recent paper [70] in which thermal motion has been included for warm dark matter, a set-up somewhat different from what is studied here. Neutrino clustering in the small-scale limit has been studied using a completely different approach [71, 72] where the full Boltzmann equation has been solved for neutrinos in a background given by pure cold dark matter (CDM), i.e. no feed-back is included and neutrinos are treated as tracer particles in the underlying gravitational potential. This method allows for arbitrarily high resolution, but is not truly self-consistent.

In Section 6.2 we describe the linear theory evolution and the set-up of initial conditions for our neutrino N-body simulations. In Section 6.3 we describe how our N-body simulations are performed, and in Section 6.4 the results are described in detail. Finally, Section 6.5 contains a discussion and our conclusions.

6.2 Linear evolution of perturbations and initial conditions

6.2.1 Linear theory

Evolving the primordial density perturbations set down by inflation to the present involves several steps. As long as perturbations remain small the evolution can be calculated precisely using the linearised Einstein and Boltzmann equations [9], using software such as CAMB [12] or CMBFAST [73].

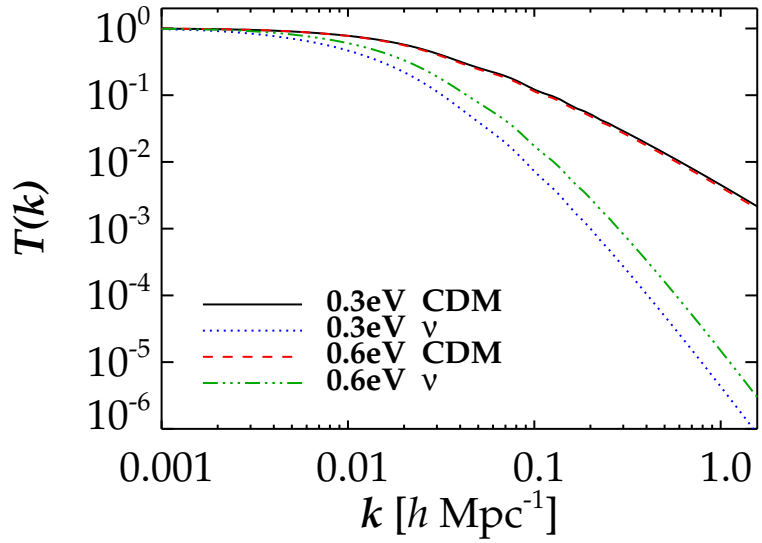

Figure 6.1: The linear theory transfer functions at $z = 4$ for the CDM and neutrino components.

In this regime the power spectrum can be factorised into a primordial component, $P_0(k)$, and a transfer function (TF), $T(k, z)$, which contains all information about the evolution of structure so that $P(k, z) = P_0(k)T^2(k, z)$.

However, once structure enters the non-linear regime precision studies require the use of N-body simulations. To set up the initial conditions (ICs) for our simulations we have calculated the TFs using CMBFAST (using CAMB yields similar results).

We have assumed a flat cosmological model with density parameters $\Omega_b = 0.05$, $\Omega_m = 0.30$ and $\Omega_\Lambda = 0.70$ for the baryon, matter and cosmological constant components, respectively, and a Hubble parameter of $h = 0.70$. We vary the CDM and neutrino density parameters (Ω_c and Ω_ν, respectively) fulfilling the condition $\Omega_c + \Omega_\nu = 0.25$. We have assumed a primordial power spectrum of the form $P_0(k) = Ak^{n_s}$ with $n_s = 1$, i.e. a standard scale-invariant Harrison-Zel'dovich spectrum. The amplitude, giving $\sigma_8 = 0.89$ for a pure ΛCDM model, is chosen so as to fit the CMB [74] on large scales.

Different TFs at a redshift of 4 are shown in Fig. 6.1. The effect of neutrino free-streaming on the TF is clearly seen, and is more pronounced in the lower mass neutrino case.

6.2.2 Initial conditions with two species

The TFs are used to generate the position and velocity ICs for the N-body particles. The Zel'dovich Approximation (ZA) [23], based on first-order Lagrangian perturbation theory, is a standard way to calculate the ICs. Using second-order Lagrangian perturbation theory (2LPT) [24, 25] it is possible to generate ICs in the quasi-linear regime. We are particularly interested in these second-order corrections because the presence of neutrino thermal velocity noise requires simulations to be started at low redshift, close to the non-linear regime.

We have used a modified version of the 2LPT initial conditions code of [75] to generate the ICs for our simulations. The modifications are described in detail below.

In the N-body simulations we include two particle species, CDM and neutrinos. It is not possible

to generate particle ICs for each species simultaneously with the ZA+2LPT formalism. Instead we generate ICs one particle species at a time by using their respective TFs (for CDM we have used a weighted sum of the CDM and baryon TFs for consistency, even though this only matters at high redshift). Thereafter, the N-body particle masses for each species are scaled so that they make up their proper fraction of Ω_m.

The initial positions for the N-body particles are found by adding a displacement field to a regular grid. A standard way to get the particle velocities is to differentiate the initial position displacements. This procedure involves using several numerically determined fitting factors, and therefore breaks down when two species with different TFs are present since then the growth factor is both species and mode dependent. Instead, we get the velocities by generating two displacement fields centered around our starting redshift and then take the time difference. We have tested that these velocities do not depend on the distance in redshift between the two extra displacement fields in a suitable range around our starting redshift.

2LPT involves a relation between the first- and second-order growth factors. But since the perturbed energy density even at $z_i = 4$ (z_i designates the N-body starting redshift) is vastly dominated by CDM, we can neglect the neutrino contribution to the driving term for the CDM growth factor since this would give a small correction to a second-order term. Because the neutrinos are smoothly distributed, first-order theory is very accurate for them, and therefore the second-order corrections give negligible contributions to the neutrinos. We note that this is somewhat similar to the approach taken in Refs. [19, 77, 87] for the case of semi-analytic power spectrum modelling.

In the top row of Fig. 6.2 the CDM and neutrino distributions are shown at $z_i = 4$. Since we run simulations with different numbers of CDM and neutrino N-body particles, the amplitude and phase of the common large-scale modes of each species have been generated with the same random numbers. Therefore, from Fig. 6.2 one can identify the components as having the same large-scale structure. Because of the higher value of the CDM TF at small scales, this component has additional clearly visible small-scale structure. As expected, the neutrino distributions are more homogeneous than their CDM counterpart. The $\sum m_\nu = 0.6\,\mathrm{eV}$ and $\sum m_\nu = 0.3\,\mathrm{eV}$ distributions are similar at $z_i = 4$, with the latter distribution being marginally more homogeneous, as can also be inferred from the TFs in Fig. 6.1.

6.2.3 Thermal velocities

Since the neutrino mass is small the thermal velocities cannot be neglected even at low redshift if percent level precision is to be obtained. Instead, the velocity of a given neutrino N-body particle contains a thermal component drawn from an equilibrium Fermi-Dirac (FD) distribution. Assuming isotropy for the thermal component the probability, Pr, for a neutrino having a momentum smaller than p is given by

$$Pr(<p) = N \int_0^p \frac{p'^2}{e^{p'c/k_b T_\nu} + 1} dp', \tag{6.1}$$

where N is a normalisation which ensures that the probability is bounded between 0 and 1. Fig. 6.3 shows the cumulative FD distributions for different one-particle neutrino masses. The magnitudes of the neutrino thermal velocities were drawn randomly from the FD velocity distribution, and the directions of the thermal velocities were drawn at random as well. This reflects the fact that the neutrino velocity can be split into two uncorrelated contributions. An equilibrium, random contri-

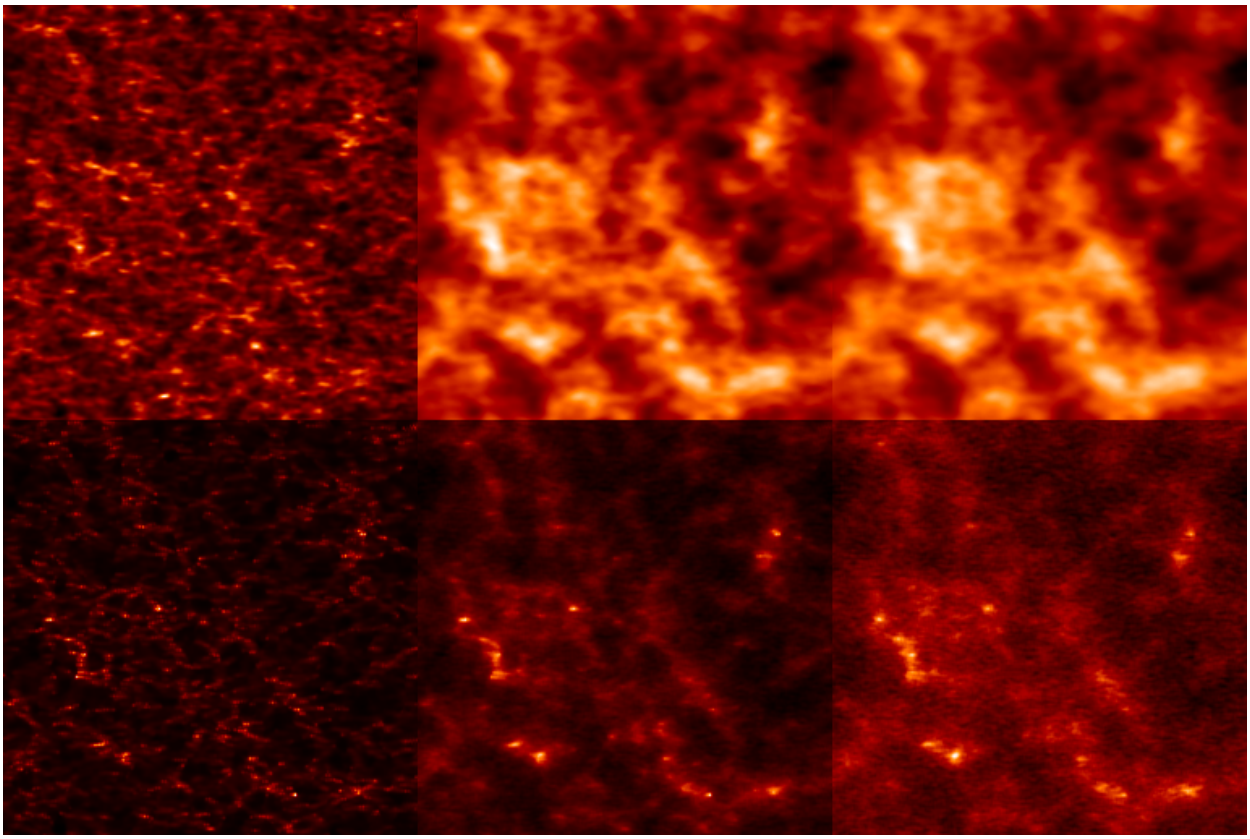

Figure 6.2: Images of the CDM and neutrino density distributions in a slice of the simulation volume. The images span $512\,h^{-1}\,\mathrm{Mpc}$ on a side and has a depth of $10\,h^{-1}\,\mathrm{Mpc}$. To produce the images we have interpolated the masses of the N-body particles to a regular grid with the adaptive smoothing kernel of [76]. The images show the densities for the CDM component (left), neutrinos with $\sum m_\nu = 0.6\,\mathrm{eV}$ (middle), and neutrinos with $\sum m_\nu = 0.3\,\mathrm{eV}$ (right). The top row is at $z_i = 4$ and the bottom row at $z = 0$. To enhance the dynamic range of the CDM structures the square root has been taken of the CDM density field in the $z = 0$ image. The $\sum m_\nu = 0.3\,\mathrm{eV}$ neutrino image at $z = 0$ displays artificial small-scale structures in the voids caused by neutrino N-body particle shot-noise. All the images are made from simulations with 512^3 neutrino N-body particles.

bution arising from the FD distribution and an out-of-equilibrium gravitational flow contribution found from the ZA+2LPT formalism.

The neutrinos decoupled from the baryon-photon plasma before the annihilation of electrons and positrons, and as a result the neutrino temperature is related to the photon temperature by the approximate relation $T_\nu \simeq T_\gamma (4/11)^{1/3}$. Assuming $p \ll m_\nu$ at late times the 3 neutrino generations contribute the following to the present neutrino density parameter [78, 79, 80, 81, 82, 83, 84, 85]

$$\Omega_\nu \simeq \frac{\sum m_\nu}{94\,h^2\,\mathrm{eV}}. \tag{6.2}$$

The finite number of neutrino N-body particles gives rise to noise in the power spectrum. Physically this leads to spuriously strong clustering of neutrinos on small scales, even at early

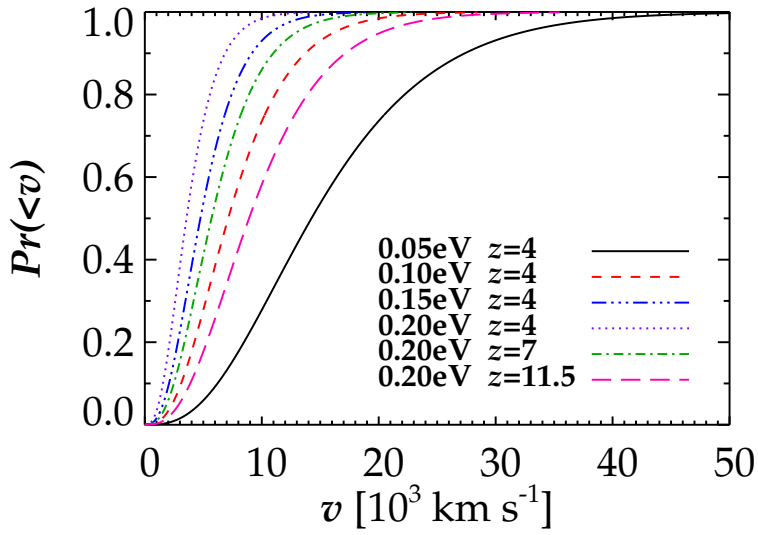

Figure 6.3: The cumulative Fermi-Dirac distributions as a function of velocity for most of the simulations listed in Table 6.1.

times. As will be discussed below we have carefully checked that this noise term is negligible on the scales of interest in our simulations.

However, since the neutrino thermal velocity distribution redshifts as a^{-1}, and the neutrino and CDM out-of-equilibrium density contrasts and velocity fields increase with the expansion of the Universe, it is paramount to start the N-body simulations as late, and therefore as close to the non-linear regime, as possible. This in turn constrains the scales on which clustering can be reliably calculated.

We have tested the validity of starting the N-body simulations as late as $z_i = 4$. This has been done by starting 4 pure ΛCDM simulations, at $z_i = 49$, 11.5, 7 and 4, and evolving them to the present. The difference in the matter power spectrum between these simulations is at the few percent level on small scales. Since the neutrino simulations include a smaller amount of CDM this is an upper limit. The 2LPT corrections were crucial for achieving such a small discrepancy. Since we are interested in quantifying the relative effect of including neutrinos, and *not* the exact absolute value of the matter power spectrum, we are justified in choosing $z_i = 4$ as the lowest starting redshift for our N-body simulations. If the absolute power spectrum is desired at the percent level a higher starting redshift should be chosen, but we stress that this will have a minimal effect on the relative change in the matter power spectrum coming from including the neutrino component.

6.3 N-body simulations

The N-body simulations were performed with the publicly available N-body code GADGET-2 [26] run in the hybrid TreePM mode. Gas physics was neglected, since it does not significantly affect the scales of interest.

The N-body simulations are evolved with Newtonian dynamics. There are several reasons for this. First, the ZA+2LPT formalism is stricly Newtonian. Second, even though the neutrino thermal velocities approach up to 15% of the speed of light, the relativistic corrections are much

	S_1^0	S_2^0	S_3^0	S_4^0	$S_1^{0.15}$	$S_2^{0.15}$	$S_3^{0.15}$	$S_4^{0.15}$	$S_5^{0.15}$	$S_6^{0.15}$	$S_1^{0.3}$	$S_2^{0.3}$	$S_3^{0.3}$	$S_4^{0.3}$	$S_5^{0.3}$	$S_1^{0.45}$	$S_2^{0.45}$	$S_3^{0.45}$
$N_{\nu,\mathrm{part}}$	0	0	0	0	256^3	0	128^3	256^3	256^3	0	256^3	0	128^3	256^3	512^3	256^3	0	256^3
$\sum m_\nu$ [eV]	0	0	0	0	0.15	0.15	0.15	0.15	0.15	0.15	0.3	0.3	0.3	0.3	0.3	0.45	0.45	0.45
Ω_ν [%]	0	0	0	0	0.33	0.33	0.33	0.33	0.33	0.33	0.65	0.65	0.65	0.65	0.65	0.98	0.98	0.98
FD	No	No	No	No	No	No	Yes	Yes	No	No	No	No	Yes	Yes	Yes	No	No	Yes
z_i	4	7	11.5	49	4	4	4	4	49	49	4	4	4	4	4	4	4	4

	$S_1^{0.6}$	$S_2^{0.6}$	$S_3^{0.6}$	$S_4^{0.6}$	$S_5^{0.6}$	$S_6^{0.6}$	$S_7^{0.6}$	$S_8^{0.6}$	$S_9^{0.6}$	$S_{10}^{0.6}$	$S_{11}^{0.6}$	$S_{12}^{0.6}$	$S_{13}^{0.6}$	$S_{14}^{0.6}$	$S_{15}^{0.6}$	$S_{16}^{0.6}$	$S_{17}^{0.6}$	$S_{18}^{0.6}$	$S_{19}^{0.6}$
$N_{\nu,\mathrm{part}}$	256^3	0	32^3	64^3	128^3	256^3	512^3	1024^3	256^3	0	128^3	256^3	256^3	0	128^3	256^3	128^3	256^3	512^3
$\sum m_\nu$ [eV]	0.6	0.6	0.6	0.6	0.6	0.6	0.6	0.6	0.6	0.6	0.6	0.6	0.6	0.6	0.6	0.6	0.6	0.6	0.6
Ω_ν [%]	1.3	1.3	1.3	1.3	1.3	1.3	1.3	1.3	1.3	1.3	1.3	1.3	1.3	1.3	1.3	1.3	1.3	1.3	1.3
FD	No	No	Yes	Yes	Yes	Yes	Yes	Yes	No	No	Yes	Yes	No	No	Yes	Yes	Yes	Yes	Yes
z_i	4	4	4	4	4	4	4	4	7	7	7	7	11.5	11.5	11.5	11.5	49	49	49

Table 6.1: Parameters for our N-body simulations. $N_{\nu,\mathrm{part}}$ is the number of neutrino N-body particles. $\sum m_\nu$ is the total neutrino mass, and it is in all cases related to the one-particle neutrino mass, m_ν, by $\sum m_\nu = 3m_\nu$. Ω_ν is the fraction of the critical density contributed by the neutrinos today (see Eq. 6.2), and FD indicates whether or not the neutrinos have been given a thermal velocity from the relativistic Fermi-Dirac distribution (see Eq. 6.1). Finally, z_i indicates the N-body starting redshift. Note that $N_{\nu,\mathrm{part}} = 0$ combined with $\sum m_\nu > 0$ indicates that the neutrino distribution has been kept totally homogeneous in the N-body simulation.

smaller than the desired accuracy.

The simulations are listed in Table 6.1, and include 256^3 CDM particles in a $512h^{-1}\,\mathrm{Mpc}$ box. By running a simulation with 512^3 CDM particles we have tested the validity of using 256^3 CDM particles. The simulation with the highest number of N-body particles gave a correction to the matter power spectrum which was at the one percent level on small scales. Since we only quantify the relative effect of including neutrinos, 256^3 CDM particles is sufficient. To test the convergence of the matter and neutrino power spectra we have made runs with different numbers of neutrino N-body particles.

As a reference, and in order to test how the neutrino thermal velocity affect the power spectra, we have run simulations with 256^3 neutrinos with no thermal velocities included.

We have also tested how much the neutrinos contribute to the matter power spectrum by running simulations with the neutrinos included in the linear evolution but neglecting the perturbed neutrino component in the N-body simulations. Here, the neutrinos were still included in the calculation of the Hubble parameter so that the background evolution is identical. Physically, this corresponds to keeping the neutrino distribution totally homogeneous in the N-body simulation.

The gravitational Tree part in GADGET-2 sets the time-step according to the gravitational acceleration, not the neutrino thermal velocity, so that the fast moving neutrinos may not be accurately evolved. We have tested if the neutrino time-step was small enough to simulate the scales of interest by decreasing it by roughly a factor of 5 in the Tree part. The correction found was well below 0.1%. This very small correction can be explained by the fact that the neutrino small-scale structure does not contribute to the matter power spectrum on the smallest scales simulated.

Finally, we have investigated the effect of the finite box size for the case with $\sum m_\nu = 0.6\,\mathrm{eV}$ and $z_i = 4$. This has been done by reducing the size of the simulation volume as well as the number

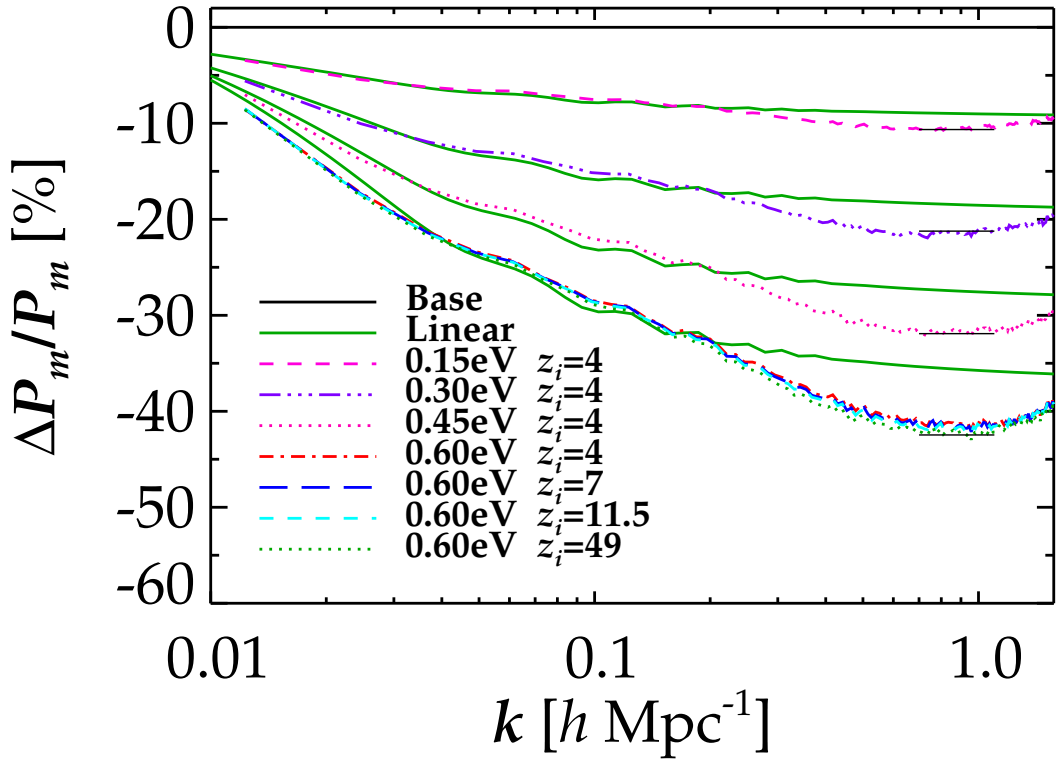

Figure 6.4: Relative differences in the matter power spectra at $z = 0$ between pure ΛCDM models and models with neutrinos included. The differences expected from linear theory are also shown. The horizontal black lines indicate a relative power spectrum suppression of $-9.8\,\Omega_\nu/\Omega_m$.

of CDM particles by a factor of two. A different set of random numbers was used to generate the initial conditions. The amount of suppresion due to neutrinos and the position of the turnover in the difference power spectrum were found to be consistent with the results presented in Fig. 6.4.

6.4 Results

6.4.1 Damping and convergence of the power spectrum

Fig. 6.4 shows the well-known scale dependent damping of power when neutrinos are included. As expected, the damping is much larger in the $\sum m_\nu = 0.6\,\mathrm{eV}$ case as compared to $\sum m_\nu = 0.15\,\mathrm{eV}$ because Ω_c is smaller in the former case even though the neutrino thermal velocity is largest for the lower mass neutrino.

From Fig. 6.4 it can be seen that in the $\sum m_\nu = 0.6\,\mathrm{eV}$ case the damping is almost independent of z_i. Note that the relative decrease in power for a given simulation with neutrinos is taken with respect to a ΛCDM simulation started at the same z_i. This has been done to remove the dependence

on the starting redshift when comparing the models.

Fig. 6.4 also shows the damping expected from linear theory, which is accurate out to $k \sim 0.2h\,\mathrm{Mpc}^{-1}$. On smaller scales non-linear theory predicts a substantially larger damping of the power spectrum. The departure from linear theory increases with higher $\sum m_\nu$. Note that non-linear theory predicts a turnover in the difference power spectrum. At the starting redshift, z_i, this turnover is not present, neither in the TFs nor when the ICs have been calculated.

From a mode-coupling point of view the turnover occurs because the small-scale modes ($k \sim 1\,h\,\mathrm{Mpc}^{-1}$) in the simulations with neutrinos get relatively more out of their coupling to the large-scale modes than do the same modes in the pure ΛCDM simulations. The turnover does not appear because of mode-coupling between the small-scale modes themselves. Physically, large-scale potential gradients are needed to make the small-scale structures grow substantially, and the large-scale perturbations are less affected by neutrino free-streaming than are the small-scale perturbations. The non-linear collapse of the halos then gives mode-coupling and, combined with the characteristic damping of the difference power spectrum caused by neutrino free-streaming, gives the turnover.

The turnover is not caused by clustering of the neutrino component on small scales. This can be seen by comparing the two figures in the top panel of Fig. 6.5 (see below for further comments on Fig. 6.5). If small-scale neutrino clustering did contribute to the matter power spectrum on scales $k \sim 1\,h\,\mathrm{Mpc}^{-1}$ then the matter power spectrum should be affected by the different noise levels seen in the neutrino power spectra. But since the matter power spectrum has converged for 128^3 to 1024^3 neutrino N-body particles the turnover is not caused by neutrino small-scale clustering.

The characteristic scale at which the turnover appears, k_{turn}, moves to smaller k as Ω_ν is decreased. k_{turn} is not directly proportional to Ω_ν and therefore to the neutrino free-streaming length. Instead, k_{turn} is related to the amount of Ω_c. Since we keep Ω_m fixed, decreasing Ω_ν increases the amount of CDM, and more CDM makes the halos collapse on larger scales. Since the turnover is related to the non-linear collapse of structures, k_{turn} moves to larger scales as Ω_ν is decreased. Since there is a linear boundary condition at $k \sim 0.2h\,\mathrm{Mpc}^{-1}$, the turnover cannot propagate beyond this value for Ω_ν approaching zero.

The maximum relative magnitude of the power spectrum suppression is roughly given by

$$\left.\frac{\Delta P}{P}\right|_{\mathrm{max}} \sim -9.8\frac{\Omega_\nu}{\Omega_m}, \tag{6.3}$$

which is about 20% larger than the linear theory prediction of $\Delta P/P|_{\mathrm{lin}} \sim -8\Omega_\nu/\Omega_m$ [10, 86]. With future high precision measurements of the matter power spectrum approaching the 1% precision on these scales this effect must be taken into account even for hierarchical neutrino masses.

The differences for the matter power spectra in the $\sum m_\nu = 0.6\,\mathrm{eV}$ case as a function of different numbers of neutrino N-body particles are shown in the top left panel of Fig. 6.5. By using different mass assignment methods, Nearest-Grid-Point, deconvolved Clouds-In-Cells, the adaptive smoothing kernel of [76] as well as dividing the simulation volume into equal cubical cells and superposing the particle distributions for attaining higher spacial resolution, we have tested that the power spectra do not have any artificial features caused by the particular mass assignment method used. For all neutrino masses simulated it is necessary to include at least 128^3 neutrinos in the N-body simulation and give them a thermal velocity to calculate the matter power spectrum at percent level accuracy on the relevant scales. For the $\sum m_\nu = 0.6\,\mathrm{eV}$ case and $z_i = 49$ it is furthermore necessary to include 512^3 neutrino N-body particles to achieve convergence.

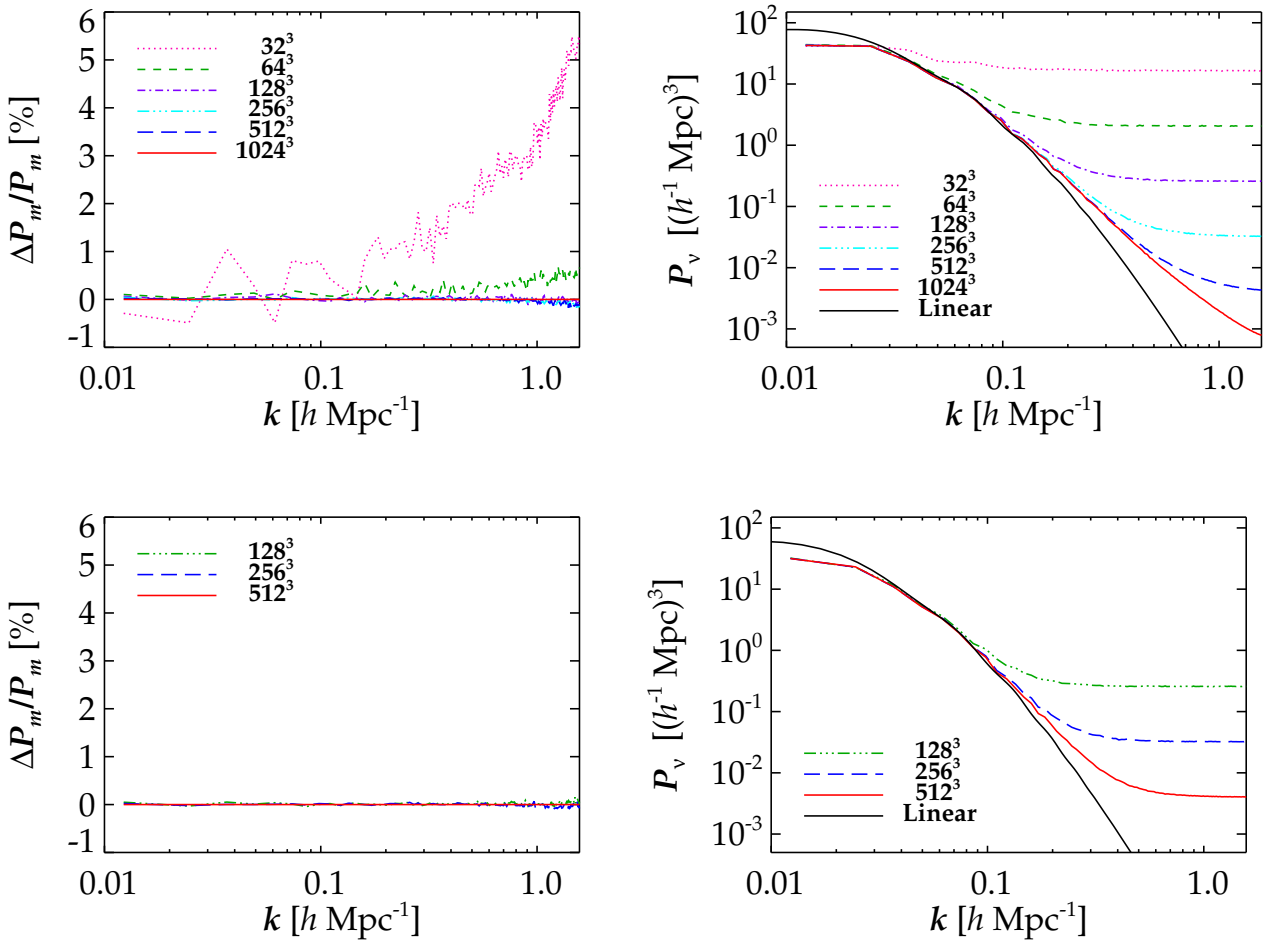

Figure 6.5: Top left: Differences in % in the matter power spectra at $z = 0$ with $\sum m_\nu = 0.6$ eV neutrinos and $z_i = 4$. The differences are taken with respect to the 1024^3 neutrino simulation. Top right: Neutrino power spectra at $z = 0$ with $\sum m_\nu = 0.6$ eV neutrinos and $z_i = 4$. Bottom left: Differences in % in the matter power spectra at $z = 0$ with $\sum m_\nu = 0.3$ eV neutrinos and $z_i = 4$. The differences are taken with respect to the 512^3 neutrino simulation. Bottom right: Neutrino power spectra at $z = 0$ with $\sum m_\nu = 0.3$ eV neutrinos and $z_i = 4$.

The neutrino power spectra for $\sum m_\nu = 0.6\,\mathrm{eV}$ as a function of different numbers of neutrino N-body particles are shown in the top right panel of Fig. 6.5. On small scales the neutrino power spectrum is in most cases completely flat because the coarse sampling of the neutrino velocity distribution introduces a white noise term. That this is indeed the reason can be seen from the fact that the noise level decreases rapidly when more neutrino N-body particles are used. For runs with 128^3 to 1024^3 neutrino N-body particles the noise effect on the matter power spectrum is kept well below the 1% level on relevant scales. It can also be seen that the neutrino power spectra for $N_{\nu,\mathrm{part}} = 256^3$ and $N_{\nu,\mathrm{part}} = 512^3$ converge out to $k \simeq 0.2\,h\,\mathrm{Mpc}^{-1}$ and that the $N_{\nu,\mathrm{part}} = 512^3$ and $N_{\nu,\mathrm{part}} = 1024^3$ simulations converge out to $k \simeq 0.5\,h\,\mathrm{Mpc}^{-1}$.

In the bottom panel of Fig. 6.5 the corresponding convergence of the matter power spectra (left)

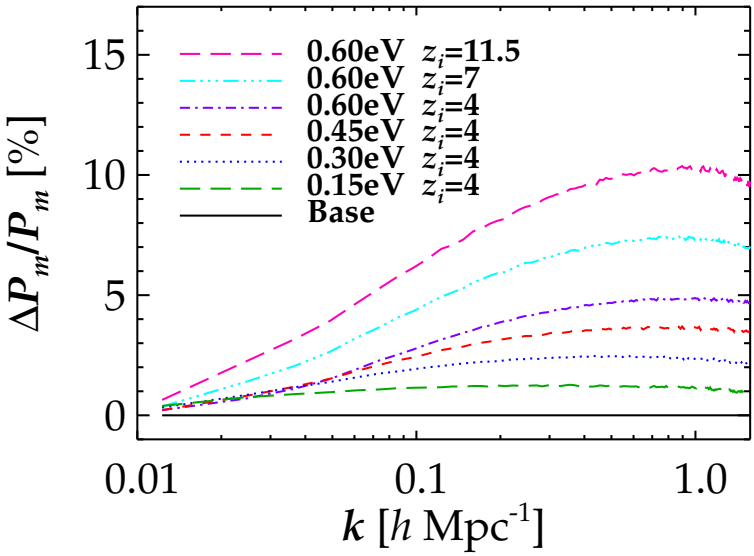

Figure 6.6: The effect on the matter power spectrum at $z = 0$ of neglecting thermal velocities in the N-body simulations. The neutrinos have been correctly included in the linear evolution.

and the neutrino power spectra (right) for the $\sum m_\nu = 0.3\,\mathrm{eV}$ case are shown. The same general trends from the $\sum m_\nu = 0.6\,\mathrm{eV}$ case can be seen.

6.4.2 The effect of neglecting the thermal component

Fig. 6.6 shows the effect of neglecting the neutrino thermal velocity in the simulations. In the figure the power spectra are normalized with respect to the simulation with the highest number of neutrino N-body particles for a given mass and starting redshift. As expected, neglecting the thermal velocity component increases the amplitude of the power spectrum, because without thermal velocities the neutrinos act as an extra CDM species, and the effect of free-streaming is neglected once the simulation is started. The effect is more pronounced at smaller scales, and is largest in the highest mass neutrino case, since it contributes a larger fraction of Ω_m, even though it has a smaller omitted thermal velocity component than in the cases of the lower mass neutrinos.

For the case of $\sum m_\nu = 0.6\,\mathrm{eV}$ the effect is as large as $\sim 5\%$ for $z_i = 4$ increasing to $\sim 10\%$ for $z_i = 11.5$ on scales relevant for future large-scale surveys. For higher starting redshifts the effect is even larger. We note that for a given starting redshift the effect is proportional to $\sum m_\nu$ as expected.

6.4.3 High z_i low m_ν approximation

Including neutrinos with a total mass in the range $0.3 \sim 0.6\,\mathrm{eV}$ in N-body simulations can be done consistently even at redshifts required for getting the absolute power spectrum accurately. However, for very light neutrinos, $\sum m_\nu \sim 0.15\,\mathrm{eV}$, the thermal velocities are semi-relativistic at $z = 49$. This will not only render Newtonian dynamics inaccurately but will also, depending on the number of neutrino N-body particles used, erase the initial neutrino large-scale structure since typical neutrino gravitational flow velocities are of order $\sim 5\,\mathrm{km\,s^{-1}}$, much smaller than

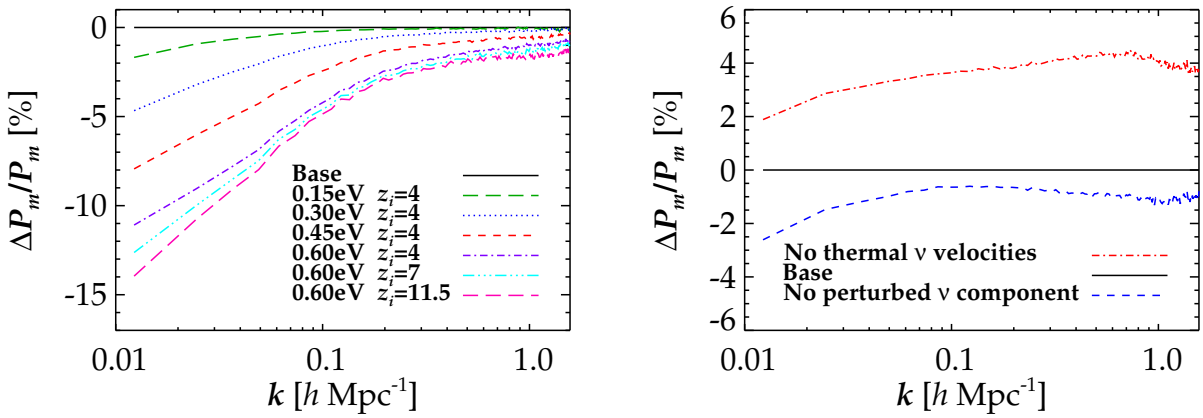

Figure 6.7: Left: The effect of neglecting the perturbed neutrino component at $z = 0$ in the N-body simulations. Right: The effect of neglecting the thermal velocities or the perturbed neutrino component for $\sum m_\nu = 0.15\,\mathrm{eV}$ and a starting redshift of 49. The 'Base' has been estimated, as explained in the text. In all cases the neutrinos have been correctly included in the linear evolution.

the thermal velocities of individual particles. Furthermore, the high neutrino velocities make the N-body simulation timestep very short, increasing simulation times substantially.

For these reasons it is desirable to develop an approximate method which can be used to calculate the matter power spectrum at the 1% level without including thermal velocities. In Fig. 6.7 (left) we show the effect of neglecting the perturbed neutrino component in the N-body simulations. The CDM N-body particle mass is still scaled according to the total matter density. As expected this gives less power because of the lack of feed-back from the large-scale modes of the neutrino component to the CDM component. By increasing z_i the neutrino perturbations are omitted over a longer time span and therefore affect and decrease the power spectrum more.

It is important to notice, that this lack of power is very small in the $\sum m_\nu = 0.15\,\mathrm{eV}$ case for $k > 0.1\,h\,\mathrm{Mpc}^{-1}$, i.e. on scales where non-linear corrections become important.

Ideally, the ratio of a pure ΛCDM power spectrum to that of a power spectrum with a given neutrino mass, $P_{\Lambda\mathrm{CDM}}/P_{\nu\Lambda\mathrm{CDM}}$, should be independent of N-body starting redshift, as long as z_i is not too low. The presence of non-linearities at the time when the ICs are calculated make this power spectrum ratio marginally dependent on z_i, which is also visible in Fig. 6.4 in the $\sum m_\nu = 0.6\,\mathrm{eV}$ case.

Now, focusing on the $\sum m_\nu = 0.15\,\mathrm{eV}$ case and $z_i = 49$, we would like to estimate the error made by not including the perturbed neutrino component in the N-body simulation. Because the damping of the power spectrum is nearly independent of z_i it is possible to estimate the matter power spectrum with neutrinos and thermal velocities without actually performing the simulation. More specifically, assuming that the damping effect is independent of z_i, the matter power spectrum at $z = 0$ for an N-body simulation started at $z_i = 49$ with neutrinos and thermal velocities can be found from $P_{\Lambda\mathrm{CDM}}(z_i = 4)/P_{\nu\Lambda\mathrm{CDM}}(z_i = 4) = P_{\Lambda\mathrm{CDM}}(z_i = 49)/P_{\nu\Lambda\mathrm{CDM}}(z_i = 49)$. This estimated power spectrum is used as the 'Base' in the right panel of Fig. 6.7. This figure shows the error made by neglecting the perturbed neutrino component. On scales relevant for N-body simulations, i.e. $k > 0.1\,h\,\mathrm{Mpc}^{-1}$, the error made is at the 1% level. For comparison the effect of neglecting the

thermal velocities is also shown, and it can be seen that it is a better approximation to neglect the perturbed neutrino component than to include it but neglect the thermal velocity component.

In the $\sum m_\nu = 0.6\,\mathrm{eV}$ case we have all the relevant power spectra at starting redshifts of 4 and 49. Therefore we can test the validity of estimating the power spectrum with neutrinos and thermal velocities. We have found that the 'Base' in the right panel of Fig. 6.7 is overestimated so that the error made by neglecting the perturbed neutrino component is an upper bound.

We have tried to decrease the error made by neglecting the perturbed neutrino component. This has been done by including the perturbed neutrino component without thermal velocities in the N-body simulation, but switching off the effect of the gravitational field on the neutrinos, so that the gravitational flow velocities of the neutrinos at z_i are frozen in time. This should improve the estimate of the matter power spectrum in two ways: First, by including the perturbed neutrino component the power spectrum will increase. Second, by switching off gravity, artificial small-scale structures will not form. With this method the error was decreased, especially on large scales in the $\sum m_\nu = 0.6\,\mathrm{eV}$ case for $z_i = 4$, but the error did not approach percent level precision. On the contrary, in the $\sum m_\nu = 0.15\,\mathrm{eV}$ case and for $z_i = 49$ the error *increased* to the 10-15% level. The reason is that at such a high redshift the neutrino gravitational flow velocities and density perturbations are very small effectively freezing the neutrinos on a regular grid. Because of neutrino N-body particle shot-noise this stationary regular grid deflects the CDM particles and therefore reduces the amount of structure forming.

6.5 Discussion and conclusions

We have performed a precise calculation of the effect of including neutrino dark matter on the matter power spectrum. The effect of thermal neutrino motion has been included directly, and we have shown that this effect changes the matter power spectrum significantly.

Specifically, we find that the suppression of power due to the presence of massive neutrinos is increased by non-linear effects. Whereas in linear theory the suppression of power on small scales is given roughly by $\Delta P/P \sim -8\Omega_\nu/\Omega_m$, the full non-linear calculation gives $\Delta P/P \sim -9.8\Omega_\nu/\Omega_m$ at a scale of $k \sim 0.5 - 1\,h\,\mathrm{Mpc}^{-1}$, i.e. an increase of about 20%.

On smaller scales the non-linear contribution to the suppression decreases again. This effect has previously been noted in semi-analytic studies such as [87], and occurs on a scale which depends upon the amount of CDM and the neutrino free-streaming length.

The increased suppression due to non-linear effects is highly relevant for future high precision large-scale structure and weak lensing surveys. Even for neutrino masses approaching the lower bound, found from oscillation experiments, it is large enough to bias the estimate of other cosmological parameters. Conversely, it provides a very distinct signature which could allow for the detection and measurement of even very low-mass neutrinos.

For $k > 0.1\,h\,\mathrm{Mpc}^{-1}$, which include the modes for which N-body simulations are needed, it is a better approximation to the "true" power spectrum to neglect the perturbed neutrino component than to include it without thermal velocities. In both cases the approximation to the "true" power spectrum is better than if a standard ΛCDM model was assumed.

But only in our lowest mass neutrino case, $\sum m_\nu = 0.15\,\mathrm{eV}$, is the error on the non-linear matter power spectrum made by neglecting the perturbed neutrino component in the N-body simulation at the desired 1% level for the relevant modes, even for an N-body simulation with a starting redshift as high as 49. The error would be decreased further for smaller neutrino masses.

An alternative method for implementing the physics of neutrinos in N-body simulations is to represent the neutrino component as a fluid and solve the corresponding fluid equations on a grid. This method would be particularly useful for neutrino masses close to the lower observational bound.

Acknowledgements

We acknowledge computing resources from the Danish Center for Scientific Computing (DCSC). We thank Yvonne Wong for discussions and comments.

Chapter 7

Grid Based Linear Neutrino Perturbations in Cosmological N-body Simulations

Jacob Brandbyge, Steen Hannestad

Abstract We present a novel, fast and precise method for including the effect of light neutrinos in cosmological N-body simulations. The effect of the neutrino component is included by using the linear theory neutrino perturbations in the calculation of the gravitational potential in the N-body simulation. By comparing this new method with the full non-linear evolution first presented in [1], where the neutrino component was treated as particles, we find that the new method calculates the matter power spectrum with an accuracy better than 1% for $\sum m_\nu \lesssim 0.5\,\mathrm{eV}$ at $z = 0$. This error scales approximately as $(\sum m_\nu)^2$, making the new linear neutrino method extremely accurate for a total neutrino mass in the range $0.05 - 0.3\,\mathrm{eV}$. At $z = 1$ the error is below 0.3% for $\sum m_\nu \lesssim 0.5\,\mathrm{eV}$ and becomes negligible at higher redshifts. This new method is computationally much more efficient than representing the neutrino component by N-body particles [2].

7.1 Introduction

Next to photons neutrinos are the most abundant particles in our Universe. The fact that at least two of the three neutrino mass eigenstates have masses much larger than the current temperature, $m_i \gg T_0$, means that neutrinos contribute to the matter density and are important for cosmological structure formation. The mass differences established by oscillation experiments mean that the heaviest mass eigenstate must have a mass of at least $m \sim 0.05$ eV. This in turn will have the effect of suppressing the power spectrum of matter fluctuations by $\sim 5\%$, an effect which is significantly larger than the precision with which the matter power spectrum can be measured in upcoming surveys.

This has two interesting consequences, first it means that neutrino mass *must* be included in the analysis of future data in order to avoid seriously biasing the measurements of parameters such

as the dark energy equation of state, w [55]. Second, it means that future large-scale structure surveys potentially have the power to probe neutrino masses as low as the current *lower* bound from oscillation experiments [77, 88].

Consequently this has led to a much increased interest in gaining a detailed understanding of how neutrinos affect structure formation. In linear theory the effect is extremely well understood and can be calculated to a precision much better than 1%. However, these results apply only on very large scales, $k \ll 0.1\,h\mathrm{Mpc}^{-1}$, whereas most of the cosmologically relevant information from large-scale structure surveys is in the range $k \sim 0.1 - 0.5\,h\mathrm{Mpc}^{-1}$. On these intermediate scales it is mandatory to correct for non-linear effects, even if surveys are carried out at intermediate redshifts where non-linearity is weaker.

Non-linear corrections can be found in a number of ways: The most accurate, but also most time-consuming method is to use full N-body simulations with neutrinos included in a self-consistent way. In a previous publication we carried out a large suite of simulations with neutrinos included [1], and found a significant non-linear correction caused by neutrinos. The effect is large enough to be important even for masses as low as 0.05 - 0.1 eV. Another way is to use higher order perturbation theory which, however, is applicable only up to $k \sim 0.1 - 0.2\,h\mathrm{Mpc}^{-1}$ today, if the precision needs to be better than 1-2%. Finally it is possible to use semi-analytic methods such as the halo model which has been calibrated using ΛCDM simulations. Neutrinos can be included fairly easily in this scheme, but the accuracy can only be tested against full N-body simulations.

In conclusion, a very large number of high-resolution N-body simulations with neutrinos included will be necessary for future data analysis. The method used in [1] is well suited for large neutrino masses with $\sum m_\nu \gtrsim 0.5$ eV at low redshift, but for all masses the simulations inevitably become noise dominated at high redshift, unless extremely many neutrino N-body particles are used.

In the present paper we describe a novel, fast and precise method for simulating low mass neutrinos in N-body simulations which uses the fact that low mass neutrinos have very little non-linear clustering even at low redshift. Instead of simulating neutrinos as particles with individual velocities we describe the local neutrino density on a grid. This density is evolved forward in time by using linear theory. The CDM/baryon component is followed simultaneously using the full TreePM method, with the neutrino component contributing to the long range force calculated using the PM method. As will be shown below the accuracy of this method is better than 1% for the matter power spectrum today on *all* scales for all neutrino masses below $\sum m_\nu \sim 0.5$ eV.

The method is very powerful, both because it speeds up simulations with neutrinos very significantly (by factors of order ~ 10), *and* because it can be applied to any other component of energy density which is almost linear. This could for example be dark energy with linear perturbations. The only requirement is that the linear component can be included in a Boltzmann solver like CAMB [12].

We note that our new method is conceptually similar to the perturbative approaches presented in [19, 21], except for the fact that we give the CDM component a full non-linear treatment.

In Section 7.2 we describe our cosmological model and the set-up of initial conditions for our neutrino N-body simulations. In Section 7.3 we present our results and in Section 7.4 we show that our results have converged. Finally, Section 7.5 contains a discussion and our conclusions.

7.2 Initial conditions

7.2.1 The cosmological model and particle initial conditions

As long as the evolved primordial density perturbations set down by inflation remain small, their evolution can be calculated precisely using the linearised Einstein and Boltzmann equations [9]. However, once structure enters the non-linear regime precision studies require the use of N-body simulations. To set up the initial conditions (ICs) for our simulations we have calculated the transfer functions (TFs) using CAMB [12]. The further evolution is followed in GADGET-2 [26] run in the hybrid TreePM mode.

We have assumed a flat cosmological model with density parameters $\Omega_b = 0.05$, $\Omega_m = 0.30$ and $\Omega_\Lambda = 0.70$ for the baryon, total matter and cosmological constant components, respectively, and a Hubble parameter of $h = 0.70$. We vary the CDM and neutrino density parameters (Ω_c and Ω_ν, respectively) such that they fullfill the condition $\Omega_c + \Omega_\nu = 0.25$. We have assumed a primordial power spectrum of the standard scale-invariant Harrison-Zel'dovich form. The amplitude gives $\sigma_8 = 0.878$ for a pure ΛCDM model.

To generate the ICs for our simulations we have built a parallelized IC generator directly into GADGET-2. The TFs are used to generate the position and velocity ICs for the N-body particles. In addition to the Zel'dovich Approximation (ZA) [23], we have included a correction term from second-order Lagrangian perturbation theory (2LPT) [25, 24]. Due to our high N-body starting redshift ($z = 49$), this second-order term is small, and therefore basically does not affect our results.

The neutrino component is included in the N-body simulation either as real space particles or on a grid in Fourier space. The CDM component is always treated as particles and for its initial power spectrum we have used a weighted sum of the CDM and baryon TFs. Gas physics is not included in the N-body simulation, since it does not significantly affect the scales simulated. The initial conditions for the CDM and neutrino components have been generated with the same set of random numbers, to enforce the assumption of adiabatic initial fluctuations. In the neutrino particle method we add a thermal velocity drawn from a relativistic Fermi-Dirac distribution to the neutrino N-body particles. When considering the power spectrum this thermal velocity acts as a wavenumber dependent suppression term (see [1] for further details).

7.2.2 Initial conditions and evolution of the neutrino grid

When the linear neutrino component is represented on a grid in the N-body simulation, there are no neutrino N-body particles. The representation is done as follows. A realisation of the neutrino TF is generated with the ZA only, using the same set of random numbers as was used to make the initial conditions for the CDM particles. The neutrino component stays in the Fourier domain throughout the N-body simulation. The linear neutrino modes are added directly to their CDM counterparts whenever the long-range force is calculated, taking proper care of the fact that only the latter modes should be deconvolved from the smoothing effect of the Clouds-in-Cells (CIC) mass assignment used in GADGET-2. Whenever the long-range force is calculated the neutrino component is evolved by interpolating between a library of TFs which span the redshift range over which the power spectrum is to be evolved in the N-body simulation.

The neutrinos are not included in the short-range Tree part. To compensate for this fact the neutrino modes are not smoothed in Fourier space with the Gaussian factor $\exp(-k^2 r_s^2)$, where $r_s = 1.25\,h^{-1}$Mpc, as are the CDM modes (see [31] for an analysis of the TreePM method). This

	A_1	B_1	B_2	C_1	C_2	C_3	C_4	C_5	C_6	C_7	C_8	C_9	C_{10}	D_1	D_2	D_3
$N_{\rm CDM}$	512^3	512^3	512^3	512^3	512^3	512^3	256^3	256^3	256^3	256^3	512^3	512^3	512^3	512^3	512^3	512^3
$N_{\nu,\rm part}$	0	0	256^3	0	256^3	512^3	0	256^3	0	256^3	0	256^3	0	0	256^3	512^3
$N_{\nu,\rm grid}$	0	512^3	0	512^3	0	0	256^3	0	512^3	0	1024^3	0	0	512^3	0	0
$N_{\rm PM}$	512	512	512	512	512	512	256	256	512	512	1024	1024	512	512	512	512
$R_{\rm BOX}$ [h^{-1}Mpc]	512	512	512	512	512	512	256	256	512	512	512	512	512	512	512	512
$\sum m_\nu$ [eV]	0	0.3	0.3	0.6	0.6	0.6	0.6	0.6	0.6	0.6	0.6	0.6	0.6	1.2	1.2	1.2
Ω_ν [%]	0	0.65	0.65	1.3	1.3	1.3	1.3	1.3	1.3	1.3	1.3	1.3	1.3	2.6	2.6	2.6

Table 7.1: Parameters for the N-body simulations used to make the power spectra presented in this paper. $N_{\rm CDM}$ and $N_{\nu,\rm part}$ is the number of CDM and neutrino N-body particles, respectively. $N_{\nu,\rm grid}$ is the size of the neutrino Fourier grid. $\sum m_\nu$ is the total neutrino mass, and it is in all cases related to the one-particle neutrino mass, m_ν, by $\sum m_\nu = 3m_\nu$. Ω_ν is the fraction of the critical density contributed by the neutrinos today. $N_{\rm PM}$ is the number of one-dimensional PM grid points and $R_{\rm BOX}$ is the size of the simulation volume. All simulations have a starting redshift of 49. Note that in model C_{10} the neutrino distribution has been kept totally homogeneous in the N-body simulation. We will use the notation X_i/X_j to indicate a relative power spectrum calculated between the models X_i and X_j from $(X_i/X_j - 1)\cdot 100\%$.

lack of smoothing could be a problem since the accuracy of the PM method breaks down as the PM grid mesh size is approached (see Section 7.4).

A concern about the neutrino grid method could be that there are rotations in the CDM density field in real space, which could bring the CDM and neutrino components out of phase. But as long as only the linear neutrino density distribution contributes to the matter power spectrum these offsets due to rotations are negligible. Another more serious problem could arise since the linear part of the neutrino power spectrum and the CDM power spectrum are evolved in two different time integrators, CAMB and GADGET-2, respectively. Force calculation errors in the two integrators could lead to discrepancies, which would not only affect the absolute power spectrum but also the relative power spectrum between the neutrino grid and particle approaches. In Section 7.4 we address these issues.

7.3 Results

This section will focus on our main results, whereas the next section will contain a description of detailed convergence tests. Table 7.1 shows most of our performed N-body simulations.

Fig. 7.1 shows the difference in the total matter (neutrino plus CDM) power spectrum for 3 different neutrino masses, between simulations where the neutrino component is represented either on a grid or as N-body particles. The difference between the two methods are shown at various redshifts. At our initial N-body starting redshift, $z = 49$, the two methods are identical, as they should be. In the simulation where the neutrino component is represented by particles the neutrino N-body particles free-stream out of the gravitational potential wells and generate a white noise term as soon as the simulation is started. This white noise term affects the difference power spectra in Fig. 7.1 for $k > 0.1 - 1h\,\mathrm{Mpc}^{-1}$ (the actual wavenumber depending on redshift, neutrino mass and the number density of neutrino N-body particles), and is solely due to the finite number of

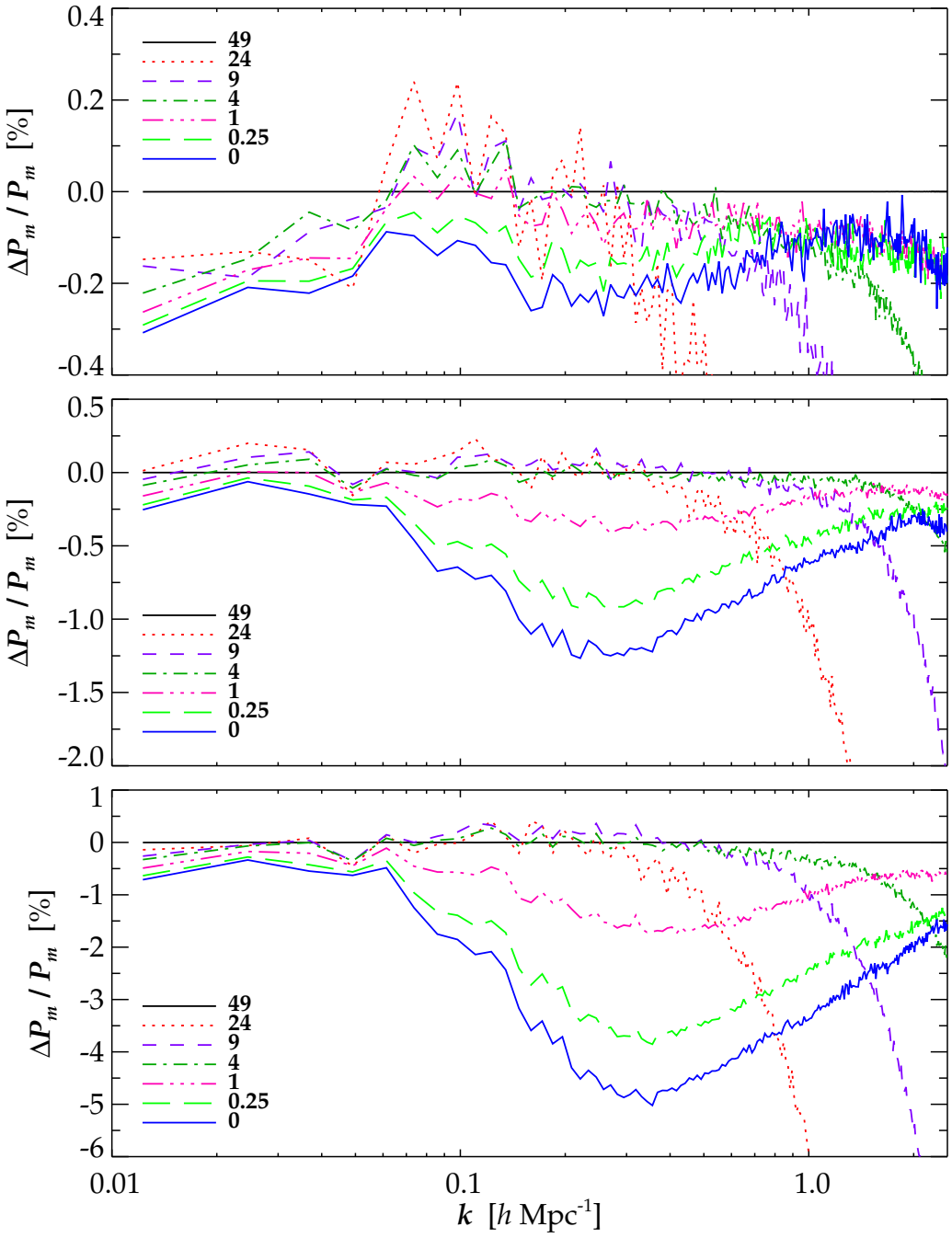

Figure 7.1: Percentage differences in the total matter power spectrum at different redshifts between simulations where the neutrino component is represented in the N-body simulation either on a grid or as particles. A negative power difference indicates more power in the particle simulations. From top to bottom the total neutrino mass is 0.3 eV (B_1/B_2), 0.6 eV (C_1/C_3) and 1.2 eV (D_1/D_3), respectively. All the power spectra presented in this paper have been calculated on a 1024^3 grid, using a deconvolved CIC mass assignment scheme for the N-body particles.

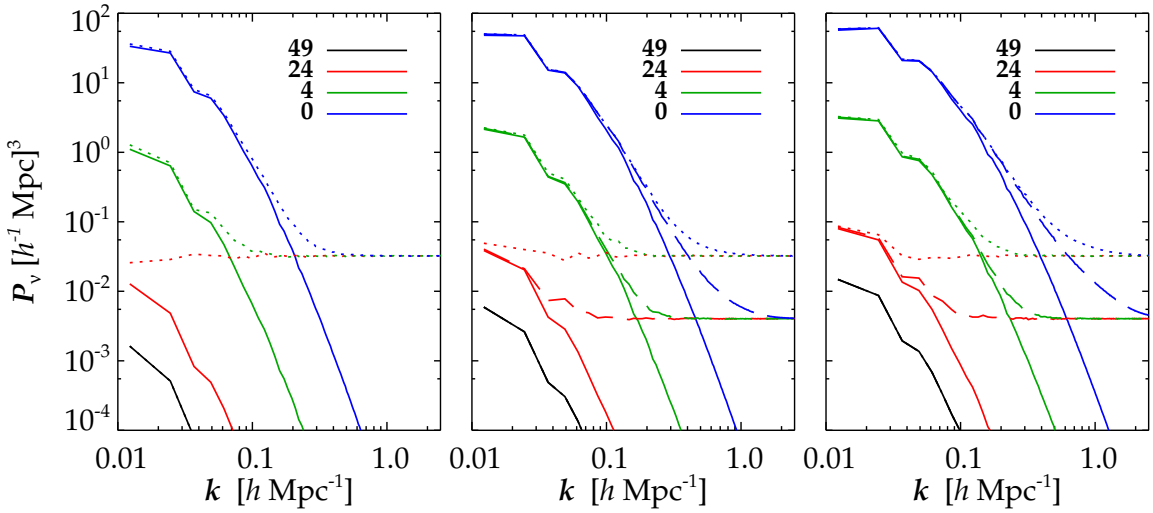

Figure 7.2: Neutrino power spectra for a total neutrino mass of 0.3 eV (left), 0.6 eV (middle) and 1.2 eV (right) at various redshifts. The linear theory neutrino power spectrum, convolved with our chosen random numbers, are shown with solid lines (models B_1, C_1 and D_1), simulations with 256^3 neutrino particles with dotted lines (models B_2, C_2 and D_2) and finally simulations with 512^3 neutrino particles are shown with dashed lines (models C_3 and D_3).

neutrino N-body particles. That this is indeed a white noise term can be seen from Fig. 7.2 where the neutrino power spectrum is shown for all neutrino masses simulated. This white noise term can furthermore be seen in Fig. 7.3, where the neutrino N-body particle density distribution is shown at $z = 4$ (i.e. the central panel).

From Fig. 7.2 it can be seen that the neutrino N-body particle white noise term is frozen on small scales, i.e. there is a maximum white noise level, which is determined by the number of neutrino N-body particles. Note that for $\sum m_\nu = 0.3\,\mathrm{eV}$ and $z = 24$ even the neutrino fundamental mode is white noise dominated. This noise term persists and can be identified in the top panel of Fig. 7.1.

As the simulation evolves the CDM density perturbations grow so that the neutrino white noise term in the matter power spectrum dominates only on ever smaller scales. This is clearly seen in Fig. 7.1 where the agreement between the grid and particle representations improves on small scales as the simulation evolves. At $z = 4$ the two methods give basically identical results until $k > 1h\,\mathrm{Mpc}^{-1}$. The disagreement beyond this wavenumber is caused by the white noise term.

In sum, for $\sum m_\nu = 0.6\,\mathrm{eV}$ the neutrino grid method is accurate at the 0.1% level for all scales until $z = 4$. This very low discrepancy is impressive given the fact that the neutrino component contribute up to more than 10% at this redshift (see the left panel of Fig. 7.8), as well as the fact that the neutrino component is evolved in two different integrators.

As the redshift falls below 4 the two representations begin to differ in the range $k \simeq 0.1 - 1\,h\mathrm{Mpc}^{-1}$. This difference is a non-linear correction coming from the fact that the neutrino N-body particles are coupled to the non-linear gravitational potential whereas the neutrino grid is only

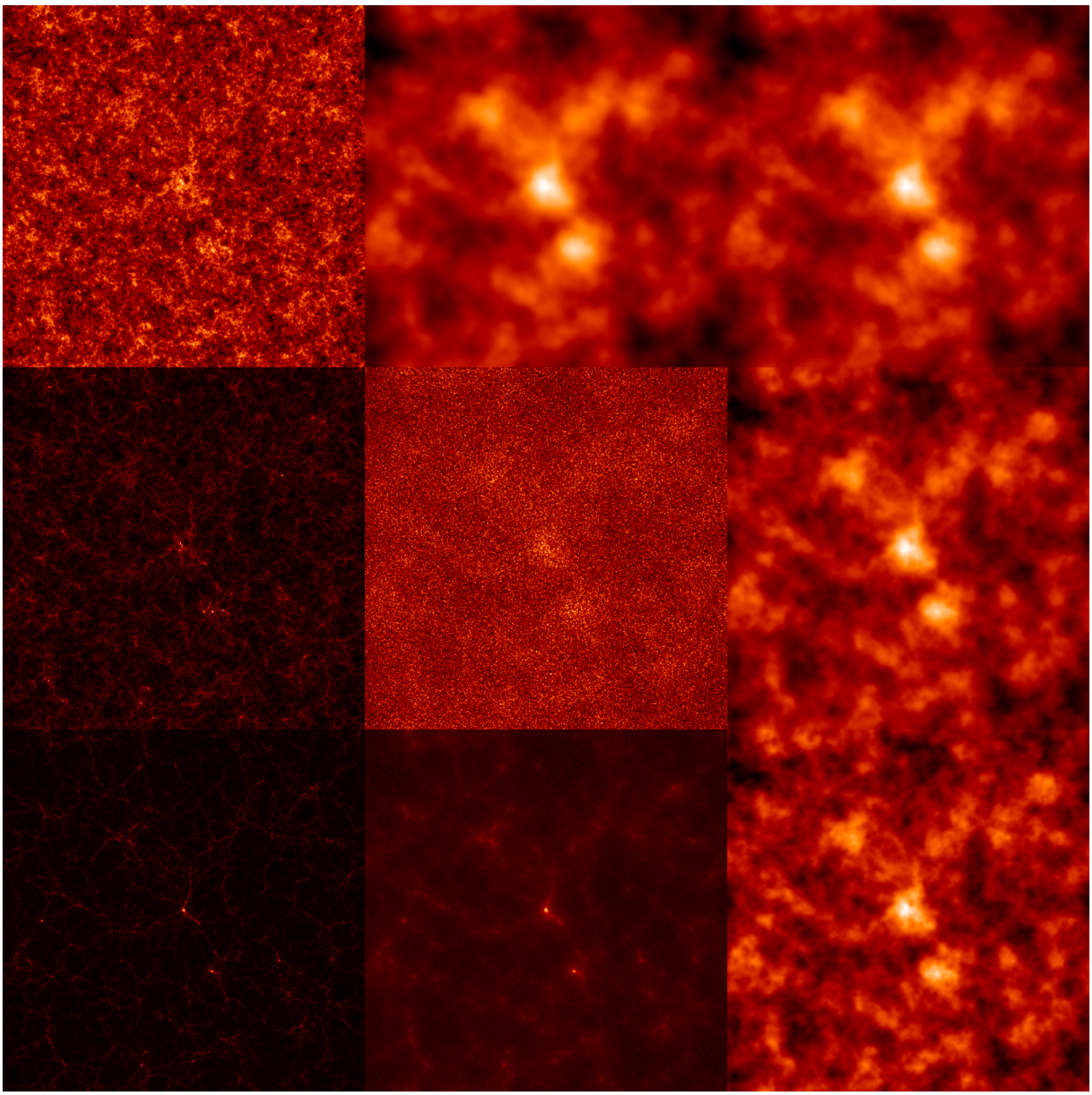

Figure 7.3: Density grids for the CDM (left), neutrino particle (middle) and neutrino grid (right) components. In all cases the total neutrino mass is 0.6 eV. The top row is at $z = 49$, the middle row at $z = 4$, and the bottom row at $z = 0$. In the bottom row the square root has been taken of the first two density distributions. The images are centered at the highest density region in the simulation volume and they have a thickness of $20\,h^{-1}$Mpc and a side length of $512\,h^{-1}$Mpc. The particle density distributions are found using the adaptive smoothing length kernel from [76] (taken from model C_3), and the neutrino grid density distribution is an inverse FFT of the linear neutrino Fourier grid imbedded in the N-body simulation volume (model C_1).

evolved in linear theory. The wavenumber range where this difference appears can be explained by the convolution of two terms. A non-linear term growing rapidly on small scales and the fact that the neutrinos contribute most on large scales, as can be seen in Fig. 7.8.

The lowest wavenumber at which this non-linear correction term becomes important, can also be identified in the middle and right panel of Fig. 7.2, as the range from where the particle neutrino power spectra break away from the linear theory evolution. The highest wavenumber at which the non-linear correction term matters is not only determined by non-linear neutrino modes at that scale but also by mode-coupling between the CDM perturbations at that scale and the extra non-linear neutrino contribution at larger scales.

In the $\sum m_\nu = 0.6\,\mathrm{eV}$ case at $z = 0$ the two methods differ by at most 1.25% at roughly $k \simeq 0.25\,h\mathrm{Mpc}^{-1}$. Focusing on the $\sum m_\nu = 1.2\,\mathrm{eV}$ case[1], we see from Fig. 7.1 that the non-linear correction is at the 5% level. As expected the non-linear correction is greater as the neutrino mass is increased because Ω_ν increases and the neutrino thermal velocity decreases. Since Ω_ν is proportional to the total neutrino mass and the thermal velocity is roughly inverse proportional to the one-particle neutrino mass this explains the $(\sum m_\nu)^2$ dependence on the size of the non-linear neutrino correction term. This scaling can also be seen to roughly hold in the $\sum m_\nu = 0.3\,\mathrm{eV}$ case, where the maximum non-linear neutrino correction to the matter power spectrum is at a negligible 0.25% level today (the discrepancy at large scales is due to a finite number of neutrino N-body particles, see Section 7.4). Note that as expected the wavenumber corresponding to the maximum non-linear neutrino correction propagates slightly from $k \simeq 0.3\,h\mathrm{Mpc}^{-1}$ in the $\sum m_\nu = 1.2\,\mathrm{eV}$ case to $k \simeq 0.2\,h\mathrm{Mpc}^{-1}$ in the $\sum m_\nu = 0.3\,\mathrm{eV}$ case. In sum, the percentage maximum non-linear correction to the neutrino component today is well fitted by the relation $(\sum m_\nu/0.54\,\mathrm{eV})^2$.

Finally, in Fig. 7.4 we show the evolution of the difference in the matter power spectrum between a pure ΛCDM simulation (A_1) and model C_1 with 0.6 eV neutrinos represented on a grid. For the scales simulated it can be seen that the turn-over in the difference power spectrum is created at low redshift, $z \simeq 1 - 4$, and that it propagates to larger scales. The almost perfect agreement between linear and non-linear theory seen in the figure at $z = 24$ can in practice only be achieved by representing the neutrino component on a grid.

7.4 Convergence tests

In the two approaches the neutrino component is evolved in different integrators. In the grid approach the neutrino component is evolved in CAMB with the full general relativistic equations and no cosmic variance. In the particle approach the neutrino component is evolved in GADGET-2, with an accuracy limited by the finite box size, a finite number of CDM and neutrino N-body particles (particle shot noise), as well as finite time-steps and force resolution. It is important that the neutrino component is evolved accurately in both integrators[2], so that our results are not compromised.

Since we are interested in quantifying the non-linear neutrino correction term, we need to verify that the relative differences in the power spectrum between the two approaches have converged sufficiently. This demand is not as challenging as simulating a converged absolute power spectrum. We note that small-scale differences in the total matter power spectrum are acceptable since this part is dominated by the CDM component, which is evolved in the same integrator in both the grid and

[1] This high neutrino mass was only used to illustrate when the linear neutrino approach breaks down.

[2] The accuracy with which CAMB calculates the linear power spectrum is far better than 1% on all scales.

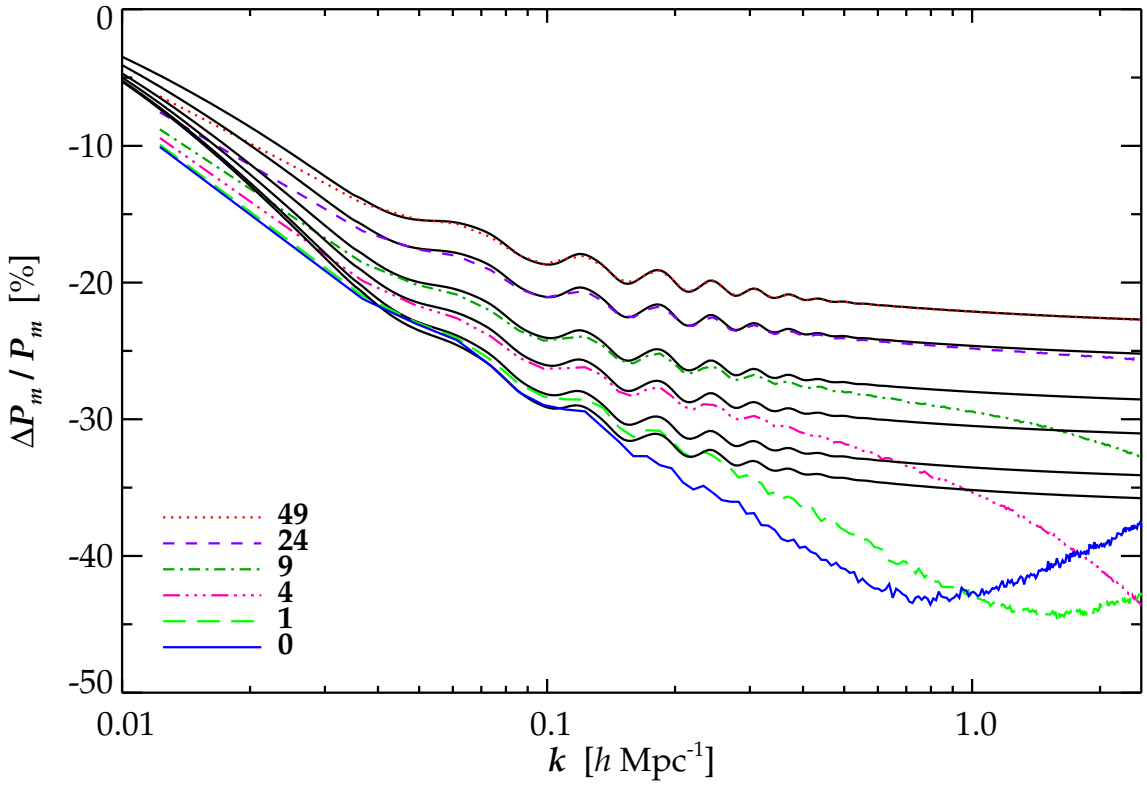

Figure 7.4: Evolution of the difference in the total matter power spectrum between a pure ΛCDM model (A_1) and a model with $\sum m_\nu = 0.6\,\mathrm{eV}$ neutrinos on a grid (C_1). The difference expected from linear theory is also shown (black solid lines).

particles approaches. Small inaccuracies at small scales will therefore cancel out when comparing power spectra which only differs at the few percent level. But since the two neutrino representations are evolved in different integrators, we need a converged absolute neutrino power spectrum at the scales where the neutrino component contributes to the total matter power spectrum.

Those test runs described in this section which are not listed in Fig. 7.1 are evolved in a $512\,h^{-1}$Mpc box and all have 256^3 CDM particles and a 512^3 PM grid.

7.4.1 Initial velocities and their evolution

We have found the gravitationally induced initial N-body velocities by taking the time difference between two displacement grids centered around our N-body starting redshift by some small Δz. We have run 3 simulations varying Δz in the range $0.5 - 2$, and found that our choose of $\Delta z \simeq 1$ has converged at a few tens of a percent.

In GADGET-2 particle velocities are redshifted, not the momentum. This Newtonian evolution is very well justified for CDM particles but could pose a problem for low mass neutrinos, since at high redshift their Fermi-Dirac distributed thermal velocities can approach half the speed of light.

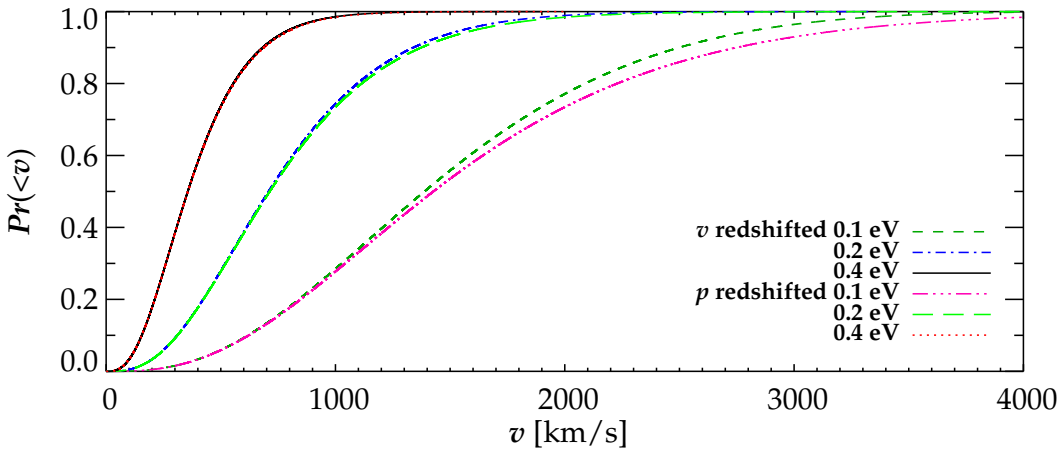

Figure 7.5: The figure shows the effect of redshifting either the Fermi-Dirac thermal velocity or momentum from $z = 49$ until $z = 0$, for 3 different neutrino one-particle masses.

In Fig. 7.5 we have calculated the cumulative neutrino thermal velocity distribution today in two different ways for our 3 neutrino one-particle masses simulated. Either by redshifting the velocity or the momentum from our N-body starting redshift of 49. From the figure it can be seen that for our highest simulated neutrino mass of 0.4 eV, it is very accurate to redshift the velocity. In the 0.2 eV case redshifting the velocity or momentum gives the same result except for a slight difference at the high end of the velocity distribution tail. This small difference will not affect our results. In the 0.1 eV case this difference is slightly larger, but since it is mainly the neutrino N-body particles with a thermal velocity drawn from the low end of the distribution which contribute to the matter power spectrum, redshifing the velocity is accurate enough. Likewise relativistic velocity addition is not necessary. Note that redshifting the velocity instead of the momentum leads to a lower thermal velocity and therefore *more* structure formation, so that from this point of view the size of the non-linear correction to the neutrino component in Fig. 7.1 is an upper bound.

7.4.2 Box size and particle shot noise

The finite size of the simulation volume as well as a limited number of N-body particles can significantly affect the simulated power spectrum (see [89] for a recent analyses). We have chosen a box size of $512\,h^{-1}$Mpc from the considerations that a significant number density of neutrino N-body particles was needed to suppress the thermal velocity white noise term on small scales. Increasing the box size by a factor of 2 would demand a factor of 8 more neutrino N-body particles, stretching our computational resources, especially CPU time, to the limits.

But, as shown in the left panel of Fig. 7.6, our chosen box size is sufficiently large for testing the neutrino grid method. The figure shows the non-linear correction from our highest resolution runs with $\sum m_\nu = 0.6\,\text{eV}$ (C_1/C_3), compared against a simulation where the box size, number of CDM and neutrino particles as well as the PM grid have been scaled down by a factor of 2 per dimension (C_4/C_5). Note that the two sets of simulations have been started from different initial

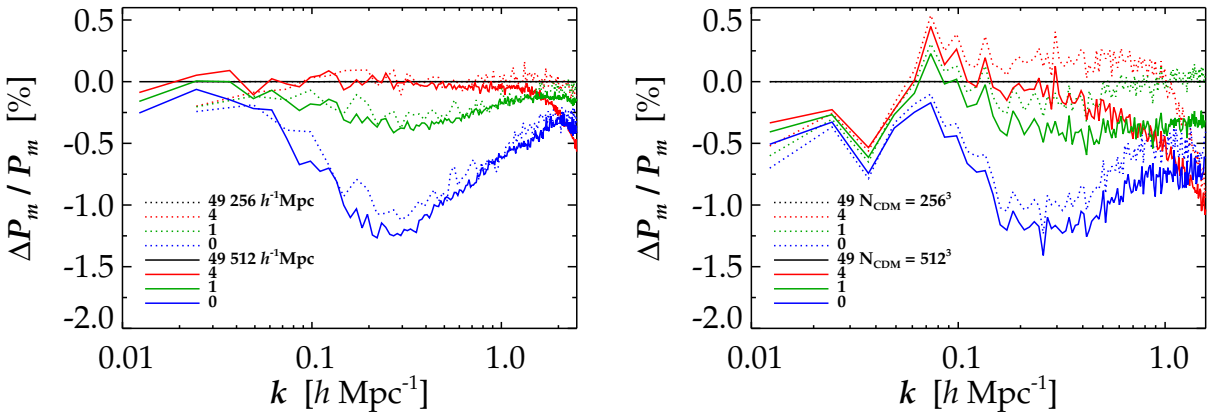

Figure 7.6: Left: The non-linear neutrino correction as a function of the simulation volume and redshift. Dotted lines is for a $256\,h^{-1}$Mpc box (C_4/C_5) and solid lines for our standard $512\,h^{-1}$Mpc box (C_1/C_3). Right: Convergence as a function of the number of CDM N-body particles at different redshifts. Dotted lines is for 256^3 CDM particles (C_6/C_7) and solid lines for 512^3 CDM particles (C_1/C_2). In both figures $\sum m_\nu = 0.6\,\mathrm{eV}$.

random numbers. The difference in the calculated non-linear correction is at the 0.2% level at most. Since we expect rapid convergence as the box size is increased, the chosen box size of $512\,h^{-1}$Mpc is sufficient.

Including enough CDM particles is important for calculating the gravitational potential accurately since the neutrino N-body particles move on this background. The difference between including 256^3 (C_6/C_7) and 512^3 (C_1/C_2) CDM particles on the calculation of the non-linear neutrino correction is seen in the right panel of Fig. 7.6. At higher redshift the difference is largest at smaller scales, but the two sets of simulations begin to converge at low redshift. Note that the lower resolution CDM simulation predicts a slightly smaller non-linear neutrino correction at the 0.2% level. Again, expecting the size of the non-linear neutrino correction term to converge rapidly as the number of CDM particles are increased, our choose of 512^3 CDM particles is sufficient. Also note that the neutrino particle and grid methods approach each other at the largest scales as more CDM particles are included and that the differences between the two CDM resolutions mainly build up at high redshift, where the particle distributions are most homogeneous.

Fig. 7.7 shows convergence as a function of 256^3 or 512^3 neutrino N-body particles in the $\sum m_\nu = 0.6\,\mathrm{eV}$ and $1.2\,\mathrm{eV}$ cases. Focusing on the lower mass neutrinos it can be seen that the discrepancy between the 256^3 and 512^3 simulations is largest at the smallest and largest scales simulated. At the smallest scales since here the neutrino white noise term contributes substantially to the total matter power spectrum, and at the largest scales since a noise term generated at high redshift is added to a real significant gravitational signal and therefore persists today. We conclude that in the range $k \simeq 0.1 - 1\,h\mathrm{Mpc}^{-1}$ where non-linear correction terms to the neutrino component are important the difference between the neutrino grid and particle methods has converged as a function of the number of neutrino N-body particles.

In the $\sum m_\nu = 1.2\,\mathrm{eV}$ case the noise term is even more pronounced at small scales, $k \gtrsim 0.3\,h\mathrm{Mpc}^{-1}$, since now Ω_ν is larger even though the thermal velocity is smaller. As demonstrated

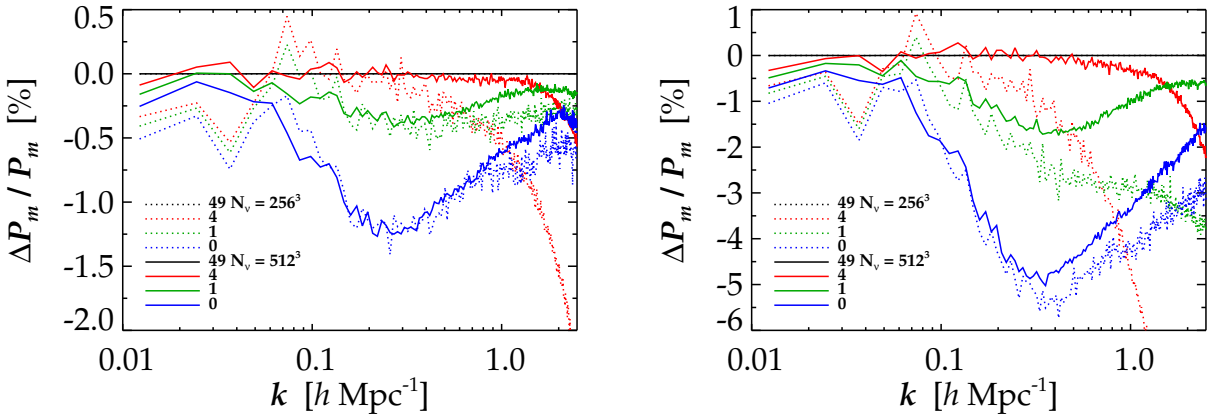

Figure 7.7: Convergence as a function of neutrino N-body particles at various redshifts. Left: $\sum m_\nu = 0.6\,\mathrm{eV}$, dotted lines is for 256^3 neutrino particles (C_1/C_2) and solid lines for 512^3 neutrino particles (C_1/C_3). Right: $\sum m_\nu = 1.2\,\mathrm{eV}$, dotted lines is for 256^3 neutrino particles (D_1/D_2) and solid lines for 512^3 neutrino particles (D_1/D_3).

in [1] the noise term decreases rapidly as the number of neutrino N-body particles is increased, therefore we expect the difference between the neutrino grid and particle methods to have almost converged for 512^3 neutrino N-body particles.

Since the maximum non-linear neutrino correction in the 1.2 eV case has almost converged for 512^3 neutrino N-body particles, and it has converged for 0.6 eV neutrinos, scaling to the 0.3 eV case we see that the 0.25% correction here should also have converged.

With respect to the neutrino grid we (usually) have a Nyquist frequency of $\pi\,h\mathrm{Mpc}^{-1}$. This is an oversampling of the neutrino perturbations, so that linear neutrino modes are not missing at scales where they contribute. We chose a cut-off in the neutrino grid modes at the grid Nyquist frequency.

7.4.3 Time and force resolution

To get the neutrino Fourier modes at a specified redshift we have interpolated linearly in the scale factor between the TFs in the library. These TFs are themselves equally spaced in the scale factor. To test the accuracy of this method we have run simulations with $\sum m_\nu = 0.6\,\mathrm{eV}$ where the number of TFs in the library were decreased from 500 by a factor of 5. On scales where the neutrinos contribute to the matter power spectrum, the difference found was below 0.05% for all redshifts. Also note that the non-linear neutrino correction term found is not due to an inaccurate sampling of the TFs, since such an error would manifest itself especially on the largest scales where the neutrino component contributes the most.

We also tested our choices for the GADGET-2 parameters ErrTolIntAccuracy = 0.025 and MaxSizeTimeStep = 0.03 by decreasing them by a factor of 4 and 6, respectively. At $k < 1\,h\mathrm{Mpc}^{-1}$ the difference is at most 0.1 % in each case, so regarding these two parameters the absolute power spectrum is evolved accurately in the region where we have the non-linear neutrino correction. We also ran the code with double precision and found an absolute error below 0.1%, which only manifested itself on small scales.

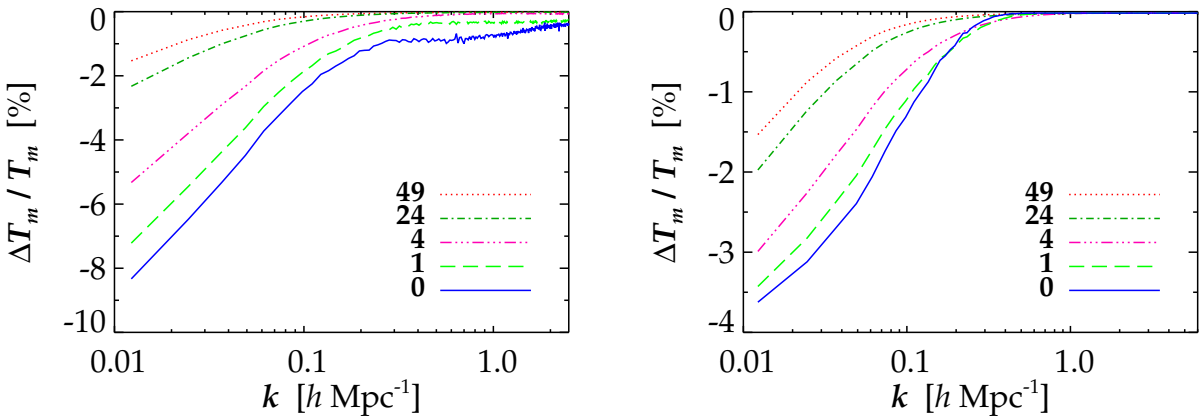

Figure 7.8: Left: The effect on the square root of the matter power spectrum (an effective non-linear matter TF, T_m) of neglecting the perturbed neutrino component, $\sum m_\nu = 0.6\,\mathrm{eV}$, in the N-body simulation when it is started at $z = 49$ (C_{10}/C_1). Right: The effect on T_m of neglecting the neutrino component, $\sum m_\nu = 0.6\,\mathrm{eV}$, only when the power spectrum is calculated at a given redshift (model C_1).

Since the neutrino particle component mainly contributes to the gravitational potential in the region coverged by the PM grid, testing for convergence of the long-range force is important, so as not to introduce errors when comparing the neutrino grid and particle methods. Therefore, we have run two simulations with a PM grid size of 1024 (models C_8 and C_9). These simulations gave an almost identical calculation of the non-linear neutrino correction term compared to the $N_{\mathrm{PM}} = 512$ case.

In the standard TreePM approach the long-range force is Gaussian filtered. Since we do not filter the neutrino grid modes, these modes contribute at smaller scales than do the neutrino particle long-range modes. Since the PM approach breaks down at small scales, it is necessary to test how much this lack of filtering contributes. We have done this by running our 3 neutrino grid simulations (models B_1, C_1 and D_1) with the Gaussian filtering included.

In the $\sum m_\nu = 1.2\,\mathrm{eV}$ case the non-linear neutrino correction term increases by only $\simeq 0.25\%$ with the smoothing turned on. For the lower neutrino masses the effect is negligible ($\lesssim 0.05\%$). Therefore, including the neutrino grid modes via the PM approach without a Gaussian filtering is well justified, since the neutrinos do not contribute substantially to the gravitational potential on scales where the PM method breaks down. Or equivalently, it is extremely well justified to neglect the linear neutrino component in the Tree part (for our chosen N-body specific parameters, i.e. $R_{\mathrm{BOX}} = 512\,h^{-1}\mathrm{Mpc}$, $N_{\mathrm{PM}} = 512$, $r_{\mathrm{s}} = 1.25$ and $r_{cut} = 4.5$).

7.4.4 The extent in Fourier space of the neutrino grid

In order not to oversample the neutrinos in the grid approach it is usefull to find a maximum wavenumber beyond which the neutrinos do not contribute to the formation of structure. In the left panel of Fig. 7.8 we show the effect of neglecting the $\sum m_\nu = 0.6\,\mathrm{eV}$ neutrino grid from $z = 49$ onwards, i.e. throughout the whole N-body simulation. The neutrino component is still included in the calculation of the background evolution. The effect is of course pronounced at large scales,

but even a lack of power is visible at small scales. The neutrino modes corresponding to these small scales do not contribute to this difference, as can be seen from the right panel of Fig. 7.8. Instead, it is power missing from a lack of mode-coupling between the small-scale CDM modes and large-scale CDM plus neutrino modes. Note that we have shown the difference in the square root of the matter power spectrum, since it is this quantity that is related to the gravitational potential calculated in Fourier space in GADGET-2.

To find a maximum wavenumber beyond which the neutrino grid does not contribute to the gravitational potential, the difference in the square root of the matter power spectrum with and without the neutrino grid is shown in the right panel of Fig. 7.8 for $\sum m_\nu = 0.6\,\mathrm{eV}$. The grid is only taken out when the power spectrum is calculated and the neutrino modes are therefore included in the evolution of the matter perturbations. The wavenumber at which the difference goes to zero can then be used to find the required extent of the neutrino grid in Fourier space. For $\sum m_\nu = 0.6\,\mathrm{eV}$ a conservative value for this maximum wavenumber is $k \simeq 1\,h\,\mathrm{Mpc}^{-1}$. Notice that this maximum wavenumber is not found by considering the power spectra today, but at a redshift of $\simeq 4$. For $\sum m_\nu = 0.3\,\mathrm{eV}$ the maximum wavenumber is $\simeq 0.5\,h\,\mathrm{Mpc}^{-1}$. We caution that these maximum wavenumbers depend on Ω_m.

7.5 Discussion and conclusions

We have presented a new method for implementing neutrinos in N-body simulations which works extremely well for a total neutrino mass below ~ 0.5 eV. For such masses the difference in the matter power spectrum compared with simulations where neutrinos are treated as particles is always below 1% on all scales. The precision is better for smaller masses, with the difference scaling roughly as m_ν^2, and the gain in computational speed compared to representing the neutrinos as N-body particles is very large (scaling roughly as m_ν^{-1}). For all masses this is the only computationally feasible way to include neutrinos in simulations at the required level of precision, especially for high N-body starting redshifts.

We also note that the method presented here will work for any type of energy density which has almost linear perturbations.

Finally we caution that although the method is very accurate for calculating all observables related to matter fluctuations, i.e. the power spectrum, halo mass functions etc, it is not accurate at the 1% level in describing the neutrino fluctuations alone. For predicting quantities such as the local density of relic neutrinos additional steps should be taken. One possibility is to use the 1-particle Boltzmann technique [71, 72]. In its simplest form, however, this method represents the neutrino component only in an approximate way. Another path is to solve with the method presented here until z becomes sufficiently low (in practise $z \lesssim 4$) that the noise from the neutrino thermal velocity can be kept under control. At this point the grid simulation can be used as the initial condition for a simulation with neutrinos treated as particles.

Acknowledgements

We acknowledge computing resources from the Danish Center for Scientific Computing (DCSC). We thank Troels Haugbølle, Julien Lesgourgues and Bjarne Thomsen for discussions.

Chapter 8

Resolving Cosmic Neutrino Structure: A Hybrid Neutrino N-body Scheme

Jacob Brandbyge, Steen Hannestad

Abstract We present the first simulation capable of resolving the structure of neutrino clustering on Mpc scales. The method combines grid- and particle-based methods and achieves very good accuracy on both small and large scales, while keeping CPU consumption under control. Such simulations are not only ideal for calculating the non-linear matter power spectrum but also particularly relevant for studies of how neutrinos cluster in galaxy- or cluster-sized halos. We perform the largest neutrino N-body simulation to date, effectively containing 10 different neutrino hot dark matter components with different thermal properties [3].

8.1 Introduction

In the non-linear regime the most accurate, but also most time-consuming method to calculate how neutrinos affect structure formation is to use full N-body simulations with neutrinos included in a self-consistent way. In a previous publication we carried out a large suite of simulations with neutrinos included [1], and found a significant non-linear correction caused by neutrinos.

In a recent paper [2] we showed that for realistic neutrino masses, quantities such as the power spectrum can be calculated very reliably on all scales, using a grid-based method which tracks the linear neutrino density contrast on a grid while using the full non-linear structure of CDM.

The problem with both the particle-based and the grid-based methods is that they cannot reliably probe the small-scale structure of neutrinos. In particle-based codes the problem is that the thermal velocity of the neutrino component is so large that it introduces noise at an unacceptable level. The grid-based method does not resolve neutrino bound structures and therefore by construction does not allow us to probe for example the neutrino content of a halo.

In the present paper we present a hybrid method which retains the good features of both methods and still runs at an acceptable speed. The idea is to start with neutrinos described on a grid, and then convert part of the grid to N-body particles when the thermal motion of neutrinos decreases to a few times the flow velocities in the simulation. The neutrino N-body particles

are created in different momentum bins, with individual transfer functions and thermal velocities. We therefore present N-body simulations with 15 different neutrino hot dark matter species. In a following paper we will use this hybrid method to investigate neutrino clustering on sub Mpc scales.

In section 8.2 we outline the theoretical framework and problems with combining particle and fluid approaches. Section 8.3 gives a technical description of the implementation of the hybrid method and Section 8.4 presents our results. Finally, Section 8.5 contains our discussion and conclusions.

8.2 Theory

8.2.1 The Boltzmann equation

In this subsection we will briefly outline how the evolution of massive neutrinos is followed in linear theory. The notation is identical to [9] (see 2.3.3 for further details). In a perturbed universe the phase-space distribution function is expanded to first order as follows

$$f = f_0 + \frac{\partial f_0}{\partial T}\delta T = f_0(1+\Psi), \tag{8.1}$$

with the perturbation parametrised by $\Psi = -d\ln f_0/d\ln q \ \delta T/T$.

Expanding the perturbation Ψ in a Legendre series the perturbed neutrino energy density is given by a weighed sum over neutrino momentum states

$$\delta\rho_\nu(k) = 4\pi a^{-4}\int q^2 dq\epsilon f_0\Psi_0, \tag{8.2}$$

where $\epsilon = (q^2 + a^2m^2)^{1/2}$. Note that f_0 and not f is used to weigh the individual momentum bins, an assumption which breaks down when the gravitational flow velocity approaches the thermal velocity of the individual momentum states.

From the Boltzmann equation the Ψ_l's are related to each other and the metric potentials by

$$\dot{\Psi}_0 = -k\frac{q}{\epsilon}\Psi_1 - \dot{\phi}\frac{d\ln f_0}{d\ln q}, \tag{8.3}$$

$$\dot{\Psi}_1 = k\frac{q}{3\epsilon}(\Psi_0 - 2\Psi_2) - k\frac{\epsilon}{3q}\psi\frac{d\ln f_0}{d\ln q}, \tag{8.4}$$

$$\dot{\Psi}_l = k\frac{q}{(2l+1)\epsilon}(l\Psi_{l-1} - (l+1)\Psi_{l+1}) \ , \ l \geq 2. \tag{8.5}$$

The quantity calculated in linear theory is the transfer function (TF) which evolves the initial primordial perturbation Ψ_0^I as

$$\Psi_0(k,q,z) = T(k,q,z)\Psi_0^I(k,q), \tag{8.6}$$

with Ψ_0^I given by

$$\Psi_0^I = -\frac{\delta_\nu}{4}\frac{d\ln f_0}{d\ln q}. \tag{8.7}$$

8.2.2 Qualitative behaviour

Eq. (8.7) states that neutrinos with different initial momenta have different initial perturbations, also on large scales. Specifically, $\Psi_0^I \to 0$ for $q/T \to 0$, meaning that neutrinos with zero (read: almost zero) momentum are unperturbed. The reason for this is that at each spatial location the neutrino distribution is initially locally a Fermi-Dirac distribution with zero chemical potential, as is also reflected in Ψ_0^I. As $q/T \to 0$ the Fermi-Dirac distribution always tends to $f \to 1/2$, independent of T, and this means that the distribution function is unperturbed.

According to the Boltzmann equation, neutrinos with $q = 0$ always stay unperturbed. When gravity acts on neutrino particles with $q = 0$, thereby perturbing them, their momenta change, and they are therefore shifted out of the $q = 0$ momentum bin, leaving this bin unperturbed. This fact is contained in the Boltzmann hierarchy for the Ψ_l's through the term $d\ln f_0/d\ln q$, which multiplies the gravitational potentials (ϕ, ψ) so that different neutrino momentum bins are affected differently by gravity [1].

The effect of linear as well as non-linear forces on the momenta of neutrino particles changes the shape of f_0 beyond linear order. Therefore the weighing of the individual Ψ_0's in the momentum integral changes. This means that the value of $\delta\rho$ changes, not only at non-linear wavenumbers but also in the linear regime. Therefore the linear theory average neutrino TF is not even valid at very large scales, though becoming more accurate for lower neutrino masses.

8.2.3 Converting the density grid to N-body particles

When we convert densities on the grid into particles we are faced with a potential problem. Imagine that neutrino energy in the first i momentum bins are converted to particles at some redshift, while keeping the remaining neutrinos on the grid. At some later time, some of the created particles will have been moved to higher velocities by gravity and therefore really belong to the grid, whereas some density on the grid would have moved to lower velocity, and should have been converted to particles. This "leakage" is problematic because the evolution of the grid is done in CAMB [12] while the evolution of particles is followed in GADGET-2 [26].

The problem is even more severe because the leakage to higher and lower momentum bins are qualitatively different: Imagine we dump all neutrino grid bins with momenta less than $q_{\rm cut}$ to N-body particles at a certain redshift, and let the particles evolve. Due to energy conservation, particles gaining energy above $q_{\rm cut}$ are falling into gravitational potential wells, and are typically clustered, while particles loosing energy are moving out of potential wells, and they are typically much more homogeneous as a population. Hence one cannot simply artificially decrease the velocities of the high energy particles to account for the leakage across $q_{\rm cut}$ between grid and particles, because the topology, or specific position in phase-space, of particles crossing the momentum boundary from above and below is very different.

Ideally, the neutrino N-body particles should only sample momentum space up to $q_{\rm cut}$. In the N-body simulation neutrinos with momenta larger than $q_{\rm cut}$ should therefore not contribute to the gravitational source term (to avoid double counting). This can surely be done, by eg. zeroing the mass of these neutrino N-body particles. Furthermore, we get a zero counting of the particles which, if they had been created from the grid at $q > q_{\rm cut}$, would have moved to $q < q_{\rm cut}$. One could include zero mass ghost particles with initial momentum states covered by the grid as tracer

[1] Note that this is purely a phase-space phenomenon and has nothing to do with the gravitational force felt by particles.

particles in the N-body volume, and then turn their mass on if they leak down to momentum states smaller than $q_{\rm cut}$. But in practise the linear assumption of a constant $f \simeq f_0$ is violated beyond linear order in the N-body simulation: There is a significant net flow of neutrino mass to higher momentum states. Therefore, turning the neutrino mass on / off as particles cross $q_{\rm cut}$ will lead to a net reduction of overall neutrino mass. Furthermore, particles moving to $q > q_{\rm cut}$ carry large non-linear corrections which are not found in the corresponding linear grid bins, making the idea with ghost particles less appealing.

However, a simple solution which works well in practise is to convert a sufficiently large number of momentum bins at the same time because that keeps the leakage between converted and non-converted bins to a minimum. We will discuss this issue in the next sections and demonstrate that errors can be kept under control at the required precision.

8.3 Implementation of the hybrid neutrino method

We have used the following parameters in a flat cosmology: $(\Omega_{\rm c} + \Omega_\nu,\ \Omega_{\rm b},\ \Omega_\Lambda,\ h,\ \sigma_8,\ n_s) = (0.25,\ 0.05,\ 0.7,\ 0.7,\ 0.878,\ 1)$. The value for σ_8 is for a pure ΛCDM model without massive neutrinos. We use values of $\sum m_\nu = 0.6$ eV and 1.2 eV with particular emphasis on the latter value, since a high neutrino mass affect structure formation more, thereby testing the accuracy of the hybrid method better.

The primordial density perturbations are followed with the linearised Einstein and Boltzmann equations, solved in CAMB [12]. At $z = 49$ the CDM component is taken out of CAMB and followed in GADGET-2 [26] run in the TreePM mode. The N-body initial conditions are generated with the Zel'dovich Approximation [23] as well as a second-order correction term [25] added to the CDM particles only.

As input to the N-body code the linear neutrino TF is needed. Normally this TF is found from Eq. (8.2) by integrating over all momenta. However, in our case we need the momentum dependent TFs because when particles are extracted from the grid they are taken in a certain momentum range and the neutrino TFs are highly momentum dependent (because the free-streaming length depends on q). In Fig. 8.1 we show the momentum dependent TFs for $\sum m_\nu = 1.2\,{\rm eV}$ at $z = 0$, from which the neutrino momentum dependence on the power spectrum is clearly seen. The effect of free-streaming at small scales is most pronounced for the highest neutrino momentum states, but these states do have the largest TF at large scales.

To follow the neutrino component we combine the neutrino particle and grid representations, first explored in [1] and [2], respectively. Initially, the neutrinos are represented on a grid, and there are no neutrino N-body particles. When the neutrino thermal velocity falls below a few times the average gravitational flow velocity, calculated from the CDM N-body particles, the lowest momentum part of the neutrino grid energy is converted into N-body particles. Here there are 3 things to consider.

First, the energy on the neutrino grid should be decreased. We have 15 neutrino TF bins (the standard output from CAMB, the number can easily be modified), where q/T runs from 1 to 15 (upper limits) in integer steps, corresponding to a bin width of $\simeq 125\,{\rm km/s}$ in comoving coordinates for $\sum m_\nu = 1.2\,{\rm eV}$. When the first bin with the lowest neutrino momentum states is converted to particles, only the remaining 14 bins are summed to get the neutrino grid Fourier modes. The phases of the neutrino particles are made with the same set of random numbers as were the CDM particles at $z = 49$.

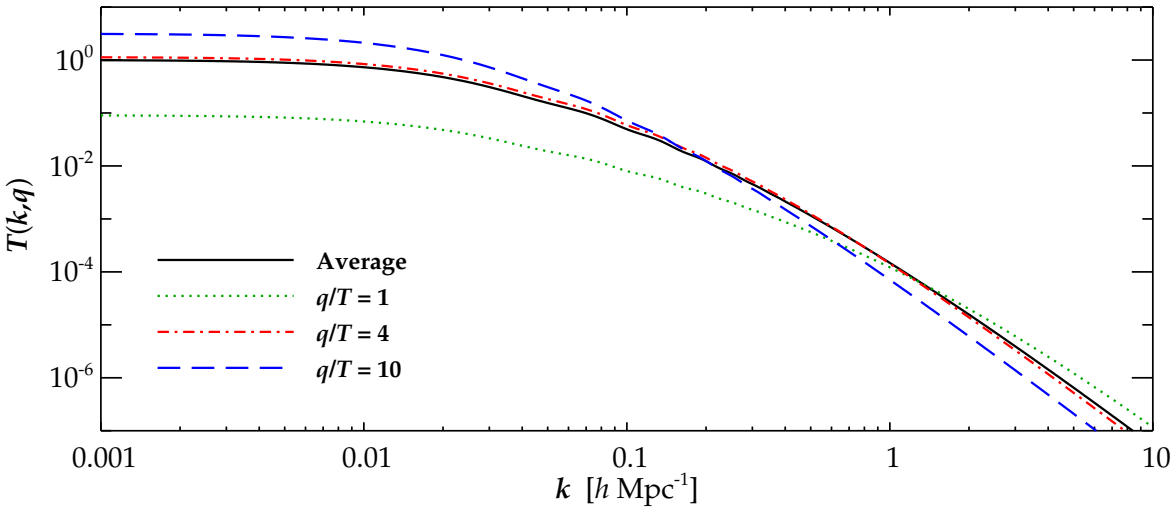

Figure 8.1: Momentum dependent neutrino TFs at $z = 0$ for $\sum m_\nu = 1.2\,\mathrm{eV}$.

Second, the neutrino N-body particle mass should correspond to the mass removed from the grid.

Third, when neutrino N-body particles are created in a certain momentum range, the thermal velocity they recieve lies within this range as well. This is based on the fact that at the conversion redshift the thermal velocity is much larger than the gravitational flow velocity, meaning that neutrinos in a given bin can at most have originated from the adjacent bins. It is therefore a very good approximation to give the neutrino particles a thermal velocity corresponding to the bin and assuming that there is no correlation between the thermal and flow components. This reduced bin mixing caused by the thermal velocity is fortunate, since disentangling these two components would be impossible.

The thermal velocities for a given particle grid position in two succeeding neutrino grid-to-particle conversions are drawn with the same random numbers, but with momenta pointing in opposite directions. This ensures an approximate local conservation of momentum. In [1] local conservation was not enforced due to a higher neutrino particle starting redshift, and since only the average TF was used as input power spectrum.

The neutrino gravitational velocity is found from the difference of two position grids centered around (with $\Delta a = 0.01$) our neutrino grid-to-particle conversion redshift (first described in [1]). When we add the gravitational flow velocity, some neutrinos will have a total momentum which lies outside of the bin. This is a problem when part of the neutrino grid is converted to particles at times when the neutrino thermal velocity is only a few times the gravitational velocity, though effectively being a problem only for the low momentum neutrinos.

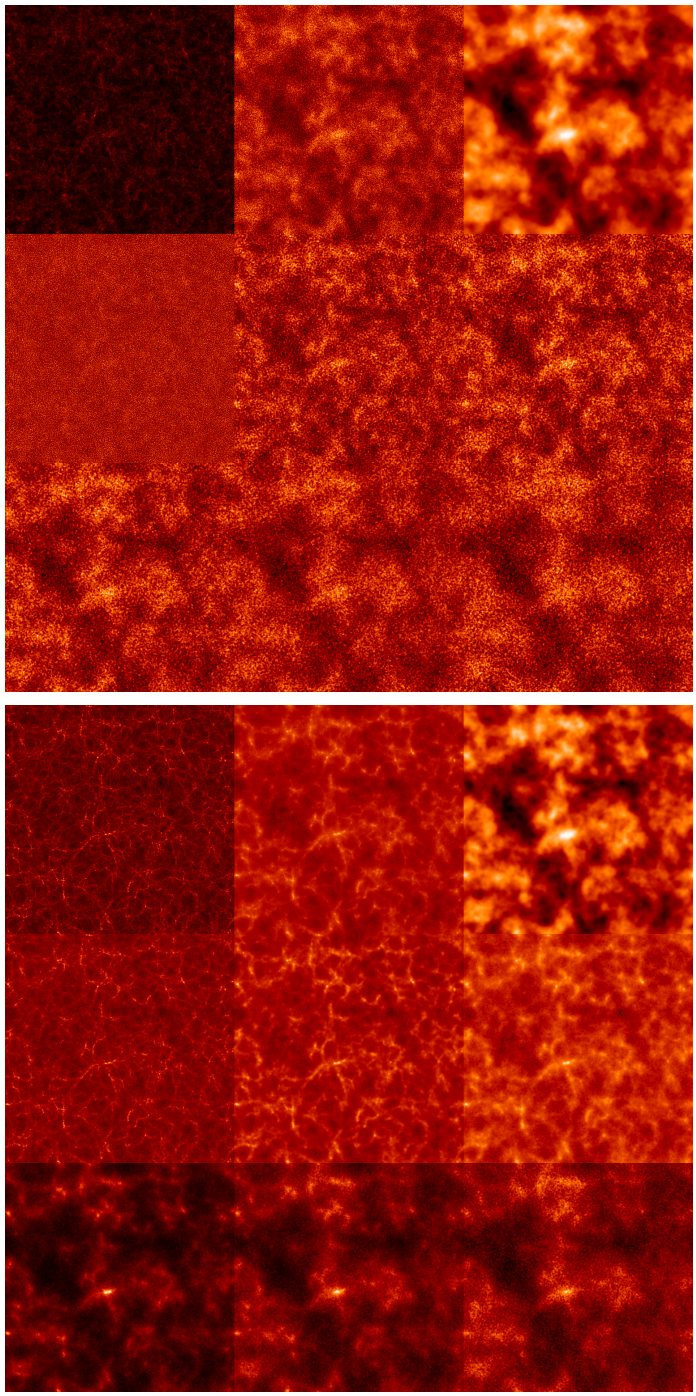

Figure 8.2: Density grids from the hybrid simulation A_1 with $\sum m_\nu = 1.2\,\mathrm{eV}$ found with the adaptive smoothing length kernel from [76]. Top mosaic: $z = 4$. Bottom mosaic: $z = 0$. Top row: CDM, neutrino particles and neutrino grid. Middle row: $q/T = 1$, 2 and 3. Bottom row: $q/T = 5$, 7 and 10. Bottom mosaic: The CDM, neutrino particle, $q/T = 1$, 2 and 3 density grids have been raised to the power of 0.25 to enhance the dynamical contrast. The density slices have a thickness of $20h^{-1}\,\mathrm{Mpc}$ and are $512h^{-1}\,\mathrm{Mpc}$ on a side.

	A_1	A_2	A_3	B_1	B_2	B_3	B_4	B_5	B_6	C_1	C_2	C_3	C_4	D_1	D_2	D_3
$N_{\rm CDM}$	512^3	512^3	512^3	256^3	256^3	256^3	256^3	256^3	256^3	256^3	256^3	256^3	256^3	256^3	256^3	256^3
$N_{\nu,\rm grid}$	512^3	0	512^3	256^3	256^3	256^3	256^3	256^3	256^3	256^3	256^3	256^3	256^3	256^3	256^3	256^3
$q_{\rm cut}/T$	10	∞	0	4	5	6	7	10	15	10	10	10	10	10	10	10
$f_{\rm flow}$	4	∞	0	4	4	4	4	4	4	2	4	8	16	2	4	8
$\sum m_\nu$ [eV]	1.2	1.2	1.2	1.2	1.2	1.2	1.2	1.2	1.2	1.2	1.2	1.2	1.2	0.6	0.6	0.6
Ω_ν [%]	2.6	2.6	2.6	2.6	2.6	2.6	2.6	2.6	2.6	2.6	2.6	2.6	2.6	1.3	1.3	1.3

Table 8.1: Parameters for our N-body simulations presented in this paper. $N_{\rm CDM}$ is the number of CDM N-body particles and $N_{\nu,\rm grid}$ is the size of the neutrino Fourier grid. $q_{\rm cut}/T$ indicates how much of neutrino momentum space is converted to particles, and the number of neutrino N-body particles can be found from $q_{\rm cut}/T \cdot N_{\nu,\rm grid}$. When the average CDM gravitational flow velocity times $f_{\rm flow}$ has increased above $q/T = 1$, the conversion from grid to particles is made. $\sum m_\nu$ is the total neutrino mass, and it is in all cases related to the one-particle neutrino mass, m_ν, by $\sum m_\nu = 3m_\nu$. Ω_ν is the fraction of the critical density contributed by the neutrinos today. In all simulations $R_{\rm BOX} = 512h^{-1}$Mpc, and the size of the particle mesh grid is equal to the number of CDM particles. All simulations have a starting redshift of 49. Note that model B_5 is identical to model C_2.

8.4 Results

In Fig. 8.2 we show density grids from the hybrid A_1 simulation (see Table 8.1). Some features can immediately be seen from this. As expected the part of the neutrino distribution remaining on the grid is much less clustered on small scales than the neutrino particles, while the opposite is true on the largest scales. Interestingly, it can also be seen that the $q/T = 1$ bin is initially only weakly clustered on all simulated scales (i.e. at $z = 4$), but quickly starts tracking the CDM component, and at $z = 0$ has as much clustering as the next momentum bin. Note that the individual neutrino density grids are found from the original binning of the neutrino particles at the grid-to-particle conversion redshift (determined by the primordial thermal velocity), and not according to the actual neutrino particle velocities at redshifts 4 and 0.

8.4.1 Comparing the hybrid method to its building blocks

We have compared our new hybrid method (A_1) with the full non-linear simulation (A_2), where neutrino N-body particles are created at $z = 49$, and with the simulation where the neutrino component stays linear on a grid (A_3).

On the left-hand side of Fig. 8.3, it can be seen that the new method gives almost the same total matter power spectrum as the full non-linear simulation, except at low redshift where the hybrid method gives slightly less power for $k \gtrsim 0.2\,h\mathrm{Mpc}^{-1}$. In the full non-linear simulation it can be seen from [2] that the matter power spectrum has not converged for 512^3 neutrino particles. The discrepancy seen in Fig. 8.3 is therefore due to a complete suppression of the noise term in the hybrid simulation, which we have verified by running simulations with $10 \cdot 256^3$ (C_2) and $10 \cdot 512^3$ (A_1) neutrino N-body particles with the hybrid method.

On the right-hand side of Fig. 8.3 we show the neutrino power spectrum for the different methods. With the hybrid method we are now able to simulate the non-linear neutrino power

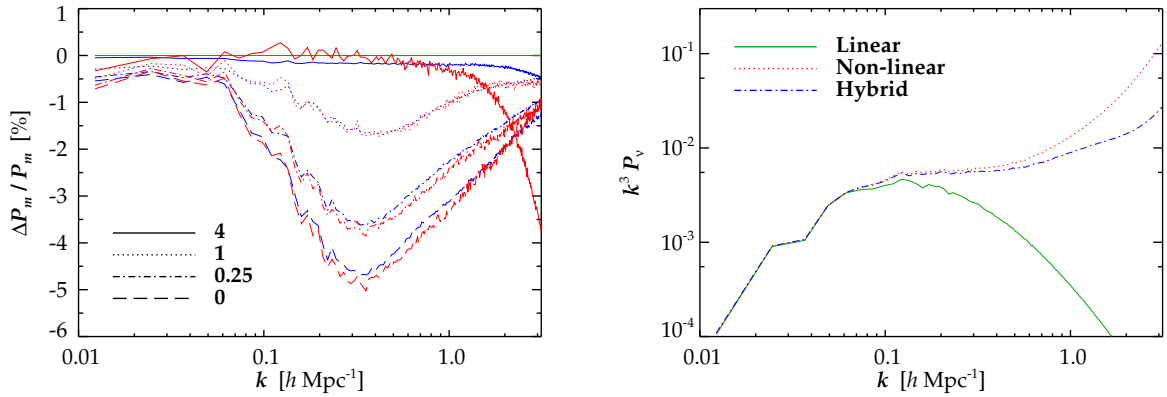

Figure 8.3: $\sum m_\nu = 1.2\,\mathrm{eV}$. Left: Difference between the linear simulation A_3 (green) and the full non-linear A_2 (red) and hybrid A_1 (blue) methods at various redshifts. Right: Absolute neutrino power spectra at $z = 0$.

spectrum accurately out to $k \simeq 1\,h\mathrm{Mpc}^{-1}$, even with $R_{\mathrm{BOX}} = 512\,h^{-1}\,\mathrm{Mpc}$. The extra accuracy is of course achieved by including more neutrino particles, but with a comparable amount of CPU time.

8.4.2 Converting part of neutrino momentum space to particles

Since only a small fraction of the neutrino mass resides in the high momentum tail it is desirable to find a momentum cut-off above which the neutrinos do not contribute significantly to structure formation at a given scale. Such a cut-off will reduce the simulation time, because the time-step criterion depends in part on the total velocity of the particles, and particles in the highest momentum bins have thermal velocities much higher than the gravitional flow velocities even at $z = 0$.

In Fig. 8.4 we show the total matter (left) and neutrino (right) power spectra for simulations with a cut-off at $q_{\mathrm{cut}}/T = 4$, 5, 6, 7, 10 and 15. For $q_{\mathrm{cut}}/T = 5$ and 10, 86% and 99.7% of the neutrino mass is converted to particles, respectively. The total matter power spectrum is almost identical for $q_{\mathrm{cut}}/T = 10$ and 15. For $q_{\mathrm{cut}}/T = 5$ the matter power spectrum increases by 2%. This is due to leakage of power across the momentum cut-off scale. But a 1% error in the large-scale perturbation field hardly affect the formation of small-scale structure. For cases (such as the study of halo profiles) where only the small-scale structure of neutrinos is important, $q_{\mathrm{cut}}/T \simeq 5$ would be sufficient.

In the neutrino power spectra the same trends can be identified. There is no significant double counting of perturbations at small scales, since at these scales the linear grid does not contribute for $q > q_{\mathrm{cut}}$. The fact that the $q_{\mathrm{cut}}/T \lesssim 6$ simulations give less power at $k \gtrsim 1\,h\mathrm{Mpc}^{-1}$, can be attributed to both neutrino N-body particle shot noise and a lack of non-linear corrections from the non-converted grid bins. We leave the relative importance of these two effects to people with too much CPU time.

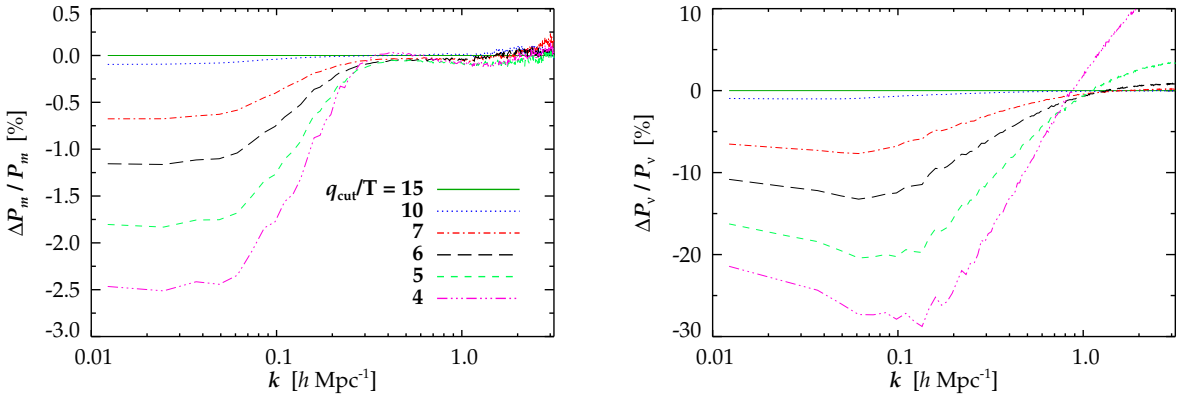

Figure 8.4: $\sum m_\nu = 1.2\,\mathrm{eV}$ and $z = 0$. Left: Hybrid simulations B_i with q_{cut}/T ranging from 4 to 15 compared to $q_{\mathrm{cut}}/T = 15$ (B_6). Right: Corresponding neutrino power spectra.

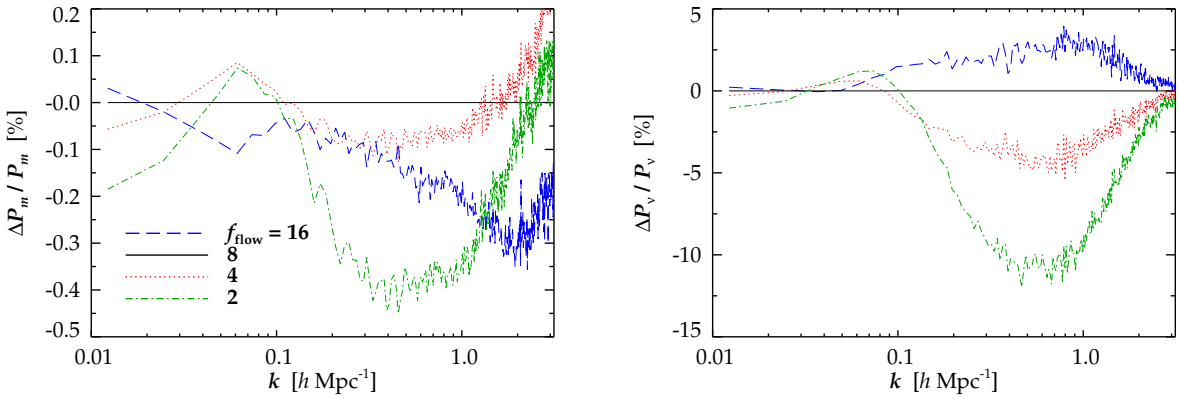

Figure 8.5: $\sum m_\nu = 1.2\,\mathrm{eV}$. Left: Matter power spectra from simulations C_i at $z = 0$ with grid-to-particle conversion factors of $f_{\mathrm{flow}} = 2$, 4, 8 and 16 relative to $f_{\mathrm{flow}} = 8$ (C_3). Right: Corresponding neutrino power spectra.

8.4.3 The optimal grid-to-particle conversion redshift

The optimal grid-to-particle conversion redshift is found as a trade-off between ensuring that non-linearities in the neutrino component is accurately simulated and that the finite number of neutrino N-body particles do not introduce a significant noise term. The first requirement is satisfied by a high and the second by a low conversion redshift.

In Fig. 8.5 we show the difference in the matter and neutrino power spectra with $\sum m_\nu = 1.2\,\mathrm{eV}$ for different conversion redshifts. The conversion criterion used was when the upper velocity limit of the $q/T = 1$ momentum bin had fallen below some factor f_{flow} of the average CDM N-body particle flow velocity. This quantity is related to the strength of the gravitational field, and therefore to the ability of neutrino particles to cluster beyond linear order. We have run simulations with $f_{\mathrm{flow}} = 2$, 4, 8 and 16, corresponding to conversion redshifts of 3.1, 5.5, 9.4 and 15.7, respectively. It can be seen that with $f_{\mathrm{flow}} = 8$ the matter power spectrum can be found with 0.2% precision and the

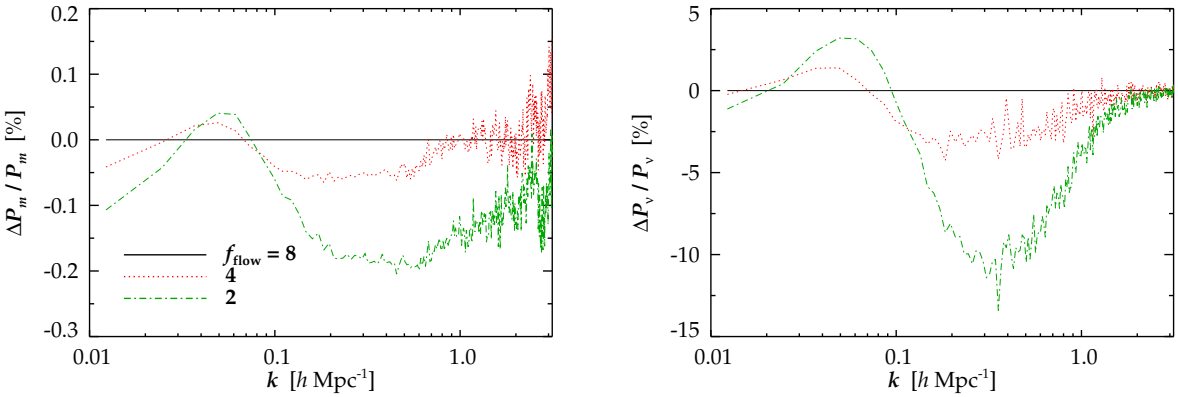

Figure 8.6: $\sum m_\nu = 0.6\,\mathrm{eV}$. Left: Matter power spectra from simulations D_i at $z = 0$ with grid-to-particle conversion factors of $f_{\rm flow} = 2$, 4 and 8 relative to $f_{\rm flow} = 8$ (D_3). Right: Corresponding neutrino power spectra.

neutrino power spectrum with at precision at the 2-4% level. The simulation with $f_{\rm flow} = 2$ clearly lacks non-linear corrections due to the late conversion redshift.

By running simulations with the particle grids down-scaled by 2^3 we have found that these results have not yet converged, though they have converged at an acceptable level to demonstrate the robustness of the hybrid method. Likewise, we have found that the lower value of the matter power spectrum with $f_{\rm flow} = 16$ compared to $f_{\rm flow} = 8$ is a noise term, making the neutrino distributions decorrelate with its CDM counterpart, giving rise to less structure.

In Fig. 8.6 the same case is examined with $\sum m_\nu = 0.6\,\mathrm{eV}$, and the same general trends can be identified. The relative error in the matter power spectrum is proportional to Ω_ν and the relative error in the neutrino power spectrum is roughly independent of Ω_ν.

Finally we have checked our results by varying the particle and the linear neutrino grid sizes. In Fig. 8.7 we show the difference in the matter power spectrum between the linear and hybrid methods. We have used the base parameters from models A_1 and A_3, and then down-scaled the particle grids and the linear neutrino grid by factors of 2^3 and 4^3. It can be seen that it is sufficient to use 256^3 grids to achieve converged results (for more convergence-tests related to grid sizes see [1, 2]).

8.5 Discussion and conclusions

We have presented a new scheme for resolving the small-scale structure of neutrinos. It combines features from grid simulations [1] which are fast and accurately track neutrinos in the linear regime with particle simulations [2] capable of resolving neutrino structures in the highly non-linear regime.

The hybrid scheme is ideal for calculating the non-linear matter power spectrum for neutrino masses around the current upper bound $\sum m_\nu \simeq 0.5\,\mathrm{eV}$. For lower neutrino masses the grid approach has an accuracy better than 1%. Furthermore, the hybrid scheme with separate momentum dependent initial TFs and corresponding separate thermal velocities reproduces our earlier results from [1] and [2], where the average neutrino TF was used.

For $\sum m_\nu = 1.2\,\mathrm{eV}$ converting 5 to 10 momentum bins at redshifts $z \simeq 5 - 10$ will accurately

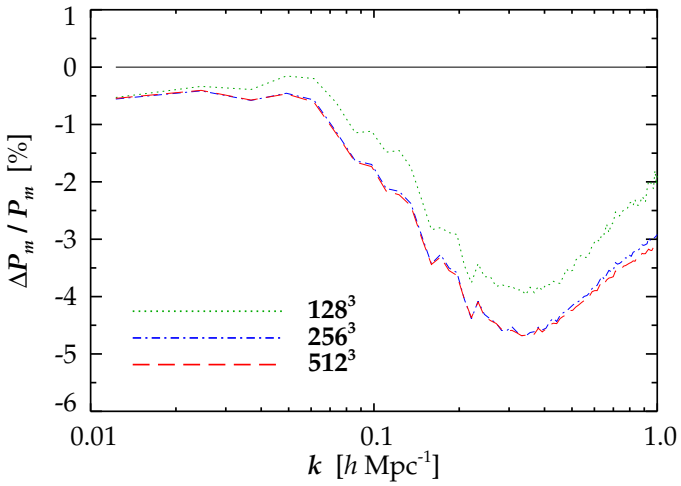

Figure 8.7: $\sum m_\nu = 1.2\,\mathrm{eV}$. Difference in the matter power spectrum at $z = 0$ between the linear (A_3) and hybrid (A_1) simulations (red), and simulations where the particle and linear neutrino grids are down-scaled by factors of 2^3 (blue) and 4^3 (green).

reproduce the matter power spectrum together with the neutrino power spectrum on small scales. For lower neutrino masses the particles can be created later due to their higher thermal velocities and a smaller part of the neutrino energy needs to be converted to particles to accurately simulate neutrino small-scale structure.

In the present work we have focused on features in the power spectrum and limited our discussion to scales of $k \lesssim 1\,h\,\mathrm{Mpc}^{-1}$, where our code can easily keep errors under control at the 1% level. Achieving a comparable level of accuracy in pure particle-based simulations would require a prohibitive amount of CPU time.

Even more interestingly, this hybrid scheme is capable of resolving much smaller neutrino structures, such as galaxy- or cluster-sized halos. This will be the topic of a follow-up paper [4] (see the next chapter).

Acknowledgements

We acknowledge computing resources from the Danish Center for Scientific Computing (DCSC). We thank Troels Haugbølle and Yvonne Wong for discussions and comments on the manuscript.

Chapter 9

Neutrinos in Non-linear Structure Formation - The Effect on Halo Properties

Jacob Brandbyge, Steen Hannestad, Troels Haugbølle, Yvonne Y. Y. Wong

Abstract We use N-body simulations to find the effect of neutrino masses on halo properties, and investigate how the density profiles of both the neutrino and the dark matter components change as a function of the neutrino mass. We compare our neutrino density profiles with results from the N-one-body method and find good agreement. We also show and explain why the Tremaine-Gunn bound for the neutrinos is not saturated. Finally, using N-body simulations we study how the halo mass function changes as a function of the neutrino mass and compare our results with the Sheth-Tormen semi-analytic formulae. Our results are important for surveys which aim at probing cosmological parameters using clusters, as well as future experiments aiming at measuring the cosmic neutrino background directly [4].

9.1 Introduction

Massive neutrinos are known to have a significant effect on cosmic structure formation [90, 91]. In the early universe they contribute to the relativistic energy density and influence the transition from radiation to matter domination. At late times they contribute to the dark matter density, and therefore also to cosmic structure formation. However, as opposed to Cold Dark Matter (CDM), they do not contribute to structure formation on physical scales smaller than the free-streaming scale, roughly equal to the distance traversed before the neutrinos become non-relativistic. This suppression of small-scale structure leaves a very distinct imprint on large-scale structure observables such as the matter power spectrum, which can in turn be used to probe neutrino physics.

While most neutrino mass constraints at present have been derived using large-scale structure correlation functions (or power spectra), there are other observables that are potentially just as interesting. One prime example is cluster number counts which are in principle very sensitive to

the neutrino mass [92]. However, in order to fully utilise such data it is necessary to have accurate theoretical predictions, which so far do not exist for ΛCDM models extended with massive neutrinos (see, however, [93] for an early calculation based on the old mixed dark matter scenario). In the present paper we calculate the halo mass function in ΛCDM cosmologies with massive neutrinos included for a variety of neutrino masses. However, before proceeding to this and a discussion of other observables related to halo properties, let us briefly review how neutrinos affect structure formation in the linear regime.

9.1.1 The effect of neutrinos

The effect of neutrinos on structure formation in linear theory has been studied numerous times in the literature (see, e.g., [10]), and the effect can roughly be separated into two regimes. On scales much larger than the free-streaming scale,

$$k_{\rm FS} \sim 0.8 \frac{m_\nu}{\rm eV}\, h\,{\rm Mpc}^{-1}, \tag{9.1}$$

where m_ν is the one-particle neutrino mass, neutrinos behave essentially like CDM, while on smaller scales they suppress structure formation. We define the matter density parameter as $\Omega_m = \Omega_c + \Omega_b + \Omega_\nu$, where Ω_c, Ω_b and Ω_ν are the corresponding CDM, baryonic and neutrino components, respectively. Then very naïvely one might expect the suppression arising from replacing a fraction of the CDM component with neutrinos to be of order $\Delta P/P \sim -\Omega_\nu/\Omega_m$ because neutrinos do not cluster. However, this grossly underestimates the true effect because massive neutrinos also influence the background expansion around the time of matter-radiation equality. The final result in linear theory is that the suppression is approximately given by [86]

$$\frac{\Delta P}{P} \sim -8\frac{\Omega_\nu}{\Omega_m}. \tag{9.2}$$

This shows that most of the effect actually comes from the modification to the background, i.e., sub-eV to eV scale neutrinos lead to a longer radiation era. This effect is also much larger than the effect of replacing a fraction $\Delta\Omega_m$ of the CDM energy density with Λ. In this case, i.e. for a ΛCDM cosmology, we find that the change in the matter power spectrum on small scales (with the large-scale normalisation held constant, i.e., ignoring the effects of $\Delta\Omega_m$ on the growth factor) is very approximately given by

$$\frac{\Delta P}{P} \sim \left(\frac{\Omega_m^{'}}{\Omega_m}\right)^{7/2} \sim -3.5(1-\Omega_m^{'}/\Omega_m), \tag{9.3}$$

where $\Omega_m^{'} = \Omega_m + \Delta\Omega_m$, for small changes in $\Delta\Omega_m \ll \Omega_m$. The effect here is approximately two times smaller than that due to assigning $\Delta\Omega_m$ to massive neutrinos.

Since neutrinos have such a strong effect on the power spectrum even in linear theory it is natural to expect a similarly strong effect in the non-linear regime. This was tested in detail for the power spectrum in a number of papers [1, 2, 3], and a significant enhancement in the power spectrum suppression was indeed found: The maximum suppression is increased from $-8\Omega_\nu/\Omega_m$ to approximately $-9.8\Omega_\nu/\Omega_m$,[1] with a pronounced feature at $k \sim 0.7\,h\,{\rm Mpc}^{-1}$.

[1] This finding was confirmed in the very recent paper [57].

Another issue which has so far not been addressed with precision N-body simulations is how the presence of massive neutrinos affect halo formation. Here we study how CDM halo properties are altered by the presence of massive neutrinos, and we also present detailed results for the corresponding neutrino halos. This last point is important for example for understanding the prospects for a direct experimental detection of the cosmic relic neutrino background.

The paper is organised as follows: In Section 9.2 we present the numerical setup required for the analysis. In Section 9.3 we present results on halo profiles for both the neutrino and matter components. In Section 9.4 we discuss how the halo mass function is altered in models with massive neutrinos, and finally Section 9.5 contains our conclusions.

9.2 Numerical setup

9.2.1 Initial conditions and N-body simulations

Our N-body simulations are carried out using the modified version of the GADGET-2 code [26] described in [3]. The code utilises a hybrid scheme for simulating the neutrino component: All neutrinos with velocities much higher than the average gravitational flow velocities in the simulation are treated using linear perturbation theory, and their effect on the gravitational potential in the N-body simulation is included via a Fourier grid. At low redshift the low velocity neutrinos, with $q/T < 6$, are followed separately in 6 momentum bins by N-body particles (q is the comoving momentum and T the comoving temperature). In Fig. 9.4 it can be seen that the higher part of momentum space, $q/T > 6$, do not contribute to neutrino clustering in halos.

The initial conditions (ICs) for the CDM and neutrino components are generated with the same set of random numbers for a given box size. This reflects the assumption of adiabatic primordial ICs. The CDM distribution is followed with CAMB [94] until $z = 49$, where the Zel'dovich approximation [23] and a second-order correction calculated with second-order Lagrangian perturbation theory [25] are used to generate the CDM N-body particle initial displacements and gravitational flow velocities.

When the maximum thermal velocity of the first neutrino momentum bin, $q/T = 1$ (upper limit), has fallen below $f_{\rm flow} = 4$ times the average CDM gravitational velocity,[2] the low momentum neutrinos, which have non-linear clustering, are converted to N-body particles with the Zel'dovich approximation and followed with GADGET-2. The high velocity part is retained on the grid. The ICs for each bin are generated from a momentum dependent TF, and in addition to the gravitational flow velocities the neutrino N-body particles receive a thermal, Fermi-Dirac distributed, velocity corresponding to the particular bin. In effect we are simulating 6 different Hot Dark Matter components with different thermal properties. We employ a new timestep criterion for the neutrino component $\propto (1+z)/\Omega_\nu$.

The TF for each momentum bin is calculated with CAMB. By default CAMB uses 15 neutrino momentum bins, which is sufficient for sub-percent accuracy in the momentum *averaged* TFs. However, for our purpose, we need percent level accuracy in each individual momentum bin, and to ensure this we use a total of 480 individual TFs such that each of the 15 momentum bins is

[2]When the box size is increased the average CDM gravitational velocity increases as well due to extra large-scale velocity flows. As a result, the neutrino N-body particles are created earlier in large simulation volumes, and not due to larger non-linearities which of course would justify a larger conversion redshift. But this effect is small, at the order of 5% in redshift. Ideally, the velocities should be interpolated to a grid, Fourier transformed and then convolved with a window function eliminating large-scale velocity modes.

reconstructed from 32 separate TFs. See [3] for further information on the hybrid implementation of neutrinos in N-body simulations.

The hybrid method has the advantage that all neutrino masses can be simulated without compromising computational speed or accuracy (treating low mass neutrinos as particles leads to prohibitively high CPU time consumption[3] and particle shot noise, and, conversely, treating high mass neutrinos in linear perturbation theory leads to loss of accuracy). The code allows us to accurately calculate halo number densities and properties over a wide mass range. Since neutrinos cluster much less than CDM ultrahigh resolution is in most cases not necessary.[4] For example, since the neutrino halo profiles flatten at small r one does not encounter the same resolution problem as with CDM. Likewise there is hardly any neutrino halo substructure because neutrino halos are primarily formed by late time neutrino infall on already existing CDM structures.

Parameter setup We assume a standard flat cosmology with $h = 0.7$, $\sigma_8 = 0.878$ (for a model without massive neutrinos), $n_\mathrm{s} = 1$, $A_\mathrm{s} = 2.3 \cdot 10^{-9} (\Omega_m/0.3)^2$, $\Omega_b = 0.05$ and varying amounts of Ω_c and Ω_ν. In cosmologies with massive neutrinos we assume 3 degenerate neutrino species. We note that the exact parameter values are not that important since we want to understand the effect of neutrinos on halo properties and not perform a parameter estimation. Table 9.1 shows parameters for the various N-body simulations presented in this paper.

By running simulations in simulation volumes of 32, 128 and $256\,h^{-1}\,\mathrm{Mpc}$ we found that the neutrino halo profiles were almost identical in the latter two box sizes, and that the smallest box significantly affected the density profiles for the larger halos. In sum, we only present results for simulation volumes larger than $256\,h^{-1}\,\mathrm{Mpc}$.

We have chosen $f_\mathrm{flow} = 4$ as the criterion for creating neutrino N-body particles, which we have shown to be a reasonable value by comparing with simulations in which $f_\mathrm{flow} = 2$ and 8.

Finally, when we present matter density profiles for cosmologies with $\sum m_\nu = 0.15\,\mathrm{eV}$ and $0.3\,\mathrm{eV}$ neutrinos, only the homogeneous neutrino component has been added. This seems reasonable since these low mass particles contribute insignificantly to the overall matter density profile.

Fig. 9.1 shows the CDM and neutrino N-body particles in halos with different masses. Here, individual N-body particles can be identified, with small and bright particles lying in high density regions, and larger and darker particles in lower density areas.

Fig. 9.1 clearly illustrates the lack of neutrino particle statistics in halo centers. Neutrino clustering is determined by the combined effects of gravity and thermal velocity. The smaller the neutrino and the halo masses the less clustering. To simulate such small overdensities a very fine initial N-body particle grid is required. From the figure it can also be seen that only $q/T \lesssim 3$ trace the underlying CDM distribution on the scales shown, whereas structure in the higher momentum bins can only be seen on larger scales. This is also consistent with Fig. 9.4.

[3] Further investigations for an appropriate Courant timestep condition for the neutrino component could alleviate this problem.

[4] Ultrahigh resolution can be achieved by making zoom simulations, though for neutrinos the advantage of such a setup is smaller, since fast-moving neutrinos can easily leak out of the high-resolution region, and hence the initial volume of the zoomed neutrinos has to be considerably larger than the initial CDM volume (though a periodic volume around the halos could alleviate this problem at higher redshift).

	$N_{\rm CDM}$	$N_{\nu,\rm grid}$	$N_{\nu,\rm part}$	$q_{\rm cut}/T$	$f_{\rm flow}$	$R_{\rm BOX}$ [h^{-1}Mpc]	$\sum m_\nu$ [eV]	Ω_ν [%]	Ω_m [%]
A_1	512^3	0	0	0	-	256	0	0	30
A_2	512^3	512^3	0	0	0	256	0.15	0.325	30
A_3	512^3	512^3	0	0	0	256	0.3	0.65	30
A_4	512^3	512^3	$6\cdot512^3$	6	4	256	0.6	1.3	30
A_5	512^3	512^3	$6\cdot512^3$	6	4	256	1.2	2.6	30
B_1	512^3	0	0	0	-	1024	0	0	30
B_2	512^3	512^3	0	0	0	1024	0.15	0.325	30
B_3	512^3	512^3	0	0	0	1024	0.3	0.65	30
$B_3^{'}$	512^3	512^3	$6\cdot512^3$	6	4	1024	0.3	0.65	30
B_4	512^3	512^3	$6\cdot512^3$	6	4	1024	0.6	1.3	30
B_5	512^3	512^3	$6\cdot512^3$	6	4	1024	1.2	2.6	30
C_1	512^3	0	0	0	-	4096	0	0	30
C_2	512^3	512^3	0	0	0	4096	0.15	0.325	30
C_3	512^3	512^3	0	0	0	4096	0.3	0.65	30
C_4	512^3	512^3	$6\cdot512^3$	6	4	4096	0.6	1.3	30
C_5	512^3	512^3	$6\cdot512^3$	6	4	4096	1.2	2.6	30
D_1	512^3	0	0	0	-	256	0	0	28.7
D_2	512^3	0	0	0	-	1024	0	0	28.7
D_3	512^3	0	0	0	-	4096	0	0	28.7
E_1	512^3	0	0	0	-	256	0.6	1.3	30
E_2	512^3	0	0	0	-	1024	0.6	1.3	30
E_3	512^3	0	0	0	-	4096	0.6	1.3	30
E_4	512^3	0	0	0	-	256	0.6	1.3	30
E_5	512^3	0	0	0	-	1024	0.6	1.3	30
E_6	512^3	0	0	0	-	4096	0.6	1.3	30

Table 9.1: N-body simulation parameters: $N_{\rm CDM}$ and $N_{\nu,\rm part}$ are the number of CDM and neutrino N-body particles respectively, $N_{\nu,\rm grid}$ the size of the linear neutrino Fourier grid, $q_{\rm cut}/T$ the cut-off below which the neutrino component is converted to particles, and $f_{\rm flow}$ determines the redshift of this conversion. The simulation box size is represented by $R_{\rm BOX}$, $\sum m_\nu$ is the total neutrino mass roughly related to the neutrino density parameter, Ω_ν, by $\Omega_\nu = \sum m_\nu/(94\,h^2{\rm eV})$, with $\Omega_m = \Omega_c + \Omega_b + \Omega_\nu$. The exotic simulations E_{1-3} have no δ_ν in the N-body simulation, but the neutrinos are still included in the background evolution, while E_{4-6} have a CDM N-body particle mass corresponding to $\Omega_m = 0.3$ and the ICs are calculated from weighed CDM and baryon TFs from a cosmology with neutrinos included. The E-simulations have been performed to assess whether it is possible to achieve the desired accuracy with a model which is easier to implement and less demanding with respect to CPU time.

9.2.2 Halo finding

We use the Amiga Halo Finder (AHF) [95] to identify halos and their centers within the simulations. Only bound particles have been used to calculate halo centers and their virial radii. From the halo centers we calculate the matter and the neutrino halo profiles for halo masses of 10^{12}, 10^{13}, 10^{14} and $10^{15}\,{\rm M}_\odot$. We show matter halos and not CDM halos, since it is the former quantity which is the measurable one.

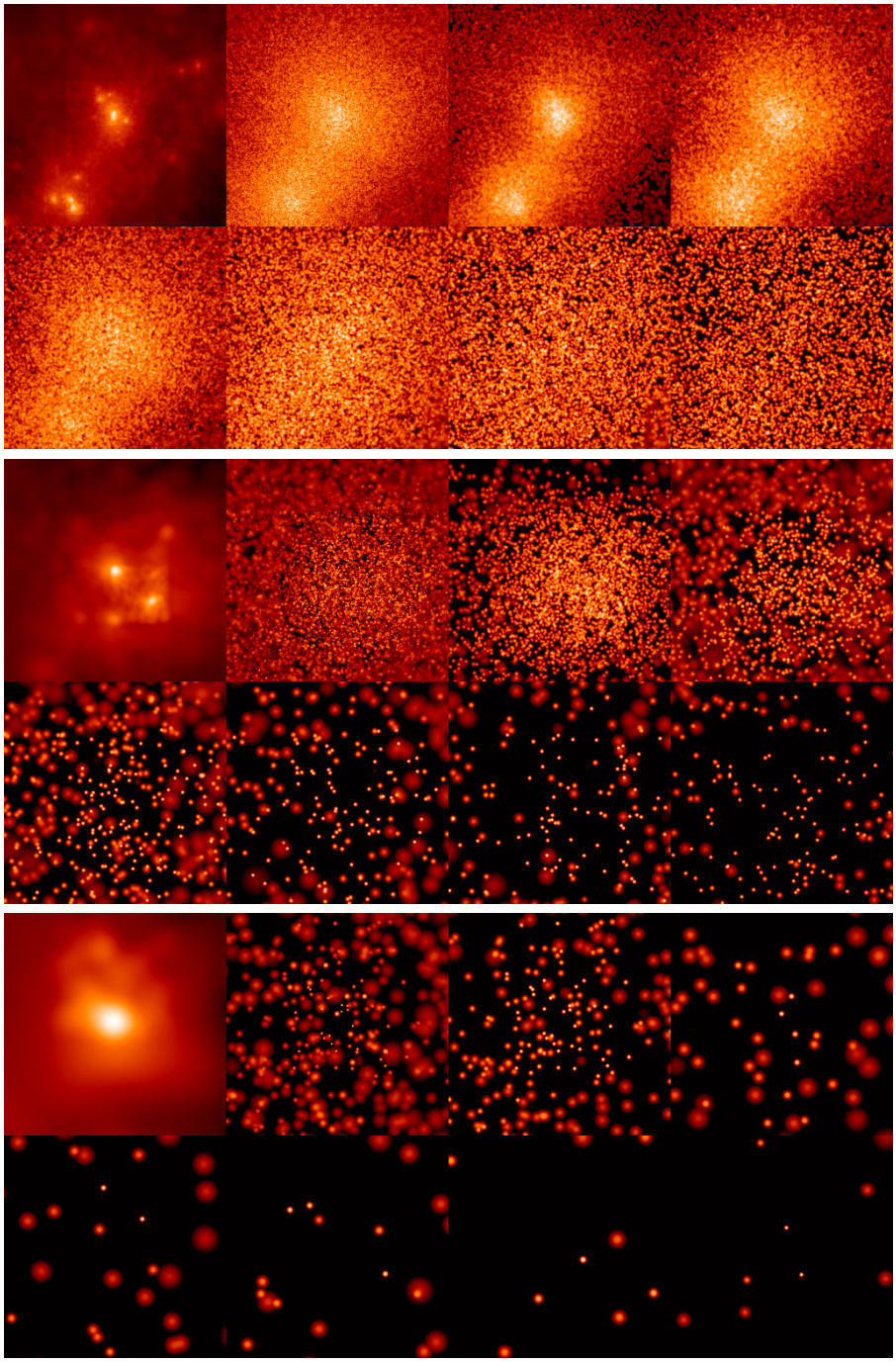

Figure 9.1: CDM and $\sum m_\nu = 1.2\,\mathrm{eV}$ neutrino distributions for halo masses $\simeq 5 \cdot 10^{14}\mathrm{M}_\odot$ (top), $\simeq 10^{14}\mathrm{M}_\odot$ (middle) and $\simeq 10^{13}\mathrm{M}_\odot$ (bottom), where the masses only correspond to the central halos in the upper two mosaics. Dimensions in each image are 5, 2 and 1 $h^{-1}\,\mathrm{Mpc}$, respectively. In each mosaic the images correspond to CDM, total neutrino, and $q/T = 1$ to 6 from top-left to bottom-right. Individual neutrino N-body particles can be identified.

We stack halos in mass bins with a bin width of 10% of the central halo mass. These widths are narrow enough to ensure a reliable halo profile calculation of the desired halo masses, while at the same time providing enough halos to stack. The N-body density profiles presented in this paper have been found by fitting a smooth curve through the data points, though we note that this is mainly important in the inner part of the neutrino density profiles for low neutrino and halo masses, where particle statistics is low.

Furthermore, to compare with the N-one-body method, we have only used halos with an average overdensity within the virial radius, $\Delta_{\rm vir}$, in the range $330 - 340$ for $\Omega_m = 0.3$ ($340 - 350$ for $\Omega_m = 0.287$). This criterion eliminates, e.g., gravitationally stripped halos with a very high central density.

9.2.3 The N-one-body method

The N-one-body method was introduced in [72]. It is a restricted method devised to solve, approximately, the (non-linear) collisionless Boltzmann equation for the neutrino phase space based on the following observation: In the limit $\rho_\nu \ll \rho_m$ density perturbations in the CDM fluid dominate the total gravitational potential, and not only will the CDM halo be gravitationally blind to the neutrinos, gravitational interaction between the neutrinos themselves will also be negligible. This allows us to treat the CDM halo as an external gravitational source, and compute the trajectory of each neutrino phase space element as a test particle moving in an external potential one at a time in N independent simulations. An obvious advantage of this technique is that it requires virtually no computing power when compared with a full scale N-body simulation with the same, large N, and is thus particularly useful for resolving the clustering of neutrinos on small scales.

In principle the N-one-body method can be applied to any given CDM density distribution. Here, however, we focus exclusively on spherically symmetric CDM halos whose density profiles are parameterised by fitting functions. Apart from possible deviations in the innermost cores, dark matter halos are well described by the universal Navarro-Frenk-White (NFW) profile [96], with a density given by

$$\rho_{\rm halo}(r) = \frac{\rho_{\rm s}}{(r/r_{\rm s})(1 + r/r_{\rm s})^2}, \tag{9.4}$$

where $\rho_{\rm s} = 4\rho(r_{\rm s})$ is a characteristic inner density at the characteristic radius $r_{\rm s}$. $r_{\rm s}$ is related to the virial radius $r_{\rm vir}$ via the concentration parameter c

$$c \equiv \frac{r_{\rm vir}}{r_{\rm s}}. \tag{9.5}$$

In a ΛCDM cosmology, a good analytical expression for the concentration parameter is [97]

$$c(z = 0) \simeq 9\left(\frac{M_{\rm vir}}{1.5 \times 10^{13} h^{-1}{\rm M}_\odot}\right)^{-0.13}, \tag{9.6}$$

where $M_{\rm vir}$ is the virial mass lying within $r_{\rm vir}$, and $c(z) \sim c(0)/(1 + z)$. We expect c to be smaller for cosmologies with neutrinos since the neutrinos free-stream out of the inner density cores and effect the halo formation process. Defining the average overdensity within $r_{\rm vir}$ to be $\Delta_{\rm vir}$, we have

$$M_{\rm vir} \equiv \frac{4\pi}{3}\Delta_{\rm vir}\bar{\rho}_{\rm m,0} r_{\rm vir}^3 = 4\pi\rho_{\rm s} a^3 r_{\rm s}^3 \left[\ln(1 + c) - \frac{c}{1 + c}\right], \tag{9.7}$$

so that a halo of a given mass is fully described in terms of its concentration parameter alone. The overdensity $\Delta_{\rm vir}$ can also be approximated by the overdensity at virialisation from the spherical top-hat collapse model,

$$\delta_{\rm th} \simeq \frac{18\pi^2 + 82[\Omega_m(z) - 1] - 39[\Omega_m(z) - 1]^2}{\Omega_m(z)}, \tag{9.8}$$

with $\Omega_m(z) = \Omega_m/(\Omega_m + \Omega_\Lambda a^3)$ [98]. For $\Omega_m = 0.3$, we find $\delta_{\rm th} \simeq 337$ ($\delta_{\rm th} \simeq 346$ for $\Omega_m = 0.287$), which explains why we only use the range $\Delta_{\rm vir} = 330 - 340$ $(340 - 350)$ when analysing N-body data.

We model the CDM distribution as a NFW halo sitting on top of a uniform distribution of CDM, i.e., the N-one-body method assumes that all halos are completely isolated. In order that the halo overdensity merges smoothly into the background density, we extend the NFW profile to beyond the virial radius. The initial neutrino distribution is taken to be spatially uniform,[5] with a momentum distribution described by relativistic Fermi-Dirac statistics. This initial distribution is divided into small chunks in both real and momentum space, and each chunk is allowed to move under the external potential of the CDM halo, but independently of each other. A low resolution run is first carried out for each set of neutrino and halo masses. All chunks that end up at $z = 0$ inside a sphere of radius 50 h^{-1} Mpc centered on the halo are traced back to their origin, subdivided into smaller chunks, and then re-simulated. The process is repeated until the inner ~ 10 h^{-1} kpc is resolved.

The N-one-body simulations are started at the same redshifts as when the neutrino N-body particles are created. This redshift is neutrino mass and halo mass dependent. Note that when comparing the density profiles with the two methods, the underlying CDM profiles are not identical, since the neutrino component do contribute to the gravitational potential and not least the halo merger history in the N-body simulations.

9.3 Halo structure

9.3.1 Neutrino clustering

The gravitational effect of a host halo or a nearby massive halo, which need not be the host halo, is relatively much more important for neutrinos than for the CDM component: Due to free-streaming neutrinos will almost completely stream out of small halos ($\simeq 10^{12}{\rm M}_\odot$), and any measured value $\delta_\nu > 0$ will be caused by the nearby massive object. The radial profile of δ_ν will therefore be a superposition of a dominant flat profile from the nearby massive object on top of a sub-dominant contribution from the $\simeq 10^{12}{\rm M}_\odot$ halo itself. This fact can be seen in Fig. 9.2.

Since it is the isolated halo profile that the N-one-body method calculates, we have found the neutrino density profiles from isolated halos in the N-body simulations. We used the criterion that for a halo to be considered isolated it should be separated by at least a certain distance from all heavier halos in the simulation. This distance should be at least 10 times the virial radius of these heavier halos. With this criterion the agreement between the two methods improves *significantly* for masses $\lesssim 10^{13}{\rm M}_\odot$, in effect confirming the robustness of both the N-body and the N-one-body methods. It can also be seen that for $\sum m_\nu = 0.3\,{\rm eV}$ there is a significant contribution to δ_ν even in

[5] We have run one N-body simulation where the neutrino particles were assigned homogeneous ICs, which in general confirmed the validity of this assumption.

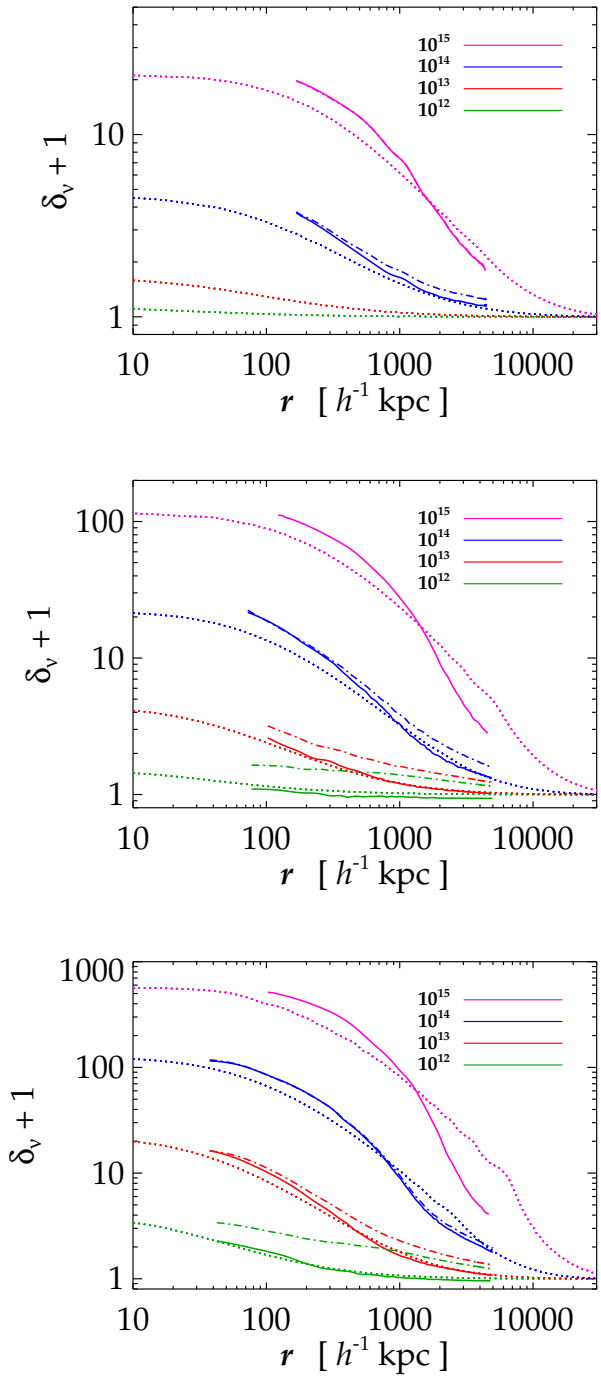

Figure 9.2: Neutrino halo profiles for $\sum m_\nu = 0.3\,\mathrm{eV}$ (top), $\sum m_\nu = 0.6\,\mathrm{eV}$ (middle) and $\sum m_\nu = 1.2\,\mathrm{eV}$ (bottom) for halo masses of 10^{12}, 10^{13}, 10^{14} and $10^{15}\,\mathrm{M}_\odot$. Profiles are calculated with the N-one-body method (dotted) and the N-body method with a halo isolation criterion (solid) and without (dot-dashed).

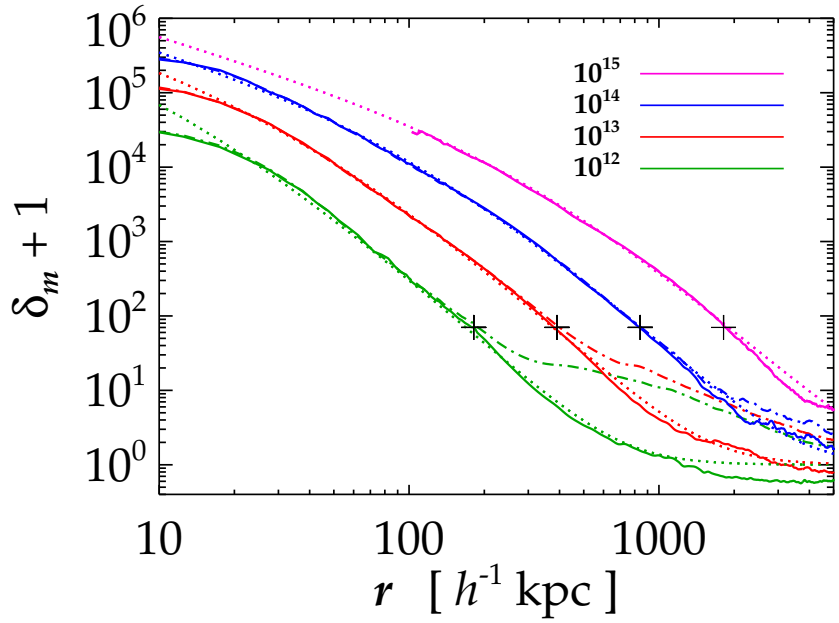

Figure 9.3: Halo profiles from N-body simulations for a model without massive neutrinos, with isolated halos (solid) and all halos (dot-dashed). The halo masses are 10^{12}, 10^{13}, 10^{14} and $10^{15}\,\mathrm{M}_\odot$. The profiles for the lowest 3 halo masses are taken from the $256\,h^{-1}\,$Mpc box and the profile for the most massive halo is taken from the $1024\,h^{-1}\,$Mpc box. NFW profiles are also shown (dotted), and the halo mass dependent virial radii are indicated by the '+' signs.

a $\simeq 10^{14}\mathrm{M}_\odot$ halo from heavier halos, which is not the case for more massive neutrino states. This is caused by the fact that as the neutrino mass decreases, neutrinos free-stream out of ever larger halos, so that the relative effect of even larger, more massive halos must be taken into account.

The effect of tidal truncation on the N-body halo profiles can easily be seen in Fig. 9.2. This effect is not included in the N-one-body approach. Furthermore, for the $10^{12}\mathrm{M}_\odot$ halos it can be seen that the neutrino density falls below its cosmic average beyond the virial radius. This could be due to either the presence of underdensities at particular distances from the halo centers, or due to the fact that we only select isolated halos, which are more likely to be found in low density regions.

From the pure ΛCDM N-body simulations presented in Fig. 9.3 it can be seen that our matter halos are perfectly fitted by a NFW profile over the mass range $M_{\rm vir} = 10^{12} - 10^{14}\mathrm{M}_\odot$ until $20\,h^{-1}\,$kpc from the halo centers. Here our N-body results begin to lack particle resolution. The profile for the larger halo mass is taken from a $1024\,h^{-1}\,$Mpc box with the same number of particles, and this halo is therefore only resolved until $\sim 100\,h^{-1}$kpc. Note that our dominant background NFW profiles in the N-body simulation are valid down to scales significantly smaller than the scales at which we present neutrino density profiles. Therefore, our neutrino density profiles are not affected by insufficient CDM N-body particle resolution.

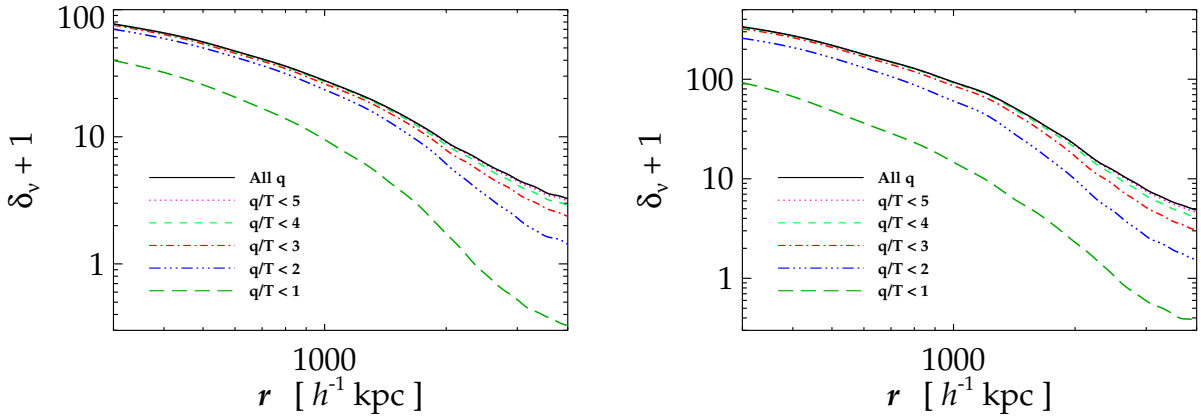

Figure 9.4: Cumulative neutrino halo density profiles, calculated with the N-body method, as a function of momentum in a $10^{15}\mathrm{M}_\odot$ halo, for $\sum m_\nu = 0.6\,\mathrm{eV}$ (left) and $\sum m_\nu = 1.2\,\mathrm{eV}$ (right). The neutrino density with $q/T > 6$ has been added as a homogeneous term to all profiles.

Since the CDM component is much more clustered than its neutrino counterpart, the flat profile from the host halo or a nearby massive halo is only dominant relative to the contribution from the halo itself on scales beyond the virial radius (see Fig. 9.3). From this figure it can also be readily understood why the neutrino density profiles differ when only low mass isolated halos are considered: The underlying CDM gravitational source term is roughly flat beyond the virial radius, and within the virial radius the neutrinos free-stream out of the small mass halos, in sum producing a roughly flat neutrino density profile also within the virial radius.

In Fig. 9.4 we show the cumulative neutrino density profile for a $10^{15}\mathrm{M}_\odot$ halo, for total neutrino masses of 0.6 eV (left) and 1.2 eV (right). It can be seen that only neutrinos with $q/T < 3$ contribute within the inner $1000\,h^{-1}\,\mathrm{kpc}$, whereas neutrinos with momenta up to $q/T \simeq 5$ is needed to simulate profiles beyond $\simeq 2000\,h^{-1}\,\mathrm{kpc}$. It can also be seen that as the neutrino mass is increased higher neutrino momentum bins contribute to neutrino clustering on a given scale. Finally, the figures confirm the accuracy of only converting neutrinos with $q/T < 6$ to N-body particles. Since this result is accurate for a $10^{15}\mathrm{M}_\odot$ halo, it is certainly also accurate for lower mass halos where only neutrinos with a momentum from the very low end of the Fermi-Dirac distribution cluster.

The Tremaine-Gunn bound Based on purely theoretical grounds one should expect the following scenario. Neutrinos cluster in a halo of given mass M_{vir} and radius r_{vir}, so that the escape velocity at r_{vir} of a given halo is

$$v_e \sim \sqrt{\frac{M_{\mathrm{vir}}}{r_{\mathrm{vir}}}}. \tag{9.9}$$

Only neutrinos up to this velocity can be bound in the halo and the central density should therefore be

$$\rho_\nu \sim \int_0^{v_e m_\nu} m_\nu p^2 f(p) dp. \tag{9.10}$$

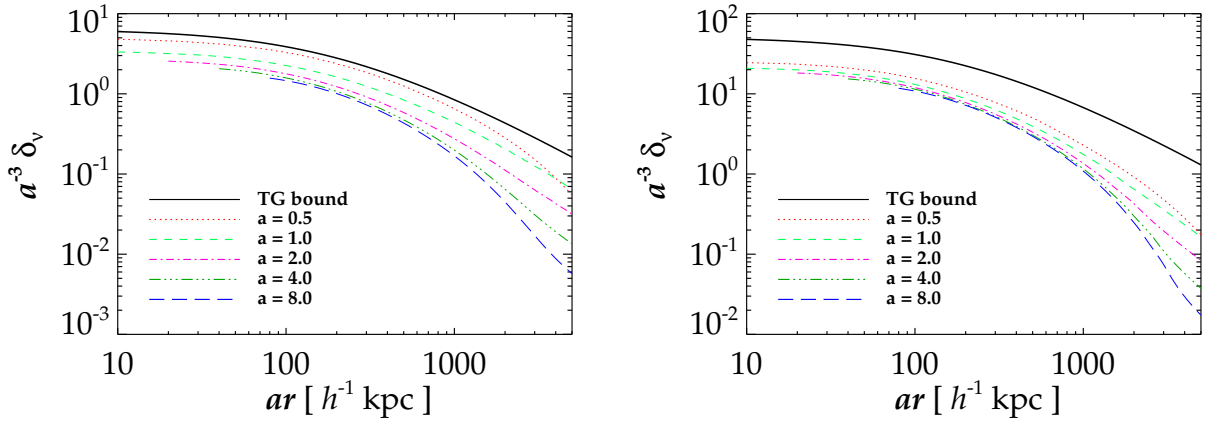

Figure 9.5: The evolution of the neutrino density profile, calculated with the N-one-body method, around a static NFW halo of $10^{14}\mathrm{M}_\odot$ for $\sum m_\nu = 0.3$ eV (left) and $\sum m_\nu = 0.6$ eV (right). The physical density perturbation, $a^{-3}\delta_\nu$, as a function of the physical radius, ar, is time-independent in the TG limit.

For small p, f is approximately $1/2$, and we have

$$\rho_\nu \sim \left(\frac{M_{\rm vir}}{r_{\rm vir}}\right)^{3/2} m_\nu^4, \tag{9.11}$$

leading to

$$\delta_\nu \sim \left(\frac{M_{\rm vir}}{r_{\rm vir}}\right)^{3/2} m_\nu^3. \tag{9.12}$$

This is the Tremaine-Gunn (TG) bound [99], and is essentially the same result quoted in Eq. (7.3) of [72] for a NFW halo.

However, in practice the neutrino halo density almost never saturates the Tremaine-Gunn bound, as was also seen in Fig. 7 of [72]. Fig. 9.5 sheds some light on the actual evolution of the neutrino halos. The setting is a simplified version of the N-one-body method in which the NFW halo is taken to be *static* so that the TG bound is time-independent in physical units. For the smallest neutrino mass $\sum m_\nu = 0.3$ eV, it can be seen that the physical density perturbations of neutrinos drop as the scale factor increases, stabilising only at $a \sim 4$. At early times, i.e., $a = 1/2$, the TG bound is almost saturated because the neutrino density contrast is low and the halo is populated only with neutrinos drawn from the very low momentum end of the relativistic Fermi-Dirac distribution for which $f \sim 1/2$. However, this also means that the final neutrino phase space density deviates little from the relativistic Fermi-Dirac distribution, so that linear perturbation theory remains valid. The dilution due to the background expansion dominates until very late and the physical neutrino density perturbation only approaches a constant at $a \sim 4$, and at a value much lower than the TG bound.

For the higher neutrino mass this effect is less pronounced, i.e., the physical density levels off much earlier. However, for the higher neutrino mass the TG bound is far from saturated even at early times. The reason for this can be understood from Fig. 9.4: For the higher neutrino mass, neutrinos with $q/T > 1$ make up most of the halo. However, since the initial neutrino phase

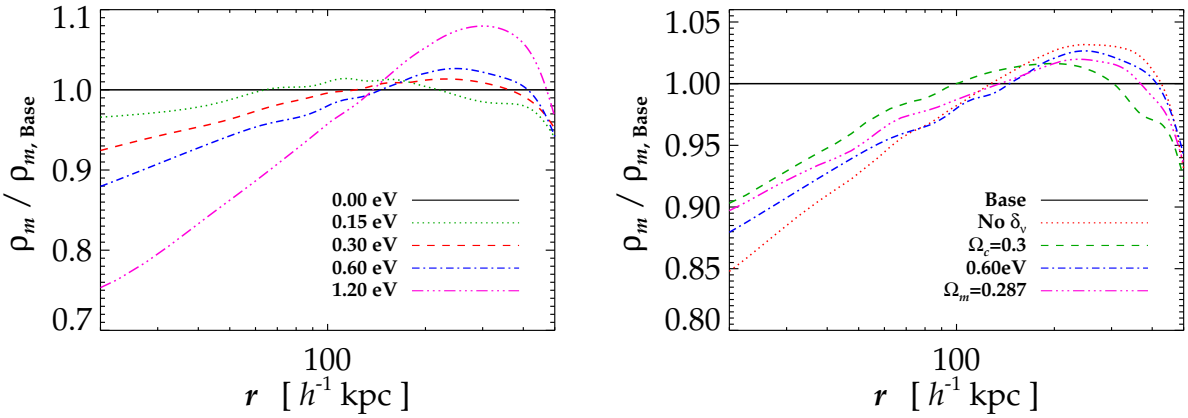

Figure 9.6: Change in the matter halo profiles relative to a base model without massive neutrinos for a halo mass of $10^{13}\,\mathrm{M}_\odot$. Left: As a function of neutrino mass. Right: For different (exotic) cosmologies (see details in text). All the results are based on N-body simulations.

space density is far less than 1/2 at $q/T > 1$, it also makes it more difficult for the final coarse-grained phase space density to reach the upper limit of $f \sim 1/2$ at the higher momentum end of the spectrum. For example, the second bin with $1 < q/T < 2$ has $\bar{f} = \int_1^2 f^2(q)q^2dq / \int_1^2 f(q)q^2dq \sim 0.18$.

9.3.2 Feedback on CDM halos

Even though neutrinos make up a minute fraction of the dark matter halo mass at late times, they do have an impact on the halo formation history, i.e., they affect the halo mass dependent merger rate [100]. In this section we are interested in alterations of the halo profiles, not the number density of halos in a given mass interval (i.e., the halo mass function). This aspect will be discussed in detail in Section 9.4.

Fig. 9.6 (left) shows the relative change of the matter halo density profile as a function of neutrino mass for a $10^{13}\,\mathrm{M}_\odot$ halo. We only show results for this halo mass, since here the product of the number density of halos times the halo density is maximal. From the figure it can be seen that the presence of massive neutrinos lowers the density at radii smaller than $\sim 100\,h^{-1}\,\mathrm{kpc}$. Since we compare halos of identical total masses this is compensated by an increased density at larger radii. The reason for this effect is that halos form later in models with massive neutrinos because the linear theory TF is lowered. From pure CDM simulations it is indeed known that late forming halos are less concentrated [101], with the concentration parameter scaling roughly as $c \propto 1/a_c$, where a_c is the scale factor at formation.

From the right hand side of Fig. 9.6 it can be seen that removing the neutrino perturbations (labelled $\delta_\nu = 0$) from a cosmology with $\sum m_\nu = 0.6\,\mathrm{eV}$ in the N-body simulation leads to less concentrated halos. On the scales shown the suppresion is as large as $3-4\%$, though we caution that there is some noise in the data. It can also be seen that replacing Ω_ν by an enlarged Ω_c (labelled $\Omega_c = 0.3$) when the N-body simulation is started gives a profile which is too steep at the few % level, as compared to the exact calculation (labelled $\sum m_\nu = 0.6\,\mathrm{eV}$). Finally, a cosmology with $\Omega_m = 0.287$ (labelled $\Omega_m = 0.287$) is placed somewhere between the aforementioned cosmologies.

9.4 The halo mass function

We now turn our attention to the number density of halos in a given mass interval, the halo mass function (HMF). All results presented in this section are based on N-body simulations. In Fig. 9.7 (top and middle figures) we show the HMFs for cosmologies with different neutrino masses. As expected the HMF is more suppressed in cosmologies with a larger neutrino mass. The suppression is largest for the heaviest, late forming halos.

The last panel in Fig. 9.7 shows that the cosmologies where the $\sum m_\nu = 0.6\,\mathrm{eV}$ neutrino component is replaced by CDM at the redshift where the N-body simulation is started as well as the one with $\Omega_m = 0.287$ predict HMFs with different shapes. Only a model without neutrino perturbations in the N-body simulation gives roughly the same result as the full calculation: The suppression of the HMF is mainly caused by the suppression of the initial TF in the linear regime and not by neutrino clustering effects in the N-body simulation.

In Fig. 9.8 we compare our HMFs calculated from N-body simulations with HMFs from the Sheth-Tormen (ST) semi-analytic formulae [102].[6] The ST fit is based on the fact that, as first pointed out by Press and Schechter [105], the HMF can be written as

$$\frac{M dM}{\bar{\rho}} \frac{dn(M,z)}{dM} = \nu f(\nu) \frac{d\nu}{\nu}, \tag{9.13}$$

with $\nu \equiv [\delta_{\rm sc}(z)/\sigma(M)]^2$, where $\delta_{\rm sc}(z) = 1.686$ is the overdensity required for spherical collapse at z, and $\bar{\rho} = \Omega_m \rho_c$. $dn(M,z)$ is the number density of halos in the mass interval M to $M + dM$. The variance of the linear theory density field, $\sigma^2(M)$, is given by

$$\sigma^2(M) = \int \frac{dk}{k} \frac{k^3 P_{\rm lin}(k)}{2\pi^2} |W(kR)|^2, \tag{9.14}$$

where $P_{\rm lin}(k)$ is the linear theory matter power spectrum, and the Top-Hat window function is given by $W(x) = (3/x^2)(\sin x - x\cos x)$ with $R = (3M/4\pi\bar{\rho})^{1/3}$.

The ST fit to $\nu f(\nu)$ is

$$\nu f(\nu) = A \left(1 + \frac{1}{\nu'^p}\right) \left(\frac{\nu'}{2}\right)^{1/2} \frac{e^{-\nu'/2}}{\sqrt{\pi}}, \tag{9.15}$$

with $\nu' = 0.707\nu$ and $p = 0.3$. $A = 0.3222$ is determined from the integral constraint $\int f(\nu) d\nu = 1$.

The upper panel in Fig. 9.8 shows that the agreement is poor if $\Omega_m = \Omega_c + \Omega_b + \Omega_\nu$ is used in the ST formalism. However, this is due to a wrong definition of the halo mass: Even for the very largest cluster halos the neutrino component contributes very little to the halo mass. In reality, the mass inside the collapsing region should be calculated using $\Omega_c + \Omega_b$, not Ω_m. This amounts to neglecting the weakly clustering neutrino component when calculating the halo mass. The two lower panels in Fig. 9.8 shows the same ST fit, but using $\Omega_c + \Omega_b$ instead of Ω_m. In this case the ST HMFs provide an excellent fit to the relative change to the HMF caused by neutrinos. As the figure at the bottom clearly demonstrates, the agreement is better than $\sim 3\%$ at halo mass scales where our N-body HMFs are accurate (we do not consider our N-body HMFs to be accurate by more than a few % on any mass scale, M). Although the absolute HMFs, even for CDM simulations, do not match the ST HMFs more precisely than at the $\sim 10\%$ level, the *relative* change from adding neutrinos can be calculated significantly more accurately.

[6] See [103, 104] for other semi-analytic fits to the mass function, which we found to work less well for models with massive neutrinos.

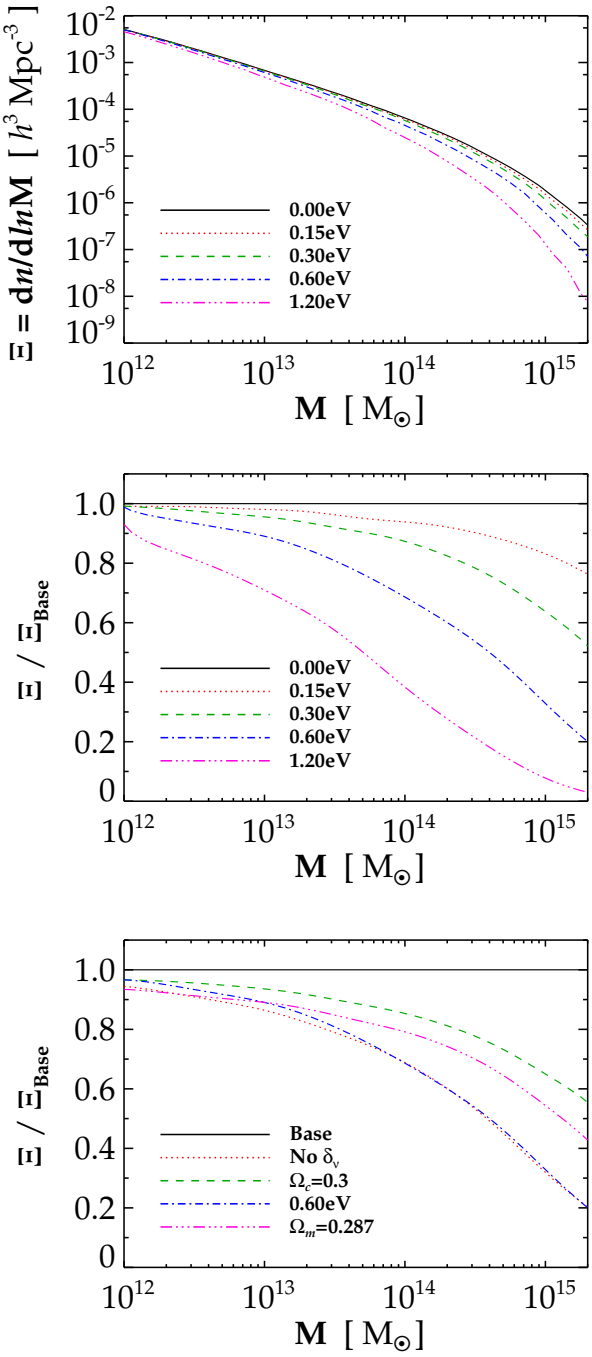

Figure 9.7: Absolute (top) and relative (middle) halo mass functions, $\Xi \equiv dn/d\ln M$, for 5 different neutrino cosmologies. The halo mass functions have been splined and smoothed together to obtain sufficient accuracy in the halo mass range 10^{12} to 10^{15} $M_\odot$. Bottom: Relative change in our halo mass function for different (exotic) cosmologies.

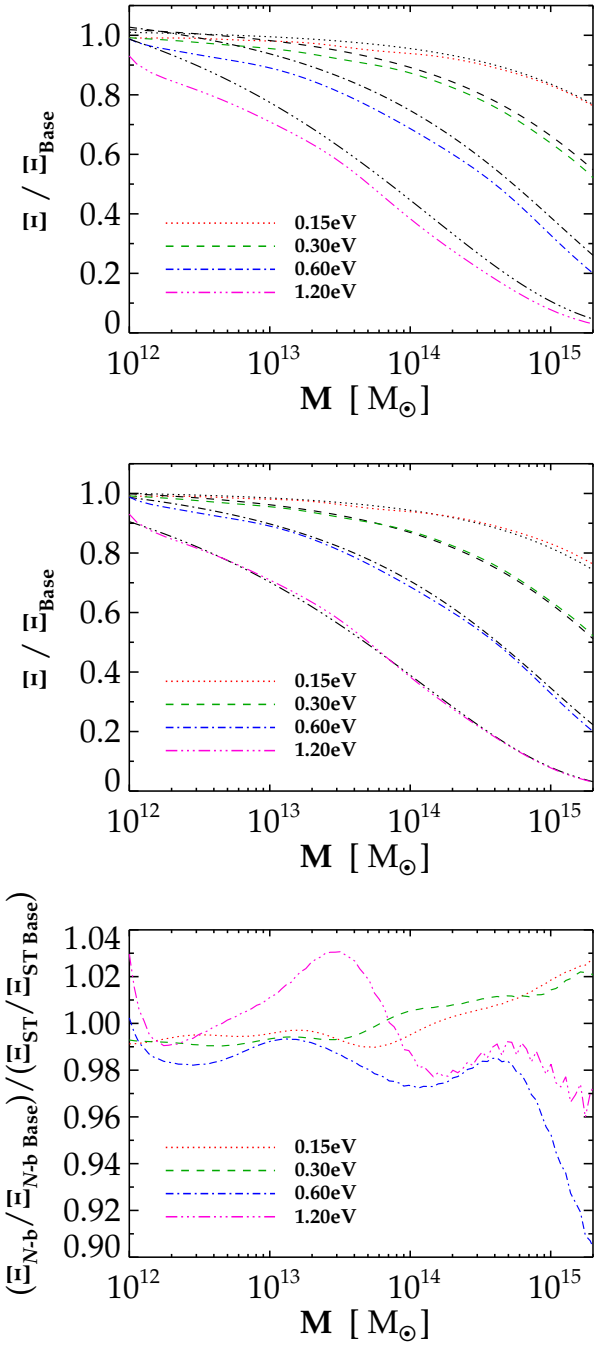

Figure 9.8: Relative halo mass functions for different neutrino cosmologies compared with the predictions from the Sheth-Tormen formulae (black lines). Top: With $\Omega_m = \Omega_c + \Omega_b + \Omega_\nu$ in the ST formulae. Middle: With $\Omega_c + \Omega_b$ used instead of Ω_m in the ST formulae. Bottom: Differences between the N-body and the ST predictions.

9.5 Conclusions

We have performed a detailed study of halo properties in ΛCDM cosmologies with massive neutrinos included. An important goal was to study the neutrino density profiles in dark matter halos. To this end we employed detailed N-body simulations across a wide range of scales to test halo masses from Milky Way size ($10^{12}\,\mathrm{M}_\odot$) to large clusters ($10^{15}\,\mathrm{M}_\odot$), as well as the N-one-body method developed to solve the neutrino Boltzmann equation approximately around existing CDM halos. In general we found good agreement between the full N-body and the N-one-body results. The difference between the N-body and N-one-body methods arise from the fact that the latter assumes the CDM halo to be monolithic and at all times describable in terms of a NFW profile, i.e., it does not take into account halo substructure and larger merger events. It also assumes an analytic evolution of the concentration parameter. We also discussed in some detail how the density profiles of neutrino halos can be understood in terms of the Tremaine-Gunn bound, i.e., the bound coming from the fact that a coarse-grained distribution can never attain values exceeding the maximum of the original fine-grained distribution.

For smaller halo masses, the neutrino profiles in isolated halos are in excellent agreement with the prediction from the N-one-body method. This result is not too surprising since this is exactly the case where the infall on an existing spherical NFW halo is most realistic. However, many smaller mass halos are embedded in larger cluster halos and for the smaller neutrino masses the local neutrino profile in such a halo is dominated by the background of neutrinos bound in the much larger cluster halos.

In terms of the local neutrino density enhancement, which is relevant for possible future attempts at direct CνB detection, a Milky Way-size galaxy halo is too small to have a significant overdensity, even when taking a possible cluster background into account.

We also briefly studied how neutrinos impact on the density profiles of the CDM halos. While neutrinos contribute very little to the total density in the halo, the presence of massive neutrinos in the model leads to slightly later formation of halos with a given mass and consequently to generally lower concentration parameters, c.

Finally, we calculated halo mass functions for ΛCDM models with massive neutrinos. Since large cluster surveys will become available in the coming years, the halo mass function is an important cosmological observable. As expected, we find a very strong suppression of halo formation with increasing neutrino mass. As noted in previous analytic or semi-analytic studies the suppression is particularly marked for massive halos because the suppression in linear theory power from massive neutrinos shifts the maximum cluster mass down, i.e. the scale beyond which the halo mass function is exponentially suppressed.

We then compared the halo mass functions from simulations with halo mass functions calculated using the semi-analytic method developed by Sheth and Tormen. If used naïvely, i.e. just processing the linear theory power spectrum without any adjustment to the method, the agreement is poor. However, it is easy to see that the disagreement arises because the ST method implicitly assumes that all matter clusters in the same way (the value of Ω_m used is $\Omega_c+\Omega_b+\Omega_\nu$). However, even large clusters bind relatively few neutrinos and for all halos it is true that neutrinos make a negligible contribution to the halo mass. If the ST formalism is corrected for this by using $\Omega_m = \Omega_c + \Omega_b$, i.e. taking into account only the clustering species (but of course using the correct initial power spectrum and the correct background evolution), the agreement between the modified ST and the N-body results is remarkable. On all measurable scales it is better than 2-3%. This is important for analysing future cluster surveys because it means that existing semi-analytic methods can be

used instead of having to perform time consuming simulations for all neutrino masses.

Alternatively, neglecting the neutrino perturbations in the N-body simulation will also be a very accurate approximation for $\sum m_\nu \lesssim 0.5\,\mathrm{eV}$ as long as only matter halo properties are considered. This approximation is not valid for a precise calculation of the matter power spectrum [1]. In general the accuracy of the approximation is determined by contrasting the neutrino free-streaming length with the physical extent of the scales simulated: Considering halo properties and realistic neutrino masses, this approximation is very good.

Acknowledgements

We acknowledge computing resources from the Danish Center for Scientific Computing (DCSC).

Chapter 10

The Cosmic Neutrino Background Anisotropy - Linear Theory

Steen Hannestad, Jacob Brandbyge

Abstract The Cosmic Neutrino Background (CνB) anisotropy is calculated for massive neutrino states by solving the full Boltzmann equation. The effect of weak gravitational lensing, including the Limber approximation, is also derived for massive particles, and subsequently applied to the case of massive neutrinos [5].

10.1 Introduction

The Cosmic photon Microwave Background (CMB) is currently our main source of information about the physical content of the Universe. Observations of the CMB anisotropy provides detailed information about the curvature of the Universe, the matter content, and a plethora of other parameters [106].

Standard model physics likewise predicts the presence of a Cosmic Neutrino Background (CνB) with a well defined temperature of $T_\nu \sim (4/11)^{1/3} T_\gamma$. While it remains undetected in direct experiments, the presence of the CνB is strongly hinted at in CMB data. The homogeneous CνB component has been detected at the 4-5σ level in the WMAP data (see e.g. [106, 107, 108, 109, 110, 111]). Furthermore, this component is known to be free-streaming, i.e. to have an anisotropic stress component consistent with what is expected from standard model neutrinos (see [112, 113, 114, 115, 116, 117, 118]). Finally the standard model neutrino decoupling history is also confirmed by Big Bang Nucleosynthesis (BBN), the outcome of which depends on both the energy density and flavour composition of the CνB.

While this indirect evidence for the presence of a CνB is important, a direct detection remains an intriguing, but almost impossible goal. The most credible proposed method is to look for a peak in beta decay spectra related to neutrino absorption from the CνB [119, 120, 121], although many other possibilities have been discussed [72, 122, 123, 124, 125, 126, 127, 128]. The neutrino absorption method was first investigated by Weinberg [119], based on the possibility that the primordial neutrino density could be orders of magnitude higher than normally assumed due to

the presence of a large chemical potential. Although a large chemical potential has been ruled out because it is in conflict with BBN and CMB [129, 130, 131, 132, 133], the method may still work and recently there has been renewed interest in detecting the CνB using beta unstable nuclei.

Although the direct detection of the CνB is already very challenging, one might speculate on the possibility that in the more distant future anisotropies in the CνB will be detectable. For massless neutrinos the calculation of the CνB proceeds in a way which is almost identical to the standard CMB calculation. The massless CνB anisotropy spectrum was first presented in [134] and subsequently calculated in [135] in a highly simplified way which contains some, but not all of the essential physics.

For massive neutrinos the calculation is much more complicated, and the CνB anisotropy is changed considerably: If the mass is sufficiently high, neutrino velocities can be as low as the escape velocities of galaxies. In this case the CνB is entirely determined by non-linear gravitational clustering. The current thermal velocity of a non-relativistic homogeneous neutrino background is given roughly by $\langle v \rangle \sim 1500\,\mathrm{km\,s^{-1}} \left(\frac{0.1\,\mathrm{eV}}{m_\nu}\right)$, which should be compared to gravitational streaming velocities which are up to $\sim 1000\,\mathrm{km\,s^{-1}}$. For small masses (i.e. non-degenerate, $m_\nu \lesssim 0.1$ eV) it is possible to make a calculation which is analogous to what is done for the CMB. As will be explained later the CνB spectrum is shifted to larger angular scales, mainly because the much shorter distance to the neutrino last scattering surface changes the relation between angular scales and length scales. Furthermore the amplitude of the anisotropy greatly increases at small multipoles because the gravitational source term becomes much more important as neutrinos become increasingly non-relativistic at late times.

In addition to this change in the primary CνB spectrum, the effect of gravitational lensing is also very different from the case of massless neutrinos. As is the case for the primary spectrum, gravitational lensing becomes increasingly important at low l as the mass increases. A detailed calculation of the lensing of massive neutrinos is presented in section 3. First, however, we derive the necessary equations for the primary CνB anisotropy in section 2 and present a numerical calculation of the CνB power spectra for different masses. In section 4 we combine the results of sections 2 and 3 to derive the form of the lensed massive CνB. Finally, section 5 contains a discussion of our results and our conclusions.

10.2 The primary CνB

10.2.1 Theory - The Boltzmann equation

The evolution of any given particle species can be described via the Boltzmann equation. Our notation is similar to that of Ma and Bertschinger [9] (see 2.3.3 for further details).

We write the distribution function as

$$f(x^i, q, n_j, \tau) = f_0(q)[1 + \Psi(x^i, q, n_j, \tau)], \tag{10.1}$$

where $f_0(q)$ is the unperturbed distribution function. For a fermion which decouples while relativistic, this distribution function is

$$f_0(q) = [\exp(q/T_0) + 1]^{-1}, \tag{10.2}$$

where T_0 is the present-day temperature of the species.

In conformal Newtonian (longitudinal) gauge the Boltzmann equation for neutrinos can be written as an evolution equation for Ψ in k-space [9]

$$\frac{1}{f_0}L[f] = \frac{\partial\Psi}{\partial\tau} + ik\frac{q}{\epsilon}\mu\Psi + \frac{d\ln f_0}{d\ln q}\left[\dot{\phi} - ik\frac{\epsilon}{q}\mu\psi\right] = 0, \tag{10.3}$$

where $\mu \equiv n^j\hat{k}_j$ and ψ and ϕ are the metric perturbations.

The perturbation to the distribution function can be expanded as follows

$$\Psi = \sum_{l=0}^{\infty}(-i)^l(2l+1)\Psi_l P_l(\mu), \tag{10.4}$$

so that the collisionless Boltzmann equation can be written as a moment hierarchy for the Ψ_l's as

$$\dot{\Psi}_0 = -k\frac{q}{\epsilon}\Psi_1 - \dot{\phi}\frac{d\ln f_0}{d\ln q}, \tag{10.5}$$

$$\dot{\Psi}_1 = k\frac{q}{3\epsilon}(\Psi_0 - 2\Psi_2) - k\frac{\epsilon}{3q}\psi\frac{d\ln f_0}{d\ln q}, \tag{10.6}$$

$$\dot{\Psi}_l = k\frac{q}{(2l+1)\epsilon}(l\Psi_{l-1} - (l+1)\Psi_{l+1}) \ , \ l \geq 2. \tag{10.7}$$

By integrating the neutrino perturbation over momentum

$$F_{\nu l} = \frac{\int dq q^2\epsilon f_0(q)\Psi_l}{\int dq q^2\epsilon f_0(q)}, \tag{10.8}$$

one finds a set of equations equivalent to those used to follow the perturbations in photons or massless neutrinos, i.e a set of equations for $F_{\nu l}$.

The distortion to the sky intensity can also be found using the perturbation to the temperature, Θ, related to the distribution function via

$$f(q) = [\exp(q/[T_0(1+\Theta)] + 1]^{-1}. \tag{10.9}$$

Equating Eqs. (10.1) and (10.9), Ψ and Θ are related by

$$\Theta(q) = -\left(\frac{d\ln f_0}{d\ln q}\right)^{-1}\Psi(q). \tag{10.10}$$

Since the transformation between Ψ and Θ is mass-independent, the normalisation of the angular power spectrum is not significantly affected. [135] used the transformation $-\left(\frac{d\ln f_0}{d\ln\epsilon}\right)^{-1}$ which introduces an extra factor of v^2 relative to our definition. The v^2 factor, by construction, suppresses the perturbations for the higher neutrino masses significantly.

By substituting Θ into the Boltzmann equation, Eq. (10.3), it can be seen that Θ is q-independent in the massless case. For massless particles it is therefore convenient to calculate the angular power spectrum of the temperature perturbation. For massive particles Θ is q-dependent giving rise to spectral distortions in the temperature field. Since it is convenient to have results similar to the CMB in the massless neutrino case we calculate the massive neutrino anisotropy spectrum of the quantity $\Theta_l(q)$ related to $\Theta_{\nu l}$ by

$$\Theta_{\nu l} = \frac{\int dq q^2\epsilon f_0(q)\Theta_l(q)}{\int dq q^2\epsilon f_0(q)}. \tag{10.11}$$

Of course, the quantity which is actually measurable will depend on the type of experiment used. A typical experiment will measure either a number flux, a momentum flux, or a kinetic energy flux as a function of angle. For massless particles these quantities are trivially related by a momentum independent number, i.e. the number flux anisotropy is $3\Theta_{\nu l}$ and the momentum/energy flux anisotropy is $F_{\nu l} = 4\Theta_{\nu l}$. For massive particles this is no longer true and one must calculate the appropriate quantity for any given experiment.

Similarly to the photon case one can then construct the CνB sky brightness fluctuation angular power spectrum as

$$C_l^{\Theta}(q) = (4\pi)^2 \int k^2 dk P_I(k) \Theta_l^2(q,k). \tag{10.12}$$

Here $P_I(k)$ is the primordial potential fluctuation power spectrum, $P_I(k) \propto k^{n-4}$. Throughout the paper we assume a flat Harrison-Zel'dovich spectrum so that $n = 1$ with cosmological parameters $(\Omega_b,\ \Omega_m,\ \Omega_\Lambda,\ h,\ A_s) = (0.05,\ 0.3,\ 0.7,\ 0.7,\ 2.3{\cdot}10^{-9})$. As can be seen, a given l gets contributions from all k. The extra q-dependence arises because in principle one should perform the q-dependent lensing of $C_l^{\Theta}(q)$ in q-bins. The total C_l^{Θ} is found by averaging over momenta at the present time τ_0

$$C_l^{\Theta} = \left[\frac{\int dq q^2 \epsilon(\tau_0, q) f_0(q) \sqrt{C_l^{\Theta}(q)}}{\int dq q^2 \epsilon(\tau_0, q) f_0(q)} \right]^2 . \tag{10.13}$$

C_l^{Θ} does not include lensing, since the second-order term encoding deflections has been left out of the Boltzmann equation. Note that mapping the neutrino anisotropic sky in different momentum bins (anisotropic neutrino momentum tomography) will probe structures at different spacial distances from us. Furthermore, the observed CνB will be a superposition of the spectra for each individual neutrino mass.

10.2.2 Gauge effects

As noted we use the conformal Newtonian gauge, since this gauge is directly related to physically measurable quantities. In the Synchronous gauge the velocity perturbation, θ, for the CDM component is, by definition, zero. Therefore θ_ν, which is a momentum integral over Ψ_1, is a gauge dependent quantity. In contrast, the anisotropic stress, which is a momentum integral over Ψ_2, is a gauge independent quantity. Since all moments Ψ_l with $l > 2$ is recursively related to Ψ_2, these higher order moments are gauge independent as well.

Since we cannot separate the CMB/CνB dipole from our own peculiar motion, we are only interested in modelling the C_l^{Θ}'s with $l \geq 2$ when comparing with observations. But C_1, the lowest mode containing physically relevant information, is gauge dependent. We have taken this into account by working in the physical conformal Newtonian gauge.

We also note that the transfer functions are gauge dependent, though for the Synchronous and conformal Newtonian gauges they are almost identical inside the horizon for the massive components. Therefore we have calculated the transfer functions used to get the lensing contribution in the Synchronous gauge with CAMB [12].

10.2.3 Numerical results

We have used the COSMICS code [136] to solve the Boltzmann hierarchy for the neutrinos. In practise we have solved the system going up to $l = 500$ with 64 bins in q, equally spaced from

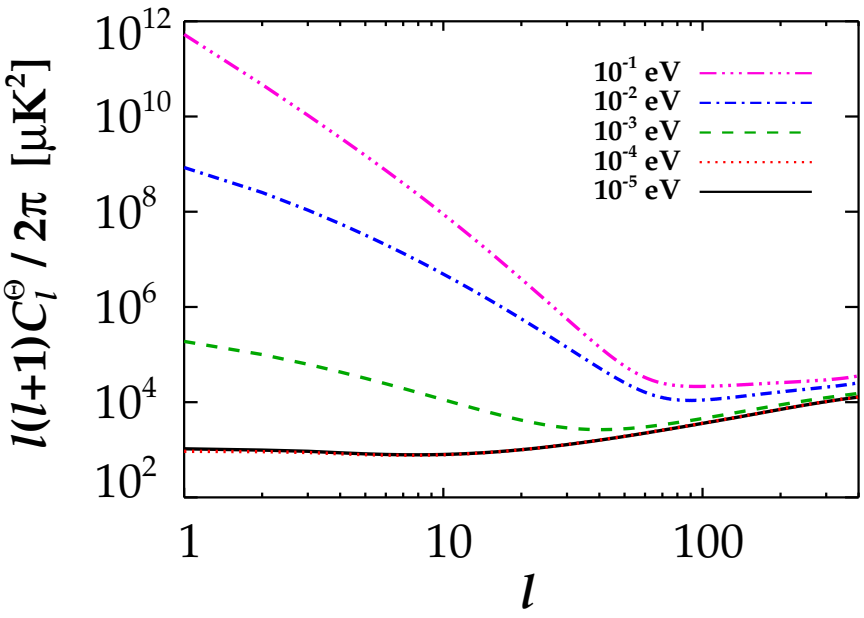

Figure 10.1: Primary CνB spectrum for different neutrino masses.

$q/T_0 = 0$ to 15. In Fig. 10.1 we show results for C_l^Θ for various masses and Fig. 10.2 shows sky map realisations for these spectra.

The massless case (i.e. 10^{-5} eV) is consistent with the result of [134]. At high l the spectra are almost identical, and do not depend on the neutrino mass. The reason for this can be understood from the following argument: Above a certain k-value, $k_{\rm FS}$, neutrinos are completely dominated by free-streaming and this k-value is proportional to m_ν. In order to convert this to an l-value one then uses the relation $l_{\rm FS} \sim k_{\rm FS}\chi^*$ (where χ^* is the comoving coordinate from which the neutrinos originate) and since $\chi^* \propto m_\nu^{-1}$ for non-relativistic particles [138], $l_{\rm FS}$ does not depend on m_ν. Inserting numbers one finds $l_{\rm FS} \sim 100$ which is in good agreement with Fig. 10.1. At smaller angular scales, $l \gtrsim l_{\rm FS}$, the anisotropy comes from the Sachs-Wolfe effect during radiation domination.

For smaller l-values the anisotropy increases dramatically as the mass increases. This can be understood as follows. As soon as neutrinos go non-relativistic the $\frac{\epsilon k}{3q}\psi\frac{d\ln f_0}{d\ln q}$ term in $\dot\Psi_1$ begins to dominate the Boltzmann hierarchy evolution. This quickly makes the higher l modes increase as well, and the final amplitude simply depends on the time elapsed after neutrinos go non-relativistic.

The effect can be seen in Fig. 10.3 which shows the evolution of Ψ_1, Ψ_2 and Ψ_{10} for three different neutrino masses and two different k-values. As soon as neutrinos go non-relativistic Ψ_1 immediately begins to grow, and the higher Ψ_l's follow with a slight delay for $k = 0.1\,h\,{\rm Mpc}^{-1}$. This exactly matches the low l behaviour seen in Fig. 10.1. Note also the behaviour of Ψ_{10} for $k = 0.01\,h\,{\rm Mpc}^{-1}$ and $m_\nu = 0.1$ eV. For this mass and k-value, the q/ϵ term in the $\dot\Psi_l$ equations becomes sufficiently important to suppress the propagation of the gravitational source term to high

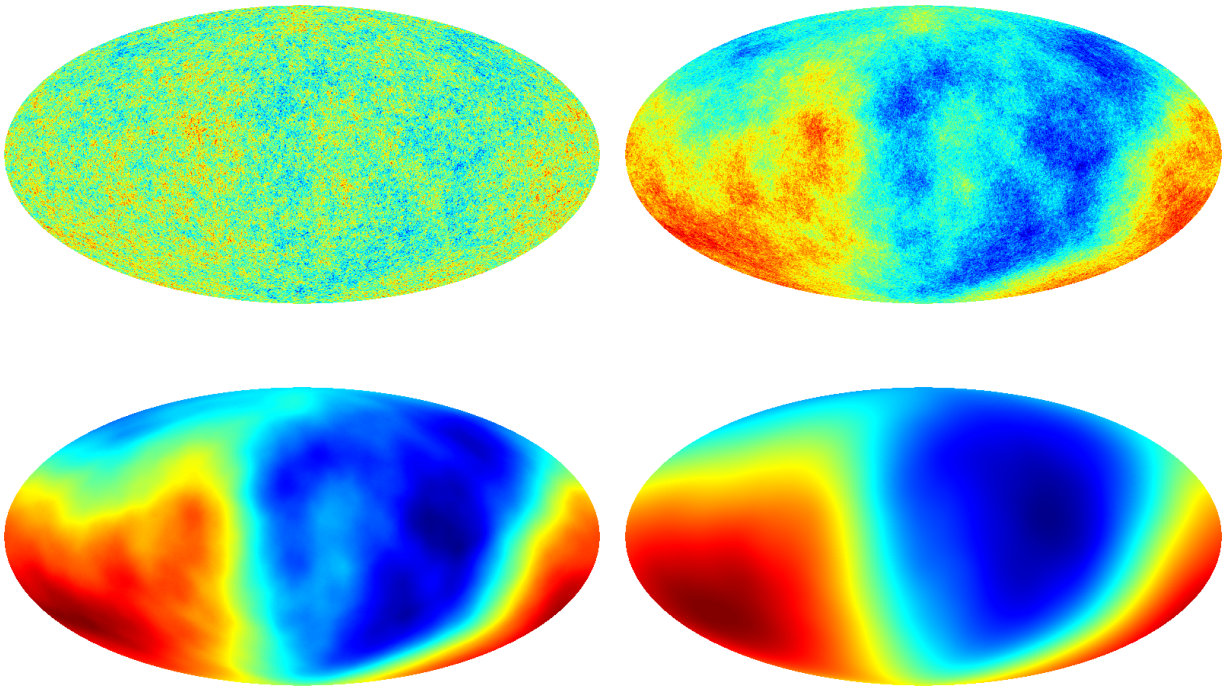

Figure 10.2: Sky maps of the primary neutrino power spectra, C_l^Θ, with the dipole included, for $m_\nu = 10^{-5}$ eV (top-left), 10^{-3} eV (top-right), 10^{-2} eV (bottom-left) and 10^{-1} eV (bottom-right). The maps have been generated with the same underlying random numbers with the HEALPIX package [137].

l. At higher k this is no longer true.

For high mass neutrinos ($\gtrsim$ 0.1eV) gravitational distortion is so strong that the dominant contribution comes from the local galactic and/or cluster halo. This case is similar to the study of the WIMP flux anisotropy and requires N-body simulations [3]. This will be treated separately in a later paper while in the present paper we limit ourselves to the framework of linear theory.

10.3 The lensing distortion

10.3.1 Theory

For strictly massless neutrinos the lensing distortion is identical to that for photons [139, 140, 141]. The change in angle $d\alpha$ per unit path $d\chi$ is proportional to the transverse derivative of the gravitational potential, ψ,

$$\frac{d\alpha}{d\chi} = -2\nabla_\perp \psi, \tag{10.14}$$

where $\nabla_\perp \psi$ is the component perpendicular to the line of sight. Relaxing the assumption of relativistic particles and solving the geodesic equation for a neutrino propagating in a weak potential,

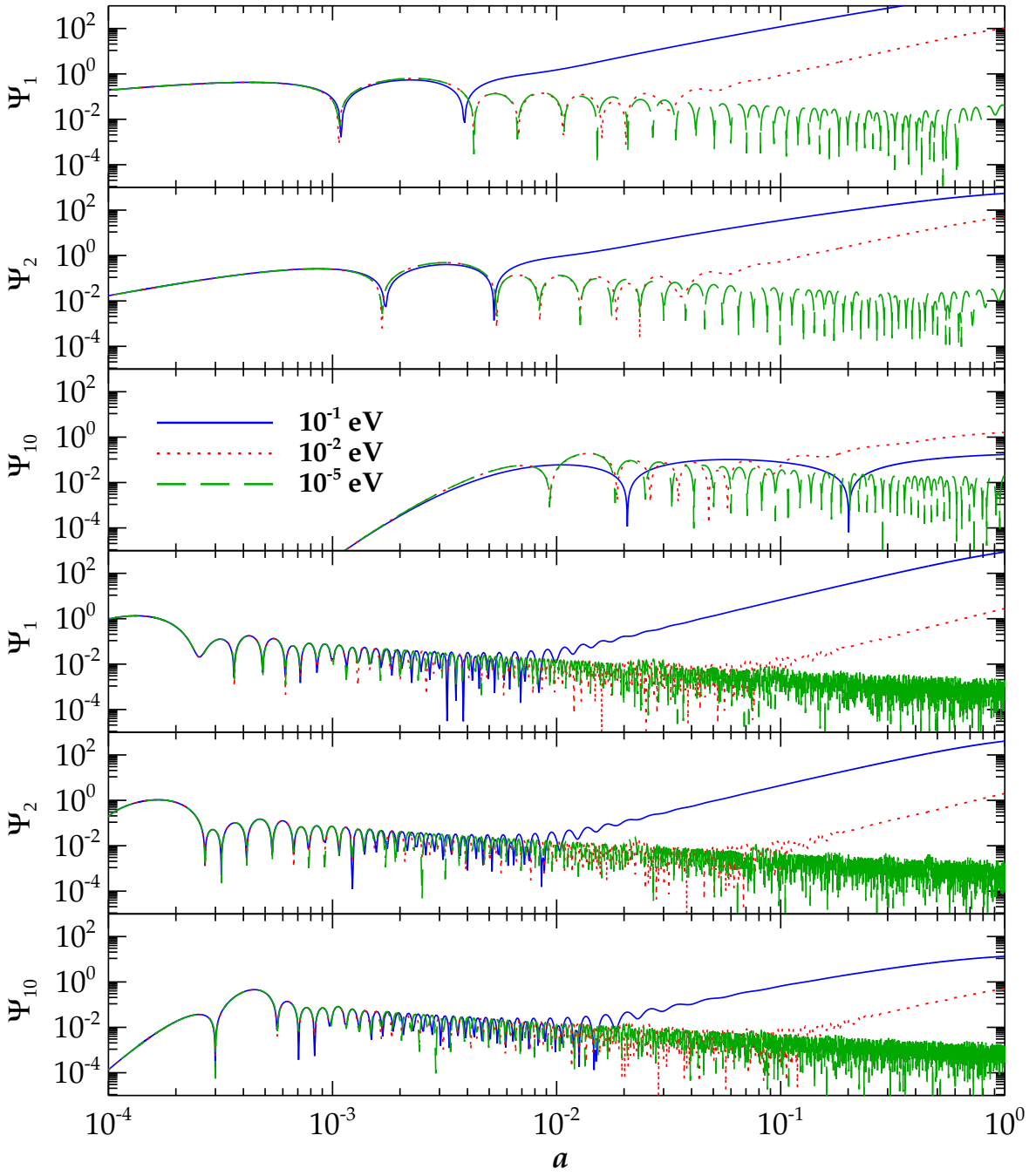

Figure 10.3: Ψ_l's for 3 neutrino masses with momentum $q/T_0 = 3$ as a function of the scale factor. The upper three panels are for $k = 0.01\,h\,\mathrm{Mpc}^{-1}$ and the lower three panels for $k = 0.1\,h\,\mathrm{Mpc}^{-1}$.

one arrives at the result

$$\frac{d\alpha}{d\chi} = -\frac{1+v^2}{v}\nabla_\perp \psi. \tag{10.15}$$

Note that this result reduces to the ordinary Newtonian expression $\frac{d\alpha}{dx} = -\frac{1}{v}\nabla_\perp\psi$ in the limit $v \to 0$. It should also be noted that the expression diverges as $v \to 0$ because the assumption $v > v_{\rm esc}$ is violated, i.e. particles with low velocity will be gravitationally bound in the potential.

From Eq. (10.15) we can calculate the distortion spectrum in a manner similar to what is done for the usual gravitational lensing spectrum. This is done with the assumption of Gaussian perturbations and using the Born approximation [141].

The total deflection angle $\boldsymbol{\alpha}$ is related to the lensing potential, Π, by

$$\boldsymbol{\alpha} = \nabla_{\hat{\mathbf{n}}}\Pi. \tag{10.16}$$

In a flat universe the normal formula for the angular lensing power spectrum, $\langle \Pi_{lm}\Pi^*_{l'm'}\rangle = \delta_{ll'}\delta_{mm'}C_l^\Pi$, is given by

$$C_l^\Pi = 16\pi \int \frac{dk}{k}\left[\int_0^{\chi^*} d\chi \mathcal{P}_\psi^{1/2}(k,\tau_0-\chi) j_l(k\chi)\left(\frac{\chi^*-\chi}{\chi^*\chi}\right)\right]^2, \tag{10.17}$$

derived using Eq. (10.14). Here the power spectrum, $\mathcal{P}_\psi$, is related to the ordinary matter power spectrum in the density contrast by $\mathcal{P}_\psi \propto a^{-2}P_m/k$. χ^* is the conformal distance at which the photons (or neutrinos) decoupled, taken to be a single source sphere, and j_l is a spherical Bessel function. $j_l(k\chi)(\chi^*-\chi)/(\chi^*\chi)$ is an effective window function, which distributes power in k-space along the particle trajectory to angular l-space.

However, several changes are necessary when particles are allowed to have mass. The relation $d\chi = -d\tau$ must be replaced with $d\chi = -vd\tau$ (the minus sign accounts for the fact that time and space run in different directions, i.e. $\int_0^{\chi^*} d\chi \sim \int_{\tau_0}^{\tau^*} d\tau$ with $\tau^* \simeq 0$, so that the observer is at the origin). In addition, the power spectrum $\mathcal{P}_\psi(k,\tau_0-\chi)$ should be replaced by $\mathcal{P}_\psi(k,\tau)$. With these modifications, the expression for massive particles becomes

$$C_l^\Pi(q) = 4\pi \int \frac{dk}{k}[\Delta_l^\Pi(q,k)]^2, \tag{10.18}$$

with

$$\Delta_l^\Pi(q,k) = \int_0^{\tau_0} d\tau \Delta_l^\Pi(q,k,\tau), \tag{10.19}$$

and

$$\Delta_l^\Pi(q,k,\tau) = [1+v^2(q,\tau)]\mathcal{P}_\psi^{1/2}(k,\tau) j_l(k\chi(q,\tau))\left[\frac{\chi^*(q)-\chi(q,\tau)}{\chi^*(q)\chi(q,\tau)}\right], \tag{10.20}$$

where $v(q,\tau) = q/\epsilon = 1/\sqrt{1+a^2(\tau)m^2/q^2}$. χ^* is now momentum dependent since neutrinos with different velocities have different distances to their respective last scattering surfaces, though they still scattered at the same time τ^*.

We calculate an average quantity of the lensing power spectrum found by doing an energy average over the $C_l^\Pi(q)$'s

$$C_l^\Pi = \left[\frac{\int dq q^2 \epsilon(\tau_0,q) f_0(q)\sqrt{C_l^\Pi(q)}}{\int dq q^2 \epsilon(\tau_0,q) f_0(q)}\right]^2. \tag{10.21}$$

Using the orthogonality of the Bessel functions together with the fact that they pick out the scale $k \simeq l/\chi$ at high l, the high l limit of the above equations reduce to the Limber approximation

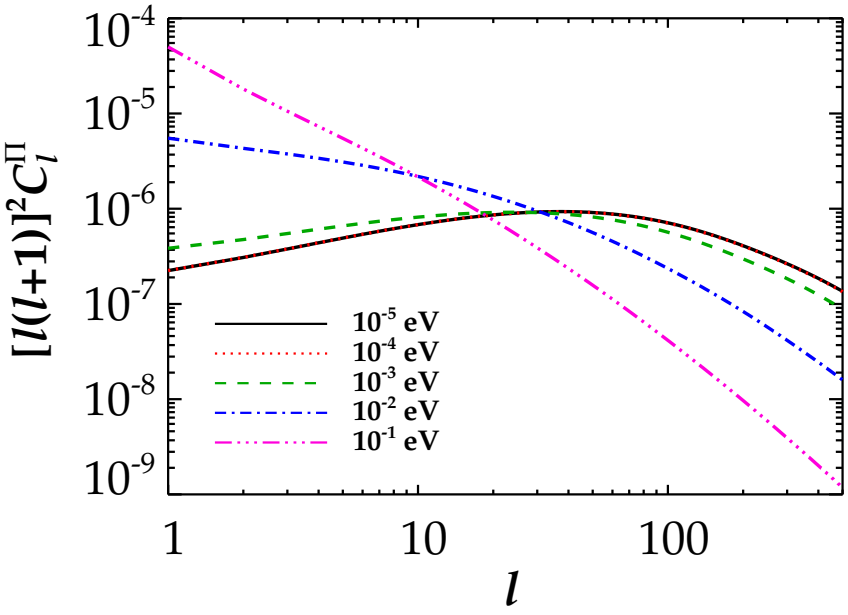

Figure 10.4: The lensing potential angular power spectrum, C_l^{Π}, for 5 different neutrino masses.

(see e.g. [142, 143]) for massive particles

$$C_l^{\Pi}(q) \simeq \frac{2\pi^2}{l^3}\int_0^{\tau_0} d\tau \frac{\chi}{v}[1+v^2]^2 \mathcal{P}_\psi(l/\chi,\tau)\left[\frac{\chi^*-\chi}{\chi^*\chi}\right]^2. \tag{10.22}$$

For $l \gtrsim 100$ this approximation is very good for all masses simulated.

10.3.2 Numerical results

In Fig. 10.4 we show $l^2(l+1)^2C_l^{\Pi}$ for various neutrino masses[1], all in a ΛCDM background model, and Fig. 10.5 shows realisations of these spectra. We have done the calculation in linear theory only. As can be seen, for higher neutrino masses the lensing distortion peaks at lower l because a given k-scale corresponds to lower l when $v < c$. Basically there is no contribution from modes with $k \lesssim l/\chi^*$. This also means that for higher masses C_l^{Π} picks up a much larger contribution from high k. This can be seen explicitly in Fig. 10.6 which shows the contribution to C_l^{Π} from various scales. For the higher masses there are significant high-k contributions to lensing already at low l.

From the Limber approximation it is also straightforward to understand how C_l^{Π} changes with neutrino mass. At high l, very approximately we can set $v \propto \chi$ in Eq. (10.22), which means that $\frac{\chi}{v}\left[\frac{\chi^*-\chi}{\chi^*\chi}\right]^2 \propto 1/\chi^2$. The potential power spectrum changes from $\mathcal{P}_\psi(l/\chi,\tau) \sim$ *Const.* at low l to

[1]Compared to C_l^{Θ} their is an extra factor of $l(l+1)$ since the physically relevant quantity is the deflection angle.

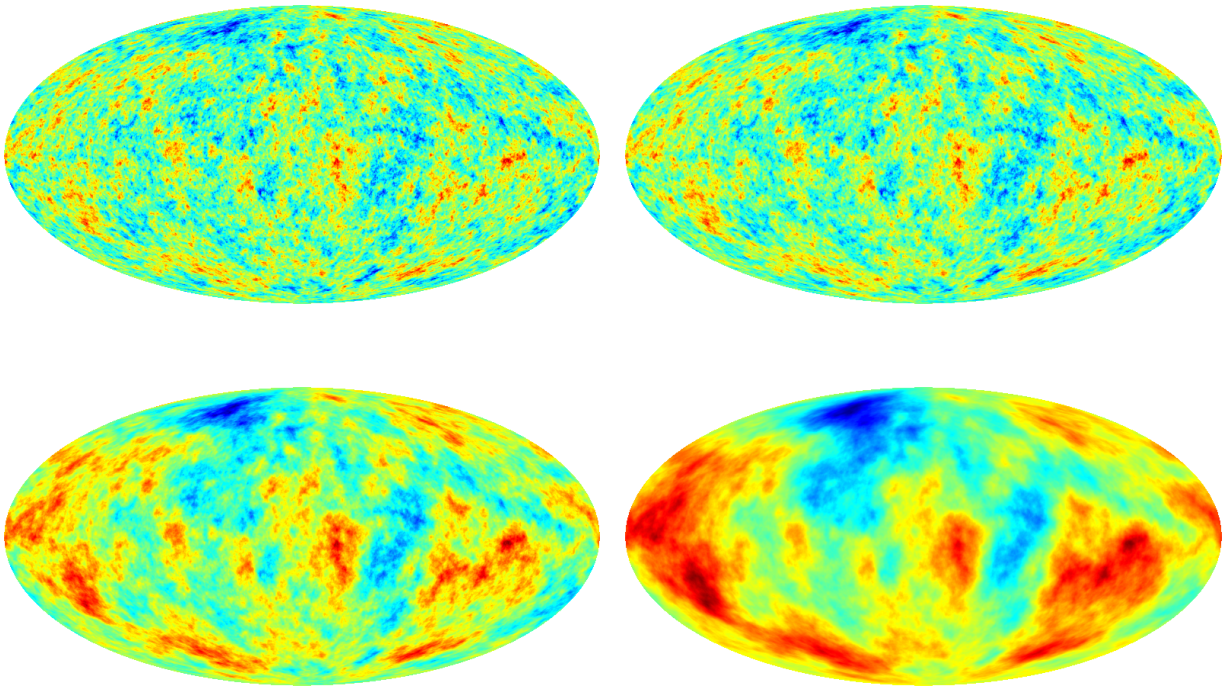

Figure 10.5: Sky maps of the lensing deflection $l(l+1)C_l^{\Pi}$ with the dipole included, for $m_\nu = 10^{-5}$ eV (top-left), 10^{-3} eV (top-right), 10^{-2} eV (bottom-left) and 10^{-1} eV (bottom-right).

$\mathcal{P}_\psi(l/\chi, \tau) \sim \chi^4$ at high l. Thus, at high l the integrand is proportional to χ^2 which is proportional to m_ν^{-2}. This explains the lower overall lensing power at high l for high masses.

From Figs. 10.1 and 10.4 it can be seen that there is a large cross-correlation between C_l^{Θ} and C_l^{Π} at low l. This was also shown in [141].

In Fig. 10.7 we show the contribution to lensing from different redshifts. Almost all of the low l contribution comes at very low z. Note that for the $m_\nu = 10^{-2}$ eV case which was semi-relativistic until a fairly low redshift the high-z contribution is fairly similar to the massless case, i.e. the transition from relativistic to non-relativistic can be seen directly from the change in shape of the lensing spectrum.

10.4 The lensed CνB

10.4.1 Theory

Finally, in this section we combine the results from the two previous sections to derive the lensed CνB spectrum.

Modelling weak gravitational lensing as a second-order effect, the full-sky lensed angular neutrino power spectrum is found from

$$\tilde{C}_l^{\Theta}(q) = 2\pi \int_{-1}^{1} \tilde{\xi}(q, \beta) d_{00}^{l}(\beta) \mathrm{d}\cos\beta, \tag{10.23}$$

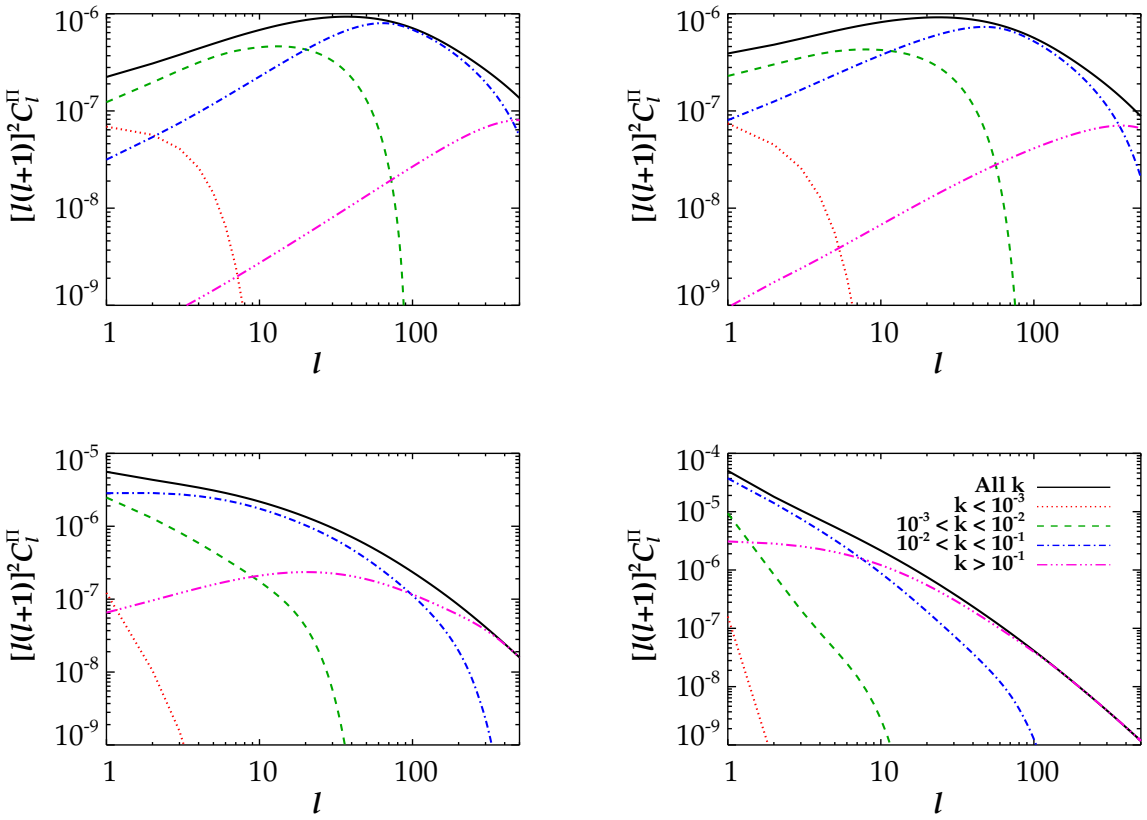

Figure 10.6: The contribution to C_l^{Π} from various scales k in units of $h\,\mathrm{Mpc}^{-1}$. From top-left to bottom-right the neutrino mass is 10^{-5} eV, 10^{-3} eV, 10^{-2} eV and 10^{-1} eV.

where $\tilde{\xi}(q,\beta)$ is the lensed correlation function and $\cos\beta = \hat{\mathbf{n}}_1 \cdot \hat{\mathbf{n}}_2$, where $\hat{\mathbf{n}}_1$ and $\hat{\mathbf{n}}_2$ indicate two directions on the sky. $d^l_{00}(\beta)$ is a special case of the reduced Wigner functions, $d^l_{mm'}(\beta)$, given by

$$d^l_{mm'}(\beta) = (-1)^{l-m'}[(l+m)!(l-m)!(l+m')!(l-m')!]^{1/2} \sum_k (-1)^k \frac{[\cos(\beta/2)]^{m+m'+2k}[\sin(\beta/2)]^{2l-m-m'-2k}}{k!(l-m-k)!(l-m'-k)!(m+m'+k)!}, \tag{10.24}$$

where the sum is over all k fulfilling the criterion that the arguments of the factorials should be non-negative.

Taking sky curvature into account $\tilde{\xi}(q,\beta)$ is given by

$$\tilde{\xi}(q,\beta) \simeq \sum_{l=1}^{\infty} \frac{2l+1}{4\pi} C_l^{\Theta}(q) e^{-L^2 C_+(q,0)/2} \sum_{mm'} d^l_{mm'}(\beta) I_{\frac{m+m'}{2}}[L^2 C_+(q,\beta)/2] I_{\frac{m-m'}{2}}[L^2 C_-(q,\beta)/2]. \tag{10.25}$$

Here $C_l^{\Theta}(q)$ is the unlensed power spectrum and in the double sum, $\sum_{mm'}$, m and m' runs from $-\,l$ to $+\,l$ in integer steps with the criterion that $m+m'$ is even. $L = l + 1/2$ and $I_n(x)$ is the

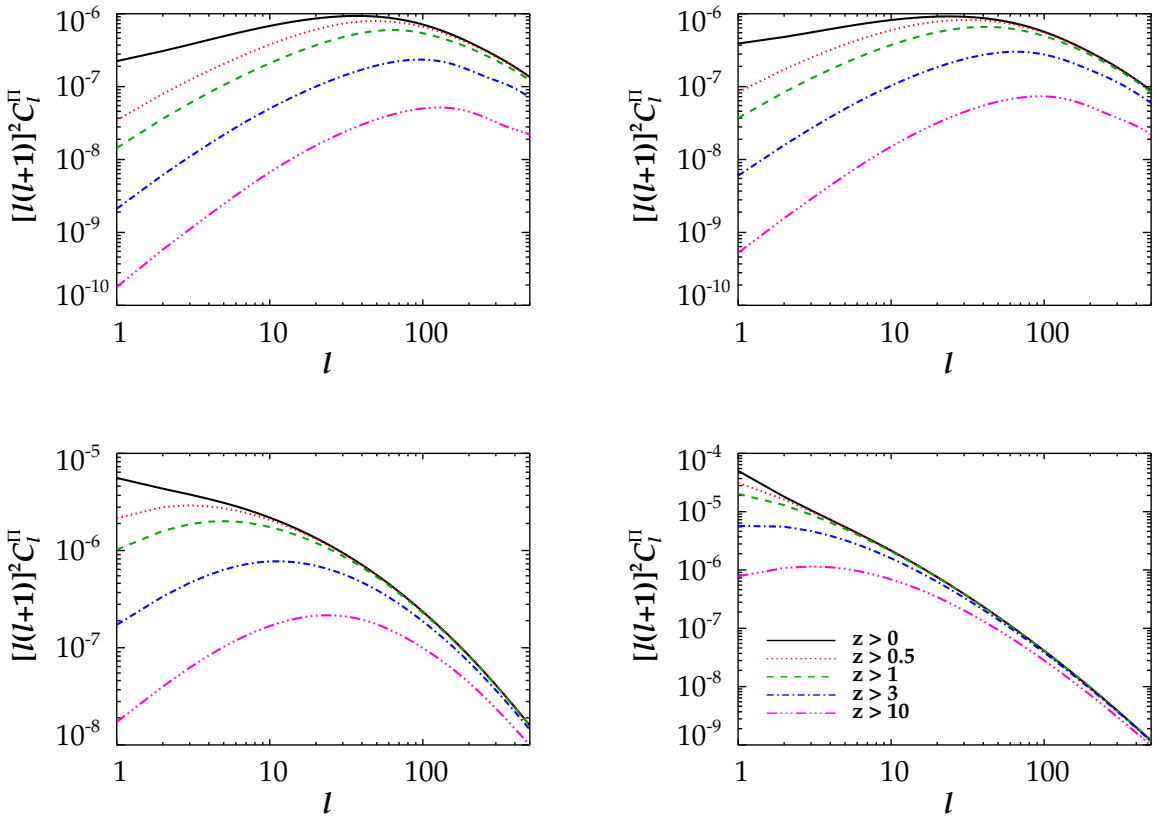

Figure 10.7: Contributions to the lensing potential, C_l^{Π}, at different redshifts. From top-left to bottom-right the neutrino mass is 10^{-5} eV, 10^{-3} eV, 10^{-2} eV and 10^{-1} eV.

modified Bessel function of the first kind. Finally

$$C_{\pm}(q,\beta) = \sum_{l=1}^{\infty} \frac{2l+1}{4\pi} l(l+1) C_l^{\Pi}(q) d^l_{\pm 11}(\beta), \tag{10.26}$$

where $C_l^{\Pi}(q)$ is the power spectrum of the lensing potential.

10.4.2 Numerical results

We have found $\tilde{C}_l^{\Theta}$ with the lensing code in CAMB and Fig. 10.8 shows the difference with respect to the unlensed spectra for the $m_\nu = 10^{-5}$ eV and 10^{-3} eV cases, as well as for the CMB. Both neutrino spectra are closely correlated with the CMB case because the main effect is to move power from the higher l modes in the primary spectra which are very similar at these l-values. Since the primary spectrum dips to a minimum at a somewhat higher l for $m_\nu = 10^{-3}$ eV than for $m_\nu = 10^{-5}$ eV the lensing effect also kicks in later, as can be seen in Fig. 10.8.

We have not presented lensing results for the higher masses because the relative effect of lensing becomes less important at low l, and because numerical noise from the truncation of both primary

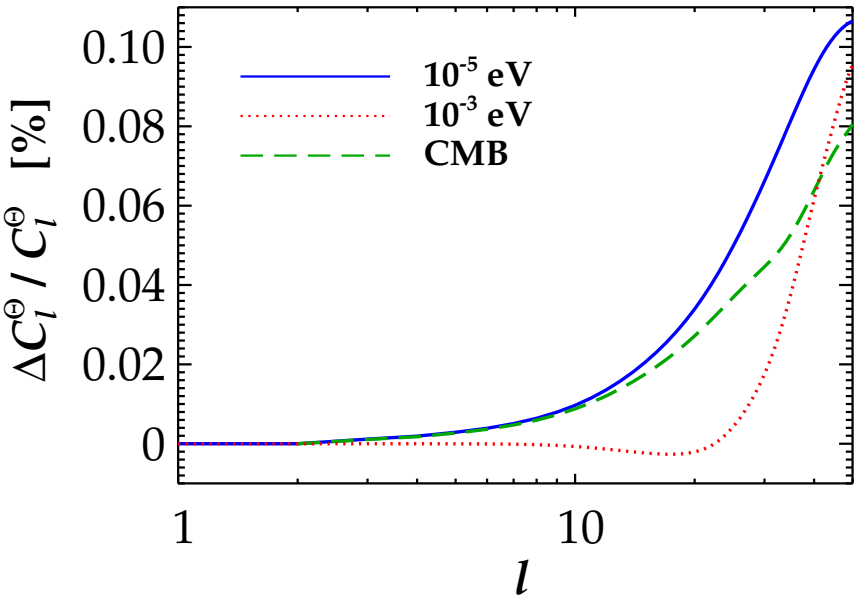

Figure 10.8: Percentage difference between the lensed and unlensed angular power spectra, $(\tilde{C}_l^\Theta - C_l^\Theta)/C_l^\Theta$, for 2 different neutrino masses and compared with the lensing effect on the CMB. The spectra have been slightly smoothed due to finite numerical resolution.

and lensing spectra at $l = 500$ prevents a reliable calculation of the lensed CνB spectrum much beyond $l \sim 10$ for the most massive cases.

Note that we have found $\tilde{C}_l^\Theta$ by lensing the average primary spectrum with the average lensing spectrum. For small neutrino masses with $v \simeq c$ this is surely a good approximation. For higher masses it will be more important to lense each $C_l^\Theta(q)$ with its corresponding $C_l^\Pi(q)$ and then calculate an energy average, though the order of averaging should not significantly affect the total $\tilde{C}_l^\Theta$.

10.5 Discussion and conclusions

We have calculated the anisotropy of the CνB in linear theory which applies to neutrino masses of less than ~ 0.1 eV. For massless neutrinos the power spectrum of CνB fluctuations closely resembles the usual CMB spectrum, but with the baryon-photon acoustic oscillations absent.

At high l the neutrino spectra are almost identical, independent of the neutrino mass. The reason is that at high l all neutrinos are dominated by free-streaming which in l-space has approximately the same impact for all masses.

For smaller l-values the anisotropy increases dramatically as the mass increases, because the gravitational source term becomes much more important at late times for massive particles. This initially increases the lowest multipoles but via the Boltzmann hierarchy the effect quickly propa-

gates to higher l.

We then proceeded to calculate the effect of weak gravitational lensing for massive neutrinos and found it to be much stronger at low l, and correspondingly weaker at high l, as compared to the massless case. Finally we calculated the effect of lensing on the primary CνB spectra and found the effect to be unimportant (with relative changes at the per mille level up to $l \sim 50$), but with some differences depending on the neutrino mass.

It is worth mentioning that any direct experimental measurement of the CνB anisotropy will most likely measure flavour states, not mass states. The actual anisotropy measured will therefore be a superposition of anisotropies for three different mass states, weighed with their individual flavour content.

We should finally again stress that our results are only valid for masses of $\lesssim 0.1$ eV. For higher masses linear perturbation theory breaks down because neutrino streaming velocities become comparable to the typical gravitational flow velocities so that a significant fraction of neutrinos are bound in structures. In this case the CνB spectrum must be found from N-body simulations of neutrino clustering [3]. This can also be seen from the fact that the anisotropy at low l is a factor $\sim 10^9$ higher for $m_\nu = 0.1$ eV than for massless neutrinos. Since the anisotropy for massless particles corresponds to $\delta\rho/\rho \sim 10^{-5}$ the corresponding $\delta\rho/\rho$ for 0.1 eV neutrinos is of order one, indicating that perturbation theory breaks down.

Acknowledgements

We acknowledge computing resources from the Danish Center for Scientific Computing (DCSC).

Part III

Reflections

Chapter 11

Comparisons

The effect of massive neutrinos on the non-linear matter power spectrum has been investigated by several scientific groups within the last 3 years. It is therefore possible and potentially interesting to compare the scientific results presented in this dissertation with the results from these groups. These results are based on Perturbation Theory (PT) and N-body simulations.

11.1 Perturbation theory

Theory In perturbation theory the basic idea is to expand the density and velocity variables in progressively higher orders as

$$\delta_i = \delta_i^{(1)} + \delta_i^{(2)} + \delta_i^{(3)}..., \tag{11.1}$$

and

$$\theta_i = \theta_i^{(1)} + \theta_i^{(2)} + \theta_i^{(3)}..., \tag{11.2}$$

with i equal to cb or ν and where cb is an average taken over the CDM and baryonic components. For a 3 species component the total matter power spectrum can be written as

$$P_m = N(T_{cb}f_{cb} + T_\nu f_\nu)^2 k = f_{cb}^2 P_{cb} + 2f_{cb}f_\nu P_{cb,\nu} + f_\nu^2 P_\nu, \tag{11.3}$$

where $f_i \equiv \Omega_i/\Omega_m$. Including the one-loop corrections, i.e. going to third-order in perturbations we get

$$P_{cb} = P_{cb}^{(11)} + 2P_{cb}^{(13)} + P_{cb}^{(22)}, \tag{11.4}$$

$$P_\nu = P_\nu^{(11)} + 2P_\nu^{(13)} + P_\nu^{(22)}, \tag{11.5}$$

and the cross-correlation power spectrum is given by

$$P_{cb,\nu} = P_{cb,\nu}^{(11)} + 2P_{cb,\nu}^{(13)} + P_{cb,\nu}^{(22)}, \tag{11.6}$$

where in general

$$P_{i,j}^{(ab)} = \frac{1}{2}[\langle \delta_i^{(a)} \delta_j^{(b)} \rangle + \langle \delta_j^{(a)} \delta_i^{(b)} \rangle]. \tag{11.7}$$

The perturbation variables are to third-order found by solving the continuity and Euler equations with higher-order terms added. The linear terms are found in the standard way, and these solutions are then recursively used to find higher-order corrections.

11.1.1 Wong & Saito *et al.*

S. Saito, M. Takada and A. Taruya [19] assumed the approximation that only the linear neutrino perturbations should be included, i.e. $P_{cb,\nu} = P^{(11)}_{cb,\nu}$ and $P_\nu = P^{(11)}_\nu$. Non-linear corrections are therefore only incorporated into P_{cb}. As pointed out by Y. Y. Y. Wong [21] the assumptions of Saito *et al.* are not consistent with neglecting the term $\langle \delta^{(1)}_\nu \delta^{(3)}_{cb} \rangle$, which must be included for a self-consistent calculation of the one-loop corrections. Wong investigated the effect of including this term and found that it can safely be neglected [21].

The higher-order terms in Eq. (11.4) are given by [19]

$$\begin{aligned} P^{(13)}_{cb}(k,z) &= \frac{k^3}{252(2\pi)^2} P^{(11)}_{cb}(k,z) \int_0^\infty dr P^{(11)}_{cb}(kr,z) \\ &\quad \left(\frac{12}{r^2} - 158 + 100r^2 - 42r^4 + \frac{3}{r^3}(r^2-1)^3(7r^2+2)\ln\left|\frac{1+r}{1-r}\right| \right), \end{aligned} \tag{11.8}$$

and

$$\begin{aligned} P^{(22)}_{cb}(k,z) &= \frac{k^3}{98(2\pi)^2} \int_0^\infty dr P^{(11)}_{cb}(kr,z) \\ &\quad \int_{-1}^1 d\mu P^{(11)}_{cb}(k\sqrt{1+r^2-2r\mu},z) \left(\frac{3r+7\mu-10r\mu^2}{1+r^2-2r\mu} \right)^2. \end{aligned} \tag{11.9}$$

Disregarding the complicated appearance of these equations it can be seen that the corrections $P^{(13)}_{cb}$ and $P^{(22)}_{cb}$ are roughly proportional to $P^{(11)}_{cb}$ squared. Therefore PT predicts an additional neutrino induced suppression of power as compared to linear theory. This finding was also confirmed by Wong [21].

At $z = 1$ PT is accurate at the 1% level for $k < 0.2\,h\,\mathrm{Mpc}^{-1}$ while at $z = 3$ the bound is $k < 0.4\,h\,\mathrm{Mpc}^{-1}$ [21]. The conclusion is that perturbation theory can only be used in the mildly non-linear regime.

11.1.2 Saito *et al.* - revisited

In a second paper Saito *et al.* [20] furthermore tried to justify their approach in their first paper by investigating non-linear corrections to the neutrino component.[1] They estimated the non-linear neutrino corrections by solving the Boltzmann hierarchy for the neutrinos with the gravitational potential in the Poisson equation sourced by the one-loop corrections. Explicitly they solved

$$k^2\phi^{\mathrm{PT}} = -4\pi G a^2 \bar{\rho}_m (f_{cb}\delta^{\mathrm{PT}}_{cb} + f_\nu \delta^{(1)}_\nu), \tag{11.10}$$

where

$$\delta^{\mathrm{PT}}_{cb} = \sqrt{1 + \frac{P^{(13)}_{cb} + P^{(22)}_{cb}}{P^{(11)}_{cb}}}\,\delta^{(1)}_{cb}. \tag{11.11}$$

[1] Saito *et al.* also calculated the redshift- and scale-dependence of higher-order CDM and baryonic growth functions, and found that the k-dependence of these higher-order growth functions can be neglected. At $z = 0$ this leads to a lack of at most 1% in power for k smaller than $1\,h\,\mathrm{Mpc}^{-1}$ and $\sum m_\nu = 0.6\,\mathrm{eV}$, though it should be remembered that their theory is not accurate in this region of (z,k) parameter space.

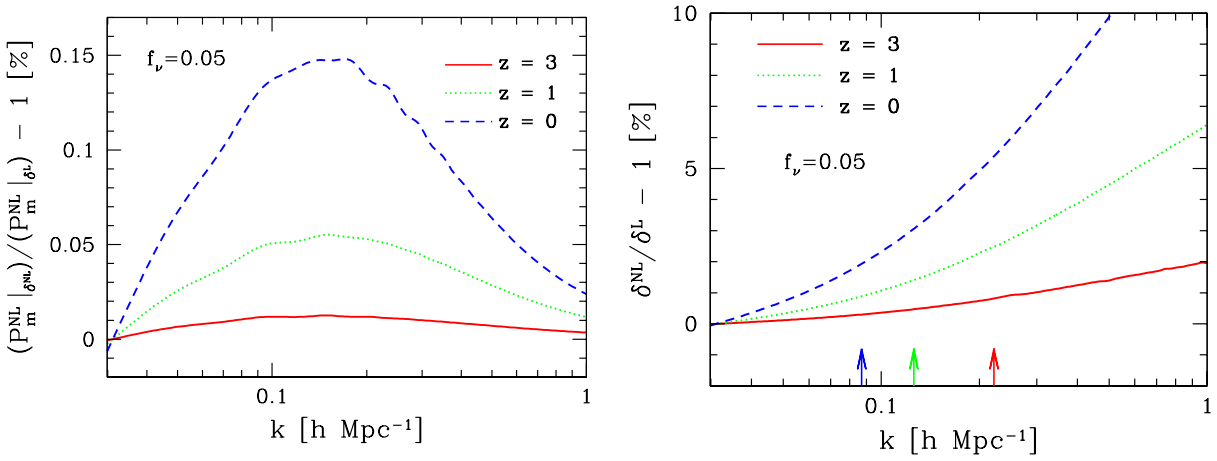

Figure 11.1: The left panel shows the difference in the total matter power spectrum at different redshifts found by sourcing the neutrino Boltzmann hierarchy by either the linear gravitational potential or a PT corrected version. The right panel shows the neutrino corrections themselves. $f_\nu = 0.05$ corresponds to $\sum m_\nu = 0.6\,\mathrm{eV}$. The figures are taken from Saito *et al.* [20].

Before proceeding it will be useful to clarify the various non-linear corrections to the total matter power spectrum encountered in this dissertation. First, we have a non-linear correction to the relative matter power spectrum caused by replacing part of the CDM component with massive neutrinos (see Chapter 6). This extra correction of $\sim 9.8\,\Omega_\nu/\Omega_m$, which should be compared to the linear theory prediction of $\sim 8\,\Omega_\nu/\Omega_m$, mainly arises from additional non-linear clustering in the CDM component. Second, we have a non-linear neutrino correction to the total matter power spectrum, which we found by comparing the grid and particle approaches (see Chapter 7). This difference arises by including or excluding *all* higher-order neutrino perturbations in N-body simulations. This non-linear neutrino correction is the correct one, since it has been calculated in a model where the perturbations to the CDM component is correctly evolved. Then there exist approximations to this non-linear neutrino correction, which leads us to the third variant of a non-linear correction. It is the one presented in this subsection, and only arises by using ϕ^{PT}, instead of the ordinary linear potential, to source the *linear* neutrino Boltzmann hierarchy. In this case there are no higher-order neutrino perturbation terms and no higher-order Boltzmann equations, but the linear neutrino term, $\delta_\nu^{(1)}$, is increased. And finally we have a fourth non-linear neutrino correction which we will encounter in the next subsection. This correction to the total matter power spectrum is found by either using all the higher-order neutrino terms, up to third order in perturbations in Eqs. (11.3) - (11.6), or only including linear neutrino perturbations in this same set of equations.

With these clarifications we are now ready to discuss the Saito *et al.* results presented in Fig. 11.1 (with NL $\equiv$ PT) for $f_\nu = 0.05$, or equivalently $\sum m_\nu = 0.60\,\mathrm{eV}$, and $\Omega_m = 0.24$. It displays the redshift-dependence of the non-linear neutrino correction to the total matter power spectrum (left) as well as the non-linear neutrino correction itself (right). The evolution in the left panel is to some extent consistent with the one we found by comparing the grid and particle approaches (see the middle panel of Fig. 7.1 on page 69). At $z = 3$ the correction is basically non-existing and thereafter only slowly begins to develop. They also found that the largest part of the correction develops for redshifts smaller than ~ 1 and that the correction at $z = 1$ comprises roughly 30% as compared to

the correction at $z = 0$. Furthermore, like us they found that the maximum of the correction lies around $k \sim 0.15 - 0.2\,h\,\mathrm{Mpc}^{-1}$, i.e. just inside the non-linear regime but at scales large enough that the matter power spectrum is not completely dominated by the CDM and baryonic components.

The Saito *et al.* results only differ significantly from ours when the amplitude of the correction is considered. Comparing our results at $z = 0$ we find a non-linear neutrino correction which is roughly at factor of 8 *larger* than the Saito *et al.* result. This discrepancy can easily be explained by the fact that Saito *et al.* solve PT equations, which are not valid at $z = 0$, whereas we solve the full equations taking corrections to *all* orders into account.

To sum up, the correct calculation of the non-linear neutrino correction does not significantly alter the shape and position of the maximum of this correction, but only the amplitude.

11.1.3 Shoji *et al.*

Theory M. Shoji and E. Komatsu calculated the matter power spectrum to third-order in perturbations [22] using WMAP-5 cosmological parameters. They did not assume that $\delta_\nu = \delta_\nu^{(1)}$ but included higher-order neutrino terms. Their formalism is based on calculating the Jeans filtering function up to third-order, which is generally defined as

$$g_n(k) = \frac{\delta_\nu^{(n)}(k)}{\delta_{cb}^{(n)}(k)}, \tag{11.12}$$

where n is the order. With this definition of the filtering function, the neutrino power spectrum and the cross-correlation power spectrum between neutrinos and the non-relativistic matter components are given by

$$P_\nu = g_1^2 P_{cb}^{(11)} + 2 g_1 g_3 P_{cb}^{(13)} + g_2^2 P_{cb}^{(22)}, \tag{11.13}$$

and

$$P_{cb,\nu} = g_1 P_{cb}^{(11)} + (g_1 + g_3) P_{cb}^{(13)} + g_2 P_{cb}^{(22)}. \tag{11.14}$$

They used the fluid approximation, i.e. truncated the Boltzmann hierarchy at $l_{\max} = 2$, which gives a closed set of equations. This approximation is more accurate for higher neutrino masses at low redshift, i.e. in the non-relativistic regime. Shoji and Komatsu investigated the validity of the fluid approximation by comparing the truncated Boltzmann hierarchy with the full calculation [144]. They found that the fluid approximation is accurate at sub-percent level for $m_\nu > 0.05\,\mathrm{eV}$ at $z < 100$ and $k < 1.0\,h\,\mathrm{Mpc}^{-1}$.

Shoji and Komatsu included the effect of neutrino free-streaming in the sound speed term in the Euler equation, and they proposed the following first-order filtering function which is accurate at the 10% level today

$$g_1(k) = \frac{1}{1 + (k/k_J)^2}, \tag{11.15}$$

where the Jeans wavenumber, k_J, is given by

$$k_J(\tau) \equiv \frac{\sqrt{6}}{c_s(\tau)\tau}, \tag{11.16}$$

with $\tau \equiv 2/(aH)$. The definition of $g_1(k)$ has the desired property that it approaches unity on large scales, where neutrinos and CDM cluster identically, and is inversely proportional to c_s^2 (c_s^2

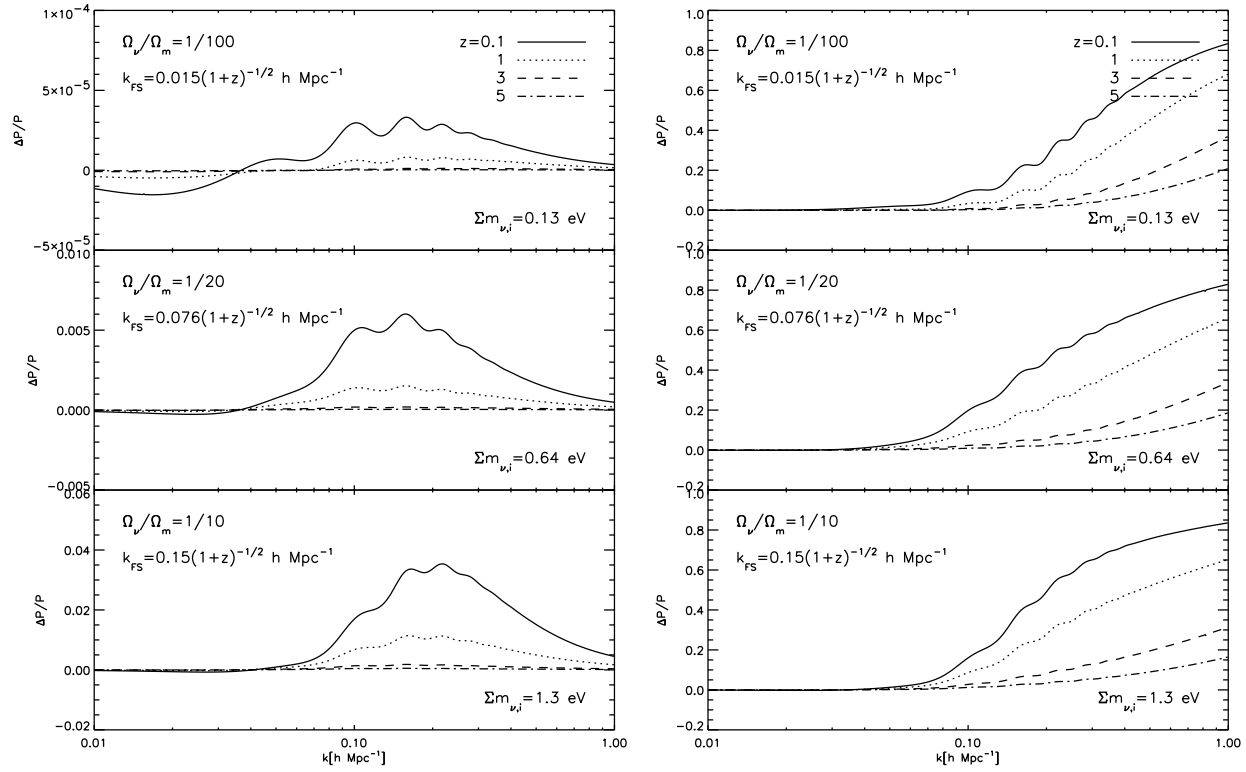

Figure 11.2: The left panel shows the difference in the total matter power spectrum with and without higher-order neutrino perturbations for different redshifts and neutrino masses. The right panel shows the corresponding neutrino corrections where it should be noted that $\Delta P/P = 1 - P_\nu^{(11)}/P_\nu$. The figures are taken from Shoji and Komatsu [22].

enters the Euler equation) on small scales where the neutrino thermal velocity suppresses structure formation. It should be noted that even though the filtering function has the desired asymptotic limits, it is not a unique solution. The higher-order filtering functions, $g_2(k)$ and $g_3(k)$, have roughly similar functional dependencies on k_J. It was assumed that $k_J \propto a^2 H$ is redshift independent, which is only strictly valid for radiation domination, though at low redshift, say, smaller than 1, H does not depend heavily on a. In sum, this assumption should not qualitatively affect their results.[2]

Now, the sound speed should be related to the neutrino thermal velocity, which suppresses structure formation through the Euler equation. Defining the neutrino velocity dispersion as

$$\sigma_\nu^2 \equiv \frac{\int d^3q (q/\epsilon)^2 f_0}{\int d^3q f_0}, \tag{11.17}$$

which in the non-relativistic limit is proportional to a^{-1} as required, and using $c_s^2 = \dot{\bar{P}}/\dot{\bar{\rho}}$, it can be

[2]M. Shoji, personal communication.

shown that in the non-relativistic limit [144]

$$c_s^2 \simeq \frac{5}{9}\sigma_\nu^2. \tag{11.18}$$

Results Using the above outlined theory, Shoji and Komatsu calculated the effect on the matter power spectrum caused by including higher-order neutrino perturbations. Their results are shown in Fig. 11.2, where it should be noted that they do not present results at $z = 0$ but at a slightly higher redshift of $z = 0.1$. Their middle panel has a total neutrino mass of 0.64 eV which is very similar to the 0.6 eV case considered above in relation to the work of Saito *et al.* They found non-linear neutrino corrections at the 0.6% level, which is a factor of two smaller than our result, but a factor of 4 larger than the Saito *et al.* result. Focusing on the bottom panel and a 1.3 eV total neutrino mass they found a 3.5% correction where we found ∼5% for a slightly smaller neutrino mass of 1.2 eV.

Overall, the Shoji and Komatsu results show the same redshift dependencies on the correction term as Saito *et al.* and we found. Shoji and Komatsu also found the maximum of the correction occuring at $k \sim 0.15 - 0.2\,h\,\mathrm{Mpc}^{-1}$. But again, the amplitude of the correction is predicted differently and must be explained by the use of a different driving term together with a different implementation of the neutrino free-streaming effect. The N-body method includes corrections to all orders and that method should therefore be used at redshifts smaller than 1, when a calculation of the non-linear neutrino correction is desired.

11.1.4 Lesgourgues *et al.*

Theory The Renormalization Group time-flow (TRG) approach was presented by M. Pietroni [145]. The method uses the continuity, Euler and Poisson equations to calculate the matter power spectrum and the bispectrum. The system of equations is truncated at the trispectrum, i.e. the trispectrum is set to zero, which prevents higher-order corrections from cascading down to the power spectrum. Standard one-loop PT can be retrieved by making simplifications to the TRG approach, which itself goes beyond PT and therefore should be more accurate.

Results The approach of M. Pietroni was extended by Lesgourgues *et al.* to include massive neutrinos [146]. As can be seen from Fig. 11.3, TRG and our N-body simulations are in excellent agreement for $\sum m_\nu = 0.6\,\mathrm{eV}$ at $a = 0.3$ out to $k \sim 1.4\,h\,\mathrm{Mpc}^{-1}$. At $a = 0.5$ there is only agreement out to $k \sim 0.3\,h\,\mathrm{Mpc}^{-1}$.

Lesgourgues *et al.* also calculated the relative power spectrum between models with $\sum m_\nu = 0.3\,\mathrm{eV}$ or $\sum m_\nu = 0.6\,\mathrm{eV}$ neutrinos and a massless neutrino cosmology. Their results can be seen in the bottom panel of Fig. 11.3. At $a = 0.2$ TRG and our N-body simulations predict the same suppression, but at just slightly lower redshifts the methods produce different results. In all cases our N-body results are better reproduced by TRG than by PT.

11.2 N-body simulations

11.2.1 Agarwal *et al.*

Methods Very recently S. Agarwal and H. Feldman published a paper where they included the effect of neutrinos in N-body simulations [147]. They used a very simplified approach, where the

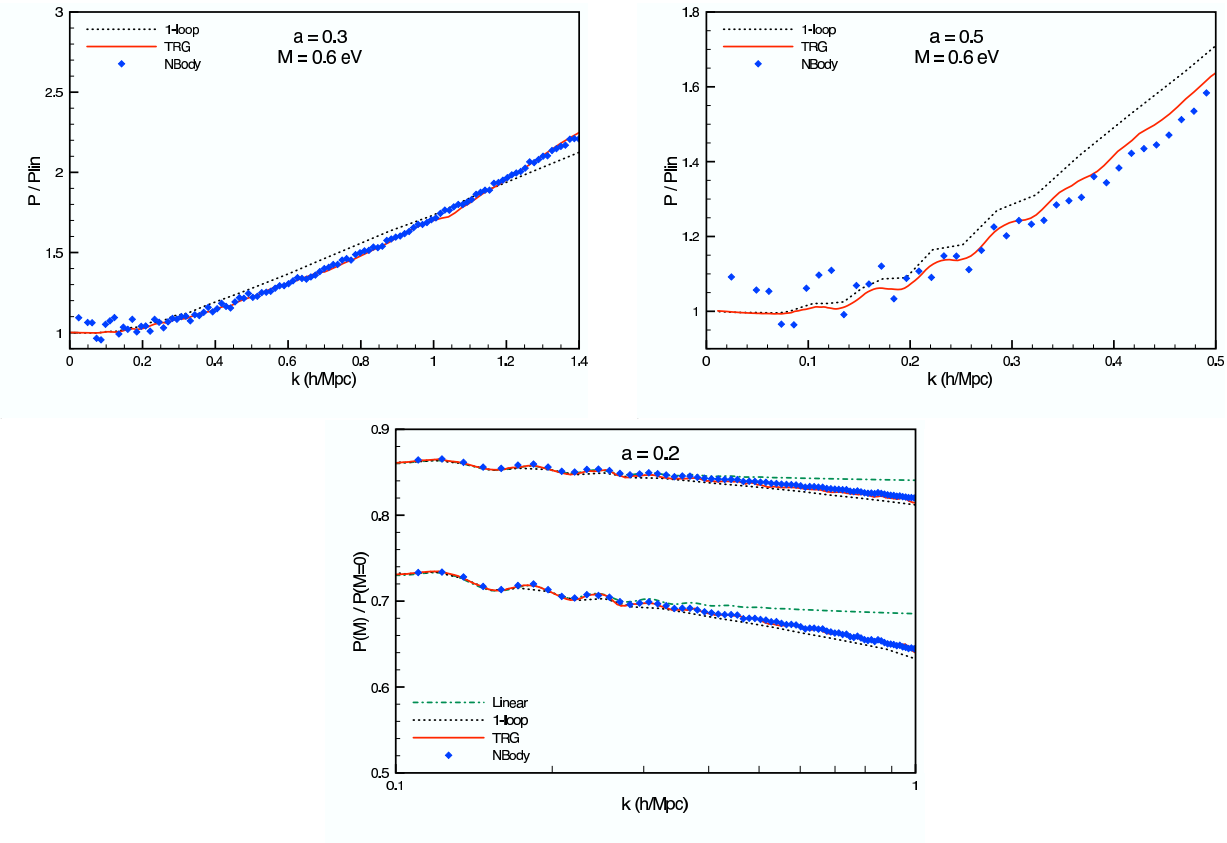

Figure 11.3: The figures are taken from Lesgourgues *et al.* [146] and include N-body data, with the neutrino component represented as particles, taken from the suite of simulations presented in our grid paper [2]. The upper two panels show matter power spectra calculated with the PT, TRG and N-body methods for $\sum m_\nu = 0.6\,\mathrm{eV}$ at $a = 0.3$ (left) and $a = 0.5$ (right). The spectra have been divided by the linear theory power spectrum. The bottom panel shows the suppression caused by neutrinos relative to a model with massless neutrinos at $a = 0.2$. In this panel the upper group of lines are for $\sum m_\nu = 0.3\,\mathrm{eV}$ and the lower group for $\sum m_\nu = 0.6\,\mathrm{eV}$.

effect of neutrinos was only included in the linear theory evolution and therefore only in the TFs which were used to generate the N-body initial conditions.[3] The effect of neutrinos was therefore not included as particles or on a linear Fourier grid in the N-body simulation. Apparently, the linear theory neutrino power spectrum was added to the total matter power spectrum at the end of the simulation at $z = 0$. They used WMAP 7-year parameters.

Results Despite the simplistic inclusion of neutrinos, the results reached by Agarwal and Feldman are qualitatively and most likely also more or less quantitatively correct for $k \gtrsim 0.5\,h\,\mathrm{Mpc}^{-1}$, i.e. at scales where the effect of neutrino perturbations in the N-body simulation is small. It is therefore interesting to note that for a total neutrino mass of 0.475 eV they found the maximum suppression to the non-linear matter power spectrum caused by massive neutrinos to be around $10.0\,\Omega_\nu/\Omega_m$. We found the value $9.8\,\Omega_\nu/\Omega_m$ (see Fig. 6.4 on page 58) at the scale $k \sim 0.8\,h\,\mathrm{Mpc}^{-1}$, whereas they

[3] Personal communication with S. Agarwal, conveyed through T. Haugbølle.

locate the turnover in the difference power spectrum to around $k \sim 1\,h\,\mathrm{Mpc}^{-1}$.

11.2.2 Viel *et al.*

Methods Recently M. Viel, M. G. Haehnelt and V. Springel published an article, where they investigated the effect of massive neutrinos on both the Lyman-α forest and the matter power spectrum [57]. They included the effect of neutrinos in N-body simulations either as particles or on a grid. This paper is the first one which reproduces our developed methods regarding how neutrinos should be implemented in N-body simulations. They specifically wanted to compare their results with ours and therefore adopted the same cosmological parameters as we have used. It should be noted that Viel *et al.* also included baryons in their simulations, though this should not lead to significantly different results when the relative power spectrum is considered, and the results of Viel *et al.* and ours should therefore ideally give comparable conclusions.

Viel *et al.* do not calculate the Tree force for the neutrino particles which is a good approximation for Fourier grid mesh-spacings roughly smaller then the neutrino free-streaming length. To partly compensate for the missing force contributions in the Tree part the $\exp(-k^2 r_s^2)$ term which multiplies the long-range potential (see Eq. (3.38) on page 29) has been removed from the neutrino Fourier modes.[4] They started their N-body simulations at redshifts of 7 which, according to our work with the hybrid method, should be early enough to investigate non-linear neutrino contributions to the matter power spectrum.

Results Let us begin by stating areas where Viel *et al.* and we have found compatible results. Regarding the grid method, Viel *et al.* find a maximum suppression of 43% compared to a simulation without massive neutrinos at $z = 0$. We find the exact same suppression, i.e. 43%, with our grid method. Both codes locate this maximum suppression to the scale $k \sim 0.8\,h\,\mathrm{Mpc}^{-1}$, i.e. the two grid implementations appear to give very similar results. Furthermore, Viel *et al.* provide an independent confirmation of the turnover in the difference power spectrum.

Viel *et al.* found that the effect of neglecting neutrino thermal velocities in the ICs produces roughly the same shape and increase of the matter power spectrum as we have found (see Fig. 6.6 on page 61). Like us, Viel *et al.* also found that the Poisson noise term scale as $P(k) \propto R_{\mathrm{BOX}}^3 / N_{\nu,\mathrm{part}}$. We have tried to subtract this noise term from the neutrino power spectra presented in the top-right panel of Fig. 6.5 (see page 60). In Fig. 11.4 we present the result together with a reprint of the original figure. Since the non-linear neutrino power spectra for simulations with 256^3 to 1024^3 neutrino N-body particles have converged it can be seen that we have actually calculated a converged non-linear neutrino power spectrum at the scales shown. For a smaller number of neutrino N-body particles the signal-to-noise ratio is too small to retrieve the underlying power spectrum. With respect to the total matter power spectrum it is not really necessary to subtract the white noise term, since it can be suppressed by including a fairly small number of neutrino N-body particles.

In Fig. 11.5 we present two figures from the Viel *et al.* paper. The left panel shows the difference between the grid and particle methods at $z = 0$, 1 and 3 for $\sum m_\nu = 0.6\,\mathrm{eV}$ degenerate neutrinos. The conclusions drawn from this figure differ significantly from our results. First, at $z = 3$ they found a significant correction to the matter power spectrum arising from non-linear neutrino modes: They are of the order of $\sim 2 - 8\%$ on scales of $0.2 - 0.7\,h\,\mathrm{Mpc}^{-1}$. Viel *et al.* conclude that at this

[4] M. Viel, personal communication.

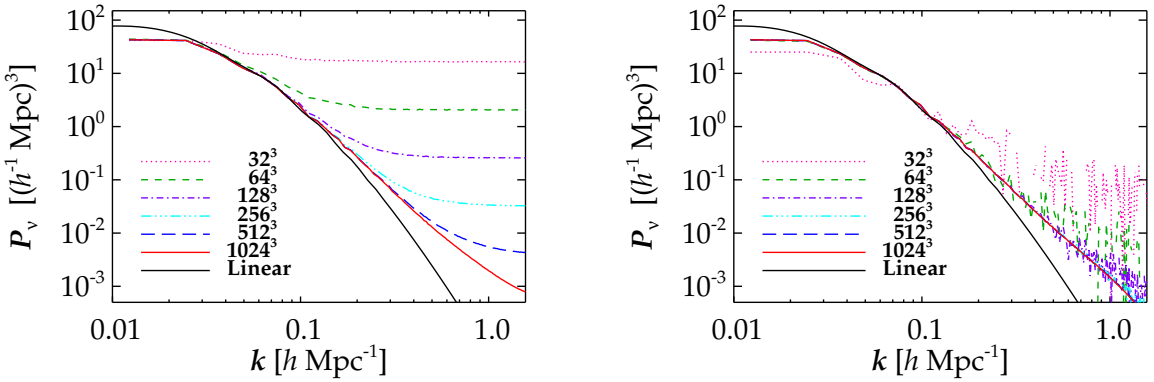

Figure 11.4: The figure presents neutrino power spectra for different numbers of neutrino N-body particles at $z = 0$ for a cosmology with $\sum m_\nu = 0.6\,\mathrm{eV}$. The left panel shows a reprint from Fig. 6.5 (see page 60) whereas the white noise term, $\propto R^3_{\mathrm{BOX}}/N_{\nu,\mathrm{part}}$, has been subtracted in the right-hand panel. In this panel the simulations with 512^3 and 1024^3 neutrino N-body particles give basically identical neutrino power spectra. Note that the power spectra in the right-hand panel with fewer N-body particles sometimes achieve negative values, as can be inferred from the broken lines.

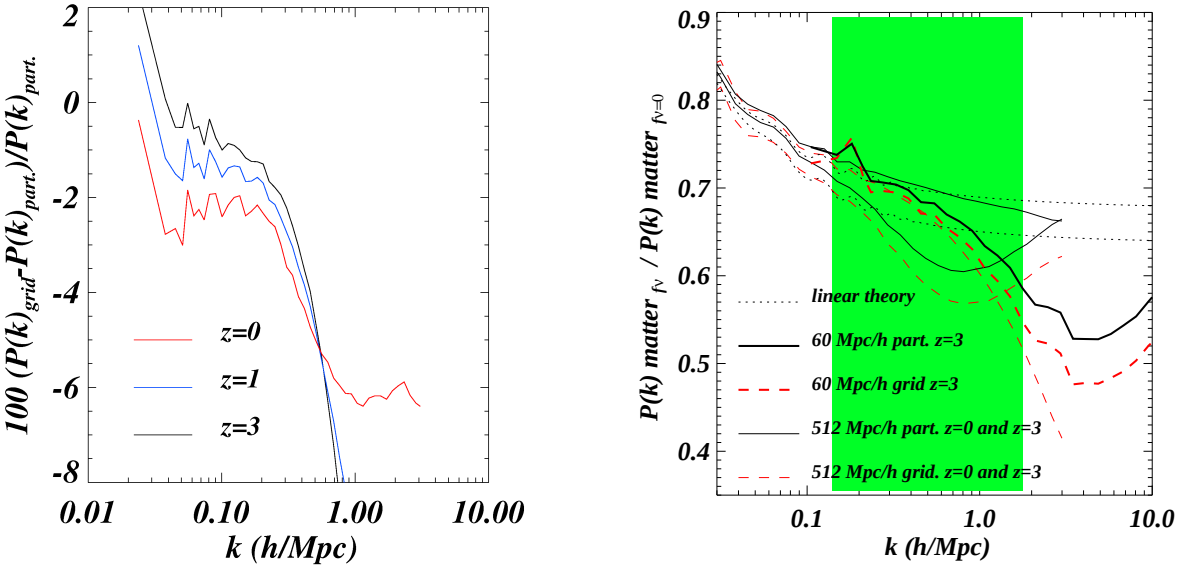

Figure 11.5: The figures are taken from Viel *et al.* [57]. The left panel shows the relative power spectrum between grid and particle simulations with $\sum m_\nu = 0.6\,\mathrm{eV}$ at various redshifts. The right panel shows the relative power spectrum between a model with $\sum m_\nu = 0.6\,\mathrm{eV}$ neutrinos and one without massive neutrinos. The text focuses on the two lines with a bump at around $k \sim 0.7\,h\,\mathrm{Mpc}^{-1}$, representing the grid and particle suppressions at $z = 0$.

redshift neutrinos have gone significantly non-linear, and that these extra non-linear corrections significantly affect the overall evolution of the matter perturbations.

On the contrary, at $z = 3$ we found that the grid and particle methods give basically *identical* results (see the middle panel of Fig. 7.1 on page 69). This difference is striking and *cannot* be explained by the use of baryons or slightly different N-body or linear theory specific parameters. Since Viel *et al.* and we have used the same number of neutrino N-body particles in the same box size, the discrepancy should not be due to an unsuppressed neutrino Poisson noise term.

It should be noted that both the amplitude, shape and redshift-dependence of the non-linear neutrino correction found by Viel *et al.* differs from ours. It should also be remembered that we found the same shape and redshift-dependence as Saito *et al.* and Shoji and Komatsu. We also stress that our results match the ones by Lesgourgues *et al.* at redshifts of $\sim 3 - 4$.

Furthermore, Viel *et al.* found that their fundamental mode gives roughly 2% more power in the grid simulation, which looks peculiar when the relative power spectrum is considered even though this region is dominated by cosmic variance. Viel *et al.* also found that the non-linear neutrino correction gives rise to 2% more power on linear scales and 6% more power around $k \sim 1\,h\,\mathrm{Mpc}^{-1}$ at a redshift of zero. Our implementation better reproduces the linear result at linear scales and we found a maximum deviation between the grid and particle approaches which was a factor of 5 *smaller* than the Viel *et al.* result at $z = 0$.

As presented earlier in this dissertation we found a suppression to the total matter power spectrum caused by neutrinos scaling as $9.8\,\Omega_\nu/\Omega_m$ (see Fig. 6.4 on page 58). Viel *et al.* reports a value of $9.5\,\Omega_\nu/\Omega_m$ though Fig. 11.5 prefers another value than the one quoted in their paper, namely $\sim 9.1\,\Omega_\nu/\Omega_m$.

In their paper they also present a slice of their simulation volume for $\sum m_\nu = 1.2\,\mathrm{eV}$ at $z = 3$. On spacial scales of $\sim 10\,h^{-1}\,\mathrm{Mpc}$ they find $\delta_\nu \sim 10\%$, which should roughly translate into $\delta_\nu \sim 5\%$ for $\sum m_\nu = 0.6\,\mathrm{eV}$, at a scale of $k \sim \pi/10\,h\,\mathrm{Mpc}^{-1} \sim 0.3\,h\,\mathrm{Mpc}^{-1}$. It should therefore be a very good approximation to use linear theory for the neutrino component at $z = 3$ for the scales presented in Fig. 11.5. But again, this figure leads to a completely different conclusion.

Since the grid approaches of Viel *et al.* and ours are similar, we conclude that the two particle implementations differ. Given that our particle implementation has been significantly tested and that the non-linear neutrino correction displays the same shape and redshift-dependence as found by Saito *et al.* and Shoji and Komatsu, we conclude that the results found by Viel *et al.* differ from other results in the scientific community. We furthermore stress that it makes sense that neutrinos should cluster more and contribute more to the matter power spectrum at lower redshift, where the neutrino thermal velocity has redshifted to a low enough level so that it can trace the CDM and baryonic distributions at smaller scales. This fact can also be seen for a linear theory calculation in Fig. 2.1 (on page 22), a result which should not qualitatively change in the non-linear regime.

Whereas Saito *et al.*, Shoji and Komatsu and we found that non-linear neutrino corrections are negligible at $z = 3$, Viel *et al.* found that this correction is very important for a precise calculation of the matter distribution at redshifts relevant for Lyman-α forest data. On the contrary, we believe that the grid implementation would have been ideal.

Chapter 12

Conclusions and Outlook

This chapter will present our conclusions for this PhD dissertation as well as a short discussion (outlook) on how the developed methods can be improved and extended.

Conclusions From observations of solar and atmospheric neutrinos it is known that neutrinos oscillate between the 3 known active flavours, namely the ν_e, ν_μ and ν_τ neutrinos, and that these observable states are a superposition of mass eigenstates. This in turn leads to the conclusion that neutrinos are massive with a total mass of at least 0.05 eV or 0.1 eV, depending on whether the neutrino mass hierarchy is normal or inverted, respectively. At the other end of the mass scale, cosmology constrains the total neutrino mass to be less than roughly 1.5 eV at the 2σ level.

This PhD dissertation has presented scientific research on how massive neutrinos affect non-linear structure formation. It has described 3 newly developed methods to include neutrino perturbations in N-body simulations, namely the *particle*, *grid* and *hybrid* methods, and these methods have been used to calculate important cosmological observables.

With the *particle* method [1] (see Chapter 6) the neutrinos are implemented as N-body particles with initial conditions taken from the linear theory neutrino transfer function. The neutrino particles are assigned both a gravitational flow velocity as well as a relic primordial thermal velocity drawn from a Fermi-Dirac distribution.

Using the particle method it was found that the effect of the neutrino thermal velocity component is to reduce the matter power spectrum in the non-linear regime by a factor of $9.8\,\Omega_\nu/\Omega_m$ with this maximum occurring around the scale $k \sim 0.8\,h\,\mathrm{Mpc}^{-1}$. This should be compared with the linear theory result of $8\,\Omega_\nu/\Omega_m$, i.e. an extra suppression of almost 25%. This turnover in the difference power spectrum is not present in linear theory. Since future large-scale structure observations will measure the matter power spectrum with a precision at the 1% level, neutrinos *must* be included in the theoretical models. In turn, these observations can be used to measure the total neutrino mass.

The standard implementation of the particle method significantly increases the total N-body simulation time. This is caused by the large neutrino thermal velocity, which leads to a reduction in the simulation time-step. Furthermore, to conserve neutrino momentum on small scales a very high number density of neutrino N-body particles is needed, which in turn leads to a prohibitively large memory consumption. In sum, the particle method is less well suited for a high N-body starting redshift, $z \sim 50$, and especially if neutrino structures should be simulated.

With the *grid* method [2] (see Chapter 7) the neutrino component is represented on a Fourier

grid in the N-body simulation. This grid is updated whenever the N-body long-range force is calculated and it is evolved with linear theory equations which themselves are sourced by the linear gravitational potential. Compared to the exact calculation with neutrinos represented by particles, the grid method leads to a loss of power due to the omitted non-linear corrections to the neutrino component. This translates into a 1% error in the matter power spectrum today for $\sum m_\nu \simeq 0.5\,\mathrm{eV}$. This error scale as $(\sum m_\nu)^2$ and especially appears at redshifts smaller than 1.

The grid method is much faster than the particle method, especially for smaller neutrino masses, and it also leads to a smaller memory consumption. For redshifts larger than ~ 4 the grid method is more accurate than the particle method since the former does not suffer from Poisson noise.

With the *hybrid* method [3] (see Chapter 8) the neutrino component is initially represented with the grid method until a redshift of $5-10$, with the exact redshift depending on the neutrino mass and therefore on when non-linear neutrino perturbations will become important. Then the lowest clustering part of neutrino momentum space, with momentum to temperature values of $q/T \lesssim 5-10$, is extracted from the grid and converted to neutrino N-body particles. Initial conditions for these particles are created from momentum dependent transfer functions and with thermal velocities corresponding to the particular momentum bin. The highest, least clustering part of momentum space is retained on the grid, which has the added advantage that very fast moving neutrino N-body particles do not need to be evolved in the N-body integrator.

The hybrid method can calculate the matter power spectrum fast and precisely for *all* neutrino masses. It is furthermore the only viable method to calculate the neutrino small-scale distribution. The only real problem with the hybrid method (disregarding algorithmic complexity) is related to the existence of a power leakage at large, mostly linear scales, arising from the simultaneous use of particle and grid implementations, though this leakage can be controlled.

The hybrid method was used to calculate neutrino and matter density profiles in halos with masses of $10^{12}-10^{15}\mathrm{M}_\odot$, as well as the effect of neutrinos on the halo mass function [4] (see Chapter 9). It was found that for a total neutrino mass lower than $\sim 0.5\,\mathrm{eV}$ the neutrino density in a Milky Way sized halo is only marginally larger than the average neutrino density. It was also shown that the N-body results for the neutrino density profiles were in good agreement with those found with the N-one-body method [72]. For lower mass halos, $\lesssim 10^{13}\mathrm{M}_\odot$, this agreement was only achieved by considering isolated halos, since the gravitational effect of a more massive host halo has a significant impact on the neutrino density profile.

Since the effect of neutrinos on the matter density profile is to delay halo formation, the halos are less concentrated as compared to a cosmology with the same value of Ω_m but without massive neutrinos. We have found that this physical effect mainly is a result of a neutrino induced suppression of power in the linear regime.

We also calculated the effect of massive neutrinos on the halo mass function which will be measured in large cluster surveys in the coming years. It was found that massive neutrinos lead to a significant reduction of the halo mass function, especially at the high mass end as compared to a massless neutrino model with the same matter content. Again, we found that this mainly is a result of a suppression of power caused by massive neutrinos in the linear regime. We furthermore showed that the Sheth-Tormen [102] semi-analytic formulae accurately, at the 2-3% level, predicted the suppression of the halo mass function caused by massive neutrinos, provided that only the clustering CDM and baryonic components were included in the Sheth-Tormen formalism. This result is important, since it allows the effect of massive neutrinos on the halo mass function to be included analytically.

The Cosmic Neutrino Background (CνB) anisotropies were calculated with linear theory for one-particle neutrino masses smaller than 0.1 eV [5] (see Chapter 10). For almost massless neutrinos, the CνB angular power spectrum closely resembles the CMB spectrum on large scales, whereas the baryon-photon acoustic oscillations are absent on smaller scales.

The effect of neutrino free-streaming is dominating at small angular scales, $l \gtrsim 100$, and in l-space this effect is more or less neutrino mass independent. At smaller l values the more massive neutrinos get trapped in the gravitational potential and this increases the angular power spectrum significantly.

We also calculated the effect of weak gravitational lensing on the massive neutrino states and applied the results to the primary CνB spectrum. This effect was found to be negligible.

We have presented a comparison between our results and those obtained by other scientific groups (see Chapter 11). It was found that N-body simulations, perturbation theory [19, 21] as well as the Renormalization Group time-flow approach [146] all predict an additional non-linear suppression of the matter power spectrum caused by massive neutrinos. Though these analytical approximations have their validity in the semi-linear regime, the fully non-linear matter power spectrum must be calculated with N-body simulations.

The effect of including non-linear neutrino perturbations on the total matter power spectrum was also investigated within the framework of perturbation theory [20, 22]. In this case perturbation theory and N-body simulations both found the same shape and redshift effect on the matter power spectrum. Despite these similarities the amplitude of the correction differed noticeably and for a precise calculation it must be found with N-body simulations.

Finally, two other scientific groups have performed N-body simulations with the effect of neutrinos included [57, 147], and they also found a turnover in the difference matter power spectrum, at the scale $k \sim 0.8 - 1\, h\,\mathrm{Mpc}^{-1}$ today, caused by massive neutrinos. Viel *et al.* implemented both the particle and grid approaches [57], and we have found that their and our grid implementations produce very similar results. This then led to the conclusion that their particle implementation differs noticeably from ours, whereafter it was thoroughly argued that our particle method appears to be correctly implemented.

Outlook The aim of the work presented in this dissertation has been to develop viable ways to include neutrinos in N-body simulations. These various methods have then been thoroughly tested and subsequently used to calculate new physical results. Before the closing of this dissertation it would be fruitful to ask how these methods can be improved and extended, and whether or not alternative methods might exist which could be better under certain circumstances. The following short discussion will be at the qualitative level.

The N-body simulation-time could potentially be decreased by more carefully designing the time-stepping in the presence of neutrino particles. Though we already have improved the time-step criterion for the Tree part, the long-range Particle-Mesh (PM) force is calculated very often since the neutrinos quickly traverse the PM spacing. The long-range time-step criterion has been developed for the case of gravitational flow velocities, but in reality it is being triggered by neutrino thermal velocities. Ideally the long-range force time-step criterion should instead depend on the neutrino gravitational flow velocities.

The hybrid method is the only viable path to simulate neutrino bound structures. But in smaller halos the neutrino overdensity is comparable to the average neutrino density. This in turn

demands a very high number density of neutrino N-body particles, and therefore the only feasible way to simulate neutrino structures in smaller halos (if the possibility of binning similar halos is ignored) is to make a zoom simulation. Since the thermal velocity leads to a leakage of neutrinos out of the high-resolution region, this region must be made periodic for the neutrinos.

Should the total neutrino mass be found to be close to the lower mass bound, then the assumption of degenerate neutrinos is poor. In this regime the grid approach will of course be very accurate for calculating the matter power spectrum, but if one is looking for the corresponding neutrino quantity then neutrinos should be implemented with the hybrid method as follows: Three separate neutrino N-body particle sets should be created with separate transfer functions, and the N-body particle mass and thermal velocity for each species should correspond to the particular neutrino mass eigenstate.

The grid approach is accurate for $\sum m_\nu \lesssim 0.5\,\mathrm{eV}$, but it might be possible to improve its precision for larger neutrino masses without using the more time-consuming hybrid method. For $\sum m_\nu = 1.2\,\mathrm{eV}$ we found that the grid method lacks accuracy at the 5% level today when neutrinos are represented by linear theory. But by using third-order perturbation theory with higher-order neutrino perturbations most of this error, 3.5%, can be corrected [22]. It would therefore be fruitful to implement third-order perturbation theory with higher-order neutrino perturbations on a grid in the N-body simulation. If the equations were then sourced by the fully non-linear gravitational potential which can be extracted from the N-body simulation, then this approach could be very promising. It would especially be useful if it turns out that the total neutrino mass is at the 1 eV level, as was recently indicated by the MiniBooNe experiment.

Finally it should be noted that the methods presented in this dissertation are not confined to modelling the neutrino component. The grid method can be used for any component, such as perturbed Dark Energy, whose perturbations only contribute at linear or semi-linear scales. Likewise the particle implementation and all the convergence tests presented will also be relevant for a Dark Matter candidate with a non-negligible thermal velocity during the non-linear structure formation era.

This PhD dissertation has presented methods to implement the effect of massive neutrinos in N-body simulations. The current final version, the hybrid method, beautifully takes advantage of the specific numerical value of the neutrino mass, in the sense that it combines linear and non-linear theory in a single integrator, which evolves non-linear perturbations in the Universe. With this method we have calculated several cosmological observables and numerous other applications can be found.

As a closing remark, I hope that at least part of the work presented in this dissertation will contribute to the overall progress of cosmology in the future.

Acknowledgements - standing on the shoulders of giants

I would very much like to thank Troels Haugbølle, Jan Hamann, Yvonne Wong, Steen Hannestad and Bjarne Thomsen for discussions and / or comments on the manuscript. I would also like to thank Pia Brandbyge for linguistic comments.

I would like to thank my supervisor Bjarne Thomsen for long discussions and fruitful comments on my scientific work. I would also like to thank Professor Steen Hannestad for inspiring me to investigate the effect of massive neutrinos on non-linear structure formation. Without his supervision, knowledge and enthusiasm the research presented in this thesis would not have achieved its current form.

I wish to thank Troels Haugbølle for numerous discussions on our papers as well as sharing with me his knowledge on numerical simulations. Thanks to Philip Jarnhus for sharing office with me and for many discussions on cosmology and life in general.

A special thanks goes to Karsten Brogaard and Jesper Bang for discussions, support and company during my studies and to Michael Graversen for inspiring me to investigate the cosmos.

I would like to thank the cosmology and astrophysics groups, Tina, Ole, Anders, Thomas, Rasmus, Philip, Tiago, Gulnur, Katrine, Anna, Karsten, Christoffer, Jan, Hans, Søren, Jørgen, Hans, Frank, Torben, Steen and Bjarne for coffee breaks, teaching and a great time. In general I acknowledge a pretty large consumption of black coffee.

I am especially grateful to my children, Vilfred, August and Silje and to my wife, Trine, for love and support.

Bibliography

[1] J. Brandbyge, S. Hannestad, T. Haugbølle and B. Thomsen, "The Effect of Thermal Neutrino Motion on the Non-linear Cosmological Matter Power Spectrum," JCAP **0808** (2008) 020 [arXiv:0802.3700 [astro-ph]].

[2] J. Brandbyge and S. Hannestad, "Grid Based Linear Neutrino Perturbations in Cosmological N-body Simulations," JCAP **0905** (2009) 002 [arXiv:0812.3149 [astro-ph]].

[3] J. Brandbyge and S. Hannestad, "Resolving Cosmic Neutrino Structure: A Hybrid Neutrino N-body Scheme," JCAP **1001** (2010) 021 [arXiv:0908.1969 [astro-ph.CO]].

[4] J. Brandbyge, S. Hannestad, T. Haugbølle and Y. Y. Y. Wong, "Neutrinos in Non-linear Structure Formation - The Effect on Halo Properties," arXiv:1004.4105 [astro-ph.CO].

[5] S. Hannestad and J. Brandbyge, "The Cosmic Neutrino Background Anisotropy - Linear Theory," JCAP **1003** (2010) 020 [arXiv:0910.4578 [astro-ph.CO]].

[6] T. R. Bedding *et al.*, "Solar-like oscillations in the G2 subgiant beta Hydri from dual-site observations," Astrophys. J. **663** (2007) 1315 [arXiv:astro-ph/0703747].

[7] A. Cuoco, J. Brandbyge, S. Hannestad, T. Haugbølle and G. Miele, "Angular Signatures of Annihilating Dark Matter in the Cosmic Gamma-Ray Background," Phys. Rev. D **77** (2008) 123518 [arXiv:0710.4136 [astro-ph]].

[8] http://hubblesite.org/newscenter/archive/releases/cosmology/2007/31/image/b/.

[9] C. P. Ma and E. Bertschinger, "Cosmological perturbation theory in the synchronous and conformal Newtonian gauges," Astrophys. J. **455**, 7 (1995) [arXiv:astro-ph/9506072].

[10] J. Lesgourgues and S. Pastor, "Massive neutrinos and cosmology," Phys. Rept. **429**, 307 (2006) [arXiv:astro-ph/0603494].

[11] S. Dodelson, "Modern Cosmology," *Amsterdam, Netherlands: Academic Pr. (2003) 440 p.*

[12] A. Lewis and S. Bridle, "Cosmological parameters from CMB and other data: a Monte-Carlo approach," Phys. Rev. D **66** (2002) 103511 [arXiv:astro-ph/0205436].

[13] A. Einstein, "On the General Theory of Relativity," Sitzungsber. Preuss. Akad. Wiss. Berlin (Math. Phys.) **1915** (1915) 778 [Addendum-ibid. **1915** (1915) 799].

[14] E. J. Copeland, M. Sami and S. Tsujikawa, "Dynamics of dark energy," Int. J. Mod. Phys. D **15** (2006) 1753 [arXiv:hep-th/0603057].

[15] A. Riotto, "Inflation and the theory of cosmological perturbations," arXiv:hep-ph/0210162.

[16] A. R. Liddle and D. H. Lyth, "Cosmological inflation and large-scale structure," *Cambridge, UK: Cambridge Univ. Pr. (2000) 400 p.*

[17] D. H. Perkins, "Particle astrophysics," *Oxford, UK: Univ. Pr. (2003) 256 p.*

[18] E. Hubble, "A relation between distance and radial velocity among extra–galactic nebulae," Proc. Nat. Acad. Sci. **15** (1929) 168.

[19] S. Saito, M. Takada and A. Taruya, "Impact of massive neutrinos on nonlinear matter power spectrum," AIP Conf. Proc. **1040** (2008) 32 [arXiv:0801.0607 [astro-ph]].

[20] S. Saito, M. Takada and A. Taruya, "Nonlinear power spectrum in the presence of massive neutrinos: perturbation theory approach, galaxy bias and parameter forecasts," Phys. Rev. D **80** (2009) 083528 [arXiv:0907.2922 [astro-ph.CO]].

[21] Y. Y. Y. Wong, "Higher order corrections to the large scale matter power spectrum in the presence of massive neutrinos," JCAP **0810**, 035 (2008) [arXiv:0809.0693 [astro-ph]].

[22] M. Shoji and E. Komatsu, "Third-order Perturbation Theory With Non-linear Pressure," Astrophys. J. **700**, 705 (2009) [arXiv:0903.2669 [astro-ph.CO]].

[23] Y. B. Zeldovich, "Gravitational instability: An Approximate theory for large density perturbations," Astron. Astrophys. **5**, 84 (1970).

[24] F. R. Bouchet, S. Colombi, E. Hivon and R. Juszkiewicz, "Perturbative Lagrangian approach to gravitational instability," Astron. Astrophys. **296**, 575 (1995) [arXiv:astro-ph/9406013].

[25] R. Scoccimarro, "Transients from Initial Conditions: A Perturbative Analysis," Mon. Not. Roy. Astron. Soc. **299**, 1097 (1998) [arXiv:astro-ph/9711187].

[26] V. Springel, "The cosmological simulation code GADGET-2," Mon. Not. Roy. Astron. Soc. **364**, 1105 (2005) [arXiv:astro-ph/0505010].

[27] V. Springel, N. Yoshida and S. D. M. White, "GADGET: A code for collisionless and gasdynamical cosmological simulations," New Astron. **6**, 79 (2001) [arXiv:astro-ph/0003162].

[28] V. Springel, http://www.mpa-garching.mpg.de/gadget.

[29] V. Springel, http://www.mpa-garching.mpg.de/gadget/users-guide.pdf.

[30] K. Heitmann *et al.*, "The Cosmic Code Comparison Project," Comput. Sci. Dis. **1** (2008) 015003 [arXiv:0706.1270 [astro-ph]].

[31] J. S. Bagla and S. Ray, "Performance Characteristics of TreePM codes," New Astron. **8**, 665 (2003) [arXiv:astro-ph/0212129].

[32] T. R. Quinn, N. Katz, J. Stadel and G. Lake, "Time stepping N-body simulations," arXiv:astro-ph/9710043.

[33] G. L. Fogli, E. Lisi, A. Marrone and A. Palazzo, "Global analysis of three-flavor neutrino masses and mixings," Prog. Part. Nucl. Phys. **57**, 742 (2006) [arXiv:hep-ph/0506083].

[34] M. Maltoni, T. Schwetz, M. A. Tortola and J. W. F. Valle, "Status of global fits to neutrino oscillations," New J. Phys. **6**, 122 (2004) [arXiv:hep-ph/0405172].

[35] M. Fukugita and T. Yanagida, "Physics of neutrinos and applications to astrophysics," *Berlin, Germany: Springer (2003) 593 p.*

[36] R. Van de Water for the MiniBooNE Collaboration, "Updated anti-neutrino oscillation results from MiniBooNE," (Neutrino 2010, XXIV International Conference on Neutrino Physics and Astrophysics, 14-19 June 2010, Athens, Greece), see http://indico.cern.ch/event/73981.

[37] J. Hamann, S. Hannestad, G. G. Raffelt, I. Tamborra and Y. Y. Y. Wong, "Cosmology seeking friendship with sterile neutrinos," arXiv:1006.5276 [hep-ph].

[38] S. Abe *et al.* [KamLAND Collaboration], "Precision Measurement of Neutrino Oscillation Parameters with KamLAND," Phys. Rev. Lett. **100**, 221803 (2008) [arXiv:0801.4589 [hep-ex]].

[39] B. Aharmim *et al.* [SNO Collaboration], "An Independent Measurement of the Total Active 8B Solar Neutrino Flux Using an Array of 3He Proportional Counters at the Sudbury Neutrino Observatory," Phys. Rev. Lett. **101**, 111301 (2008) [arXiv:0806.0989 [nucl-ex]].

[40] M. Maltoni and T. Schwetz, "Three-flavour neutrino oscillation update and comments on possible hints for a non-zero θ_{13}," PoS **IDM2008**, 072 (2008) [arXiv:0812.3161 [hep-ph]].

[41] S. Hannestad, "Neutrino physics from precision cosmology," arXiv:1007.0658 [hep-ph].

[42] R. E. Smith *et al.* [The Virgo Consortium Collaboration], "Stable clustering, the halo model and nonlinear cosmological power spectra," Mon. Not. Roy. Astron. Soc. **341**, 1311 (2003) [arXiv:astro-ph/0207664].

[43] http://www.supernova.lbl.gov/public/papers/knop03/SCP2003SNeCMBClust.pdf.

[44] M. Tegmark *et al.* [SDSS Collaboration], "The 3D power spectrum of galaxies from the SDSS," Astrophys. J. **606** (2004) 702 [arXiv:astro-ph/0310725].

[45] M. Tegmark and M. Zaldarriaga, "Separating the Early Universe from the Late Universe: cosmological parameter estimation beyond the black box," Phys. Rev. D **66** (2002) 103508 [arXiv:astro-ph/0207047].

[46] E. Komatsu *et al.*, "Seven-Year Wilkinson Microwave Anisotropy Probe (WMAP) Observations: Cosmological Interpretation," arXiv:1001.4538 [astro-ph.CO].

[47] C. L. Reichardt *et al.*, "High resolution CMB power spectrum from the complete ACBAR data set," Astrophys. J. **694**, 1200 (2009) [arXiv:0801.1491 [astro-ph]].

[48] M. L. Brown *et al.* [QUaD collaboration], "Improved measurements of the temperature and polarization of the CMB from QUaD," Astrophys. J. **705**, 978 (2009) [arXiv:0906.1003 [astro-ph.CO]].

[49] http://www.sdss.org/includes/sideimages/sdss_pie2.jpg.

[50] B. A. Reid *et al.*, "Cosmological Constraints from the Clustering of the Sloan Digital Sky Survey DR7 Luminous Red Galaxies," Mon. Not. Roy. Astron. Soc. **404**, 60 (2010) [arXiv:0907.1659 [astro-ph.CO]].

[51] W. J. Percival *et al.*, "Baryon Acoustic Oscillations in the Sloan Digital Sky Survey Data Release 7 Galaxy Sample," Mon. Not. Roy. Astron. Soc. **401**, 2148 (2010) [arXiv:0907.1660 [astro-ph.CO]].

[52] A. G. Riess *et al.*, "A Redetermination of the Hubble Constant with the Hubble Space Telescope from a Differential Distance Ladder," Astrophys. J. **699**, 539 (2009) [arXiv:0905.0695 [astro-ph.CO]].

[53] A. G. Riess *et al.*, "Cepheid Calibrations of Modern Type Ia Supernovae:Implications for the Hubble Constant," Astrophys. J. Suppl. **183**, 109 (2009) [arXiv:0905.0697 [astro-ph.CO]].

[54] W. L. Freedman *et al.* [HST Collaboration], "Final Results from the Hubble Space Telescope Key Project to Measure the Hubble Constant," Astrophys. J. **553**, 47 (2001) [arXiv:astro-ph/0012376].

[55] S. Hannestad, "Neutrino masses and the dark energy equation of state: Relaxing the cosmological neutrino mass bound," Phys. Rev. Lett. **95**, 221301 (2005) [arXiv:astro-ph/0505551].

[56] J. Hamann, S. Hannestad, J. Lesgourgues, C. Rampf and Y. Y. Y. Wong, "Cosmological parameters from large scale structure - geometric versus shape information," arXiv:1003.3999 [astro-ph.CO].

[57] M. Viel, M. G. Haehnelt and V. Springel, "The effect of neutrinos on the matter distribution as probed by the Intergalactic Medium," JCAP **1006**, 015 (2010) [arXiv:1003.2422 [astro-ph.CO]].

[58] C. Zunckel and P. G. Ferreira, "Conservative estimates of the mass of the neutrino from cosmology," [arXiv:astro-ph/0610597].

[59] M. Cirelli and A. Strumia, "Cosmology of neutrinos and extra light particles after WMAP3," JCAP **0612** (2006) 013 [arXiv:astro-ph/0607086].

[60] A. Goobar, S. Hannestad, E. Mortsell and H. Tu, "A new bound on the neutrino mass from the SDSS baryon acoustic peak," JCAP **0606** (2006) 019 [arXiv:astro-ph/0602155].

[61] J. R. Kristiansen, H. K. Eriksen and O. Elgaroy, "Revised WMAP constraints on neutrino masses and other extensions of the minimal Lambda CDM model," Phys. Rev. D **74**, 123005 (2006).

[62] U. Seljak, A. Slosar and P. McDonald, "Cosmological parameters from combining the Lyman-alpha forest with CMB, galaxy clustering and SN constraints," JCAP **0610**, 014 (2006) [arXiv:astro-ph/0604335].

[63] S. Hannestad, "Neutrino masses and the number of neutrino species from WMAP and 2dFGRS," JCAP **0305**, 004 (2003) [arXiv:astro-ph/0303076].

[64] S. Hannestad, "Primordial neutrinos," Ann. Rev. Nucl. Part. Sci. **56** (2006) 137 [arXiv:hep-ph/0602058].

[65] S. Hannestad, "Global neutrino parameter estimation using Markov Chain Monte Carlo," arXiv:0710.1952 [hep-ph].

[66] S. Hannestad, A. Mirizzi, G. G. Raffelt and Y. Y. Y. Wong, "Cosmological constraints on neutrino plus axion hot dark matter," JCAP **0708**, 015 (2007) [arXiv:0706.4198 [astro-ph]].

[67] www.lsst.org.

[68] A. Klypin, J. Holtzman, J. Primack and E. Regos, "Structure formation with cold plus hot dark matter," Astrophys. J. **416**, 1 (1993) [arXiv:astro-ph/9305011].

[69] J. R. Primack, J. Holtzman, A. Klypin and D. O. Caldwell, "Cold + hot dark matter cosmology with m (muon-neutrino) approximates m (tau-neutrino) approximates 2.4-eV," Phys. Rev. Lett. **74**, 2160 (1995) [arXiv:astro-ph/9411020].

[70] P. Colin, O. Valenzuela and V. Avila-Reese, "On the Structure of Dark Matter Halos at the Damping Scale of the Power Spectrum with and without Relict Velocities," [arXiv:0709.4027 [astro-ph]].

[71] S. Singh and C. P. Ma, "Neutrino clustering in cold dark matter halos: Implications for ultra high energy cosmic rays," Phys. Rev. D **67**, 023506 (2003) [arXiv:astro-ph/0208419].

[72] A. Ringwald and Y. Y. Y. Wong, "Gravitational clustering of relic neutrinos and implications for their detection," JCAP **0412**, 005 (2004) [arXiv:hep-ph/0408241].

[73] U. Seljak and M. Zaldarriaga, "A Line of Sight Approach to Cosmic Microwave Background Anisotropies," Astrophys. J. **469**, 437 (1996) [arXiv:astro-ph/9603033].

[74] D. N. Spergel *et al.* [WMAP Collaboration], "Wilkinson Microwave Anisotropy Probe (WMAP) three year results: Implications for cosmology," Astrophys. J. Suppl. **170**, 377 (2007) [arXiv:astro-ph/0603449].

[75] M. Crocce, S. Pueblas and R. Scoccimarro, "Transients from Initial Conditions in Cosmological Simulations," Mon. Not. Roy. Astron. Soc. **373**, 369 (2006) [arXiv:astro-ph/0606505].

[76] J. J. Monaghan and J. C. Lattanzio, "A refined particle method for astrophysical problems," Astron. Astrophys. **149**, 135 (1985).

[77] S. Hannestad, H. Tu and Y. Y. Y. Wong, "Measuring neutrino masses and dark energy with weak lensing tomography," JCAP **0606**, 025 (2006) [arXiv:astro-ph/0603019].

[78] D. A. Dicus, E. W. Kolb, A. M. Gleeson, E. C. Sudarshan, V. L. Teplitz and M. S. Turner, "Primordial Nucleosynthesis Including Radiative, Coulomb, And Finite Temperature Corrections To Weak Rates," Phys. Rev. D **26**, 2694 (1982).

[79] S. Dodelson and M. S. Turner, "Nonequilibrium neutrino statistical mechanics in the expanding universe," Phys. Rev. D **46**, 3372 (1992).

[80] S. Hannestad and J. Madsen, "Neutrino decoupling in the early universe," Phys. Rev. D **52**, 1764 (1995) [arXiv:astro-ph/9506015].

[81] A. D. Dolgov, S. H. Hansen and D. V. Semikoz, "Non-equilibrium corrections to the spectra of massless neutrinos in the early universe," Nucl. Phys. B **503**, 426 (1997) [arXiv:hep-ph/9703315].

[82] G. Steigman, "Precision neutrino counting," arXiv:astro-ph/0108148.

[83] G. Mangano, G. Miele, S. Pastor and M. Peloso, "A precision calculation of the effective number of cosmological neutrinos," [arXiv:astro-ph/0111408].

[84] S. Hannestad, "Oscillation effects on neutrino decoupling in the early universe," Phys. Rev. D **65** (2002) 083006 [arXiv:astro-ph/0111423].

[85] G. Mangano, G. Miele, S. Pastor, T. Pinto, O. Pisanti and P. D. Serpico, "Relic neutrino decoupling including flavour oscillations," Nucl. Phys. B **729**, 221 (2005) [arXiv:hep-ph/0506164].

[86] W. Hu, D. J. Eisenstein and M. Tegmark, "Weighing neutrinos with galaxy surveys," Phys. Rev. Lett. **80**, 5255 (1998) [arXiv:astro-ph/9712057].

[87] S. Hannestad, A. Ringwald, H. Tu and Y. Y. Y. Wong, "Is it possible to tell the difference between fermionic and bosonic hot dark matter?," JCAP **0509**, 014 (2005) [arXiv:astro-ph/0507544].

[88] See e.g. J. Lesgourgues, S. Pastor and L. Perotto, "Probing neutrino masses with future galaxy redshift surveys," Phys. Rev. D **70**, 045016 (2004) [arXiv:hep-ph/0403296]; S. Wang, Z. Haiman, W. Hu, J. Khoury and M. May, "Weighing neutrinos with galaxy cluster surveys," Phys. Rev. Lett. **95**, 011302 (2005) [arXiv:astro-ph/0505390]; S. Hannestad and Y. Y. Y. Wong, "Neutrino mass from future high redshift galaxy surveys: Sensitivity and detection threshold," JCAP **0707**, 004 (2007) [arXiv:astro-ph/0703031].

[89] K. Heitmann, M. White, C. Wagner, S. Habib and D. Higdon, "The Coyote Universe I: Precision Determination of the Nonlinear Matter Power Spectrum," Astrophys. J. **715** (2010) 104 [arXiv:0812.1052 [astro-ph]].

[90] J. R. Bond, G. Efstathiou and J. Silk, "Massive neutrinos and the large-scale structure of the universe," Phys. Rev. Lett. **45** (1980) 1980.

[91] A. G. Doroshkevich, Y. B. Zeldovich, R. A. Sunyaev and M. Khlopov, "Astrophysical implications of the neutrino rest mass. II. The density-perturbation spectrum and small-scale fluctuations in the microwave background," Sov. Astron. Lett. **6** (1980) 252 [Pisma Astron. Zh. **6** (1980) 457].

[92] S. Wang, Z. Haiman, W. Hu, J. Khoury and M. May, "Weighing Neutrinos with Galaxy Cluster Surveys," Phys. Rev. Lett. **95**, 011302 (2005) [arXiv:astro-ph/0505390].

[93] L. Kofman, A. Klypin, D. Pogosian and J. P. Henry, "Mixed dark matter in halos of clusters," Astrophys. J. **470**, 102 (1996) [arXiv:astro-ph/9509145].

[94] A. Lewis, A. Challinor and A. Lasenby, "Efficient Computation of CMB anisotropies in closed FRW models," Astrophys. J. **538** (2000) 473 [arXiv:astro-ph/9911177].

[95] S. R. Knollmann and A. Knebe, "Ahf: Amiga's Halo Finder," Astrophys. J. Suppl. **182** (2009) 608 [arXiv:0904.3662 [astro-ph.CO]].

[96] J. F. Navarro, C. S. Frenk and S. D. M. White, "A Universal Density Profile from Hierarchical Clustering," Astrophys. J. **490** (1997) 493 [arXiv:astro-ph/9611107].

[97] J. S. Bullock *et al.*, "Profiles of dark haloes: evolution, scatter, and environment," Mon. Not. Roy. Astron. Soc. **321** (2001) 559 [arXiv:astro-ph/9908159].

[98] G. L. Bryan and M. L. Norman, "Statistical Properties of X-ray Clusters: Analytic and Numerical Comparisons," Astrophys. J. **495** (1998) 80 [arXiv:astro-ph/9710107].

[99] S. Tremaine and J. E. Gunn, "Dynamical role of light neutral leptons in cosmology," Phys. Rev. Lett. **42** (1979) 407.

[100] O. Fakhouri, C. P. Ma and M. Boylan-Kolchin, "The Merger Rates and Mass Assembly Histories of Dark Matter Haloes in the Two Millennium Simulations," arXiv:1001.2304 [astro-ph.CO].

[101] R. H. Wechsler, J. S. Bullock, J. R. Primack, A. V. Kravtsov and A. Dekel, "Concentrations of Dark Halos from their Assembly Histories," Astrophys. J. **568**, 52 (2002) [arXiv:astro-ph/0108151].

[102] R. K. Sheth and G. Tormen, "An Excursion Set Model Of Hierarchical Clustering : Ellipsoidal Collapse And The Moving Barrier," Mon. Not. Roy. Astron. Soc. **329**, 61 (2002) [arXiv:astro-ph/0105113]; R. K. Sheth and G. Tormen, "Large scale bias and the peak background split," Mon. Not. Roy. Astron. Soc. **308**, 119 (1999) [arXiv:astro-ph/9901122].

[103] A. Jenkins *et al.*, "Mass function of dark matter halos," Mon. Not. Roy. Astron. Soc. **321**, 372 (2001) [arXiv:astro-ph/0005260].

[104] M. S. Warren, K. Abazajian, D. E. Holz and L. Teodoro, "Precision Determination of the Mass Function of Dark Matter Halos," Astrophys. J. **646**, 881 (2006) [arXiv:astro-ph/0506395].

[105] W. H. Press and P. Schechter, "Formation of galaxies and clusters of galaxies by selfsimilar gravitational condensation," Astrophys. J. **187**, 425 (1974).

[106] E. Komatsu *et al.* [WMAP Collaboration], "Five-Year Wilkinson Microwave Anisotropy Probe (WMAP)Observations: Cosmological Interpretation," Astrophys. J. Suppl. **180**, 330 (2009) [arXiv:0803.0547 [astro-ph]].

[107] J. Hamann, S. Hannestad, G. G. Raffelt and Y. Y. Y. Wong, "Observational bounds on the cosmic radiation density," JCAP **0708**, 021 (2007) [arXiv:0705.0440 [astro-ph]].

[108] F. de Bernardis, A. Melchiorri, L. Verde and R. Jimenez, "The Cosmic Neutrino Background and the Age of the Universe," JCAP **0803**, 020 (2008) [arXiv:0707.4170 [astro-ph]].

[109] K. Ichikawa, T. Sekiguchi and T. Takahashi, "Probing the Effective Number of Neutrino Species with Cosmic Microwave Background," Phys. Rev. D **78**, 083526 (2008) [arXiv:0803.0889 [astro-ph]].

[110] J. Hamann, S. Hannestad, A. Melchiorri and Y. Y. Y. Wong, "Nonlinear corrections to the cosmological matter power spectrum and scale-dependent galaxy bias: implications for parameter estimation," JCAP **0807**, 017 (2008) [arXiv:0804.1789 [astro-ph]].

[111] L. A. Popa and A. Vasile, "WMAP 5-year constraints on lepton asymmetry and radiation energy density: Implications for Planck," JCAP **0806**, 028 (2008) [arXiv:0804.2971 [astro-ph]].

[112] S. Bashinsky and U. Seljak, "Signatures of relativistic neutrinos in CMB anisotropy and matter clustering," Phys. Rev. D **69**, 083002 (2004) [arXiv:astro-ph/0310198].

[113] R. Trotta and A. Melchiorri, "Indication for primordial anisotropies in the neutrino background from WMAP and SDSS," Phys. Rev. Lett. **95**, 011305 (2005) [arXiv:astro-ph/0412066].

[114] N. F. Bell, E. Pierpaoli and K. Sigurdson, "Cosmological signatures of interacting neutrinos," Phys. Rev. D **73**, 063523 (2006) [arXiv:astro-ph/0511410].

[115] F. De Bernardis, L. Pagano, P. Serra, A. Melchiorri and A. Cooray, "Anisotropies in the Cosmic Neutrino Background after WMAP 5-year Data," JCAP **0806**, 013 (2008) [arXiv:0804.1925 [astro-ph]].

[116] A. Basbøll, O. E. Bjælde, S. Hannestad and G. G. Raffelt, "Are cosmological neutrinos free-streaming?," Phys. Rev. D **79**, 043512 (2009) [arXiv:0806.1735 [astro-ph]].

[117] S. Hannestad, "Structure formation with strongly interacting neutrinos: Implications for the cosmological neutrino mass bound," JCAP **0502**, 011 (2005) [arXiv:astro-ph/0411475].

[118] A. Friedland, K. M. Zurek and S. Bashinsky, "Constraining Models of Neutrino Mass and Neutrino Interactions with the Planck Satellite," arXiv:0704.3271 [astro-ph].

[119] S. Weinberg, "Universal Neutrino Degeneracy," Phys. Rev. **128**, 1457 (1962).

[120] A. G. Cocco, G. Mangano and M. Messina, "Probing low energy neutrino backgrounds with neutrino capture on beta decaying nuclei," JCAP **0706**, 015 (2007) [J. Phys. Conf. Ser. **110**, 082014 (2008)] [arXiv:hep-ph/0703075].

[121] M. Blennow, "Prospects for cosmic neutrino detection in tritium experiments in the case of hierarchical neutrino masses," Phys. Rev. D **77**, 113014 (2008) [arXiv:0803.3762 [astro-ph]].

[122] T. J. Weiler, "Resonant Absorption Of Cosmic Ray Neutrinos By The Relic Neutrino Background," Phys. Rev. Lett. **49**, 234 (1982).

[123] L. Stodolsky, "Speculations On Detection Of The Neutrino Sea," Phys. Rev. Lett. **34**, 110 (1975) [Erratum-ibid. **34**, 508 (1975)].

[124] G. B. Gelmini, "Prospect for relic neutrino searches," Phys. Scripta **T121**, 131 (2005) [arXiv:hep-ph/0412305].

[125] Z. Fodor, S. D. Katz and A. Ringwald, "Relic neutrino masses and the highest energy cosmic rays," JHEP **0206**, 046 (2002) [arXiv:hep-ph/0203198].

[126] G. Duda, G. Gelmini and S. Nussinov, "Expected signals in relic neutrino detectors," Phys. Rev. D **64**, 122001 (2001) [arXiv:hep-ph/0107027].

[127] P. Langacker, J. P. Leveille and J. Sheiman, "On The Detection Of Cosmological Neutrinos By Coherent Scattering," Phys. Rev. D **27**, 1228 (1983).

[128] N. Cabibbo and L. Maiani, "The Vanishing Of Order G Mechanical Effects Of Cosmic Massive Neutrinos On Bulk Matter," Phys. Lett. B **114**, 115 (1982).

[129] S. Pastor, G. G. Raffelt and D. V. Semikoz, "Physics of synchronized neutrino oscillations caused by self-interactions," Phys. Rev. D **65**, 053011 (2002) [arXiv:hep-ph/0109035].

[130] S. Pastor, T. Pinto and G. G. Raffelt, "Relic density of neutrinos with primordial asymmetries," Phys. Rev. Lett. **102**, 241302 (2009) [arXiv:0808.3137 [astro-ph]].

[131] V. Simha and G. Steigman, "Constraining The Universal Lepton Asymmetry," JCAP **0808**, 011 (2008) [arXiv:0806.0179 [hep-ph]].

[132] Y. Y. Y. Wong, "Analytical treatment of neutrino asymmetry equilibration from flavour oscillations in the early universe," Phys. Rev. D **66**, 025015 (2002) [arXiv:hep-ph/0203180].

[133] K. N. Abazajian, J. F. Beacom and N. F. Bell, "Stringent constraints on cosmological neutrino antineutrino asymmetries from synchronized flavor transformation," Phys. Rev. D **66**, 013008 (2002) [arXiv:astro-ph/0203442].

[134] W. Hu, D. Scott, N. Sugiyama and M. J. . White, "The Effect Of Physical Assumptions On The Calculation Of Microwave Background Anisotropies," Phys. Rev. D **52**, 5498 (1995) [arXiv:astro-ph/9505043].

[135] R. J. Michney and R. R. Caldwell, "Anisotropy of the Cosmic Neutrino Background," JCAP **0701**, 014 (2007) [arXiv:astro-ph/0608303].

[136] E. Bertschinger, "COSMICS: Cosmological Initial Conditions and Microwave Anisotropy Codes," arXiv:astro-ph/9506070.

[137] K. M. Gorski, E. Hivon, A. J. Banday, B. D. Wandelt, F. K. Hansen, M. Reinecke and M. Bartelman, "HEALPix – a Framework for High Resolution Discretization, and Fast Analysis of Data Distributed on the Sphere," Astrophys. J. **622**, 759 (2005) [arXiv:astro-ph/0409513].

[138] S. Dodelson and M. Vesterinen, "Cosmic Neutrino Last Scattering Surface," Phys. Rev. Lett. **103** (2009) 171301 [Erratum-ibid. **103** (2009) 249901] [arXiv:0907.2887 [astro-ph.CO]].

[139] U. Seljak, "Gravitational lensing effect on cosmic microwave background anisotropies: A Power spectrum approach," Astrophys. J. **463**, 1 (1996) [arXiv:astro-ph/9505109].

[140] A. Challinor and A. Lewis, "Lensed CMB power spectra from all-sky correlation functions," Phys. Rev. D **71** (2005) 103010 [arXiv:astro-ph/0502425].

[141] A. Lewis and A. Challinor, "Weak Gravitational Lensing of the CMB," Phys. Rept. **429** (2006) 1 [arXiv:astro-ph/0601594].

[142] N. Kaiser, "Weak gravitational lensing of distant galaxies," Astrophys. J. **388**, 272 (1992) [arXiv:astro-ph/9603033].

[143] B. Jain and U. Seljak, "Cosmological Model Predictions for Weak Lensing: Linear and Non-linear Regimes," Astrophys. J. **484**, 560 (1997) [arXiv:astro-ph/9611077].

[144] M. Shoji and E. Komatsu, "Massive Neutrinos in Cosmology: Analytic Solutions and Fluid Approximation," Phys. Rev. D **81**, 123516 (2010) [arXiv:1003.0942 [astro-ph.CO]].

[145] M. Pietroni, "Flowing with Time: a New Approach to Nonlinear Cosmological Perturbations," JCAP **0810**, 036 (2008) [arXiv:0806.0971 [astro-ph]].

[146] J. Lesgourgues, S. Matarrese, M. Pietroni and A. Riotto, "Non-linear Power Spectrum including Massive Neutrinos: the Time-RG Flow Approach," JCAP **0906**, 017 (2009) [arXiv:0901.4550 [astro-ph.CO]].

[147] S. Agarwal and H. A. Feldman, "The Effect of Massive Neutrinos on Matter Power Spectrum," arXiv:1006.0689 [astro-ph.CO].